Crystal chemistry, melt composition and redox controls on the behavior of trace elements during lunar magmatism

Felipe Padilha Leitzke

Bonn 2018

Crystal chemistry, melt composition and redox controls on the behavior of trace elements during lunar magmatism

Dissertation
zur
Erlangung des Doktorgrades (Dr. rer. nat.)
der
Mathematisch-Naturwissenschaftlichen Fakultät
der
Rheinischen Friedrich-Wilhelms-Universität Bonn

vorgelegt von
Felipe Padilha Leitzke
aus Pelotas, Brasilien

Bonn, 2018

Angefertigt mit Genehmigung der Mathematisch-Naturwissenschaftlichen Fakultät der Rheinischen Friedrich-Wilhelms-Universität Bonn

1. Gutachter: PD Raúl O. C. Fonseca, PhD (Universität zu Köln)

2. Gutachter: Prof. Dr. Chris Ballhaus (Universität Bonn)

Tag der Promotion: 5. Dezember 2018

Erscheinungsjahr: 2018

An Eides statt versichere ich, dass die vorgelegte Arbeit abgesehen von den ausdrücklich bezeichneten Hilfsmitteln - persönlich, selbständig und ohne Benutzung anderer als der angegebenen Hilfsmittel angefertigt wurde, die aus anderen Quellen direkt oder indirekt übernommenen Daten und Konzepte unter Angabe der Quelle kenntlich gemacht sind, die vorgelegte Arbeit oder ähnliche Arbeiten nicht bereits anderweitig als Dissertation eingereicht worden ist bzw. sind, für die inhaltlich - materielle Erstellung der vorgelegten Arbeit keine fremde Hilfe, insbersondere keine entgeltlich Hilfe von Vermittlungs - bzw. Beratungsdiensten (Promotionsberater oder andere Personen) in Anspruch genommen wurde sowie keinerlei Dritte vom Doktoranden unmittelbar oder mittelbar geldwerte Leistungen für Tätigkeiten erhalten haben, die im Zusammenhang mit dem Inhalt der vorgelegten Arbeit stehen.

Felipe Padilha Leitzke

This work is dedicated to my family

who have always supported me.

"History of science and technology has consistently taught us that scientific advances in basic understanding have sooner or later led to technical and industrial applications that have revolutionized our way of life. What is less certain, and what we all fervently hope, is that man will soon grow sufficiently adult to make good use of the powers that he acquires over nature."

Enrico Fermi

Contents

List of Figures

List of Tables

Preface

This thesis is submitted in partial fulfilment of the requirements for obtaining the Ph.D. degree in Natural Sciences (Doctor rerum naturalium) at the University of Bonn. The work described herein was conducted at the Experimental Petrology Research Group of the Steinmann Institute for Geosciences between September 2014 and July 2018 under the supervision of Dr. Raúl Fonseca. The PhD. scholarship was funded by the Brazilian National Council for Scientific and Technological Development (CNPq) in cooperation with the German Academic Exchange Service (DAAD) at the "Science without Borders" (*Ciência sem Fronteiras – Wissenschaft ohne Grenzen*) exchange program, through the grant 248562/2013-4. The thesis follows a peer-reviewed articles based approach in accordance with the guidelines of the University of Bonn and includes three main chapters based on the following papers:

1. Michely, L.T., **Leitzke, F.P.**, Speelmanns, I. M., Fonseca, R.O.C. 2017. Competing effects of crystal chemistry and silicate melt composition on trace element behavior in magmatic systems: insights from crystal/silicate melt partitioning of the REE, HFSE, Sn, In, Ga, Ba, Pt and Rh. *Contributions to Mineralogy and Petrology*, v. 172, n. 39, doi: 10.1007/s00410-017-1353-1 **(Chapter 2)**.

2. **Leitzke, F.P.**, Fonseca, R.O.C., Michely, L.T., Sprung, P., Münker, C., Heuser, A., Blanchard, H. 2016. The effect of titanium on the partitioning behavior of high-field strength elements between silicates, oxides and lunar basaltic melts with applications to the origin of mare basalts. *Chemical Geology*, v. 440, p. 219-238, https://doi.org/10.1016/j.chemgeo.2016.07.011 **(Chapter 3)**.

3. **Leitzke, F.P.**, Fonseca, R.O.C., Sprung, P. Mallmann, G., Lagos, M. Michely, L.T., Münker, C. 2017. Redox dependent behaviour of molybdenum during magmatic processes in the terrestrial and lunar mantle: Implications for the Mo/W of the bulk silicate Moon. *Earth and Planetary Science Letters*, v. 474, p. 503-515, https://doi.org/10.1016/j.epsl.2017.07.009 **(Chapter 4)**.

The published articles are included as chapters of the thesis. The following conference abstracts were also written and presented in international scientific meetings during the Ph.D. period, and deal with the general topic of the thesis:

4. Leitzke, F.P., Fonseca, R.O.C, Sprung, P., Mallmann, G., Lagos, M., Michely, L.T., Münker, C. 2017. Evidence for a primitive terrestrial Mo/W of the bulk-silicate Moon. *Goldschmidt Abstracts*, n. 2259.

5. Leitzke, F.P., Fonseca, R.O.C, Mallmann, G., Sprung, P., Lagos, M., Michely, L.T., Münker, C. 2017. Redox transition and compatibility of Mo during partial melting in the lunar mantle. *Abstracts booklet of the Fifth European Lunar Symposium (ELS), NASA Solar System Exploration Research Virtual Institute (SSERVI)*, p. 132-133.

6. Leitzke, F.P., Fonseca, R.O.C, Michely, L.T., Sprung, P., Heuser, A., Münker, C. 2016. Crystal/silicate melt partitioning of HFSE, Mo, W, U and Th as a function of TiO_2, with implications for the petrogenesis of lunar mare basalts. *Proceedings of the 79th Annual Meeting of the Meteoritical Society*, n. 6232.

7. Leitzke, F.P., Fonseca, R.O.C, Michely, L.T. 2016. One atmosphere experimental study on the partitioning of the HFSE between olivine, pyroxene and lunar basaltic melts in the CMAS + Fe + Ti system. *Geophysical Research Abstracts*, v. 18. p. 1565.

Abstract

The behavior of trace elements in magmatic systems is controlled by physico-chemical conditions prevalent during mantle partial melting and magmatic differentiation. Among these controlling factors are temperature, depth, type and degree of melting, source mineralogical composition and fO_2. In order to generate a coherent, systematic dataset of crystal/silicate melt partition coefficients for trace elements as a function of crystal and silicate melt composition, and fO_2, this thesis provides new partition coefficients for the REE, Y, HFSE, Sc, Ba, Sr, Cr, U, Th, Mo, W, Sn, In, Ga, Pt, and Rh between crystalline mantle phases (Fe-Ti oxides, pyroxene, plagioclase, spinel, and olivine) and basaltic melts, in particular under conditions relevant to lunar magmatism. Experiments were conducted in vertical tube gas-mixing furnaces (1 bar) at temperatures between 1100 °C - 1300 °C, and fO_2 from 5.5 log units below the fayalite-magnetite-quartz (FMQ) redox buffer to air, thereby covering the range of temperatures and oxygen fugacities during planetary differentiation processes. At first, two element species, namely Al_2O_3 and Na_2O, were chosen to be investigated since they are known to affect the structure of silicate melts and especially clinopyroxene crystal chemistry. The amount of $^{[4]}$Al in clinopyroxene will result in an increase of $D_i^{cpx/melt}$ even after applying a correction factor to account for the effect of melt polymerization. Moreover, the positive correlation between $^{[4]}$Al and $D_i^{cpx/melt}$ is not restricted to the REE, but also applies for Sn, Ga, In, and Ba. The addition of up to 2.6 wt% Na_2O to the silicate melt universally increases the $D_i^{cpx/melt}$ without any concomitant change in crystal chemistry or a significant effect in melt polymerization. This compositional effect is likely due to the ability of Na to break REE-Al-O-complexes in the melt. Our results emphasize the importance of considering all variables that affect the behaviour of trace elements in magmatic systems before applying

the lattice strain model and derive meaningful results for changes in the parameters of crystallographic sites. A specific feature of some basaltic lunar rocks is that their TiO_2 contents can reach concentrations as high as 16 wt. %. The High-field strength elements (HFSE) group, which includes Ti, may provide valuable information on the processes that occurred in the lunar mantle to generate high-Ti mare basalts. With the exception of Nb, all $D_{HFSE}^{cpx/melt}$ show a strong negative correlation with the TiO_2 content of the silicate melt. Olivine/silicate melt partition coefficients for Zr, Hf, Nb, Ta and Th decrease slightly from 0 to ca. 5 wt. % TiO_2, above which they remain constant up to ca. 20 wt. % TiO_2 in the silicate glass. In addition, redox sensitive elements, i.e. U, Mo, and W show clearly distinct $D_M^{silicates/melt}$ at different fO_2, implying that these elements are relatively more compatible at reduced (ca. IW 1.8) than in oxidized (FMQ and air) environments. Molybdenum is shown to be volatile at oxygen fugacities above FMQ and its compatibility in pyroxene and olivine increases three orders of magnitude towards the more reducing conditions covered in this study. The partitioning results show that Mo is dominantly tetravalent at redox conditions below FMQ-4 and dominantly hexavalent at redox conditions above FMQ. Given the differences in oxidation states of the terrestrial (oxidized) and lunar (reduced) mantles, molybdenum will behave significantly differently during basalt genesis in the Earth (i.e. highly incompatible; average $D_{Mo}^{peridotite/melt}$ ca. 0.008) and Moon (i.e. moderately incompatible/compatible; average $D_{Mo}^{peridotite/melt}$ ca. 0.6). Thus, it is expected that Mo will strongly fractionate from W during partial melting in the lunar mantle, given that W is broadly incompatible at FMQ-5. Finally, the new dataset of $D_M^{crystal/melt}$ was used to perform simple melting models of the lunar mantle cumulates. Results indicate that to reproduce the fractionation of W from the HFSE, as well as U and Th observed in lunar mare basalts, metal saturation and the presence of Fe-Ti oxides in the mantle sources is required. Moreover, the depletion of Mo and the Mo/W range in lunar samples can be reproduced by simply assuming a primitive Earth-like Mo/W for the bulk silicate Moon. Such a lunar composition is in striking agreement with the Moon being derived from the primitive terrestrial mantle after core formation on Earth.

Zusammenfassung

Das Verhalten von Spurenelementen in magmatischen Systemen wird durch physikalisch-chemische Bedingungen gesteuert, die während der partiellen Aufschmelzung des Mantels und der magmatischen Differenzierung vorherr–schen. Die steuernden Faktoren dabei sind im wesentlichen Temperatur, Tiefe, Art und Grad der Aufschmelzung, sowie die mineralogische Zusammensetzung der Quelle und die Sauerstoff–Fugazität (fO_2). Um Prozesse vor allem in Hinblick auf den Mondmagmatismus zu untersuchen, wurde im Rahmen dieser Arbeit das Verteilungsverhalten ausgewhlter Spurenelemente (Lanthaniden, Y, Nb, Ti, Sc, Ba, Sr, Cr, U, Th, Mo, W, Sn, In, Ga, Pt, and Rh) zwischen kristallinen Mantelphasen (Fe-Ti-Oxide, Pyroxen, Plagioklas, Spinell und Olivin) und basaltischer Schmelze untersucht und neue Verteilungskoeffizienten in Abhängigkeit von der Sauerstoff–Fugazität und der Kristall- und Schmelzzusammensetzung bestimmt. Die Experimente wurden in vertikalen Gasmischöfen (1 bar) bei Temperaturen zwischen 1100 °C und 1300 °C und verschiedenen Sauerstoff–Fugazität (von 5,5 log Einheiten unterhalb des Fayalit-Magnetit-Quarz (FMQ) Puffers bis hin zu atmosphrischer Zusammensetzung) durchgeführt. Damit wurde der Bereich an Temperaturen und Sauerstoff–Fugazitäten abgedeckt, der für planetare Differentiation des Mondes von Bedeutung ist. Bei den Experimenten wurde außerdem gezielt der Einfluss der Komponenten Al_2O_3 und Na_2O untersucht, da sie bekanntermaßen die Struktur von Silikatschmelzen und insbesondere die chemische Zusammensetzung von Klinopyroxen–Kris–tallen beeinflussen. Die $^{[4]}$Al Gehalt im Klinopyroxen führt zu einem Anstieg von $D_i^{kpx/schmelze}$, selbst wenn ein Korrekturfaktor berücksichtigt wird, um den Effekt der Schmelzpolymerisation zu berücksichtigen. Darüber hinaus ist die positive Korrelation zwischen $^{[4]}$Al und $D_i^{kpx/schmelze}$ nicht nur auf die Lanthaniden beschränkt, sondern gilt auch für Sn, Ga, In und

Ba. Die Zugabe von bis zu 2,6 Gew.% Na_2O zu der Silikatschmelze erhöht den Verteilungskoeffizienten ohne eine gleichzeitige Änderung der Kristallchemie und der Schmelzpolymerisation. Dieser Zusammensetzungs-Effekt ist wahrscheinlich auf die Fähigkeit von Na zurückzuführen, die REE-Al-O-Komplexe in der Schmelze aufzubrechen. Unsere Ergebnisse unterstreichen die Notwendigkeit, alle Variablen in Betracht zu ziehen, die das Verhalten von Spurenelementen in magmatischen Systemen beeinflussen können, bevor a) das *Lattice Strain Model* angewandt wird; und b)aussagekräftige Ergebnisse fr die Änderung der kristallographischen Positionen gewonnen werden. Ein spezifisches Merkmal einiger basaltischer Mondgesteine ist, dass ihre TiO_2 Konzentrationen bis zu 16 Gew.% erreichen können. Somit können die sogenannten "High Field Strength Elemente" kurz *HFSE*, zu denen neben Nb, Ta, Zr, Hf auch Ti gehört, Informationen über die Prozesse liefern, die im Mondmantel zur Entstehung von Ti-reichen Mare Basalten führten. Mit Ausnahme von Nb zeigen alle $D_{HFSE}^{Kpx/Schmelze}$ eine stark negative Korrelation mit dem TiO_2–Gehalt der Silikatschmelze. Die Verteilungskoeffizienten zwischen Olivin und Silikatschmelze für Zr, Hf, Nb, Ta und Th nehmen zunächst leicht von 0 auf ca. 5 Gew. % TiO_2 zu. Darüber sind bis zu einem Gehalt von ca. 20 Gew. % TiO_2 im Silikatglas nahezu konstant. Zusätzlich zeigen redox-empfindliche Elemente, wie U, Mo und W, deutlich unterschiedliche $D_M^{Silikate/Schmelze}$ bei unterschiedlichem fO_2. Diese Elemente sind unter reduzierenden (ca. IW - 1.8) relativ kompatibler als unter oxidierten (FMQ und Luft) Bedingungen. Molybdän ist bei einer Sauerstoff–Fugazität oberhalb FMQ flüchtig, und der Einbau in Pyroxen und Olivin erhöht sich um drei Grössenordnungen gegenüber den reduzierenden Bedingungen, die in dieser Studie behandelt werden. Die Ergebnisse der Mo-Verteilungskoeffizienten zeigen, dass Mo bei Redoxbedingungen unterhalb FMQ-4 hauptsächlich vierwertig und oberhalb FMQ hauptsächlich sechswertig ist. Angesichts der Unterschiede im Oxidationsgrad zwischen dem irdischen (oxidierten) und dem lunaren (reduzierten) Mantel wird sich Molybdän während der terrestrischen Basaltgenese signifikant anders verhalten (d.h. in hohem Maße inkompatibel; durchschnittlich $D_{Mo}^{Peridotit/Schmelze} = 0{,}008$) als auf dem Mond (d.h. mäßig inkompatibel / kompatibel; Durchschnitt $D_{Mo}^{Peridotit/Schmelze} = 0{,}6$). Daher ist davon

auszugehen, dass Mo während der partiellen Aufschmelzung im Mondmantel stark von W fraktioniert wird, da W bei FMQ-5 weitestgehend inkompatibel ist. Einfache Aufschmelzmodelle der Mondkumulate basierend auf dem neuen Datensatz an $D_M^{Kristall/Schmelze}$ zeigen, dass eine Metallsättigung und das Vorhandensein von Fe-Ti-Oxiden in den Mantelquellen erforderlich ist, um die in den Maare Basalten des Mondes beobachtete Fraktionierung des W von den HFSE sowie von U und Th zu erklären. Darüber hinaus kann die Verarmung von Mo und der Wertebereich an Mo/W-Verhältnissen in Mondproben reproduziert werden, indem ein primitives terrestrisches Mo/W Verhältnis für die gesamtsilikatische Zusammensetzung des Mondes angenommen wird. Eine solche Mondzusammensetzung steht in Übereinstimmung mit der Annahme, dass der Mond nach der terrestrischen Kernbildung aus dem primitiven Erdmantel entstand.

Chapter 1

Introduction

The uniqueness of the Earth within our Solar System is undeniable, mostly due to the fact that it is the only planet which shows specific characteristics to enable the development of life. Building an habitable Earth was a protracted process punctuated by moments of great agitation, including major catastrophes (e.g. meteorite impacts, large-scale volcanic eruptions, etc.) and mass extinctions. Perhaps one of the most catastrophic moments along the way is believed to have happened earlier during Solar system formation, more than 4.4 Ga ago, when a Mars-sized body collided with the proto-Earth and ejected enough material into orbit to accrete and form our natural satellite, the Moon (e.g. Cameron and Canup, 1998; Canup and Asphaug, 2001; Barboni et al., 2017). The formation of the Moon is especially important to the development of a long-term habitat for life and our own existence in the Earth (Ward and Brownlee, 2000). For instance, without the Moon, there would be no lunar tides and the Earth would spin too fast (Brosche and Sündermann, 1978). Furthermore, the lunar mass and the gravitational attraction between the Earth and the Moon constrains Earth's obliquity at around 23°, which provides, alongside the N_2-O_2-Ar atmosphere, a relatively stable surface temperature for hundreds of thousands of years, allowing the development of complex forms of life (Ward,

1982; Laskar et al., 1993; Ward and Brownlee, 2000).

Human beings have always being intrigued by the Moon, since it is the closest celestial object to our own planet and the only one which can have its topographic features observed through naked eye. The duality between high-reflectance brighter and low reflectance darker areas in the Moon (Fig. 1.1) led to the interpretation of these being terrestrial analogues (crust, impact craters, flood basalts, sedimentary rocks or seas), which has been used to explain the lunar geological history by several authors since ancient times (Dana, 1846; Baldwin, 1949; Shearer et al., 2006). Given the large interest of the scientific community on this subject, several fields of research have developed models to resolve lunar issues. The advent of the telescope since the 17^{th} century bolstered astronomers and physicists to preferentially base their models on gravitation and magnetic field data (Taylor, 1982). On the other hand, chemists and geologists at the 20^{th} century started to emphasize that the chemical properties of the parent bodies are at least as important as those of nuclear interactions on the study of planetary evolution (Urey, 1952; Ringwood, 1979). Nevertheless, until the mid of the 20^{th} century, our entire view of the Moon was somewhat speculative, based only on remote sensing data and/or meteorites mistakenly considered to be of lunar origin, such as chondrites, euchrites and tektites (Verbeek, 1897; Urey, 1962, 1965). These interpretations led to the development of three main pre-Apollo theories for the origin of the Moon, each one of them with different constraints for lunar origin and evolution, which have been summarized in several review works (e.g., Wood, 1986; Shearer et al., 2006):

1) *Capture model*: the Moon would have been formed elsewhere in the solar system, having chondritic composition, and would be subsequently captured as it approached the Earth (Urey, 1959; Goldreich, 1966; Öpik,

1966; Gerstenkorn, 1970).

2) *Co-accretion model*: this model implied that the Earth and the Moon would have been formed from accretion or condensation in a double-planet system in the proto-planetary nebula, but did not consider the orbital relationship between both bodies (Thomson, 1864).

3) *Fission model*: tidal forces linked to the Sun-Earth system would have extracted the Moon from the Earth after core-formation, which was used to explain the difference in density among both bodies but failed to explain the lunar orbit, as well as the magnitude of the gravitational forces required for this process to occur (Darwin, 1879; Nininger, 1943).

Fortunately, the Apollo (USA) and Luna (USSR) missions, which took place during the space race on the 60's and 70's, provided the first *in situ* samples of the Moon, or for this matter, any other terrestrial body in the Solar System. Around 400 kg of samples, including hand-specimens, drill cores and dust (Meyer, 2012), some peculiar materials were found (Fig. 1.1), which would change drastically the concept of lunar origin. Due to its small size, with a radius of roughly 1740 km, i.e., almost four times smaller than the Earth, the Moon has lost its primordial heating early in its history, and has not been further disturbed by geological and tectonic activity like the Earth. Therefore, scientists often consider that understanding the origin of the Moon is a key parameter to understand the origin of the Earth and have a glimpse on the processes that occurred during the first million years of the solar system. In this regard, this dissertation provides new insights into the way that trace elements will behave during lunar magmatic processes (primordial differentiation and basaltic lava flows), and how differently this would have been when compared to the terrestrial magmatism. Specifically, changes in magma composition observed in lunar mare basalts, such as the

extreme enrichment in TiO_2, alongside the low partial pressure of O_2 in the lunar mantle will affect the behaviour of trace elements during igneous processes on the Moon.

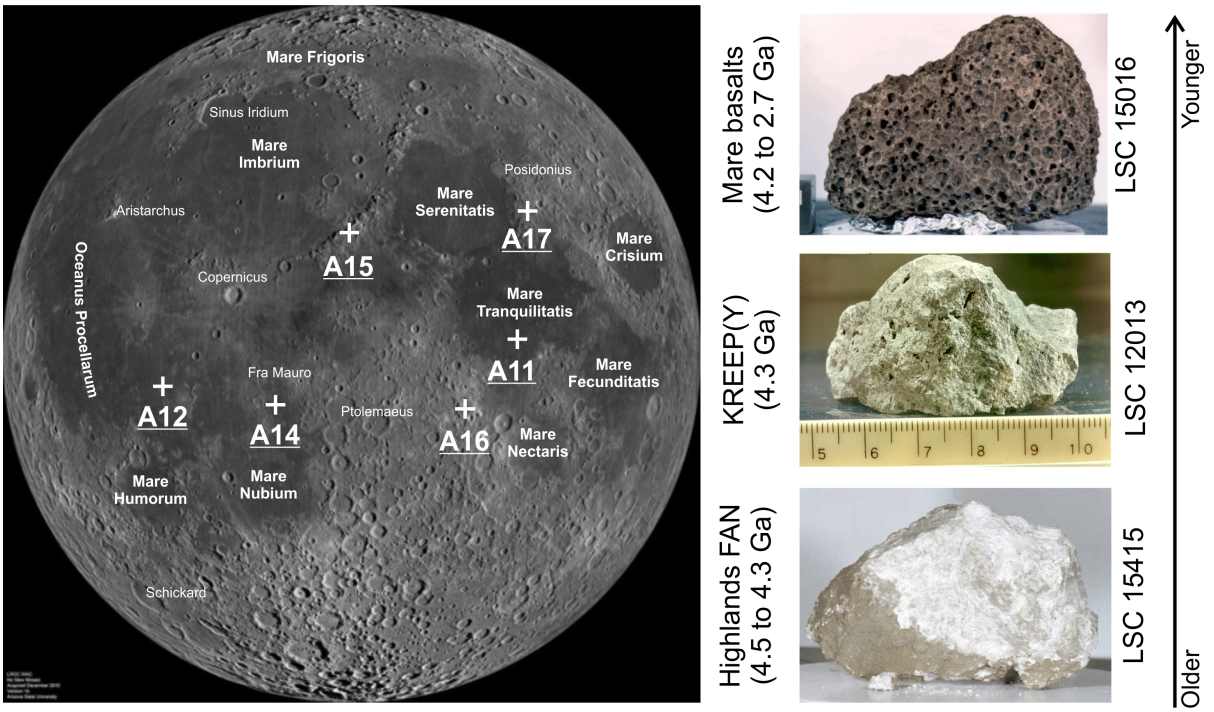

Figure 1.1: Near side of the Moon as seen from the Earth during a full-Moon phase, where it is possible to notice the duality between reflectance of regions with anorthosites and other plutonic associations, i.e. lunar crustal rocks (light) and the impact crater basins filled by basaltic lava flows (dark). FAN: Ferroan-anorthosite. Images taken from NASA gallery (*images.nasa.gov*) and Lunar Sample Compendium (Meyer, 2012). Crosses represent approximately Apollo missions landing sites. Ages are range values from radiometric dating including Nd, Pb, Ar and Sr ages as reported in the reviews by Shearer et al. (2006) and Warren and Taylor (2014).

The following sub-sections of this Introduction chapter will provide a review of the currently more accepted theories for the origin of the Moon and an overview on the main lunar lithologies and also address the state of the art regarding the distribution of trace elements between minerals and silicate melts, the latter which is necessary for a better contextualization of

this work. The two last sub-sections present the motivation and objectives *per se*, as well as an outline of the Thesis.

1.1 Origin of the Moon and Lunar petrogenesis

After the return and petrological investigation of lunar samples, the most accepted theory developed for the origin of the Moon is that of the giant impact. The Giant Impact Theory (cf. Hartmann and Davis, 1975; Cameron and Ward, 1976) can be considered an improvement of the previously proposed "Fission Model" and states that during the several collisions that aggregate material to the early Earth, the biggest one took place when a giant off-axis impact between a Mars-sized body named "Theia" and the proto-Earth would have been able to eject enough material into orbit to condensate into a new planetary body (Fig 1.2). This idea is well accepted among the scientific community, since it reasonably explains some key chemical differences between the Earth and the Moon, density differences, as well as the peculiar lunar orbit, angular momentum, and the lack of a large metallic core, evidenced by the absence of a global lunar magnetosphere (Shearer et al., 2006). Among the chemical differences between Earth and Moon explained by the Giant Impact theory are the depletion in volatile and highly siderophile elements, and enrichment in refractory elements in lunar rocks compared to the Earth, given that the first would have vaporized during the impact, and the second would have been a result of mingling and homogenization between the core of the impactor and the Earth, leaving a terrestrial mantle-like material to form the Moon. Still, there has been a lot of debate in the details of the Giant-Impact theory, such as on the velocity and angle of collision to enable non-ballistic and non-hyperbolic trajectory of debris, necessary to place it into Earth's sta-

ble orbit (e.g., Melosh and Kipp, 1989; Cameron and Benz, 1991; Cameron and Canup, 1998), size, mass, chemical composition and contribution of the impactor(s) and the proto-Earth to the Moon formation (e.g., Canup and Asphaug, 2001; Canup, 2004; Cuk and Stewart, 2012; Rufu et al., 2017). Several isotope studies on lunar and terrestrial samples (e.g., Mo, Cr, Ti, W, and O) have strongly suggest that the Earth's mantle and the Moon follow the same fractionation line, and therefore, are made of the same material (e.g., Wiechert et al., 2001; Touboul et al., 2007; Zhang et al., 2012; Kruijer et al., 2015; Bonnand et al., 2016; Sossi and Moynier, 2017). It is difficult to reconcile these isotopic similarities with hydrodynamic models of Moon formation (Melosh, 2014; Burkhardt, 2017), which predict that ca. 75 % of the Moon would have been derived from the impactor (e.g. Canup et al., 2013) that likely had a different isotopic composition (Pahlevan and Stevenson, 2007). Some of the explanations for this discrepancy include homogenization after the impact (Pahlevan and Stevenson, 2007), origin of the impactor in the same region of the protoplanetary disk as the Earth's building blocks (Dauphas et al., 2014), or that the impactor was frozen and 1/3 of it was converted from ice to steam during the impact (Wolbeck and Connoly, 2010).

Nevertheless, petrological and geochemical observations of lunar samples, when coupled with data acquired through remote sensing, geophysics and lunar meteorites allowed refining our understanding of the magmatic and thermal evolution of the Moon and its relationship with the formation of the Earth (Shearer et al., 2006). From these studies, it was possible to divide the lunar geology into two main lithologies: *mares* and *terrae*. The first are considered as impact crater basins that were flooded by basaltic lava flows produced by partial melting of the lunar mantle, mainly between 3.3 to 3.7 Ga (see Hiesinger et al., 2003). These basalts have a wide com-

positional range, which will be explained in detail on Section 1.1.3, given their importance to the topic of this Dissertation. The *terrae*, also known as highlands, are an older association of plutonic rocks (> 3.9 Ga), dominated by plagioclase-rich lihologies (e.g. iron-rich anorthosites) and occurrences of several other kinds of plutonic rocks in smaller volume (Taylor, 2009). They are considered to be the primordial lunar crust, and, in relation to the geochemistry of trace elements, they show features that are complementary to the mare basalts and their mantle sources (e.g., Brown et al., 1972; Taylor, 1975). The Moon is thus a differentiated body (Heiken et al., 1991), with a crust of anorthositic composition, a mantle enriched in olivine and pyroxene, the partial melting of which originated the basaltic lava flows, and perhaps, a small core (e.g., Weber et al., 2011; Suavet et al., 2013). The initial differentiation of the Moon into crust, mantle, and core has been recently proposed to have occurred shortly after lunar accretion and ended at about 4.4 Ga ago with the final fractionation of the lunar magma ocean (Sprung et al., 2013; Gaffney and Borg, 2014), which will be detailed in the following section.

1.1.1 Lunar Magma Ocean

One of the fundamental issues that were considered to develop the Giant Impact theory is the source of heat energy required to produce a magma ocean in the Moon, since first returned samples from Apollo 11 indicated that the Moon was a differentiated body (Smith et al., 1970; Wood et al., 1970). The most accepted theory for the initial differentiation of the Moon is that of the Lunar Magma Ocean (LMO – e.g., Wood et al., 1970; Taylor and Jakes, 1974; Shirley, 1983; Warren, 1985). According to conventional LMO fractionation models, the primordial lunar crust, composed mainly by iron-rich anorthosites, is interpreted as the result of plagioclase flotation atop the

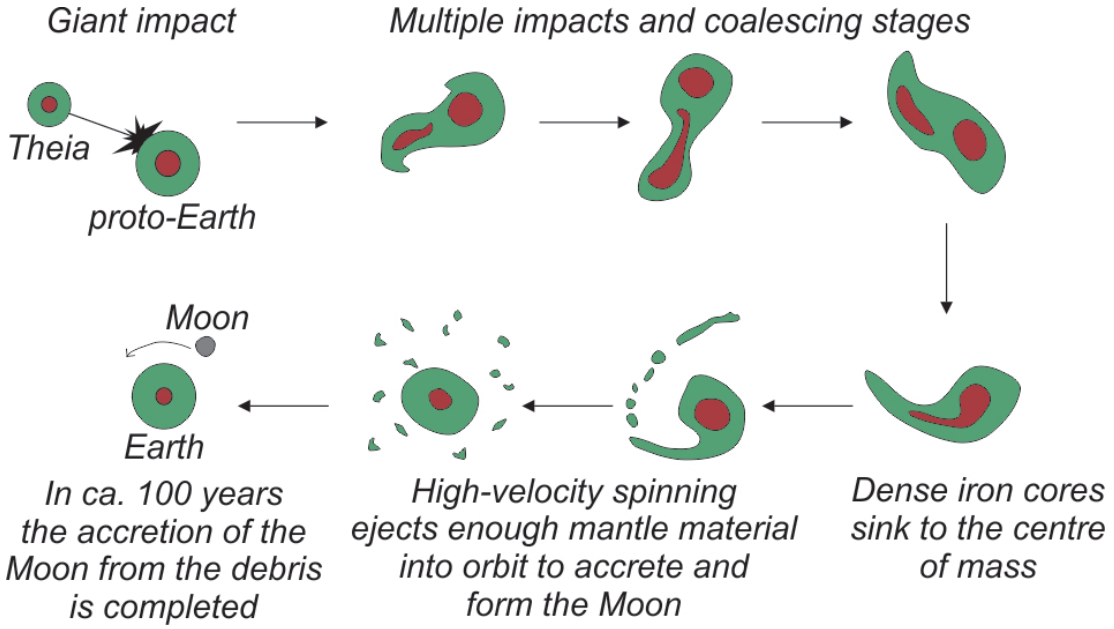

Figure 1.2: Schematic drawing of the canonical giant impact theory (modified from Canup, 2013b; Nave, 2016), where a roughly Mars-sized body collides with the proto-Earth at ca. 4.5 Ga ago. This impact would have ejected enough material into orbit to accrete and generate the Moon (see text for details).

crystallizing lunar magma ocean. The mantle sources for the mare basalts, resulted from the sinking and accumulation of denser mafic minerals, such as olivine cumulates and ilmenite-rich cumulates during a mantle overturn (e.g., Grove and Krawczynski, 2009). The last melt residue associated with the LMO is thought to be rich in incompatible elements typically known as KREEP (enriched in potassium, rare-earth elements (REE) and phosphorus - see Hawke and Head, 1978; Taylor et al., 1980). A conceptual model for the evolution of the Moon can be seen on Figure 1.3. The most striking evidence for the occurrence of a magma ocean in the Moon (e.g. Warren and Taylor, 2014) is the textural evidence for accumulation of plagioclase crystals in a matrix of gabbroic composition found in pristine non-mare samples from the Moon, as well as the highly anorthositic composition of these rocks (more than 70 % plagioclase), too high to have been generated as

a result of partial melting and differentiation of an ultramafic mantle source, coupled to low-Mg, which was extracted by the fractional crystallization of pyroxene and olivine.

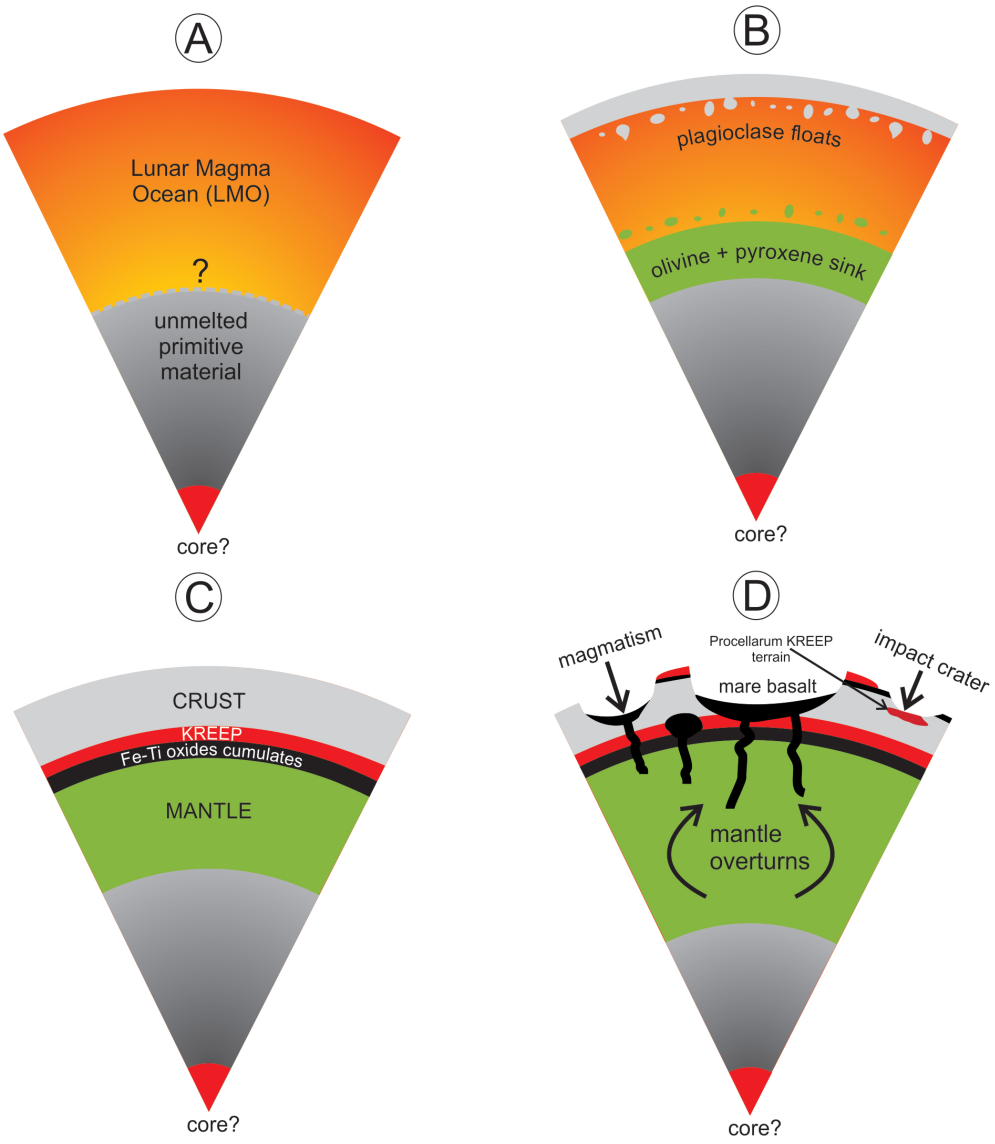

Figure 1.3: Conceptual model of the crystallization of a lunar magma ocean (cf. Smith et al., 1970; Wood et al., 1970) and the main stages of lunar evolution (not to scale).

The lunar magmasphere fractional crystallization sequence and mineralogical composition of each one of the lunar mantle cumulates has been extensively studied in the literature, through geophysical and gravimetric constraints (e.g. Buck and Toksöz, 1980; Khan et al., 2000; Wieczorek et al., 2013), geochemical models (e.g., Longhi, 1980; Snyder et al., 1992; Elkins-Tanton et al., 2002) and experimental approaches (e.g., Elkins et al., 2000; Elardo et al., 2011). Among the numerous existing models of LMO crsytallization, Snyder et al. (1992) was the pioneer in coupling major and trace element whole rock geochemistry to produce a comprehensive crystallization sequence. The LMO crystallization sequence of Snyder et al. (1992) is depicted in Figure 1.4, and starts with equilibrium crystallization of opx and olivine up to 78 % of solidified LMO, followed by fractional crystallization of different cumulates composed by plagioclase, olivine, clinopyroxene, and orthopyroxene up to 95 %, when the liquid reaches ilmenite saturation ($TiO_2 \geq 5$ wt. %). One of the main advantages of the model proposed by Snyder et al. (1992) is that it accounts that at least some interstitial liquid and plagioclase crystals became trapped as fractional crystallization took place, which is more realistic given that is in agreement to the observed inefficiency of crystal-crystal or crystal-liquid segregation in terrestrial cumulate sequences (Irvine, 1980).

Some sources of uncertainty in LMO crystallization models are the composition of the bulk silicate Moon, together with the geophysical constraints of LMO depth, thickness of the lunar crust, and the presence of a lunar core. Regarding the lunar core, even though local magnetic fields have been observed by the Lunar Prospector and also sharp magnetic anomalies detected during Apollo missions, the Moon does not have a global dipolar magnetic field like the Earth, and therefore, even if a core exists, like geophysical data suggests, it is small (250 to 430 km) and does not produce a global

geodynamo (Jacobs, 1987; Lin et al., 1998; Weber et al., 2011).

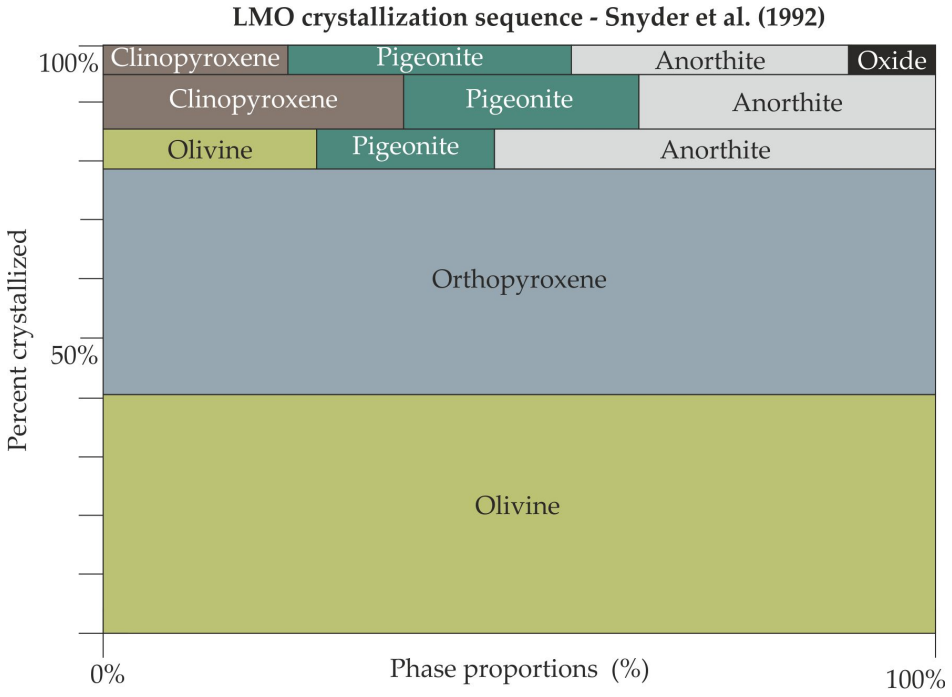

Figure 1.4: Stages of equilibrium (until 78 %) and fractional crystallization (78 - 100%) of the lunar magma ocean as proposed by Snyder et al. (1992), giving origin to a stratified lunar mantle.

The starting composition of the LMO has been extensively debated in regard to major and trace elements, and estimates can be divided into two groups, one considering the Moon has to be ca. 50 % enriched in refractory elements such as Ca and Al compared to the Earth (cf. Taylor, 1982; Taylor et al., 2006), known as Taylor Whole Moon (TWM), while the other argues in favour of a similar bulk composition between the Earth and the Moon (e.g., Longhi, 2003, 2006), known by the acronym LPUM (Lunar Primitive Upper Mantle). Numerical fractional melting modelling carried out by Longhi (2006) showed evidence that low-Al_2O_3 magmas such as the picritic Apollo 15 green glasses, which are among the most primitive rocks sampled in the Moon require a deep (1000 km) source that has fractionated

around 2.5 wt. % Al_2O_3 due to olivine and pyroxene crystallization from a magma ocean. This would imply that the molten layer of the LMO would be at least 1000 km deep, and by mass balance, the lunar crust should have a thickness between 50 and 70 km and have extracted ca. 30 wt. % Al_2O_3 of the LMO. This is clearly at odds with the estimate by Taylor et al. (2006), who have proposed a LMO 500 km deep and a refractory-rich silicate Moon. Nevertheless, recent high-resolution gravity data obtained by the GRAIL mission support a lunar crust 34–43 km thick, which would not require a bulk lunar composition enriched in refractory elements (Wieczorek et al., 2013). In any case, given that both TWM and LPUM are reasonable compositions for the Moon, it is very likely that this matter will not be settled until more samples and remote sensing data have been obtained for the Moon (Taylor, 2007), so that LMO composition and fractionation can be modelled in greater detail.

1.1.2 Age of Lunar accretion and early differentiation

Concordant Rb-Sr and U-Pb ages obtained for lunar samples showed that the Moon was already a differentiated body at 4.45 Ga (Wasserburg et al., 1977). This age is younger than the age of formation of the first solids in the solar system (SS), i.e. the CAI (Ca-Al inclusions) found in carbonaceous chondrites, which constrain the age of SS formation at 4.56 Ga (Amelin et al., 2002). To precisely date the Moon forming impact and what happened between the formation of the SS and the Moon, perhaps the most appropriate geo-chronometer is the Hf-W system, since it can be used to date rates of accretion and differentiation of planetary bodies into core and mantle (Halliday and Lee, 1999). This isotopic system is based on the β-decay of ^{182}Hf to ^{182}W with a half-life of 9 Ma and requires high-precision mass spectrometry analysis (cf. Halliday, 2000). Since both elements are

refractory, they are thought to be present in chondritic proportions on planetary bodies (Hf/W ≈ 1 – Palme and O'Neill, 2014). Additionally, while Hf is litophile (i.e., remains in the mantle during metal-silicate fractionation), W is siderophile (goes to the core during metal-silicate mantle separation), thus, the Hf/W of the mantle of planetary bodies after core formation will be strongly fractionated (Hf/W ≈ 25 for the Earth's primitive mantle – Palme and O'Neill, 2014). Therefore, if core formation takes place during the life-time of ^{182}Hf, an excess of ^{182}W will be produced in the silicate mantle of that planetary body when compared to other tungsten isotopes (e.g., Harper and Jacobsen, 1996). Using this system, it is possible to calculate, for example, that the Earth has accreted rapidly mostly in the first 10 Ma of the solar system evolution and may have extended until 30-50 Ma after solar system formation (e.g. Kleine et al., 2002; Jacobsen, 2005). Lunar samples have initially shown no discernible W isotopic composition between the bulk Moon and the bulk silicate Earth, which is consistent with Moon formation at ca. 50-60 Ma after the beginning of the solar system (Lee et al., 1997; Halliday, 2000). The interpretation of the Hf-W data, however, relies on knowledge of the initial abundance of ^{182}Hf in the SS, which was re-evaluated by Kleine et al. (2002) and pushed Moon formation to as early as 30 Ma (Kleine et al., 2002; Jacobsen, 2005). The fact that the lunar W composition is not strongly radiogenic and the high Hf/W of the lunar mantle has been used to infer that Moon formation occurred after almost all ^{182}Hf has decayed, and all W isotope variation on lunar samples may be of cosmogenic origin, via neutron capture of ^{181}Ta due to exposure of the lunar surface rocks to cosmic rays (Touboul et al., 2007). Recent methodological improvements and more precise measurements have shown a systematic enrichment in ^{182}W in lunar rocks when compared to the Earth, which is explained by the disproportional addition of late veneer material

to the Earth after the giant impact when compared to the Moon (Kruijer et al., 2015; Touboul et al., 2015), in agreement with the highly-siderophile elements (HSE) enrichment in the Earth's mantle (e.g. Walker, 2009). Considering that the Earth and the Moon are isotopically similar with regard to W, and that the Moon was derived mainly from Earth's mantle material, the Moon must have formed while ^{182}Hf was no longer available in the Earth's mantle (Kruijer et al., 2015), which would limit the Moon formation to more than 45 Ma after SS formation and less than the age of the oldest lunar rocks, i.e. 4.51 Ga (cf. Halliday, 2008; Barboni et al., 2017). However, new estimates based on high-precision HFSE data on lunar rocks have pointed to a Hf/W ratio of the Moon higher than BSE, which could mean the excess ^{182}W could have been produced by the live decay of ^{182}Hf, and the Moon to be younger than 45-60 Ma after SS formation (Thiemens et al., 2017).

1.1.3 Lunar highlands

Most of the lunar highlands have been re-worked by several impacts that stroke the Moon mainly on the first 600 Ma of its existence (Taylor, 2009). Not all impacts were large enough to produce mantle partial melting and generate mare basaltic lava flows, and impact breccias are known to have preserved clasts of the primordial (i.e., pristine) lunar crust (Wood et al., 1970). Pristine rocks on the lunar highlands are the ones thought to be formed exclusively by magmatic processes, and criteria to identify them among debris, lunar regolith and brecciated material include (cf., Warren and Wasson, 1978): igneous crystallization textures, equilibrated mineral composition, low concentration of siderophile elements (which are added to the breccias by impact of asteroids). Based on these criteria, lunar non-mare samples and meteorites may be divided in three suites (see Papike

et al., 1998; Jolliff et al., 2000; Korotev, 2005): magnesian, alkali, and ferroan-anorthosite. The ferroan-anorthosite suite (FAN) is composed of an average of 96 % vol. plagioclase crystals, and interstitial olivine and pyroxene, being geochemically enriched in Al_2O_3 and depleted in MgO, Na_2O, and trace elements when compared to the magnesian and alkali suites (Taylor, 2009). These characteristics are used to identify FAN as remnants of the actual lunar crust, formed by plagioclase fractional crystallization from the crystallizing LMO (Wood et al., 1970). FAN rock samples have been dated via Sm-Nd to be on the range between 4.3 and 4.5 Ga, which is a too wide range for their mechanism of formation, showing evidence that most of these rocks isotopic ratios were probably perturbed by additional heating during impacts to allow a precise age determination (Norman et al., 2003). The Magnesian(Mg-)suite has around 60 % plagioclase and comprises plutonic rocks classified as troctolites, norites, and gabbronorites (Shearer and Papike, 2005). A peculiar geochemical characteristic of the Mg-suite is that they have high Mg# (characteristic of primitive magmas) while being simultaneously enriched in KREEP component, i.e., potassium, rare-earth elements, phosphorous and other trace elements that are incompatible in mafic silicates, i.e., a characteristic of evolved magmas (Taylor, 2009). Petrogenetic models for the origin of the Mg-suite include deep melting of early opx-olivine cumulates (high Mg#) that assimilates a portion of late KREEP layer as it ascends towards the surface, or a massive mantle overturn, which would result from the sinking and mixing of the ilmenite-rich and KREEP rich layers in the lowermost mantle (e.g., Shearer and Floss, 1999; Shearer and Papike, 2005). The idea of a hybridized mantle source is coherent with the fact that decay of K, Th, and U originated from the KREEP layer would release enough heat to produce partial melting of the mantle, especially on the Procellarum KREEP Terrane (Shearer et al., 2006).

The alkali-suite of plutonic rocks in the lunar highlands is the least represented group of samples and the more evolved type of rock found on the Moon, and consists of anorthosites, norites, (monzo)gabbros, (monzo)diorites, as well as high-silica rocks such as granites, rhyolites, and felsites (Warren and Wasson, 1980; Snyder et al., 1994; Shearer et al., 2006). Alkali-suite rocks, as the name suggests, have more than 0.3 wt. % Na_2O and 0.1 wt. % K_2O (e.g., Hubbard et al., 1971; Brown et al., 1972), which, although not high when compared to terrestrial crustal lithologies, they nevertheless, represent a high abundance relative to the bulk silicate Moon, which is generally depleted in alkali and volatile elements (Taylor, 1982; Shearer et al., 2006). Regarding trace elements, alkali-suite rocks are enriched in REE (up to 30x chondritic abundances - cf. Snyder et al., 1994), but not as much as KREEP. Most hypothesis invoked for the origin of the alkali-suite agree that they were generated by different degrees of fractional crystallization of a KREEP-like basaltic source (cf. Taylor, 2009).

1.1.4 Basaltic volcanism on the Moon

Currently, there is a consensus that the lunar magmatism was essentially basaltic (Shearer et al., 2006), however, despite the advances in the knowledge of the Moon's geology there is still much to learn about lunar evolution. The basaltic rocks observed and sampled on the Moon, although representing only a small part of the lunar surface, allowed for the identification of two main lithologies: picritic glasses, which have a high MgO content, and the more abundant mare basalts (Papike et al., 1998; Shearer and Papike, 1999). These mafic and ultramafic volcanic rocks have filled impact crater basins during the early stages of lunar evolution, having ages ranging from 2.74 to 4.3 Ga (see compilation by Warren and Taylor, 2014). A peculiar feature of mare basalts is that they show a large range of TiO_2 contents

(Fig. 1.5), from very high values (up to 15 wt. %) to very low values (≈ 0.2 wt. %) (Delano, 1986; Papike et al., 1998; Meyer, 2012), which allows their division into into three groups: high-Ti (>6 wt. % TiO_2), low-Ti (< 1–6 wt. % TiO_2) and very-low Ti (< 1 wt. % TiO_2) (Binder, 1982; Neal and Taylor, 1992; Warren and Taylor, 2014).

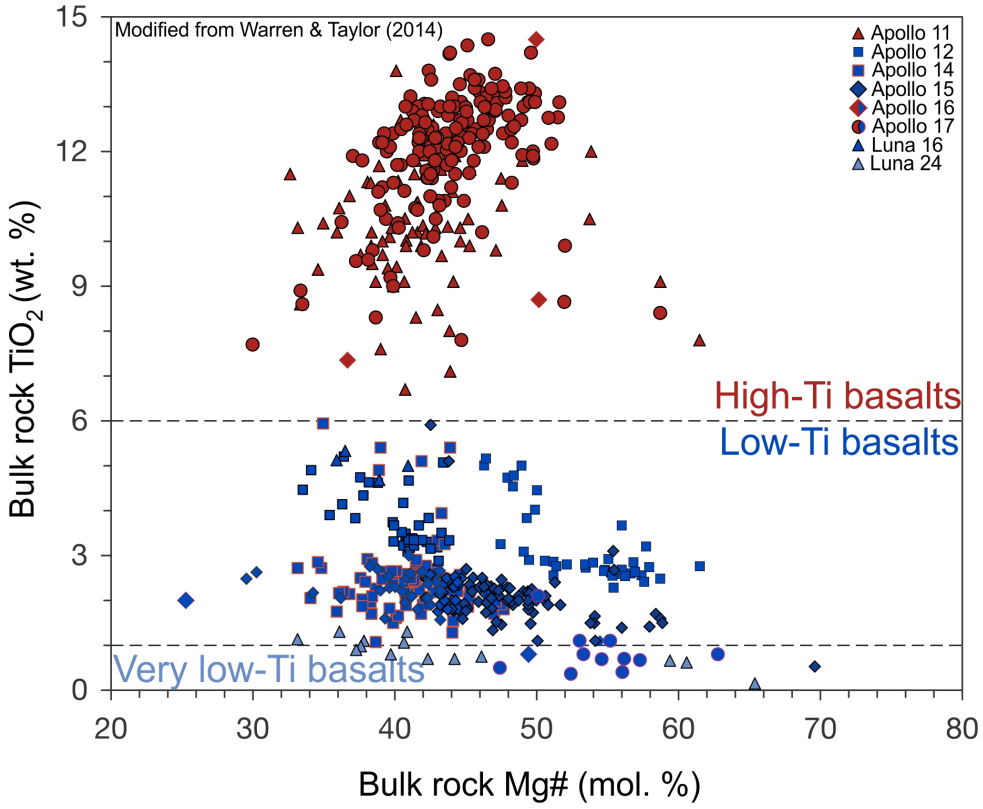

Figure 1.5: Major element variation (TiO_2 vs. Mg-number (Mg/Mg+Fe in mol) modified from the review paper by Warren and Taylor, 2014) of lunar mare basalts sampled by Apollo and Luna missions showing the enrichment in TiO_2 when compared to mid-ocean ridge basalts (MORB) average of 1.6 wt. % TiO_2 (Gale et al., 2013).

Moreover, when compared to their terrestrial analogues (i.e., mid-ocean ridge basalts - MORB), mare basalts are enriched in FeO (> 16 wt. %) and have a low Al_2O_3 content probably due to the extraction of the lunar crust during solidification of the LMO (Warren and Taylor, 2014). Mare

basalts also have a distinct accessory mineralogy, which can include sulfides (troilite), native Fe and Fe-Ti oxides, as well as a small amount of plagioclase when compared to MORB (Meyer, 2012). The TiO_2 content of the different mare basalt groups also correlates with their REE and HFSE contents (Meyer, 2012), and the different groups show distinct isotopic composition (e.g., Hf and Nd - Sprung et al., 2013). This correlation is perceived by several authors to indicate that the mantle sources of these basalts are geochemically heterogeneous, and that their partial melting probably took place over a range of redox conditions (e.g., Beard et al., 1998; Karner et al., 2000; Hagerty et al., 2006; Hallis et al., 2010; Sprung et al., 2013).

Within the context of LMO fractionation, mare basalts are thought to represent partial melts of layered olivine and pyroxene cumulates (Snyder et al., 1992; Münker, 2010). The high Ti content of some mare basalts is often explained by invoking the presence of a hybrid cumulate sources thought to be the result of mantle overturn, with the subsequent addition of late-stage ilmenite-bearing mafic cumulates to the early ultramafic - harzburgite cumulates (Ringwood and Kesson, 1976; Hess and Parmentier, 1995; Fonseca et al., 2014). Alternatively, high-Ti mare basalts have been suggested to result from the assimilation of Fe-Ti bearing minerals as magma ascended to the surface of the Moon (e.g., Wagner and Grove, 1997; Elkins-Tanton et al., 2002; Liang and Hess, 2006; Münker, 2010). In addition to the high-TiO_2 content of lunar basalts, and in regard to trace element abundances, lunar basalts are depleted in siderophile and volatile elements when compared to terrestrial basalts. The observation that the Moon is volatile element depleted has long been considered the result of the giant impact that resulted in formation of the Moon, and given that mare basalts are products of partial melting of a volatile-depleted mantle, they inherit this characteristic (Cameron and Ward, 1976).

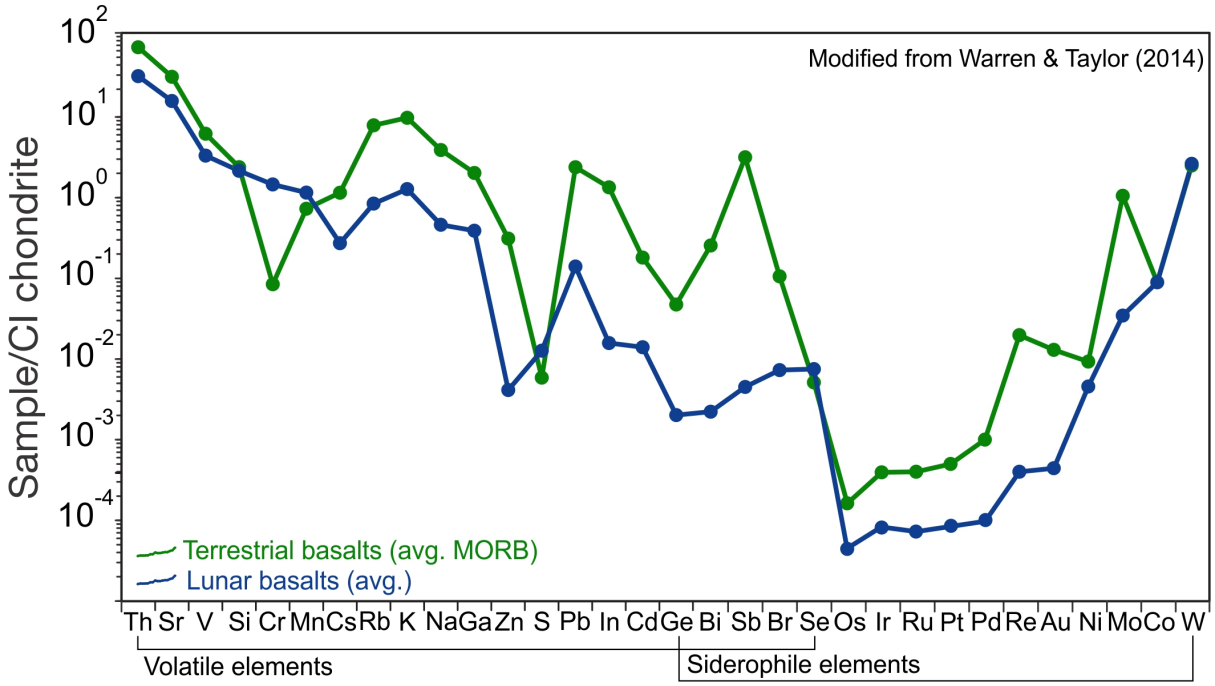

Figure 1.6: Average volatile and siderophile elements concentration in mare basalts compared to terrestrial basalts normalized to CI-chondrite abundances (modified from Warren and Taylor, 2014). Data-sources include Wolf et al. (1979); Hertogen et al. (1980); Dickinson et al. (1989); Haskin and Warren (1991); Govindaraju (1994); Walker et al. (2004); Day et al. (2007).

Depletion in siderophile elements on lunar basalts, however, has been explained by several theories. For example, depletion of Re and Mo may be explained by the greater compatibility of the reduced species (Re^{4+} and Mo^{4+}) in lunar mantle residual phases during partial melting when compared to the lower compatibility of the hexavelent species (e.g., Mallmann and O'Neill, 2007; Leitzke et al., 2017). Highly-siderophile elements depletion, on the other hand, has been explained by some metal segregation from the lunar mantle to form a lunar core, with estimates ranging between 0.15 and 5.55 wt. % of the bulk Moon (e.g. Newsom, 1984b; Rai and van Westrenen, 2014; Steenstra et al., 2016), or that just a small amount (0.02 wt. %) of late veneer material was mixed into the lunar mantle due to a "shielding"

effect of the early formed lunar crust (Day and Walker, 2015; Day et al., 2016). Moreover, some authors may include the presence of residual metal at the lunar source, which would retain to some extent the siderophile elements (e.g., Wolf and Anders, 1980; Fonseca et al., 2014; Leitzke et al., 2016), given that the mineral assemblage of mare basalts show evidence for being equilibrated below the iron-wuestite (Fe–FeO) redox buffer (Papike, 2005).

Regardless of the model invoked to explain peculiarities of lunar mare basalts composition, it is essential that geochemical models that attempt to constrain processes that took place during the petrogenesis of high-Ti basalts, have precise knowledge of the fractionation of major and trace elements in lunar melts during partial melting and crystallisation processes. In particular, it is necessary to know how variables like oxygen fugacity and melt composition have on the behaviour of trace elements during magmatic processes under conditions relevant to the Moon, which have long been shown to be substantially different than those operating on the Earth (e.g., Ringwood and Kesson, 1976; Logfren et al., 1981; Shearer et al., 2006).

1.2 Factors controlling trace element behaviour in magmatic systems

One of the fundamental questions in the Earth and Planetary Sciences is what the composition of our solar system is, and how and when Earth obtained its idiosyncratic chemistry. The analysis of extraterrestrial materials, including the Sun, the Moon and meteorites enabled to gain insights on what the average composition of our solar system is (MacPherson and Thiemens, 2011). Through such cosmochemical constraints, it has been surmised that Earth's bulk composition should resemble undifferentiated car-

bonaceous chondrites (CI). The classification of trace elements is somewhat controversial. For example, by definition, the bulk silicate earth (BSE), i.e., the Silicate Earth after segregation of the core took place, is 99.1 % composed of Ca, Mg, Al, Si, Fe and O, which are commonly referred in igneous petrology as major elements (White, 2013). The remaining 0.9 % are comprised of minor and trace elements, (i.e. those with concentrations lower than 1 wt.%). Although this definition is generally applied to igneous and metamorphic rocks, it is common knowledge that the distinction between major, minor and trace elements depends on the geochemical system of interest. For example, while K_2O is a minor to trace element in the Earth's mantle, it is a major element in calc-alkaline igneous crustal rocks (LeMaitre et al., 2005). The reason for this is that K belongs to a group of elements named large-ion litophile elements (LILE), which, due to their high ionic radius and low charge, their substitution into the crystallographic sites of common mantle mineral phases, such as olivine, pyroxene, and garnet, is unfavourable. This means that these elements concentrate themselves in the melt as a result of the partial melting of silicate-rich lithologies, such as the Earth's mantle (White, 2013). Elements that are not easily incorporated in the mantle residual crystalline phases during partial melting are called incompatible, while those that remain in the solid are deemed compatible (Shaw, 1970). The advantage of using trace elements is that because of their low concentrations, they generally do not change the physical properties of the phases that host them (White, 2013). Moreover, owing to their variety, trace elements can display a large range of oxidation states, ionic radii and spatial coordination in crystalline and amorphous phases, and will respond differently to the variable conditions prevalent in different geodynamic settings (Pearce et al., 1984).

The behaviour of trace elements in igneous systems, thus, provides valu-

able information about magmatic processes, such as differentiation of core and mantle (e.g. Li and Agee, 1996; Mezger et al., 2013), age (e.g. Münker et al., 2000; Scherer et al., 2001), source and depth of partial melting (e.g. Ellam, 1992), fractional crystallization, crustal assimilation, and tectonic settings (e.g. Myers et al., 1984; Pearce et al., 1984) and, importantly, the oxidation state of a magma (e.g. Mallmann and O'Neill, 2013). Petrogenetic models that attempt to reproduce the magmatic processes that led to elemental ratios observed in igneous rocks require precise knowledge of their partition coefficient, i.e., $D_M^{\alpha/\beta} = C_M^{\alpha}/C_M^{\beta}$, where M is the element of interest, C is the concentration and α and β are two phases which can be, for example, crystal and silicate melt or metal and silicate melt. The most reliable approach to obtain this value for endogenous processes such as crystallization and partial melting is via high-pressure and temperature experiments, where all parameters of the system can be controlled and monitored individually, as where as the achievement of chemical equilibrium can be assessed, which is not always the case in natural samples.

The rules of ionic substitution of elements into crystals have been first proposed by Goldschmidt (1937). Goldschmidt's rules state that: 1) Ions of the same valence and similar ionic radius have the same chance of entering the crystals (e.g.: Rb $\approx$ K, Ni $\approx$ Mg); 2) If the size mismatch between the crystal site and the substituting ions is less than 30 %, the smaller ion will be incorporated preferentially; 3) If the charge of the ions is different, but they have a similar size, the higher charged ion will be more compatible. For those rules to apply, both ions should have the same geochemical affinity, as defined by Goldschmidt (1937), i.e., belong to the same geochemical group: litophile (form stable complexes with oxygen), chalcophile (chemical bonding with sulfur), siderophile (dissolve into native iron or other metallic ligand), and atmophile (form a vapour-phase). The Goldschmidt's rules

of substitution, although still used for teaching and by some researchers for simplification purposes, are known to not be universally applicable (cf. Wood, 2003). The first work to question these rules was done by Ringwood (1955), who showed that, even if the size and charge criteria are reached, substitution will not occur if the competing ions have different electronegativities (e.g., Na^+ and Cu^+) and show a tendency to form different types of chemical bonding. It is clear today that there are several parameters in addition to ionic radius and valence that can affect the partitioning of elements between crystals and silicate melt. Among these controlling factors are: temperature, pressure, melt composition and structure (polymerization), volatile content, and notably the redox state of the mineral melt equilibrium (e.g., Onuma et al., 1968; Blundy and Wood, 1994; Lundstrom et al., 1994; van Westrenen et al., 2001; Mallmann and O'Neill, 2009). Therefore, to have a precise knowledge of the processes governing the behavior of trace elements during magmatic processes, it is necessary to understand the effect of each one of these variables individually. On the following sections, a brief overview of the most important factors that affect the trace element behaviour in mineral/silicate-melt systems will be given, as well as some examples to better illustrate each variable. It is worth pointing out that these factors are interdependent and challenging to individualize both in natural systems or under controlled conditions in laboratory experiments. For a more detailed review on this topic the reader can look at White (2013), and Wood and Blundy (2014).

1.2.1 Crystal chemistry

Trace elements can enter a crystal by three known mechanisms: simple substitution, coupled substitution, or in interstitial spaces (vacancies). Onuma et al. (1968) showed for the first time that a parabolic relationship exists

between the ionic radius (i_r) of cations (i) that have the same valence (e.g., La^{3+}, Lu^{3+}, Eu^{3+}, and Nd^{3+}) and the partition coefficient of these elements between clinopyroxene and melt ($D_i^{cpx/melt}$), when performing neutron activation analysis of the REE contents of pyroxenes from alkaline basalt samples found in Kyushu, Japan. Based on their results, the authors concluded that trace elements are incorporated to the crystal lattice sites rather than in interstitial spaces. Regarding the parametrization of the controlling factors on $D_i^{crystal/melt}$, Nagasawa (1966) was the pioneer to calculate the strain energy necessary to insert a large cation into a smaller crystal site, which will always be positive, producing $D_i^{crystal/melt}$ values that decrease with increasing ionic radius. This observations is in partial agreement with the theory of Goldschmidt (1937), if we only consider substituting cations that have a larger ionic radius than the site. The parabolic dependence between $D_i^{cpx/melt}$ and i_r (Onuma et al., 1968) confirmed that the main aspect that determines whether a given trace cation substitutes into a mineral lattice site will be the mismatch between the ionic radius of the host cation (e.g., Ca^{2+} in VIII-fold coordination have i_r of 1.12 Å), and that trace element ion (e.g., Sr^{2+} in VIII-fold coordination have i_r of 1.26 Å). This observation was important because it could be coupled to fundamental principles of thermodynamics to describe the differences in energy required to strain and substitute a misfit cation into a crystal lattice site (e.g., Brice, 1975; Blundy and Wood, 1994). For example, consider the substitution of Ca^{2+} by Sr^{2+} on the diopside octahedral M2 site during partial melting:

$$Sr^{2+}_{melt} + CaMgSi_2O_6 = Ca^{2+}_{melt} + SrMgSi_2O_6 \tag{1.1}$$

The difference between the free energy of clinopyroxene crystallization ($\Delta G^{cpx}_{melting}$) and the energy required to exchange a divalent metal cation (in

this case Sr^{2+}) from the silicate melt into the crystal lattice site at the same time as the host cation (Ca^{2+}) is transferred from the crystal to the melt ($\Delta G_{exchange}^{Sr^{2+}/Ca^{2+}}$) can be written as the Gibbs free energy exchange of reaction 1.1(ΔG_r):

$$\Delta G_r = \Delta G_{exchange}^{Sr^{2+}/Ca^{2+}} - \Delta G_{melting}^{cpx} \tag{1.2}$$

The partition coefficient of Sr between cpx and silicate melt will thus be a function of the free energy changes associated with the Sr-Ca substitution, as well as that associated with the process of melting, and can be written as:

$$D_{Sr}^{cpx/melt} = exp\left(\frac{\Delta G_{melting}^{cpx} - \Delta G_{exchange}^{Sr^{2+}/Ca^{2+}}}{RT}\right) \tag{1.3}$$

The difference in free energy resulting from the cation exchange will result from the deformation of the site required to accommodate an ion with a different size than the host cation, and because the silicate melt normally will possess a more flexible structure than the crystalline solid, any strain in the melt is essentially negligible when compared to the strain in the solid (Nagasawa, 1966). Therefore, considering that $\Delta G_{exchange}^{Sr^{2+}/Ca^{2+}} \approx \Delta G_{strain}$, ΔG_{strain} can be calculated as:

$$\Delta G_{strain} = 4\pi E N_A \left(\frac{r_0}{2}(r_i - r_0)^2 + \frac{1}{3}(r_i - r_0)^3\right) \tag{1.4}$$

where r_0 is the perfect ionic radius where no additional strain occurs on the crystal lattice site (in my example occupied by Ca^{2+} in a diopside crystal), r_i is the ionic radius of the substituting trace element cation (in my example Sr^{2+}), N_A is the Avogadro's number and E is the Young's Modulus, relative to the strain caused on stressing the crystal lattice by inserting a cation with $r_i \neq r_0$ (Brice, 1975). Assuming that the $\Delta G_{melting}^{cpx}$ will control the distribution of Ca between crystal and silicate melt (cf. Nagasawa, 1966)

it is possible to obtain:

$$D_{Ca}^{cpx/melt} = exp\left(\frac{\Delta G_{melting}^{cpx}}{RT}\right) \tag{1.5}$$

Combining equations 1.3, 1.4, and 1.5, $D_{Sr}^{cpx/melt}$ can be written as dependent on the $D_{Ca}^{cpx/melt}$, i.e., the crystal/silicate melt partitioning of a given host cation, temperature (T), the original size of the crystal lattice site with no substitution (r_0, or in this case r_{Ca}), the ionic radius of the substituting cation (r_i, or in this case r_{Sr} and the apparent Young's modulus of the site (E_s) when the substitution occurs, i.e., $r_0 \neq r_i$ (cf. Blundy and Wood, 1994):

$$D_{Sr}^{cpx/melt} = D_{Ca}^{cpx/melt} exp\left(\frac{-4\pi E N_A \left(\frac{r_{Ca^{2+}}}{2}(r_{Sr^{2+}} - r_{Ca^{2+}})^2 + \frac{1}{3}(r_{Sr^{2+}} - r_{Ca^{2+}})^3\right)}{RT}\right) \tag{1.6}$$

Blundy and Wood (1994) expanded this theoretical framework and showed that it can be used to predict crystal/silicate melt partitioning values for a large range of trace elements assuming that pressure, temperature and composition remain the same, in what they called "Lattice Strain Model", which is commonly applied in geochemistry today (e.g. Gaetani and Grove, 1995; Wood and Blundy, 1997; Aigner-Torres et al., 2007; Mollo et al., 2013). Even though on the example above involved the exchange between two cations with the same valence (2+), most trace elements, such as the rare-earth elements (REE) and the high-field strength elements (HFSE) will not have the same charge as the host cation in major mantle mineral phases, which will result in a energetically unfavourable substitution (see reactions 1.7 and 1.8). Wood and Blundy (2001) showed that substitutions involving, for example, a tetravalent cation (e.g., Zr^{4+}) into a originally divalent site

(M2 site of cpx - Ca^{2+}) will require so much electrostatic work, that it can be compared to replacing the same host cation by an uncharged noble gas. For example, if a diopside crystal incorporates Na^{+} or both octahedrally and tethraedrally-coordinated Al^{3+}, i.e., formation of jadeite ($NaAlSiO_3$) or Ca-Tschermak (CaTs - $CaAl_2SiO_6$) components, a charge deficit occurs (see reaction 1.7 and 1.8 – Bennet et al., 2004; White, 2013). This charge deficit may be compensated by an electrostatic favoured coupled substitution of highly-charged trace element cations in the less charged crystal lattice site (e.g., $REE^{3+} + Na^{+} = 2Ca^{2+}$) or by the creation of vacancies (V) in the crystal lattice of the mineral (e.g., $U^{4+} + V^{M2} = 2Ca^{2+} = V^{M2}USi_2O_6$), both of which will result in an overall increase of the $D_i^{cpx/melt}$ values (e.g., Purton et al., 1997; Hill et al., 2000; Wood and Blundy, 2001).

$$Na^{+}_{melt} + Sm^{3+}_{melt} + 2CaMgSi_2O_6 = 2Ca^{2+}_{melt} + 2Sm_{0.5}Na_{0.5}MgSi_2O_6 \quad (1.7)$$

$$Sm^{3+}_{melt} + Al^{3+}_{melt} + CaMgSi_2O_6 = Ca^{2+}_{melt} + Si^{4+}_{melt} + SmMgSiAlO_6 \quad (1.8)$$

1.2.2 Pressure and temperature

The interdependence between pressure, oxidation state, temperature and phase stability in the mantle of planetary bodies makes it challenging to isolate the individual effects that these parameter have on trace element partitioning behavior in magmatic systems (Blundy and Wood, 2003; Witt-Eickshen and O'Neill, 2005). Wood and Blundy (1997) correlated D_0^{3+}, i.e., the value of crystal/silicate melt partitioning for a cation that has the ideal radius to substitute Ca into the M2 cpx crystal lattice site without strain, with pressure (P), temperature (T), the free energy of fusion (enthalpy - ΔH, entropy - ΔS and volume of fusion - ΔV) of a fictive REE^{3+}-pyroxene

end-member (e.g., $SmMgAlSiO_6$), as well as degree of partial melting (i.e., melt composition represented by molar *Mg/Mg+Fe*), and atomic concentration of Mg on the M1 octahedral site (X_{Mg}^{M1}), and obtained the following relationship:

$$ln\left(\frac{D_0^{3+}.X_{Mg}^{M1}}{\left(\frac{Mg}{Mg+Fe}\right)}\right) = \frac{\Delta H_f^0 - T\Delta S_f^0 + \int_1^P \Delta V_f^0 dP}{RT} \tag{1.9}$$

The thermodynamic treatment applied by Wood and Blundy (1997) required some simplifications. One of the most important of these simplifications was to assume that the melt is quasicrystalline. In other words, Wood and Blundy (1997) assumed that a silicate melt consists of compounds with a fixed stoichiometry of six-oxygen atoms per formula unit, in similar fashion to the crystal structure of pyroxene, and that these melt components mix ideally (see Burnham, 1981; Blundy et al., 1995). This was necessary to have a simple activity-composition correlation, because there is no thermodynamic data available for the fictive $REE^{3+}MgAlSiO_6$ component (in contrast to $CaMgSi_2O_6$ and $NaAlSi_2O_6$). Despite these simplifications, Wood and Blundy (1997)'s approach was successfully used to calculate the free energy of formation of the fictive REE-cpx component, excluding any melt compositional effect on D_0, and agrees well with experimental data (Wood and Blundy, 2014). Entropies and enthalpies of fusion of mineral phases are generally positive, so it is expected that crystal/silicate melt partition coefficients increase with decreasing temperature (Blundy and Wood, 2003). The volume of fusion calculated by Wood and Blundy (1997) is positive, indicating an increase in ΔG_f (and D_0) with increasing pressure. Moreover, the thermodynamic framework developed by Wood and Blundy (1997) has been modified and successfully applied to correlate D_0 of other phases in the

Earth's mantle, such as garnet, olivine, and plagioclase and pressure, temperature, and melt composition (Taura et al., 1998; van Westrenen et al., 2000, 2001; van Westrenen and Draper, 2007).

In nature, however, the assumption that the activity coefficient of major and trace elements in silicate melts will be constant may not be valid. Adam and Green (2003) found a negative correlation between $D_{REE^{3+}}^{crystal/melt}$ for amphibole and pyroxene and pressure, contrary to the expectation of Wood and Blundy (1997). Adam and Green (2003) quantitatively model that volume reducing substitutions into cpx and amphibole octahedral sites (e.g., substitution of larger cations for smaller ones as pressure increases - $Mg^{2+} + Ti^{4+} = 2Al^{3+}$), will increase the activity of trivalent and tetravalent cations (REE^{3+} and $HFSE^{4+}$), while reducing the activity of monovalent cations (Na^{+} and K^{+}). Therefore, the dominant type of coupled substitutions induced by compression of cation polyhedra, with compensation of electrostatic valence will be crucial to changes in activity coefficients and the dependence between $D_i^{crystal/melt}$ and pressure/temperature (e.g., Adam and Green, 1994). For example, the dominant type of substitution for 1+ and 3+ cations into forsterite changes from low pressure (dominantly Si^{4+} and Mg^{2+} being replaced by Al^{3+} and Cr^{3+}) to high pressure (replacement of Si^{4+} and Mg^{2+} by $2Al^{3+}$; and of $2Mg^{2+}$ for Na^{+} and Al^{3+}), which will result in an increase in $D_i^{fo/melt}$ values for Al^{3+} and Na^{+} with pressure, while decrease in $D_i^{fo/melt}$ for Ni^{2+}, Co^{2+}, and Fe^{2+} (Taura et al., 1998).

1.2.3 Silicate melt structure and composition

Understanding the structure of silicate melts can provide information regarding physical, chemical and thermal aspects of magma formation and evolution on Earth and other terrestrial planets (Mysen, 1990). Cations occur in silicate melts as either network-formers (Si^{4+}), which are the ones at

tetrahedral coordination, bonded to four oxygen anions on a chain of interconnected components in the melt, or as network modifiers (Bottinga and Weill, 1972), that are linked to the oxygen anions not bonding (non-bridging oxygens) with other tetrahedra (Fig. 1.7). The degree of polymerization, i.e., how many of the silica-tetrahedra are connected among themselves in the melt, is described as the ratio of non-bridging oxygen per tetrahedrally coordinated cations (NBO/T), being NBO/T=0 a silica melt which has no network modifiers and all tetrahedra are completely interconnected, in other words completely polymerized (see Mysen, 1990b, 2004).

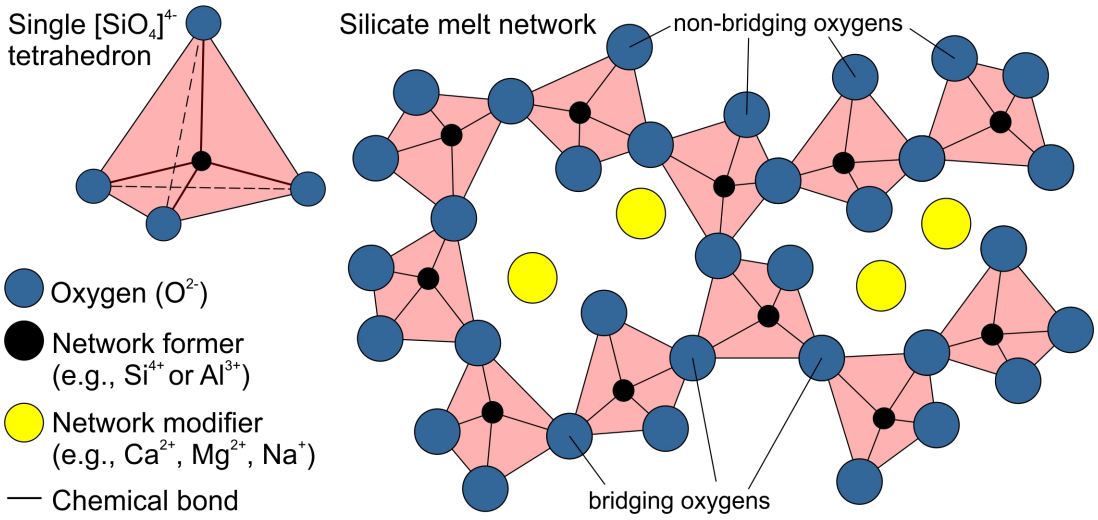

Figure 1.7: Simple schematic drawing of a silicate melt structure (modified from Mysen, 2004).

The effect of melt composition and structure on crystal-melt partitioning was first proposed by Watson (1976) and Ryerson and Hess (1978), who suggested that, for cations which possess a high charge density, such as the transition metals, $HFSE^{4+/5+}$, and the REE^{3+}, crystal-silicate melt partition coefficients increases as the polymerization of the liquid increases (e.g., Gaetani, 2004). The opposite effect is expected for low charge density cations (e.g., Na^{+}, K^{+}) while medium charge density cations, like Sr^{2+}

and Ba^{2+} would remain unaffected by variations in melt composition (Watson, 1976; Ryerson and Hess, 1978). Gaetani (2004) found unusually large $D_{REE}^{crystal/melt}$ values for highly-polymerized liquids, while after a NBO/T = 0.5 values are more or less constant, an observation that must be also valid for other trace elements, given that they are mostly network modifiers on a silicate melt (Mysen, 2004). In addition, silicate melt compositional effects on $D_i^{crystal/melt}$ not accounted by NBO/T have also been found. The lattice strain model also shows some limitations when dealing with minerals that crystallize over a wide range of melt compositions (e.g. Prowatke and Klemme, 2005). For example, several studies indicate that the Fe-Mg exchange between olivine and the basaltic melt ($D_{Mg-Fe}^{olv/melt}$) correlates with the TiO_2 content of the melt (Longhi et al., 1978; Jones, 1988; Wagner and Grove, 1997; Xirouchakis et al., 2001). Longhi et al. (1978) suggested that Al and Si tetrahedra in a melt destabilize Ti, therefore, changing the properties of Fe and Mg in melts with different chemical composition and structure. This probably is because Al-Si melt species that bridge with Fe are affected by the formation of Fe-Ti melt species. A high TiO_2 abundance in a silicate melt thus leads to the development of ferro-pseudobrookite component ($FeTi_2O_5$ - Longhi et al., 1978; Jones, 1988; Dygert et al., 2013). This component would have greater affinity for Fe than coexisting silicate minerals, and, as a consequence, decrease the $D_{Mg-Fe}^{olv/melt}$ between olivine and melt (Jones, 1988). Xirouchakis et al. (2001) reached a similar conclusion, arguing that increasing TiO_2 abundance in melt leads to an increase in Q^4 structural units (i.e., with four bridging oxygens) relative to the total number of silicate tetrahedra in the liquid, consonant with association between Ti polymers and available network formers leading to increasing melt polymerization. Longhi et al. (1978) argued that the effect that TiO_2 contents have on $D_{Mg-Fe}^{olv/melt}$ probably affects the mixing properties and crystal/silicate

melt partition coefficients of other elements as well, especially of trace elements. It is expected that elements that are chemically similar to Ti, such as the HFSE, may be affected by changes in the amount of Ti in co–existing silicate melt. Prowatke and Klemme (2005) performed experiments that investigated the effect of melt composition on the partitioning of several trace elements between titanite and silicate melt. They found that for the REE as well as for Ta, Nb and Th, partition coefficients were strongly influenced by the melt composition. On the other hand, for monovalent, divalent and tetravalent (Zr and Hf) cations the same authors did not observe significant change due to the melt composition (Prowatke and Klemme, 2005). In another study, Dygert et al. (2013) demonstrated that the partition coefficients for HFSE, between ilmenite, armalcolite and basaltic melt are affected by the TiO_2 content in the melt. Moreover, Evans et al. (2008) and Mallmann and O'Neill (2013) have shown that the partitioning of Sc, Y and the REE between olivine and silicate melt changes as a function of the molar fraction of SiO_2^{melt}, rather than with NBO/T. Their results imply that the activity coefficients of the oxide species of trivalent trace element cations in silicate melt decreases as a result of a strong bonding between REE and SiO_2 in the melt (Evans et al., 2008). Within the same framework, O'Neill and Eggins (2002) have shown that Mo may form complexes in the melt with CaO and to a lesser extent MgO. Furthermore, the association of Mo with both MgO and CaO was strong enough that it affected the position of the redox transition between Mo^{4+} and Mo^{6+} in the silicate melt, and parametrized the thermodynamic background to explain how the silicate melt major element composition must affect the partitioning of trace elements, by the formation of melt complexes which would change the activity coefficient of the trace element oxide species in the silicate melt. Following O'Neill and Eggins (2002), this behaviour can be described at equilibrium by the following

expression:

$$ln\ D_M^{crystal/melt} = RT/ - \Delta_r G^0 + \sum_Z n\ ln\ a_{ZO_{y/2}}^{melt} + ln\ \gamma_{MO_{x/2}}^{melt} - ln\ \gamma_{MO_{x/2}.\sum_Z nZO_{y/2}^{crystal}}^{crystal} - ln\ k \quad (1.10)$$

Where R is the universal gas constant, T is temperature, $\Delta_r G^0$ is the standard state free energy of the partitioning reaction, $a_{ZO_{y/2}}^{melt}$ is the activity of the major element element oxide *"$ZO_{y/2}$"* with a valence of *"y"* in the melt, $\gamma_{MO_{x/2}}^{melt}$ is the activity coefficient of a trace element oxide *"$MO_{x/2}$"* with electronic valence of *"x"* in the melt, $\gamma_{MO_{x/2}}^{crystal}$ is the activity coefficient of the trace element in the crystal and $ZO_{y/2}^{crystal}$ is the major element composition of the crystal. The k term is a constant to convert mole fraction to weight %. From equation 1.10, it is clear that the partition coefficient has to be affected by changes in temperature (as well as pressure), crystal chemistry (the "stoichiometric control") and, most importantly, by changes in the activity coefficient of a given trace element oxide species in the crystal and in the melt. The formation of melt complexes involving a major element and the trace element of interest in the melt will necessarily change the activity coefficient of the trace element, therefore affecting the overall partitioning behaviour of that element (O'Neill and Eggins, 2002). In a follow-up study, O'Neill et al. (2008) measured the solubility of W in silicate melts, and found that the XANES spectra obtained from their experimental glasses indicates that W^{6+} is tetrahedrally coordinated in silicate melt. They argued that W is likely associated with CaO forming stable $CaWO_4$ melt species, indicating that CaO (and to a lesser extent MgO) lower the activity coefficients for WO_3 in the silicate melt, which is reflected by an increase in the solubility of W in silicate melt. Based on these observations, Fonseca et al. (2014) suggested that both the mineral/melt partitioning behavior of W

and the W^{4+} to W^{6+} redox transition may be significantly affected, which would affect the overall behavior of that element during partial melting and crystallization.

1.2.4 Oxygen fugacity

Oxygen fugacity by definition is the partial pressure, or activity, of oxygen in a chemical system. This variable was first introduced to mineralogy and petrology by Eugster (1957) when trying to synthesise Annite (iron biotite), where a "buffer" assembly was used to fix the oxygen chemical potential of a series of experiments by diffusion of H_2 into the a Pt-capsule and capture enough oxygen until a chemical equilibrium is reached. Mineral redox buffers are commonly used in petrology (Frost, 1991), and one of the most common is the Fayalite-Magnetite-Quartz (FMQ) buffer, because it is approximately the state of oxidation of the Earth's Mantle, equivalent to a $Fe^{3+}/\sum Fe$ = 7-12 %, constant from primitive or evolved mid-ocean ridge basaltic (MORB) magmas (see Christie et al., 1986; Bezos and Humler, 2005; Cottrell and Kelley, 2011), described by the following reaction (O'Neill, 1987):

$$3Fe_2SiO_4 + O_2 = 2Fe_3O_4 + 3SiO_2 \tag{1.11}$$

which can be described in terms of its equilibrium constant as:

$$logK_{eq} = log(aFe_3O_4)^2 + log(aSiO_2)^3 - log(aFe_2SiO_4)^3 - log(fO_2) \tag{1.12}$$

Considering that all mineral phases are pure, their activity coefficient

will be 1, so:

$$logK_{eq} = -log(fO_2) \tag{1.13}$$

and, when chemical equilibrium is reached (i.e., ΔG = 0) we can correlate the change in free energy of formation for the reaction 1.11 (ΔG^0) with the equilibrium constant from equations 1.12 and 1.13 to obtain the fO_2 as a function of temperature:

$$log(fO_2) = \frac{-\Delta G^0}{2.303RT} \tag{1.14}$$

Even though oxygen is one of the most abundant elements in the Earth's mantle, the amount of free oxygen available at a magmatic system is usually low, for example, at 1100 °C, we can calculate fO_2 relative to the FMQ of only $10^{-9.7}$ bars. This simple calculation is based on a system at standard pressure (1 bar). It is reasonable to use FMQ buffer to approximate redox conditions at the mantle source of most terrestrial rocks (e.g., MORB, ocean island basalts, peridotite massifs, and xenoliths of spinel-peridotite, because they redox conditions range between ΔFMQ-2 to +2 (see compilation by Frost and McCammon, 2008). Oxygen fugacity tends to decrease with increasing pressure (e.g. Gudmundsson and Wood, 1995), which can be exemplified by the transition of olivine and opx to garnet (skiagite) in Earth's upper mantle, according to the reaction:

$$2Fe_3^{2+}Fe_2^{3+}Si_3O_{12} = 4Fe_2SiO_4 + 2FeSiO_3 + O_2 \tag{1.15}$$

The volume change (ΔV) for reaction 1.15 will be positive (ca. 9 cm^3/mol), meaning that pressure will favour the stability of skiagitic garnet, controlling

the Fe^{3+}/Fe^{2+} equilibrium (Frost and McCammon, 2008) and decreasing the overall fO_2 of the mantle. This trend is observed when estimating the fO_2 for several mantle garnet-peridotite xenoliths in different localities, such as the Slave and Kaapval Craton, and in the Fennoscandian shield (Luth et al., 1990; Woodland and Peltonen, 1999; Woodland and Koch, 2003; McCammon and Kopylova, 2004). Moreover, experiments have shown that FeO disproportionation will be so significant with increasing depth that a point will be reached in the Earth's upper mantle where a metallic Fe-Ni phase becomes stable (Ballhaus, 1991; Röhrbach et al., 2007), at depths below 250 km (ca. 8 GPa) and ΔFMQ $\leq$5. Although this is not directly applicable to the Moon, where at its core-mantle boundary pressure does not exceed 4 GPa (Weber et al., 2011), it has great implications for understanding the evolution of the oxidation state of the Earth from accretion to core formation (e.g., Frost et al., 2008b; Wade et al., 2012), and to present day MORB values (see review by Frost and McCammon, 2008).

Extraterrestrial mafic rocks, such as the basalts from the Moon, or depleted shergotites from Mars, and other meteorites, show evidence for being generated under redox conditions more reduced than in the Earth, with almost exclusively Fe^{2+} in the silicates and silicate glasses, as well as metallic alloys (e.g., Wadhwa, 2001; Papike, 2005). Oxygen fugacity of the lunar mantle was constrained by experiments, XANES spectroscopic measurements, as well as using solid electrolyte cells in natural samples, and ranges from 0.5 to 2 log-units below the Iron-Wüstite (IW) buffer (e.g. Sato, 1976; Delano, 1990; Sutton et al., 1993; Karner et al., 2006; Nicholis and Rutherford, 2009), which is expressed by the following reaction:

$$2FeO = 2Fe + O_2 \tag{1.16}$$

The thermodynamic calibration of the IW buffer was performed by Myers and Eugster (1983), being much more reduced than the FMQ buffer, i.e., for example at 1100 °C, the fO_2 relative to the IW equilibrium is $10^{-13.3}$ bars. Iron is the most commonly used element to estimate fO_2, given its high abundance in most rocks. The lower oxygen fugacity prevalent during partial melting of the lunar mantle will, in addition to Fe, also affect the behavior of heterovalent trace elements, which can also be used as tracers for the oxidation state of a magma (e.g. Mallmann and O'Neill, 2007; Fonseca et al., 2014). Some of the trace elements that may be present, partially or totally in a different oxidation state on the Moon and extraterrestrial samples when compared to the Earth's upper mantle are Cr and Eu (3+ to 2+), V (5+ to 3+), Ce (4+ to 3+), Mo, W, Re, and U (6+ to 4+) (e.g. Papike, 2005; Karner et al., 2006; Fonseca et al., 2014). By having a different valence, these elements will be coordinated differently in the silicate melt and have a bigger ionic radius, which results in being either preferentially incorporated or excluded from the crystallographic sites, consequently changing their $D_i^{crystal/melt}$ values. In other words, the closest the ionic radius gets to the r_o, the higher the $D_i^{crystal/melt}$ will be (see Equation 1.4 and 1.6). For example, crystal/silicate melt partitioning of Re^{6+} (valence at ΔFMQ +6) for the main phases in the upper mantle (spinel, garnet, pyroxene, and olivine) is five orders of magnitude lower than $D_{Re^{4+}}^{crystal/melt}$, which is the main oxidation state at ΔFMQ -4 (Mallmann and O'Neill, 2007), since in VI-fold coordination Re^{6+} has an i_r of 0.55 Å while Re^{4+} has an i_r of 0.63 Å (Shannon, 1976). This trend is also observed for U and V, with $D_U^{crystal/melt}$ and $D_V^{crystal/melt}$ for pyroxene, olivine, and spinel increasing by generally two to three orders of magnitude from oxidized (i.e. above ΔFMQ +2) to reduced conditions (below ΔFMQ -5) (e.g. Mallmann and O'Neill, 2009; Fonseca et al., 2014), showing evidence that this is a variable that

cannot be disregarded during petrogenesis modelling.

1.3 Motivation and objectives

As seen from the discussion in the previous sections, there are several factors that can affect crystal/silicate melt trace element partitioning during partial melting and crystallization processes. Despite of this, there are still several works that treat this value as a constant for simplification purposes, which can lead to an erroneous output or not realistic conditions for the petrogenetic modelling. All geochemical models rely on crystal/silicate melt partitioning, which in turn need to be derived from experiments performed under realistic conditions for fractional crystallization and mantle partial melting. This issue is even more important during lunar magmatism because most experimental crystal/silicate melt element partitioning studies have been done under conditions relevant to terrestrial magmatism, which are not essentially the same as in the Moon. Therefore, the aim of this thesis was to obtain crystal/silicate melt partitioning for a series of trace and minor elements as a function of silicate melt composition, crystal chemistry and oxygen fugacity, providing not only realistic partitioning date applied to modelling the crystallization sequence of the lunar magma ocean and petrogenesis of mare basalts, but also a holistic view of basic parameters controlling trace element fractionation during early geological evolution of differentiated "terrestrial" bodies of the solar system. To achieve the main objective of the research, the following specific objectives are summarized:

I. Develop different synthetic mare basalt silicate melt compositions and an experimental approach to crystallize large (at least 100 μm) silicates (olivine, orthopyroxene, clinopyroxene, plagioclase, and titanite), and oxides (ilmenite, and armalcolite) in equilibrium with silicate melt un-

der different conditions of oxygen fugacity, temperature and pressure;

II. Analyse the concentration of major and trace elements in the mineral phases and glasses;

III. Calculate the partition coefficient of trace elements between the mineral phases (silicates and oxides) and basaltic melts as a function of crystal chemistry, melt structure and composition, and fO_2;

IV. Refine the lattice strain model to take into account compositional effects of the silicate melt on trace element partitioning;

V. Reconstruct the trace element content of various lunar reservoirs throughout the crystallization of the LMO and the subsequent partial melting of its cumulates to give origin to mare basaltic lavas;

VI. Estimate LMO trace element starting abundances based on whole-rock lunar basalts trace element data.

Chapter 2

Competing effects of crystal chemistry and silicate melt composition on trace element behaviour in magmatic systems: insights from crystal/silicate melt partitioning of the REE, HFSE, Sn, In, Ga, Ba, Pt, and Rh

2.1 Introduction

The behavior of trace elements in magmatic systems is controlled by physico-chemical conditions prevalent during mantle partial melting and magmatic differentiation. Among these controlling factors are temperature, depth, type and degree of melting, source mineralogical composition and fO_2 (Onuma et al., 1968; Blundy and Wood, 1994; Lundstrom et al., 1994; Wood and Blundy, 1997; van Westrenen et al., 2001; Evans et al., 2008). Different experimental approaches exist to investigate trace element partition-

ing between crystals and coexisting melt. One approach aims to produce trace element partitioning data under conditions that are directly applicable to a specific geological process or geodynamic setting. Although such experiments might yield the most appropriate crystal/silicate melt partition coefficients for trace elements and for specific geochemical process being modeled, they may easily become less relevant if conditions differ or if their values change dynamically throughout the process (see discussion in van Westrenen et al., 2001). Another approach is to derive partition coefficients that can be applied to a wide range of dynamic settings. In this context, experiments are conducted in simple low-variance systems (i.e. only one variable is changed at a time), with the intent to assess their individual effects on trace element partitioning behaviour. In order to generate a coherent, systematic dataset of crystal/silicate melt partition coefficients for trace elements as a function of crystal composition, it is relatively straightforward to modify the bulk starting composition in order to achieve the desired change in crystal chemistry. However, it is often overlooked that it is challenging, if not impossible, to change crystal chemistry without changing melt composition, especially for phases that exhibit solid solutions, such as pyroxene and plagioclase. Because of this, it is often difficult to distinguish between the crystal chemistry and silicate melt compositional effects on trace element partitioning (e.g. O'Neill and Eggins, 2002).

The degree of melt polymerization and melt structure is often described by employing common melt descriptors such as NBO/T (number of non bridging oxygens per tetrahedrally coordinated cations) and the optical basicity parameter (OB) (e.g. Mills, 1993; Moretti, 2005). These parameters are well known to influence trace element partitioning (e.g. Gaetani, 2004). However, melt compositional effects not accounted by NBO/T or OB have also been found in recent studies. For example, Evans et al. (2008) and

Mallmann and O'Neill (2013) have shown that the partitioning of Sc, Y and the REE between olivine and silicate melt changes as a function of the mole fraction of $SiO_{2(melt)}$, rather than with NBO/T or OB. In the same sense, O'Neill and Eggins (2002) and O'Neill et al. (2008) suggested that CaO builds stable complexes with molybdenum and tungsten oxides in the melt. These stable complexes are presumably responsible for changes in the activity coefficient of these trace elements in the silicate melt (O'Neill and Eggins, 2002) and affect the way they substitute in the crystals alongside the stoichiometric control.

The aim of this study is to identify the stoichiometric controls and melt compositional effects on the behavior of trace elements partitioning between clinopyroxene (cpx), olivine (olv), and silicate melt. We chose two chemical compounds, Al_2O_3 and Na_2O, since both are known to play a significant role in changing the structure of silicate melts and clinopyroxene crystal chemistry (cf. Lundstrom et al., 1994; Gaetani and Grove, 1995; Hill et al., 2000). We present new crystal/silicate melt partitioning data for the REE, HFSE, Ga, Ba, Pt, Rh, Sn, and In obtained from experiments performed in vertical tube furnaces with temperatures ranging from 1190 to 1300 °C. The amount of sodium in the silicate melt was varied in order to cover the estimated concentration in the Earth's mantle (2590 μg/g - O'Neill and Palme, 1998), as well as the average found in mid-ocean ridge basalts (2.7 wt% - Jenner and O'Neill, 2012; Gale et al., 2013). The Al_2O_3 content in the cpx was also modified to cover a wide range of values (cf. Hill et al., 2000; Mollo et al., 2013). This enabled to eliminate the effect of melt polymerization and structure and isolate the individual effect of $^{[4]}Al$ on the crystal/silicate melt partitioning of trace elements. Moreover, the addition of Na_2O in the silicate melt enabled to identify a melt compositional effect on $D_i^{crystal/melt}$, which is yet not fully understood.

2.2 Material and Methods

2.2.1 Experimental materials and methods

Four starting compositions in the $CaO - MgO - Al_2O_3 - SiO_2$ (CMAS) system were synthesized. These compositions (Table 2.1) were chosen such that cpx was always a liquidus phase, and displayed a large enough range of $^{[4]}Al$ contents. Three compositions (HS, HE and HB) were modeled closely after Hill et al. (2000). In addition, a fourth composition (W1) was adopted from Fonseca et al. (2014) with the aim of producing $^{[4]}Al$-poor cpx. For further investigations concerning the effect of Na_2O on trace element partitioning between cpx and melt, the W1 composition was modified by adding variable amounts of Na_2O (CMAS + xNa_2O, 0 wt% $\leq$ x $\leq$ 3 wt%). The use of the previously well studied W1 composition as a basis composition allowed to minimize co-varying factors having an influence on the partitioning of trace elements between cpx and melt, as the cpx crystallized from this composition always contained a negligible amount of $^{[4]}Al$ and the coexisting melt is fairly depolymerized (NBO/T $\geq$ 1.1). A further advantage of the W1 composition is that in one-atmosphere experiments olivine and cpx can crystallize simultaneously. While a change in the sodium concentration of the starting mix may affect the crystal chemistry of cpx, the olivine crystal composition will remain constant (Evans et al., 2008). Thus, the presence of both phases can be used as a tool to assess crystal and melt compositional effects on $D_i^{crystal/melt}$.

High purity ($\geq$ 99.5 %) oxide powders (SiO_2, MgO, Al_2O_3, Fe_2O_3, Cr_2O_3 and TiO_2) were ground with $CaCO_3$ and Na_2CO_3 under acetone in an agate mortar for ca. 10 minutes. Starting powder mixes were subsequently dried, pressed into pellets and placed in a corundum crucible inside a vertical tube furnace to decarbonate overnight in air at 1 bar / 950 °C. All pressed pellets

were then re-ground under acetone and trace elements (Sc, Ni, Ga, Ge, Sn, In, Mn, Zr, Nb, Hf, Ta, Sm, Eu, Lu, La, Y, Th, and U) were added to the powders, in amounts of 500 to 1000 μg/g, as oxide powders or Specpure plasma standard solutions of 1000 μg/mL in 5% HNO_3. Barium was added as $BaCO_3$. The broad range of trace elements doped, especially to the W1 + xNa_2O, aimed at having enough cations to define the lattice strain parabolas by increasing the number of data points fitted to the lattice strain function (Blundy and Wood, 1994).

Table 2.1: Starting compositions of the powder mixtures in cg/g.

	HS	HE	HB	W1	W1 + xNa_2O
SiO_2	45.02	52.97	43.18	47.79	48.21
Al_2O_3	17.11	16.13	17.41	5.12	5.17
MgO	12.45	13.12	12.1	25.75	26.03
CaO	25.06	17.43	27.12	17.91	18.04
Na_2O	0.36	0.35	0.19	-	x[1]
Cr_2O_3	-	-	-	0.47	0.48
Fe_2O_3	-	-	-	0.49	0.50
P_2O_5	-	-	-	1	0.54
TiO_2	-	-		1	1.02
Total	99.66	99.64	99.86	99.53	100.0

[1] Variable amount of Na_2O (0 wt. % > x < 3 wt. %)

A summary of the experimental run conditions is given in Table 2.2. Starting compositions were mixed with polyethylene glycol and water into a slurry, which was then placed in a Pt-Rh wire loop. The loops were suspended from a sample holder and loaded into the hotspot of a vertical tube gas-mixing furnace. The top and bottom of the furnace were kept open to maintain log fO_2 at -0.7 (equivalent to air), where the valence of trace elements is constant and no significant loss of Na is expected. Experiments were kept for three to five hours at supraliquidus temperatures (1400 °C) to

ensure complete melting of the powders and chemical homogenization prior to crystallization. The temperature during the experiments was monitored by an internal type B ($Pt_{94}Rh_6 - Pt_{70}Rh_{30}$) thermocouple and was initially calibrated against the melting point of gold (cf. Laurenz et al., 2010, 2013), and found to be within 5 °C of it. Cooling ramps were around 0.05 °C/min to ensure adequate crystal growth (at least 100 μm) for LA-ICP-MS analysis. After reaching the target temperature, samples remained 48-86 hours in the furnace to establish equilibrium between the crystals and the coexisting melt. Subsequently, experiments were quenched in air by removing the holder from the top of the furnace, which has a water-cooling system that keeps the temperature constant at 25 °C. Loops were then mounted in epoxy resin and its surface was polished for chemical analysis.

Table 2.2: Experimental run conditions and products.

Experiment	Cooling ramp (°C/min)[1]	Temp. (°C)	Run time (h)[2]	Eq. Phases
HS1	0.1 - 1270; 0.05 - 1220	1220	3 + 74	cpx+glass
HE1	0.1 - 1280; 0.05 - 1190	1190	3 + 86	cpx+glass
HE2	0.1 - 1280; 0.05 - 1240	1240	3 + 70	cpx+glass
HB1	0.1	1270	3 + 48	cpx+an+glass
W1	0.05	1300	3 + 56	cpx+ol+glass
W1 + x Na_2O	0.05	1288	4 + 72	cpx-ol+glass[3]

[1] In the case of two-steps cooling ramp, the first step was performed on supraliquidus temperature and the second step during crystal growth.
[2] Time experiment spent above supraliquidus (50 to 100 °C above target T.) + the time spend to equilibrate after cooling;
[3] Experiments did not always crystallize both phases;

2.2.2 Analytical techniques

Concentration of major and minor elements (CaO, SiO_2, MgO, Al_2O_3, Na_2O, Fe_2O_3, Cr_2O_3 and TiO_2) in the crystals and silicate melt were acquired with a JEOL JXA-8200 electron microprobe. Analysis were carried

out using wavelength dispersive mode (WDS) employing an accelerating voltage of 15 kV and 15 nA beam current, with an electron beam defocused to 5 μm. Most of the of major element oxides were calibrated on a natural basalt from the Juan de Fuca ridge (VG2 - Jarosewich et al., 1980), while Na_2O was calibrated using a jadeite-diopside eutectic glass and TiO_2 in rutile, employing peak to background calibrations and the ZAF correction algorithm to account for the different electron absorption properties of the samples and the standards used. Major element concentrations are given as an average of five to ten representative spots on each phase.

Trace element abundances were acquired with a Resonetics Resolution M50-E 193 nm Excimer laser ablation apparatus coupled to a Thermo Scientific XSeries II Q-ICP-MS at the Steinmann Institute, University of Bonn. The nuclides ^{29}Si, ^{43}Ca, ^{45}Sc, ^{55}Mn, ^{60}Ni, ^{69}Ga, ^{71}Ga, ^{72}Ge, ^{74}Ge, ^{89}Y, ^{90}Zr, ^{91}Zr, ^{93}Nb, ^{103}Rh, ^{115}In, ^{118}Sn, ^{120}Sn, ^{121}Sb, ^{123}Sb, ^{137}Ba, ^{138}Ba, ^{139}La, ^{151}Eu, ^{153}Eu, ^{152}Sm, ^{154}Sm, ^{175}Lu, ^{177}Hf, ^{178}Hf, ^{181}Ta, ^{182}W, ^{184}W, ^{195}Pt, ^{232}Th and ^{238}U were monitored during LA-ICP-MS analysis. The spot size was set between 44 and 73 μm to avoid melt inclusions, which are ubiquitous in experimental work (see e.g., Fonseca et al., 2014). For a secure melt-free analysis of the crystals, Barium was used as a reference, because it is highly incompatible in cpx and olivine (Lundstrom et al., 1994; Mollo et al., 2013). On each sample, five spot analyses in the glass and at least ten spots in the crystals were carried out using a laser fluency of ~ 6 J/cm^2 and a repetition rate of 15 Hz. For each measured spot, 15 s of background signal were followed by 30 s of ablation signal. The NIST-SRM-612 glass (Jochum et al., 2011) was used as the external standard, with measurements carried out via standard/sample bracketing with no more than ten samples measured between each standard measurement. Additional spots were carried out in the NIST-610 glass, which was treated as an unknown to check for data ac-

curacy. Obtained concentrations on the NIST-610 were found to be within 5 to 10 % within the reported values (Jochum et al., 2011). To correct for differences in ablation efficiency count rates were normalized either by ^{29}Si or ^{43}Ca, which were used as internal standards for olivine, clinopyroxene and melt, respectively. Data reduction was carried out employing the methodology described by Longerich et al. (1996).

2.3 Experimental results

Major, minor and trace element compositions of each crystalline and melt phase were found to be widely homogeneous (Table 2.3 and Supplementary Material), indicating a close approach to chemical equilibrium during the experiments. Although several trace elements were doped to the experiments, their combined abundance did not add up to more than 2 wt%, and as such, Henry's law was likely obeyed (cf. Gaetani, 2004). Calculated partition coefficients are depicted in Table 2.4. A major concern when dealing with volatile elements (e.g., Sn, Sb, Ge and In) is their loss during the experimental run (e.g. Mallmann et al., 2015). Trace element concentrations of Sn, Sb and Ge in the experiments show a significant depletion from the initially doped amount, with final concentrations generally below 10 μg/g in the silicate glass. Indium loss was also found in the experimental runs, albeit relatively minor with a final concentrations of several hundreds of μg/g. Gallium is refractory under the experimental conditions of this study, and measured Ga concentrations do not show a depletion relative to the amount that was initially doped.

Table 2.3: Major oxide composition (wt%) of crystalline phases and silicate glass.

Exp.	Temp.	Phase	SiO_2	MgO	CaO	Al_2O_3	Na_2O	FeO	TiO_2	Cr_2O_3	T.E.	Total	total Al (apfu)	$^{[4]}$Al (apfu)	Na (apfu)	NBO/T[1]
Experiments in the CMAS - system																
HS1	1220 °C	melt	47.60 (48)	6.32 (4)	25.70 (11)	19.89 (18)	0.32 (4)				0.60	100.43				0.72
		cpx	48.39 (63)	13.55 (27)	25.55 (21)	13.47 (63)	0.04 (2)				0.44	101.44	0.570	0.270		
HE1	1190 °C	melt	55.9 (21)	7.79 (13)	16.72 (6)	18.49 (15)	0.38 (6)				0.44	99.72				0.50
		cpx	52.98 (18)	17.70 (19)	23.44 (25)	6.68 (20)	0.05 (2)				0.23	101.08	0.280	0.115		
HE2	1240 °C	melt	59.24 (34)	8.55 (16)	15.11 (15)	15.92 (15)	0.67 (2)				0.79	100.28				0.53
		cpx	54.99 (29)	18.99 (27)	22.97 (14)	3.95 (34)	0.052 (2)				0.40	101.35	0.170	0.048		
HB1	1240 °C	melt	46.72 (75)	8.34 (31)	29.31 (92)	16.47 (101)	0.21 (2)				0.78	101.83				1.04
		cpx	50.53 (50)	14.89 (32)	25.27 (33)	9.78 (83)	0.02 (1)				0.27	100.76	0.414	0.185		
W1	1300 °C	melt	54.64 (24)	15.62 (12)	16.73 (7)	8.91 (9)	0.105 (3)	0.72 (5)	1.78 (1)	0.02 (1)	0.86	99.20				1.10
		cpx	56.56 (14)	21.90 (25)	20.88 (34)	0.85 (6)		0.24 (5)	0.36 (4)	0.04 (1)	0.13	100.96	0.035			
		olivine	44.02 (14)	55.59 (63)	0.47 (4)	0.016 (10)	0.12 (9)	0.17 (2)			-	100.39	0.001			
Experiments in the CMAS +xNa_2O - system																
W1-1	1286 °C	melt	53.05 (34)	15.22 (4)	20.57 (9)	6.55 (12)	1.12 (7)	0.74 (10)	1.35 (9)	0.016 (5)	1.36	99.98				1.4
		olivine	43.07 (42)	55.82 (21)	0.58 (3)	0.026 (16)	0.023 (3)	0.19 (7)			0.57	100.28	0.001			
W1-2	1286 °C	melt	52.66 (19)	16.08 (7)	18.36 (12)	8.57 (11)	0.049 (32)	0.73 (9)	1.58 (7)	0.02 (1)	1.83	99.88				1.2
		cpx	55.61 (20)	21.35 (52)	21.82 (45)	0.82 (13)	0.03 (1)	0.18 (3)	0.31 (12)	0.05 (3)	0.30	100.47	0.034	0.019	0.002	
		olivine	42.67 (70)	55.54 (35)	0.53 (3)	0.038 (17)	0.017 (13)	0.16 (3)	0.022 (8)		0.65	99.63	0.001			
W1-3	1286 °C	melt	51.65 (18)	13.85 (9)	17.27 (7)	10.35 (7)	1.73 (9)	0.70 (6)	2.23 (9)	0.022 (16)	2.17	99.97				1.1
		cpx	55.14 (47)	20.00 (24)	23.11 (48)	1.26 (22)	0.19 (4)	0.27 (6)	0.51 (9)	0.021 (14)	0.38	100.88	0.053	0.03	0.130	
		olivine	42.67 (69)	55.52 (21)	0.63 (2)	0.02 (1)	0.017 (1)	0.18 (5)		0.011 (8)	-	99.05	0.001			
W1-4	1286 °C	melt	52.14 (3)	13.69 (9)	17.03 (12)	9.81 (18)	2.61 (10)	0.84 (3)	1.83 (6)	0.022 (12)	2.06	100.03				1.1
		cpx	54.91 (48)	19.33 (18)	23.55 (29)	1.30 (22)	0.28 (4)	0.30 (3)	0.60 (16)	0.009 (2)	0.47	100.75	0.055	0.03	0.020	
		olivine	42.17 (63)	55.48 (10)	0.71 (2)	0.04 (1)	0.024 (19)	0.15 (5)	0.03 (2)	0.014 (13)	-	98.62	0.001			
W1-5	1286 °C	melt	52.56 (14)	13.62 (11)	16.74 (9)	9.73 (9)	2.43 (6)	1.04 (5)	1.79 (8)	0.013 (12)	2.09	100.01				1.1
		cpx	54.34 (63)	19.5 (1)	23.35 (9)	1.33 (4)	0.27 (3)	0.33 (6)	0.49 (4)	0.006 (6)	0.48	100.10	0.056	0.045	0.019	
		olivine	42.89 (55)	55.49 (21)	0.66 (2)	0.04 (1)	0.029 (26)	0.15 (6)	0.018 (14)	0.011 (8)	-	99.29	0.001			
W1-6	1286 °C	melt	53.09 (46)	15.00 (8)	20.32 (12)	6.56 (7)	1.70 (9)	0.77 (3)	1.33 (5)	0.25 (20)	1.41	100.43				1.4
		olivine	42.88 (34)	55.53 (45)	0.77 (1)	0.03 (1)	0.04 (2)	0.15 (4)	0.028 (1)	0.014 (11)	0.47	99.91	0.001			

[1] NBO/T: number of non-bridging oxygens per tetrahedrally coordinated cations; OB: opticla basicity; calculated based on the methodology of Mills (1998)

T.E.: total of trace elements (LA-ICP-MS - Supplementary Table 1)

Table 2.4: Trace element crystal/silicate melt partition coefficients with one standard deviation of the mean value, given here as the last significant digits in parenthesis.

cpx/melt	D_{Al}	σ	D_{Sc}	σ	D_{Cr}	σ	D_{Mn}	σ	D_{Ni}	σ	D_{Ga}	σ	D_{Y}	σ	D_{Zr}	σ	D_{Nb}	σ	D_{Rh}	σ	D_{In}	σ
HS1											0.731	(65)	0.642	(46)							2.26	(26)
HE1											0.454	(23)	0.747	(66)							1.42	(13)
HE2											0.317	(21)	0.591	(49)							1.38	(20)
HB1											0.572	(74)	0.424	(34)								
W1											0.090	(8)	0.166	(12)								
W1-2	0.096	(15)	0.80	(10)			0.484	(46)	1.371	(99)	0.0942	(11)	0.1591	(12)	0.0214	(60)	0.0012	(2)	2.86	(24)	0.327	(27)
W1-3	0.122	(21)	1.65	(16)			0.387	(35)	1.439	(119)	0.119	(14)	0.198	(22)	0.0475	(72)	0.0021	(2)	4.26	(73)	0.831	(53)
W1-4	0.133	(22)	2.24	(14)			0.380	(26)	1.521	(78)	0.137	(6)	0.260	(35)	0.0893	(72)	0.0038	(6)	6.05	(144)	0.952	(44)
W1-5	0.137	(4)	2.32	(16)			0.358	(19)	1.363	(75)	0.146	(7)	0.251	(17)	0.1089	(160)	0.0051	(17)	5.24	(54)	0.973	(54)

cpx/melt	D_{Sn}	σ	D_{Ba}	σ	D_{La}	σ	D_{Sm}	σ	D_{Eu}	σ	D_{Lu}	σ	D_{Hf}	σ	D_{Ta}	σ	D_{Pt}	σ	D_{Th}	σ	D_{U}	σ
HS1	12.8	(29)	0.00182	(84)	0.137	(20)	0.583	(42)	0.629	(35)	0.605	(31)					0.114	(48)				
HE1	2.83	(32)	0.00168	(88)	0.112	(14)	0.586	(77)	0.675	(86)	0.661	(70)					0.060	(5)				
HE2	3.6	(11)	0.00085	(25)	0.093	(11)	0.481	(46)	0.526	(41)	0.557	(78)					0.042	(15)				
HB1	5.9	(12)	0.00081	(24)	0.084	(14)	0.357	(53)	0.400	(60)	0.428	(70)					0.043	(15)				
W1	0.48	(12)	0.00029	(23)	0.026	(4)	0.125	(11)	0.136	(11)	0.166	(13)					0.018	(5)				
W1-2	0.19	(8)	0.00012	(1)	0.025	(4)	0.123	(12)	0.134	(12)	0.150	(14)	0.047	(14)	0.00111	(39)	0.023	(6)	0.0014	(4)	0.000070	(15)
W1-3	0.46	(9)	0.00019	(2)	0.043	(2)	0.175	(18)	0.190	(20)	0.200	(19)	0.109	(16)	0.00283	(63)	0.045	(12)	0.0034	(3)	0.000203	(41)
W1-4	0.40	(7)	0.00026	(4)	0.066	(17)	0.243	(33)	0.252	(34)	0.274	(36)	0.200	(13)	0.00608	(23)	0.089	(21)	0.0046	(9)	0.000177	(23)
W1-5	0.67	(12)	0.00023	(4)	0.061	(6)	0.229	(16)	0.243	(18)	0.261	(18)	0.231	(30)	0.01072	(18)	0.106	(20)	0.0069	(16)	0.000208	(50)

olivine/melt	D_{Al}	σ	D_{Sc}	σ	D_{Cr}	σ	D_{Mn}	σ	D_{Ni}	σ	D_{Ga}	σ	D_{Y}	σ	D_{Zr}	σ	D_{Nb}	σ	D_{Rh}	σ	D_{In}	σ
W1-1	0.0040	(24)	0.099	(3)	0.97	(31)	0.820	(28)	10.5	(4)	0.0054	(9)	0.0044	(3)	0.00033	(5)			2.145	(362)	0.112	(6)
W1-2	0.0044	(19)	0.092	(6)	0.67	(19)	0.678	(22)	8.8	(2)	0.0049	(5)	0.0029	(2)	0.00020	(3)			1.843	(146)	0.081	(3)
W1-6	0.0046	(15)	0.119	(5)	1.36	(67)	0.847	(33)	10.2	(3)	0.0058	(7)	0.0062	(5)	0.00033	(1)			2.706	(325)	0.121	(8)

olivine/melt	D_{Sn}	σ	D_{Ba}	σ	D_{La}	σ	D_{Sm}	σ	D_{Eu}	σ	D_{Lu}	σ	D_{Hf}	σ	D_{Ta}	σ	D_{Pt}	σ	D_{Th}	σ	D_{U}	σ
W1-1			0.0000023	(8)	0.0000044	(18)	0.000212	(43)	0.000372	(19)	0.0177	(7)	0.00049	(9)	0.000025	(15)			0.0000012	(4)		
W1-2			0.0000015	(11)	0.0000034	(9)	0.000142	(7)	0.000244	(17)	0.0122	(6)	0.00034	(2)	0.000008	(4)			0.0000017	(14)		
W1-6			0.0000165	(77)	0.0000048	(16)	0.000365	(98)	0.000553	(65)	0.0245	(16)	0.00039	(8)	0.000046	(30)						

2.3.1 CMAS system

All experiments carried out in the CMAS system crystallized euhedral to subhedral homogeneous clinopyroxene in equilibrium with silicate glass. In one single case (HB1), clinopyroxene crystals were found inter-grown with anorthite. The silicate glass, as well as the crystal compositions, display a broad range of SiO_2 and Al_2O_3 concentration, while smaller variations are observed for CaO and MgO. The tetrahedrally coordinated Al in cpx ($^{[4]}$Al) ranges between 0 and 0.27 apfu (Table 2.3). The broad range of $^{[4]}$Al contents in cpx allows us to study its effect on $D_i^{cpx/melt}$ in a systematic fashion. Unfortunately, it was not possible to vary the $^{[4]}$Al in cpx without changing melt composition, i.e., changes in the degree of melt polymerization were unavoidable, with NBO/T ranging from 0.5 to 1.1 (Table 2.3).

Crystal/silicate-melt partition coefficients as a function of the $^{[4]}$Al content in clinopyroxene

The REE and Y show a clear positive correlation with increasing $^{[4]}$Al content in cpx for all experiments. However, for two compositions, HE1 and HE2, with $^{[4]}$Al of 0.115 and 0.048 respectively, the $D_{REE+Y}^{cpx/melt}$ are higher than the overall trend of $D_{REE+Y}^{cpx/melt}$ versus $^{[4]}$Al (Figure 2.1). Barium is more compatible in cpx as a function of $^{[4]}$Al (Figure 2.1h). Crystal/silicate melt partitioning of Sn and In as a function of $^{[4]}$Al are scarce in the literature (e.g., Hill et al., 2000; Adam and Green, 2006) and new partitioning data presented here can be used to better constrain a positive correlation between their $D_{Sn,In}^{cpx/melt}$ and $^{[4]}$Al in the cpx. Even considering that experiments were prone to volatile loss, the agreement between data of this study and that reported by Hill et al. (2000), which performed experiments with sealed capsules, suggests that equilibrium was reached in the experiments.

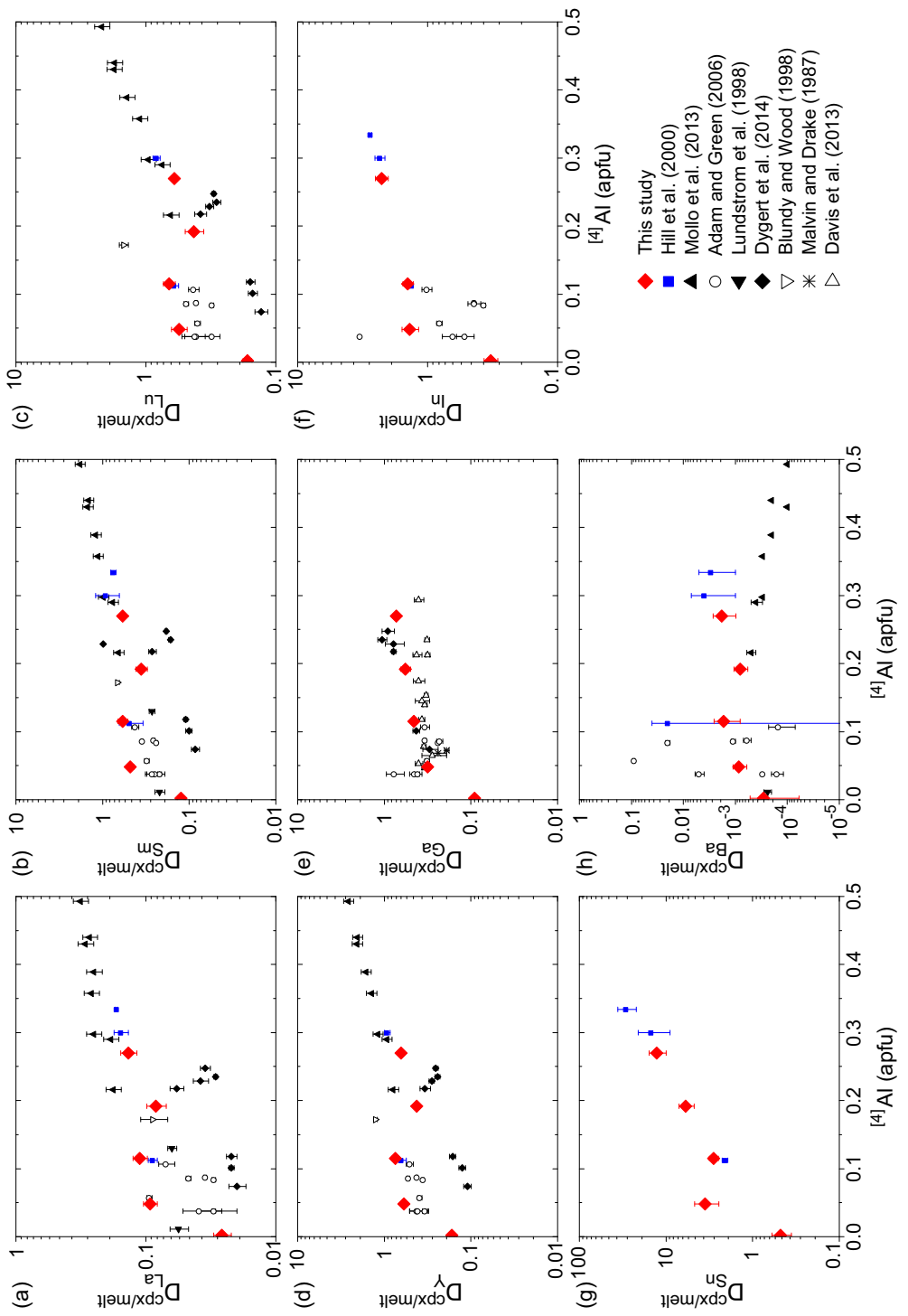

Figure 2.1: Clinopyroxene/melt partition coefficient data plotted as a function of the tetrahedrally coordinated aluminum ($^{[4]}$Al). Error bars are one standard deviation. Literature data are taken from experiments ranging from 1050 – 1300 °C and pressures up to 3 GPa (Malvin and Drake, 1987; Blundy et al., 1998; Lundstrom et al., 1998; Hill et al., 2000; Adam and Green, 2006; Davis et al., 2013; Mollo et al., 2013; Dygert et al., 2014).

2.3.2 CMAS + Na system

The second experimental series yielded fosterite and clinopyroxene crystals. Clinopyroxene crystals reached up to a mm in size, while fosterite crystals remained distinctly smaller (≤ 50 μm). In some experiments olivine crystals were too small to be analyzed using LA-ICP-MS so the olivine dataset is not as extensive as for cpx. The cpx composition shows a dependence on the amount of sodium added to the starting composition (Table 2.3). However, even though the Na_2O content of the cpx varies proportionally with the Na_2O content of the melt, it remains consistently small (0.002-0.02 Na apfu). The $^{[4]}$Al in cpx in this series was designedly low (0.02 to 0.045 Al apfu) and melt composition shows small variations between the experiments depending on the initial amount of Na_2O (0.05 to 2.61 wt%), the degree of crystallization and whether cpx and olivine co-exist. Accordingly, NBO/T (1.1 - 1.3) and OB (0.6) variation is negligible when compared to the first experimental series (compare Table 2.3).

Crystal/silicate-melt partitioning as a function of melt Na_2O

Regarding divalent cations, $D_{Ba}^{cpx/melt}$ and $D_{Pt}^{cpx/melt}$ correlate positively with $Na_2O_{(melt)}$ (Figure 2.2a-b), while $D_{Ni}^{cpx/melt}$ (Figure 2.2c) and $D_{Mn}^{cpx/melt}$ tend to be broadly insensitive to this parameter. Platinum may be tetravalent under very oxidizing conditions, such as with a pure O_2 atmosphere (Ertel et al., 1999). However, the proportion of Pt^{4+} over most of the range of fO_2 studied was deemed negligible (cf. Ertel et al., 1999), so it is very likely the Pt^{2+} is the oxidation state of Pt in the experiments. Crystal/silicate melt partitioning for trivalent cation (REE, Y, Sc, Rh and In) show a linear positive increase with $Na_2O_{(melt)}$ (Figure 2.2). The exception is Ga^{3+}, with $D_{Ga}^{cpx/melt}$ values being unaffected by the presence of Na_2O in the melt (Figure

2.2g). The most surprising crystal/silicate melt partitioning behaviour is observed for tetravalent and pentavalent cations (e.g. HFSE, Th, Sn, and Ge), with $D_i^{cpx/melt}$ values increasing by almost one order of magnitude with increasing $Na_2O_{(melt)}$ (e.g., Figure 2.2i).

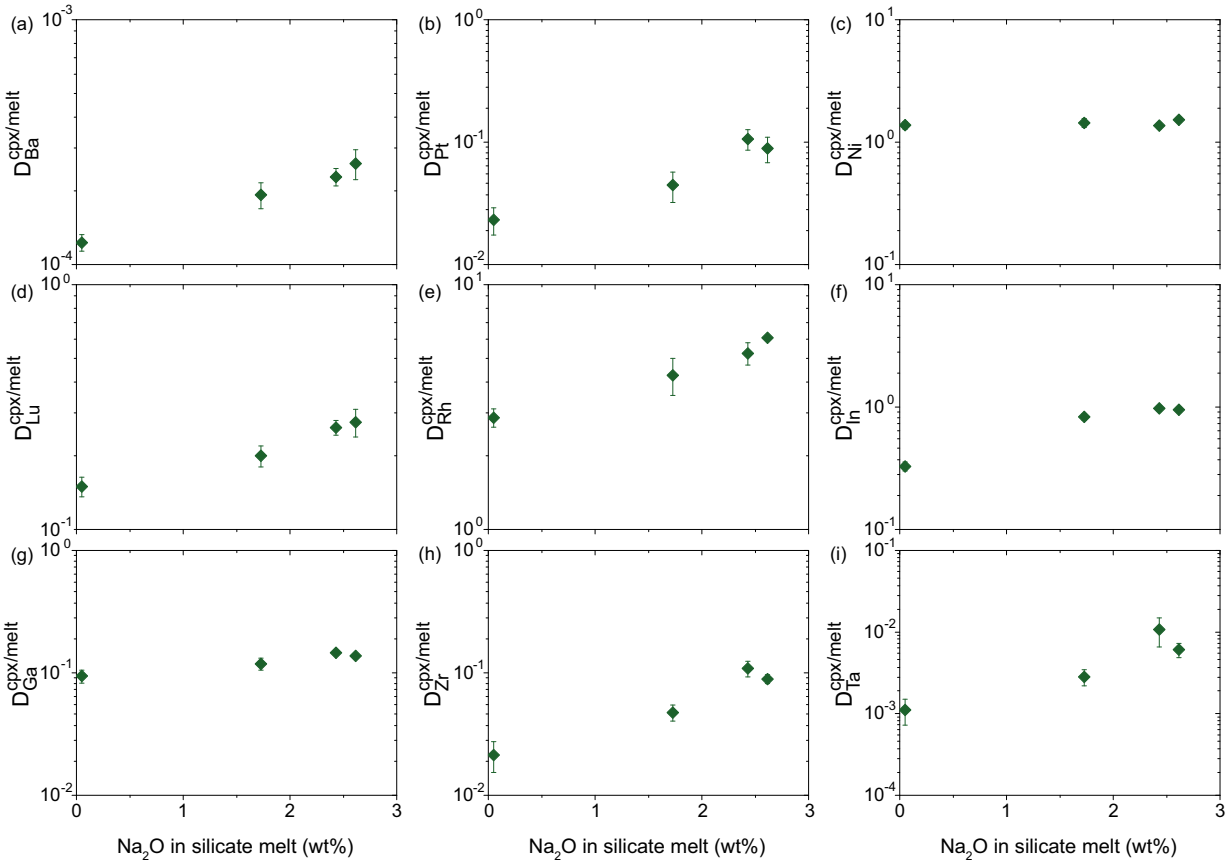

Figure 2.2: Clinopyroxene/melt partition coefficient data plotted as a function of the Na_2O (wt%) content of the melt. Error bars are one standard deviation.

Evaluating olivine/silicate melt trace element partitioning data is challenging due to their low $D_i^{olivine/melt}$ values (e.g. Mallmann and O'Neill, 2009; Fonseca et al., 2014). Therefore, analysis presented here have trace element concentrations in olivine which are at the detection limit or below. Despite this issue, it is possible to identify trends of $D_i^{olivine/melt}$ as a function of $Na_2O_{(melt)}$. Regarding divalent cations, $D_{Ba}^{olivine/melt}$ increases by

around an order of magnitude over the range of $Na_2O_{(melt)}$ (Figure 2.3a), while $D_{Mn}^{olivine/melt}$ (Figure 2.3b) and $D_{Ni}^{olivine/melt}$ (Figure 2.3c) remain constant. Olivine/melt partitioning of the trivalent REE, Y, and In show a distinct positive dependence on the amount of $Na_2O_{(melt)}$ (Figure 2.3d-f). Gallium and Sc, although also trivalent at log fO_2 = -0.7, do not show a strong increase with $Na_2O_{(melt)}$. Chromium was not intentionally added to the starting compositions, but was present in most experiments as a contaminant (max. 5 $\mu g/g$), and $D_{Cr}^{olivine/melt}$ values increase with increasing $Na_2O_{(melt)}$, albeit within uncertainty. Values for $D_{HFSE}^{olivine/melt}$ (e.g., Figure 2.3h,i) increase with $Na_2O_{(melt)}$, although with large associated errors due to their low concentration in the crystals (lower than 0.5 μg/g).

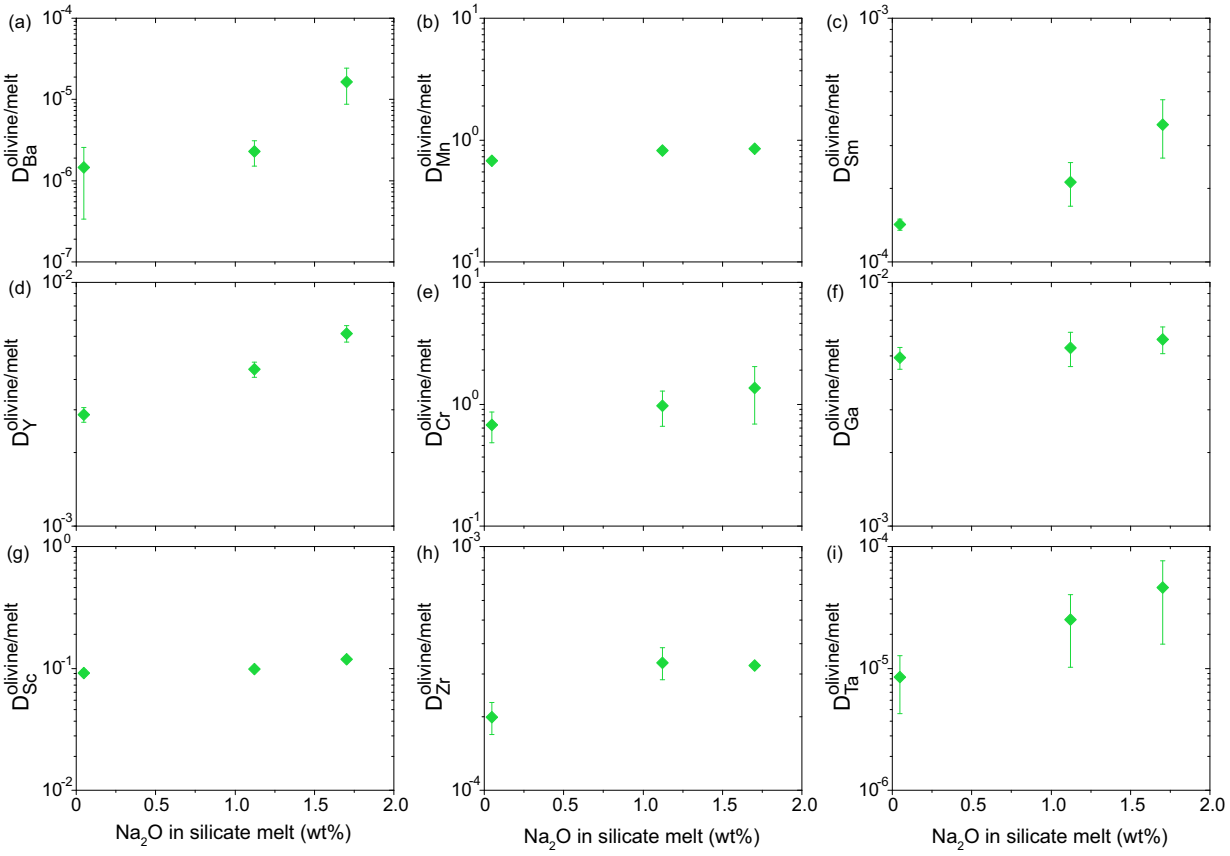

Figure 2.3: Olivine/melt partition coefficient data plotted as a function of the Na_2O (wt%) content of the melt. Error bars are one standard deviation.

2.4 Discussion

2.4.1 Interplay between $^{[4]}$Al and melt compositional and structural effects on trace element partitioning

With the exception of Eu and Ce, the REE are homovalent elements that substitute into the M2 site of clinopyroxene in [8]-fold coordination (Gaetani and Grove, 1995) and increase their $D_i^{cpx/melt}$ values with increasing $^{[4]}$Al content in cpx (e.g., Figure 2.1a-d). However, crystal/silicate melt partition coefficients obtained in two experiments (HE1 and HE2) are larger by one order of magnitude than the range of published experimental data with comparable $^{[4]}$Al in cpx (Figure 2.1a-d; cf. Adam and Green, 2006; Lundstrom et al., 1998). One likely explanation for this discrepancy is a change in the degree of melt polymerization given that the lowest NBO/T values reported here (ca. 0.5) were obtained for these two outlier experiments (HE1 and HE2). The degree of melt polymerization is not so easily decoupled from stoichiometric controls on crystal/silicate melt trace element partitioning (e.g. Ryerson and Hess, 1978; Kohn and Schofield, 1994; Blundy et al., 1998; Mysen, 2004; Gaetani, 2004; Huang et al., 2006). Several studies systematically observed the dependence of $D_{REE}^{cpx/melt}$ on the degree of melt polymerization and have shown a distinct increase of partition coefficients of the REE with increasing melt polymerization (e.g. Gaetani, 2004; Prowatke and Klemme, 2005; Huang et al., 2006). Gaetani (2004), in particular, has shown that the influence of melt structure on $D_{REE}^{cpx/melt}$ becomes significant for melt compositions with NBO/T values below 0.49, an expectation later confirmed by Huang et al. (2006). Because it is almost impossible to change cpx crystal chemistry without changing melt composition (e.g. Mallmann and O'Neill, 2009), it is necessary to find a way to isolate the individual effects of melt composition and structure from the addition of $^{[4]}$Al in the cpx

on the $D_i^{cpx/melt}$ values. To do this, we have used the experimental partitioning series for Mn and Zn between olivine and silicate melt as a function of NBO/T performed by Kohn and Schofield (1994). Because olivine composition remains the same over a range of NBO/T, one can assess the isolated effect of melt composition, which is best described by the following function:

$$D_i^{olivine/melt} = a * [NBO/T]^{\,b} \tag{2.1}$$

The empirical approach of Kohn and Schofield (1994) can be extended to any cation that is exchanged between crystal and melt, provided of course, that a large enough dataset, covering a wide range of degrees of melt polymerization, exists. We used the experimental results of Gaetani (2004) and Huang et al. (2006), because their studies were set up to systematically investigate the effect of melt structure on $D_{REE}^{cpx/melt}$, as well as additional data from the literature and plotted their partition coefficients vs. NBO/T (see Figure 2.4). The largest dataset exists for La and Sm, while Eu partitioning data were found to be too few for a meaningful regression to be obtained. The scatter of the data obtained from different studies was found to be relatively large when compared to the goodness of the correlation obtained by Kohn and Schofield (1994), which is likely a result of the covariation of the clinopyroxene crystal composition with melt composition. Additionally, differences in the experimental conditions prevalent for each dataset, as well as data accuracy may be significant. Nevertheless, crystal/silicate melt partitioning data can be fitted reasonably well to equation (1) (e.g., Figure 2.4a and b and Table 2.5). The empirical fitting parameter a (Table 2.5) was found to vary according to the ionic radii of the elements and, hence, can be fitted to the lattice strain function (see Figure 2.5), using the Levenberg-Marquardt iterative algorithm (Marquardt, 1963).

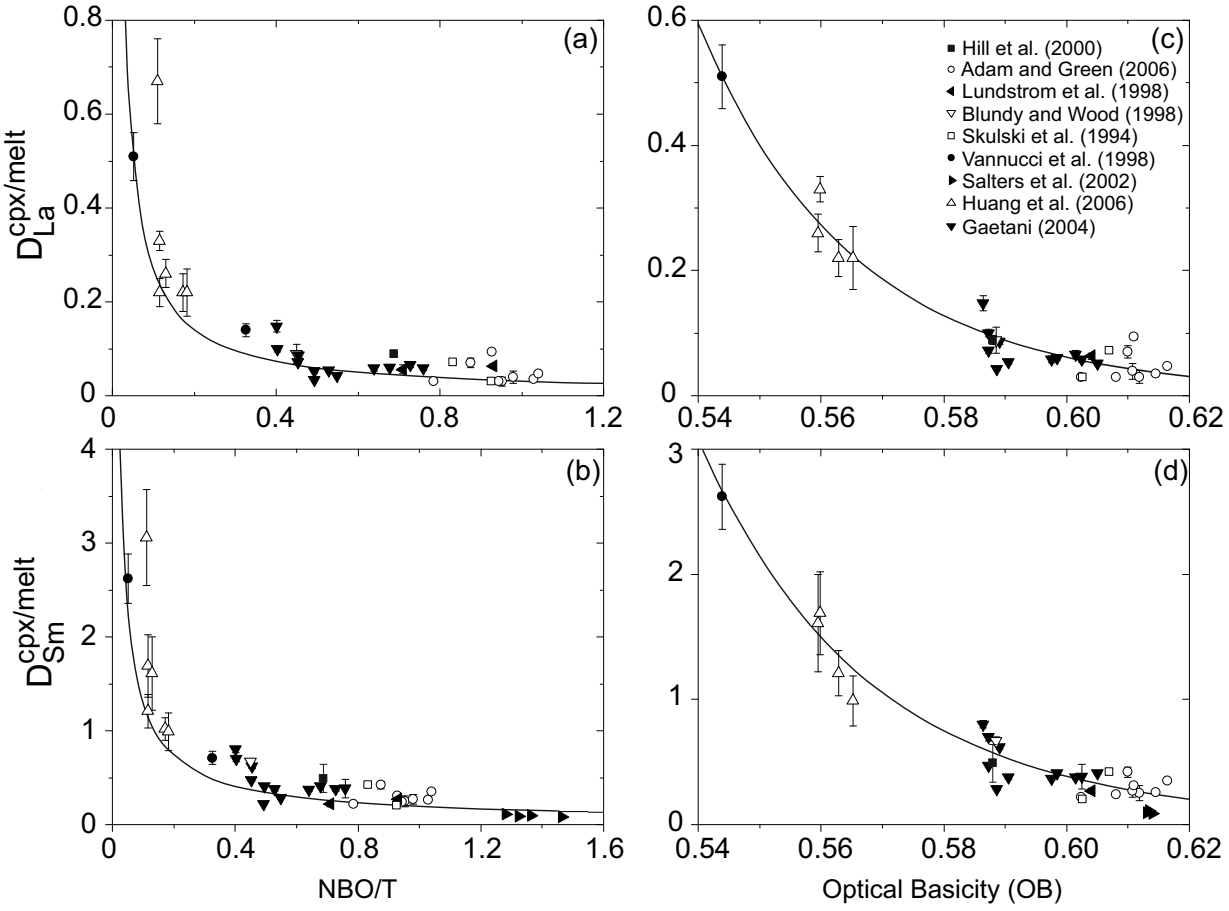

Figure 2.4: $D_i^{cpx/melt}$ values of La (a+c) and Sm (b+d) are plotted as a function of NBO/T and OB, respectively. Only partitioning data for clinopyroxenes with similar crystal composition, used to minimize uncertainty, caused here by variable stoichiometry (e.g. variable $^{[4]}$Al). Partitioning data were fitted to an exponential function, the results of which are represented by the full black lines in the diagrams (see text for discussion). Similar regressions produced for crystal/silicate melt partitioning of Lu and Y can be found in the supplementary material.

Because a is a cation specific parameter and its value is dependent on the ionic radius of a given cation, the relation between $D^{cpx/melt}_{REE+Y}$ and i_r, mimics that of the lattice strain function of Blundy and Wood (1994). The exponent b (Table 2.5) does not show any systematic dependence on any of the specific properties (e.g. the ionic radius) of each element, and is not

reflecting any physico-chemical change in the system. Therefore it is likely that the differences in the values for "b" exponents are due to variations in the experimental conditions (temperature and pressure), and starting composition from each experimental dataset.

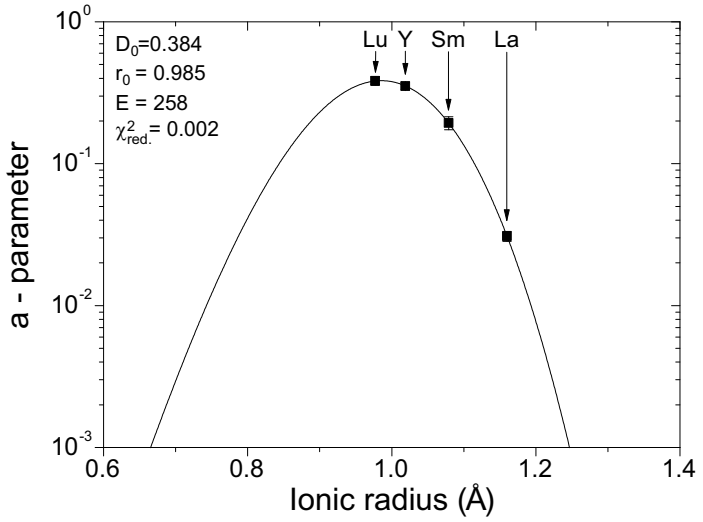

Figure 2.5: The prefactor a plotted as a function of i_r (ionic radius) regressed using the lattice strain function. If not visible, errors are smaller than symbol size.

To be able to formulate a universal descriptor for the effect of NBO/T on the crystal/silicate melt partitioning of REE and Y, we can consider an average value of exponent b, which is essentially -1:

$$D_{REE+Y}^{cpx/melt} = a * [NBO/T]^{-1} \tag{2.2}$$

As such, Equation 2.2 can be used to normalize crystal/silicate melt partition coefficients for REE and Y to the average NBO/T value of basaltic compositions (ca. 1 - Mysen, 2004). This normalization (Table 2.6) is essential to separate the combined effects of melt polymerization and $^{[4]}$Al on the partitioning behavior of the REE and Y between clinopyroxene and silicate melt. The success of this approach can be tested by assessing the

agreement between normalized $D_{REE+Y}^{cpx/melt}$ and the general trend obtained by Hill et al. (2000) as a function of $^{[4]}Al$ (Figure 2.6). Furthermore, we applied the same approach to normalize the $D_{REE+Y}^{cpx/melt}$ obtained by Mollo et al. (2013), which has NBO/T values around 0.5, and were able to achieve a similar good agreement (Figures 2.6 a and b).

Table 2.5: Parameters obtained by fitting the crystal/silicate melt partitioning data as a function of NBO/T according to the equation 2.1

$D^{cpx/melt}$	a-factor	σ	b-exponent	σ	Adj. R^2
La	0.031	0.003	-0.94	0.13	0.36
Sm	0.194	0.021	-0.83	0.16	0.38
Y	0.353	0.024	-0.78	0.11	0.52
Lu	0.383	0.028	-1.06	0.14	0.68

Levenberg-Marquardt iterative algorithm was used for the fits (see text for details)

However, the use of NBO/T has significant drawbacks, because it does not make a distinction between network modifiers like Ca or Mg (cf. Mills, 1993). Some of these caveats can be partly addressed by using optical basicity (OB) as an alternative to NBO/T. The optical basicity of a silicate melt can be used in a similar way as NBO/T to describe its network (Mills, 1993). The advantage of OB is, that it takes the bond strength between cations and oxygens anions into account, i.e. their electronic polarisabilty and electronegativity (Duffy, 1993; Mills, 1993). Thus, OB differentiates between cations like Mg, Ca and Na that are essentially indistinguishable in the calculation of NBO/T. To evaluate a possible improvement of the correlation of $D_{REE}^{cpx/melt}$ with $^{[4]}Al$ by normalizing the partition coefficients to the same OB in comparison to NBO/T, the same literature dataset of cpx/melt partition coefficients for the REE was used. The best fits of the literature partitioning data dependence on OB is through power functions

as:

$$D_{La}^{cpx/melt} = 1(\pm 0.1) * 10^{-6} * [OB]^{-21.5(8)} \quad (2.3)$$

$$D_{Sm}^{cpx/melt} = 1.6(\pm 0.8) * 10^{-5} * [OB]^{-19.8(9)} \quad (2.4)$$

The REE + Y partition coefficients were normalized to an OB value of 0.61 (2.6d and e), which is close to the average expected for mid-ocean ridge basalts (Gale et al., 2013). Crystal/silicate melt partition coefficient values that were corrected from experiments with OB values ≥ 0.62 seem to be slightly offset from the overall correlation of $D_{REE+Y}^{cpx/melt}$ as a function of $^{[4]}$Al. The inefficiency of this procedure for OB values ≥ 0.62 might be the result of the lack of data used for the regressions in Figure 2.4c and d. Nevertheless, OB seems to more accurately describe the melt compositional effect on $D_{REE+Y}^{cpx/melt}$ (Figure 2.6), as it better distinguishes different chemical elements in the melt environment. Thus, normalizing the $D_{REE+Y}^{cpx/melt}$ values to the same OB more efficiently removes the melt compositional effect, isolating the crystal compositional effect of $^{[4]}$Al in cpx on crystal/silicate melt trace element partitioning.

Barium

Hill et al. (2000) assumed little or no change for 2+ cations substituting into the M2 site with increasing $^{[4]}$Al content of clinopyroxene, because the net charge of the site remains 2+, regardless of the amount of Al^{3+} in the cpx. Thus, it is reasonable to assume no change in the partitioning behavior for 2+ trace elements entering the M2 site. Indeed, divalent cations like Sr^{2+} display $D_{Sr}^{cpx/melt}$ that are near constant over a range of $^{[4]}$Al (Hill et al., 2000). However, $D_{Ba}^{cpx/melt}$ increases slightly with $^{[4]}$Al in clinopyroxene (Figure 6),

similarly to that observed for $D_{REE+Y}^{cpx/melt}$(Figure 2.6c and f). Huang et al. (2006) have shown that an increase in the degree of melt polymerization correlates positively with increasing $D_{Sr}^{cpx/melt}$ values. As Sr and Ba are both alkali earths, it seems reasonable to assume that the partitioning of Ba between crystals and silicate melt is affected by melt polymerization similarly to Sr. As a consequence, $D_{Ba}^{cpx/melt}$ obtained for the HE1 and HE2 experiments from the present study was also corrected to take into account the degree of polymerization (Table 6), and results show that corrected $D_{Ba}^{cpx/melt}$ values correlate positively with increasing $^{[4]}$Al.

Gallium

In similar fashion to the REE, $D_{Ga}^{cpx/melt}$ is shown here to correlate positively with the $^{[4]}$Al content in cpx (Figure 2.1e), in agreement with the trend observed in literature data (Malvin and Drake, 1987; Dygert et al., 2014). Based on the new $D_{Ga}^{cpx/melt}$ data, it remains unclear to what extent $D_{Ga}^{cpx/melt}$ depends on OB. In contrast to the REE+Y and Ba, Ga is a relatively small cation and it is assumed to have a structural role in silicate melts nearly identical to that of Al (Hess, 1991). Hence, one could assume that Ga^{3+} behaves as a network-forming, instead of a network-modifier cation and, thus, may contribute to increase melt polymerization (Mysen, 1990). Nevertheless, inasmuch as results presented here are concerned, $D_{Ga}^{cpx/melt}$ is unaffected by an increase in the degree of melt polymerization.

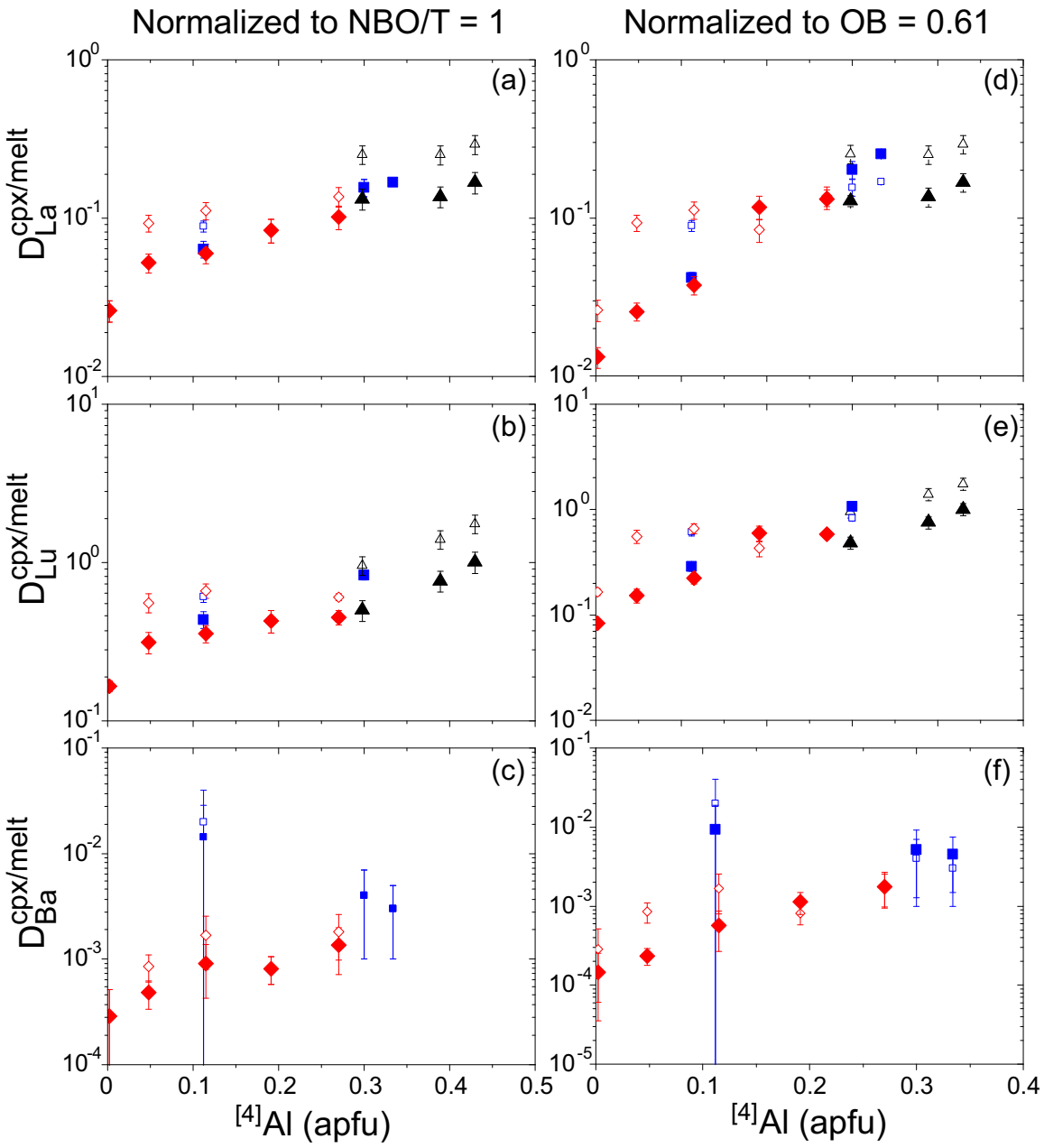

Figure 2.6: Crystal/silicate melt partition coefficients for La, Lu, and Ba normalized to NBO/T = 1 (a-c) and OB = 0.61 (d-f) plotted as a function of the aluminum content in the tetrahedral position of cpx ($^{[4]}$Al). Open symbols are representative for the uncorrected (NBO/T≠1,OB≠0.61) partition coefficients, while filled symbols represent partition coefficients, which are normalized to either NBO/T = 1 or OB = 0.61. Figures a-b and d-e are representative for all REE and Y. The Figures c and f show how applying the same normalization factors determined for the REE (see Table 2.6) improve the correlation of $D^{cpx/melt}_{Ba}$ with $^{[4]}$Al. The symbols are consistent with those depicted in Figure 2.1. Error bars are one standard deviation.

Table 2.6: Partition coefficient values normalized to NBO/T = 1 and OB = 0.61 applying correction factors (see text for details).

D normalized to an NBO/T of 1 yielding *D

Experiment	NBO/T	D_{Ba}	D_{La}	D_{Sm}	D_{Eu}	D_{Y}	D_{Lu}	norm. factor
HS1	0.72	0.0018	0.137	0.583	0.629	0.642	0.605	1.34
HE1	0.50	0.0017	0.112	0.586	0.675	0.747	0.661	1.86
HE2	0.53	0.0009	0.093	0.481	0.526	0.591	0.557	1.78
HE-Hill et al. (2000)	0.69	0.020	0.117	0.581	0.737	0.783	0.689	1.40

Experiment	$*D_{Ba}$	σ	$*D_{La}$	σ	$*D_{Sm}$	σ	$*D_{Eu}$	σ	$*D_{Y}$	σ	$*D_{Lu}$	σ
HS1	0.0014	(6)	0.102	(17)	0.434	(52)	0.469	(51)	0.478	(57)	0.451	(48)
HE1	0.0009	(5)	0.060	(9)	0.315	(46)	0.362	(52)	0.401	(45)	0.355	(44)
HE2	0.0005	(1)	0.052	(7)	0.271	(32)	0.296	(31)	0.332	(36)	0.314	(49)
HE-Hill et al. (2000)	0.0143	(140)	0.064	(8)	0.350	(12)	0.536	(65)	0.457	(70)	0.436	(53)

D normalized to an OB of 0.61 yielding ' D

Experiment	OB	D_{Ba}	D_{La}	D_{Sm}	D_{Eu}	D_{Y}	D_{Lu}	norm. factor
HS1	0.609	0.0018	0.137	0.583	0.629	0.642	0.605	1.04
HE1	0.579	0.0017	0.112	0.586	0.675	0.747	0.661	2.97
HE2	0.573	0.0009	0.093	0.481	0.526	0.591	0.557	3.65
W1	0.590	0.0003	0.026	0.125	0.136	0.166	0.166	1.98
HB	0.622	0.0008	0.084	0.357	0.377	0.424	0.428	0.72
HE-Hill et al. (2000)	0.618	0.020	0.117	0.581	0.737	0.783	0.689	0.77
HS-Hill et al. (2000)	0.588	0.004	0.16	0.92	1.02	0.93	0.83	2.13
HB-Hill et al. (2000)	0.622	0.003	0.169	0.750	0.770			0.67

Experiment	$'D_{Ba}$	σ	$'D_{La}$	σ	$'D_{Sm}$	σ	$'D_{Eu}$	σ	$'D_{Y}$	σ	$'D_{Lu}$	σ
HS1	0.0018	(8)	0.132	(19)	0.562	(41)	0.61	(3)	0.62	(5)	0.58	(3)
HE1	0.0006	(3)	0.038	(5)	0.197	(28)	0.23	(3)	0.25	(3)	0.22	(3)
HE2	0.0002	(1)	0.025	(3)	0.132	(14)	0.14	(1)	0.16	(2)	0.15	(2)
W1	0.00015	(11)	0.013	(2)	0.063	(6)	0.07	(1)	0.08	(1)	0.08	(1)
HB	0.0011	(4)	0.117	(20)	0.499	(75)	0.53	(8)	0.59	(5)	0.60	(10)
HE-Hill et al. (2000)	0.0052	(39)	0.202	(25)	1.193	(37)	1.32	(3)	1.21	(9)	1.08	(7)
HS-Hill et al. (2000)	0.0094	(94)	0.042	(4)	0.230	(7)	0.35	(3)	0.30	(4)	0.29	(3)
HB-Hill et al. (2000)	0.0045	(30)	0.253	(7)	1.121	(77)	1.15	(37)				

2.4.2 The effect of $^{[4]}$Al on cpx M2 lattice site parameters based on normalized REE crystal/silicate melt partitioning

After being able to filter the effect of melt polymerization from the dataset, we can re-evaluate how the addition of $^{[4]}$Al into the cpx T-site will have an influence on the size and form of the octahedral neighbouring sites. To do so, we fitted $D_{REE+Y}^{cpx/melt}$ normalized to the same optical basicity to the lattice strain function (Blundy and Wood, 1994):

$$D_i^{crystal/melt} = D_0 \; exp\left[\frac{-4\pi E N_A[\frac{r_0}{2}(r_i - r_0)^2 + \frac{1}{3}(r_i - r_0)^3]}{RT}\right] \qquad (2.5)$$

where D_i is the partition coefficient of an element i and D_0 is the optimum, or strain free partition coefficient that is reached when a fictive cation with an ideal ionic radius r_0 enters the crystal lattice site of interest and produces no elastic strain. The variable r_i represents the radius of a cation that enters the same site but by doing so it produces variable elastic strain. The internal strain of a crystal site that result when $r_i \neq r_0$, is quantified by the apparent Young's modulus (E). N_A is the Avogadro's Number, R is the Universal Gas Constant and T is absolute temperature (Blundy and Wood, 1994).

In order to derive D_0, r_0 and E for trivalent elements entering the M2 site of cpx, the fitting was performed using the Levenberg-Marquardt iterative algorithm (for details see Marquardt, 1963). From the fits, it is possible to observe an increase in $^{[4]}$Al coupled to a broad linear increase in the strain-free partition coefficient (D_0) (Figure 2.8). Secondly, the optimum radius of the M2 crystal lattice site shifts to higher values, but the associated errors are relatively large, such that no clear trend can be deduced from the data.

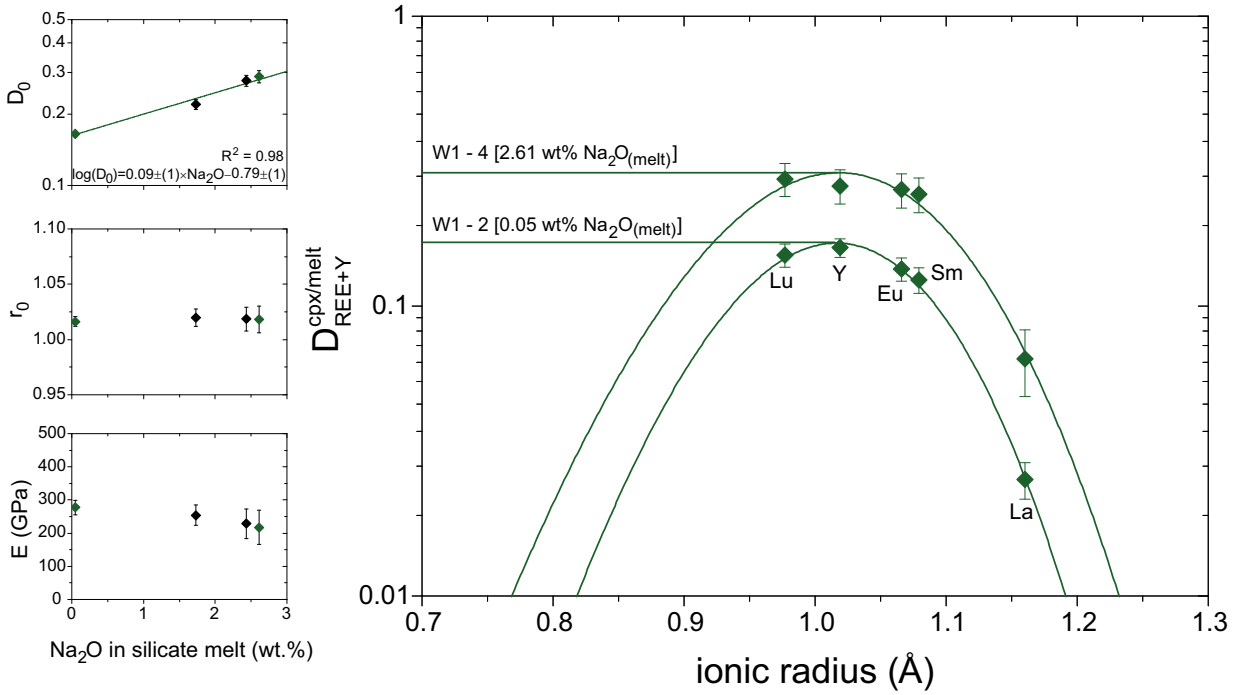

Figure 2.7: Lattice strain model fits of the M2 site of cpx, based on the partitioning data of the REE and Y and displayed for a selection of different amounts $Na_2O_{(melt)}$. Lattice strain parameters of all experiments are displayed as a function of $Na_2O_{(melt)}$. Ionic radii in [8]-fold coordination were taken from Shannon (1976). The parameters belonging to the depicted lattice strain parabolas are color coded. The values of the lattice strain parameters D_0, r_0 and E are displayed in Table 2.7. Error bars are one standard deviation.

The Young's elastic strain modulus (E) seems to be broadly constant, with exceptions for those experiments having a higher degree of melt polymerization. In a computer simulation of garnet-melt partitioning, van Westrenen et al. (2000) studied a possible dependence of r_0 and E on the coexisting melt structure. Indeed, their results show that the absolute values of r_0 and apparent E depend on the adjacent melt environment, i.e. the coordination of trace elements in the melt (e.g., Ponader and Brown, 1998; Prowatke and Klemme, 2005; van Westrenen et al., 2000). Although all variations of E obtained here have a large degree of uncertainty, the overall pattern seems to support the assumption of van Westrenen et al. (2000), i.e.

that the lattice strain parameters E and r_0 are not only stoichiometrically controlled but also depend on the melt environment.

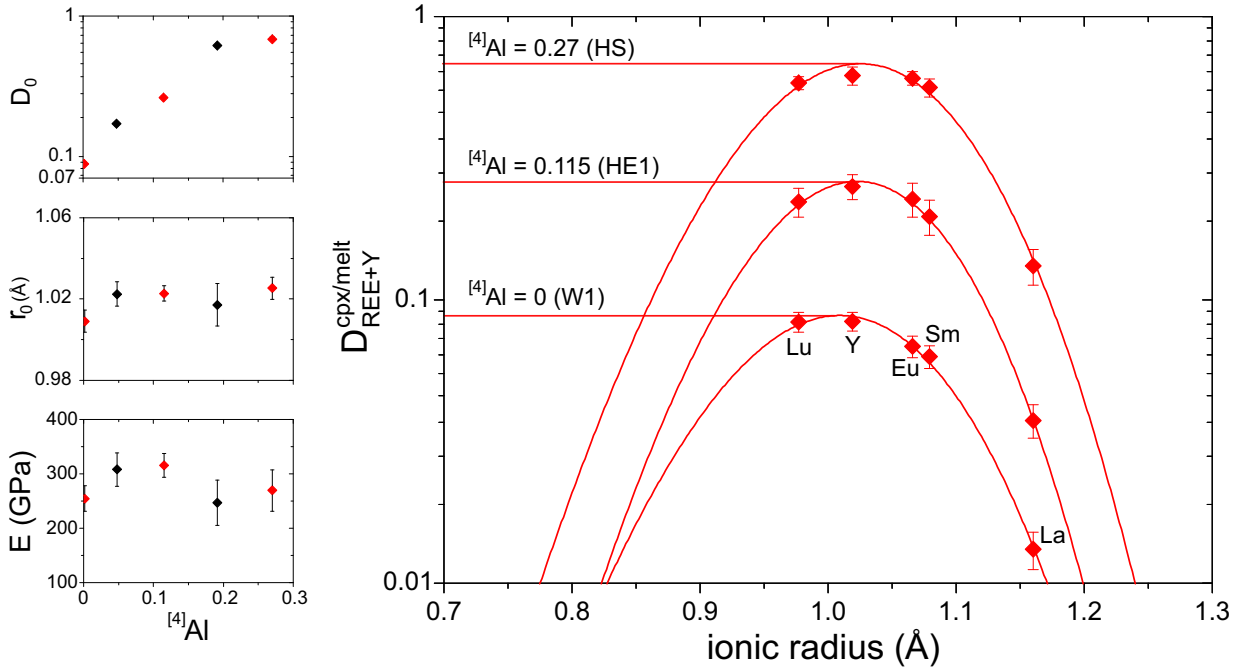

Figure 2.8: Lattice strain model fits for a selection of experiments of this study at different $^{[4]}$Al contents based on REE partition coefficients normalized to an optical basicity of 0.61. Lattice strain parameters of all experiments are displayed as a function of the $^{[4]}$Al content of cpx and listed values of these parameters can be found in Table 2.7. The lattice strain parameters belonging to the depicted lattice strain parabolas in this Figure are shown in red. Error bars are one standard deviation.

The increase in $D_{Ba}^{cpx/melt}$ as a function of the $^{[4]}$Al content in cpx might be unrelated to the increase in the number of charge balancing configurations (Hill et al., 2000), but rather to changes in the internal strain E of the crystal lattice. The lattice strain parabola for 2+ cations in the M2 site (e.g., Ba) is assumed to flatten with increasing $^{[4]}$Al content in cpx (Lundstrom et al., 1998), which will lead to an increase of the partition coefficient of cations whose ionic radius places them on the outermost edges of the lattice strain parabola. Conversely, for cations whose r_i are closer to r_0, their

respective $D_i^{crystal/melt}$ values should decrease as E and D_0 both decrease. However, given the limited amount of data for divalent elements in the M2 site available to produce a meaningful lattice strain fit, this possibility cannot be readily tested.

2.4.3 Interplay between Al and Na in the silicate melt and its effect on the partitioning behavior of trace elements between crystals and silicate melt

Even though Na_2O plays an important role in the structure of silicate melts (e.g. Mills, 1993), with contents as high as 5 wt% in mid-ocean ridge basalts (cf. Jenner and O'Neill, 2012; Chemia et al., 2015), crystal/silicate melt partitioning studies are often performed in systems with little or no Na_2O (e.g. Gaetani and Grove, 1995; Mallmann and O'Neill, 2009). Clinopyroxene/silicate melt partitioning of Na is mainly controlled by the bulk Na_2O content of the system and pressure (Blundy et al., 1995; Flemming and Luth, 2002), while the effect of temperature is assumed to be minor (Blundy et al., 1995). The crystal compositional effect on the partitioning of trace elements between cpx and silicate melt that arises due to the incorporation of sodium into the crystal lattice is most likely to be related to the increasing number of charge balancing configurations. However, previous experiments were not able to isolate the sole effect of the addition of sodium to a system on the partitioning behavior of trace elements (e.g. Bennet et al., 2004; Gaetani, 2004). In this sense, we assess if the addition of sodium to the silicate melt exerts an influence on $D_i^{crystal/melt}$ of trace elements in a way that cannot be accounted by NBO/T or OB, such as by the formation of melt complexes (e.g. O'Neill and Eggins, 2002; Dygert et al., 2013; Leitzke et al., 2016). The experiments are designed to test this hypothesis, given that Na_2O bulk

contents vary from 0 to 3 wt%, while the degree of melt polymerization and $^{[4]}$Al in cpx are constant (OB ca. 0.6 and $^{[4]}$Al $\leq$ 0.04). Moreover, the composition of both cpx and olivine remained virtually unchanged. For example, the addition of 3 wt% Na_2O to the starting composition lead to only negligible variations in the sodium content of cpx, ranging between 0.013 and 0.02 Na apfu.

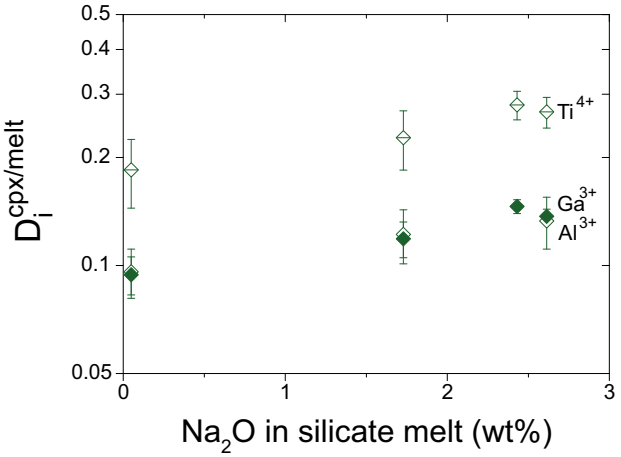

Figure 2.9: Partitioning behavior of Al, Ga and Ti as a function of Na_2O_{melt}. The partitioning of Ga, Al and Ti between cpx and the silicate melt is affected in the exact same way by the amount of Na_2O_{melt}.

The effect of Na_2O in silicate melt on the partitioning behavior of trace elements has already been hinted upon previously. For example, Schösnig and Hoffer (1998), noted that additional Na_2O in the silicate melt caused an increase in crystal/silicate melt partition coefficients of the REE, which is decoupled from any change related to crystal chemistry. They found that in the experiments crystallizing high-Al diopside, $D_{REE}^{cpx/melt}$ values were twice as large in the presence of $Na_2O_{(melt)}$ relative to a Na-free silicate melt composition. The reason would be the formation of "$REE^{3+} - Al -$ complexes", which are stable in the melt but have an offset to the ideal bonding length, bonding angle and the number of surrounding oxygen anions present, so that

their incorporation into a growing diopside crystal is hampered (Schösnig and Hoffer, 1998). When Na_2O is introduced into the system, these melt complexes may be modified or broken down to some extent, so that the compatibility of the REE into cpx increases. Within this framework, the increasing compatibility of the REE as a function of Na_2O_{melt} observed could be explained by the formation of strong bonds between Na and Al in the silicate melt, which would break the "$REE^{3+} - Al -$ complexes" apart. The detachment of the REE from the aluminum in the silicate melt by the addition of Na_2O in the system will inevitably lead to an increase in the activity coefficients of their REE-O species and, consequently, to an increase of the crystal/melt partition coefficients (O'Neill and Eggins, 2002).

Regarding crystal/silicate melt partitioning of 2+ elements, $D^{crystal/melt}_{Ba,Pt}$ increase with increasing Na_2O_{melt}, while values $D^{crystal/melt}_{Ni}$ and $D^{crystal/melt}_{Mn}$ remain broadly constant. This can be explained by the significantly larger ionic radii in [6]-fold coordination of Ba^{2+} and Pt^{2+} when compared to Ni^{2+} and Mn^{2+} (VI coordination: Ba=1.35 Å, Pt=0.8 Å, Ni=0.69 Å, Mn=0.67 Å). Barium and Pt in [6]-fold coordination would have an ionic radius more similar to the REE than Mn and Ni, and, therefore, a greater affinity for being incorporated into the "$REE^{3+} - Al -$ complexes" in the melt. In addition to the disparity found for the behavior of divalent cations, the partitioning of trivalent and tetravalent cations between clinopyroxene, olivine, and silicate melt, are affected by Na_2O_{melt} to a different extent. The $D^{crystal/melt}_{Ga,Ti,Al}$ values increase significantly less as a function of Na_2O_{melt} (Fig 2.9) when compared to the increase observed for $D^{crystal/melt}_{REE,HFSE}$ (Figure 2.2 and 2.3). This disparate behavior can be explained by the fact that Ga, Al and Ti are present in tetrahedral coordination in silicate melts (Hess, 1991), and thus, occupy the same network-forming sites in the "$REE^{3+} - Al -$ complexes" in the melt.

The lattice strain model (Blundy and Wood, 1994) can also be used to account for changes in melt composition. This is only possible if the partitioning behavior of all trace elements used to constrain the lattice strain parabola for that particular crystal site all show the same level of dependency on a given silicate melt component. This is the case for the cpx/silicate melt partitioning of REE and Y, which are equally affected by Na_2O_{melt} (Figure 2.7). Therefore, we can use $D_{REE+Y}^{cpx/melt}$ to fit the data to equation 2.5 and obtain the lattice strain parameters D_0, r_0 and E as a function of Na_2O_{melt}. Crystal/silicate melt partitioning data for In was not considered for the fits, as previous studies suggested that In partitions into both the M1 and M2 site of cpx (e.g. Hill et al., 2000). The lattice strain parameters r_0 and E remain constant over the increase in Na_2O_{melt}, while D_0 increases with the amount of Na_2O_{melt} (Table 2.7).

Constant values of r_0 and E support the hypothesis that crystal composition is not the main control on the observed variation in $D_{REE+Y}^{cpx/melt}$ with Na_2O_{melt}. Compared to the number of trivalent trace elements substituting into the M2 site, there are only a few 3+ cations (Sc, Rh, Cr and Al) entering the M1 site of cpx in the experiments (Hill et al., 2000), which limits the accuracy of the fits to equation 2.5. Nevertheless, it can be seen that E and r_0 for the M1 site of cpx change with Na_2O_{melt} (Table 2.7 and Figure 2.10), contrary to the observed for the M2 site of cpx (Figure 2.7).

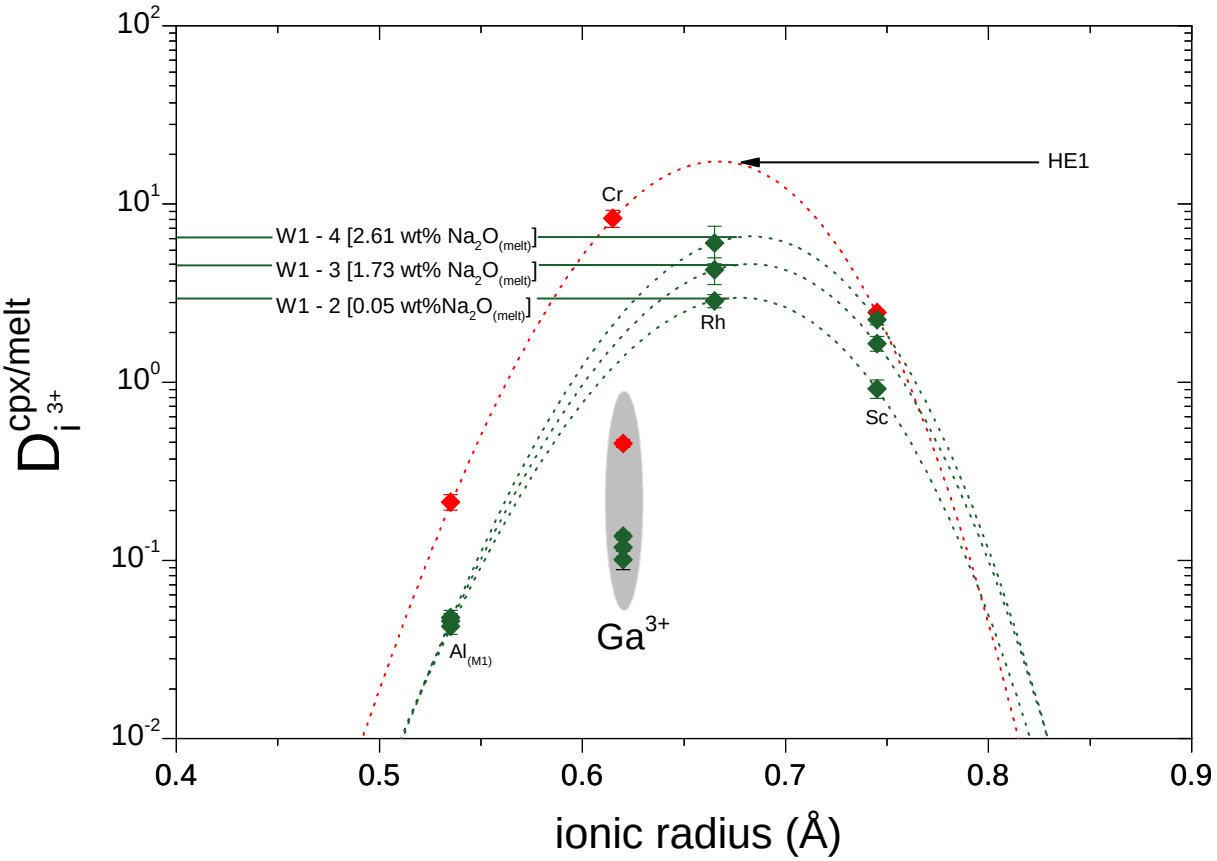

Figure 2.10: Lattice strain parabolas of trivalent trace elements substituting into the M1 site of cpx displayed for the W1-2, W1-3 and W1-4 experiment, as well as for the HE1 experiment (combined partitioning data obtained in this study and in the study of Hill et al., 2000). Dotted lines are emphasizing the weakness of the lattice strain fits, which are only based on three data points. However a general trend can be clearly taken from this approach, as both limps and the vertex of the parabola are defined. Ionic radii in [6]-fold coordination were taken from Shannon (1976). The values of the lattice strain parameters D_0, r_0 and E are displayed in Table 2.7. Error bars are one standard deviation.

The reason for the perceived variation in E is related to differences between how Al interacts with Na_2O in silicate melt when compared to Sc and Rh. In this case, the results of the lattice strain fit are not reflecting changes in the internal strain or distortion of the M1 site, but rather differences in the interaction parameters between the different trivalents

substituting into the M1 site and Na_2O. As such, care should be taken in interpreting the results from lattice strain fits as in some cases they may not represent the actual strain of the mineral sites, but rather some complex interplay between melt and crystal compositional effects.

Table 2.7: Non linear fits of the crystal/silicate melt partitioning data for homovalent elements entering the M site of clinopyroxene and olivine (Equation 2.5).

Clinopyroxene

Site	Valency	Comp.	Cations	χ^2	D_0	σ	r_0	σ	E	σ
M2	3+	HS[1]	La, Sm, Eu, Lu, Y	0.493	0.682	(29)	1.025	(5)	270	(38)
M2	3+	HE1[1]	La, Sm, Eu, Lu, Y	0.139	0.262	(7)	1.023	(4)	316	(22)
M2	3+	HE2[1]	La, Sm, Eu, Lu, Y	0.295	0.171	(6)	1.022	(6)	308	(31)
M2	3+	HB[1]	La, Sm, Eu, Lu, Y	0.518	0.617	(25)	1.017	(10)	247	(42)
M2	3+	W1[1]	La, Sm, Eu, Lu, Y	0.367	0.088	(2)	1.009	(5)	255	(24)
M2	3+	W1-2	La, Sm, Eu, Lu, Y	0.261	0.165	(4)	1.016	(4)	277	(22)
M2	3+	W1-3	La, Sm, Eu, Lu, Y	0.681	0.219	(10)	1.020	(8)	254	(31)
M2	3+	W1-4	La, Sm, Eu, Lu, Y	0.608	0.288	(17)	1.018	(12)	217	(52)
M2	3+	W1-5	La, Sm, Eu, Lu, Y	1.947	0.277	(15)	1.019	(11)	228	(45)
M1	3+	HE1	Al^2, Cr^3,Sc^3	1.64E-06	17.338	[4]	0.666		1522	
M1	3+	W1-2	Al^2, Sc, Rh	8.07E-09	2.977		0.678		1238	
M1	3+	W1-3	Al^2, Sc, Rh	4.32E-07	4.426		0.678		1064	
M1	3+	W1-4	Al^2, Sc, Rh	1.89E-07	6.310		0.679		1128	
M1	4+	W1-2	Ti, Sn, Hf, Zr	0.045	0.535	(50)	0.648		3091	(192)
M1	4+	W1-3	Ti, Sn, Hf, Zr	0.217	1.114	(132)	0.654		3623	(228)
M1	4+	W1-5	Ti, Sn, Hf, Zr	0.007	1.288	(23)	0.657		3076	(33)
M1	4+	W1-3	Sn, Hf, Zr	0.344	1.211		0.648		3091	
M1	4+	W1-5	Sn, Hf, Zr	2.575	2.349		0.648		3091	

Olivine

Site	Valency	Comp.	Cations	χ^2	D_0	σ	r_0	σ	E	σ
M1/2	3+	W1-1	Sm, Eu, Y, Lu, In	3.049	0.242	(13)	0.711		470	
M1/2	3+	W1-2	Sm, Eu, Y, Lu, In	0.998	0.182	(19)	0.711		470	
M1/2	3+	W1-6	Sm, Eu, Y, Lu, In	1.035	0.295	(18)	0.711		470	

(1) Partition coefficient of these experiments used to fit to the lattice strain function were normalized to the same OB of 0.61

(2) Partition coefficient of Al for the M1 site

(3) Partition coefficient values obtained by Hill et al. (2000) in an experiment with similar ^{IV}Al content in cpx

(4) Error is not given if less then four data points were fitted to the lattice strain function, or if parameters were fixed to a specific value

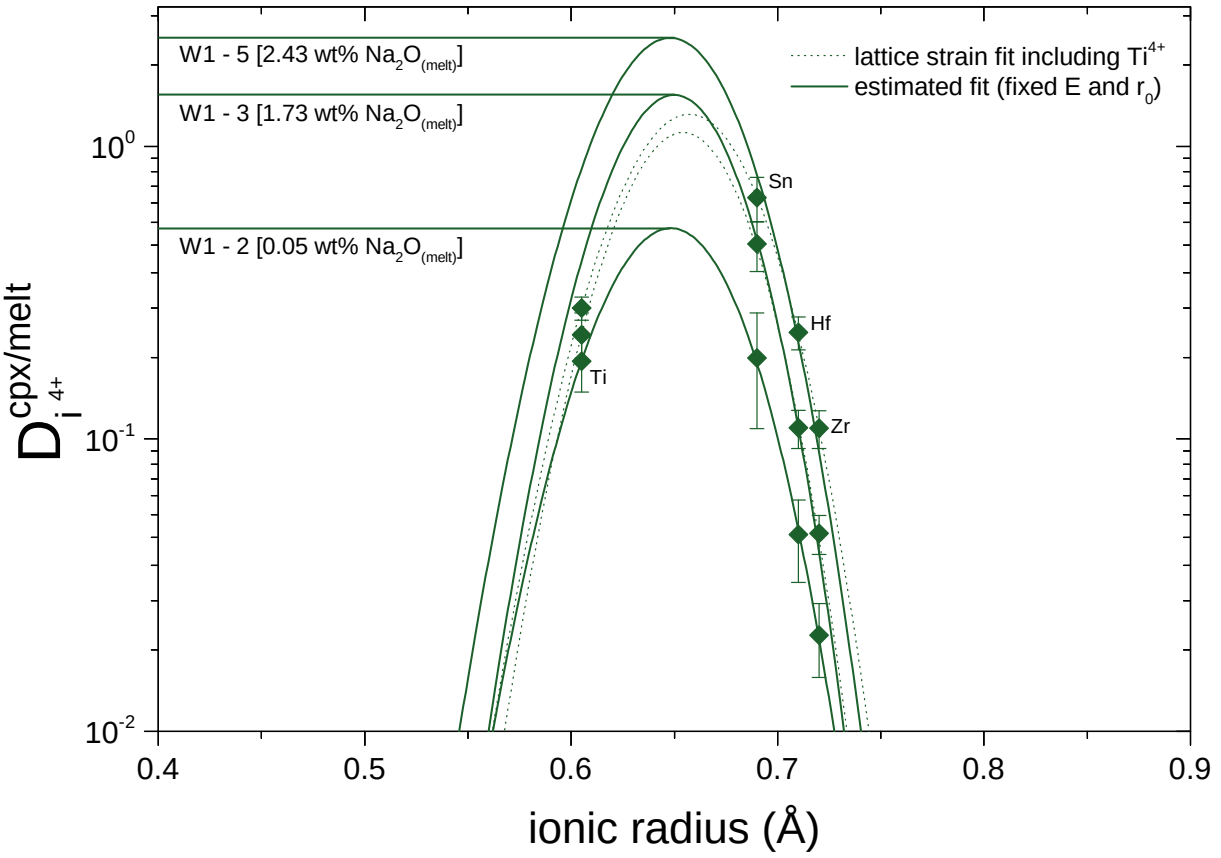

Figure 2.11: Lattice strain parabolas of tetravalent trace elements substituting into the M1 site of cpx. E and r_0 obtained from the fitting cpx/melt partitioning data to the lattice strain function, were used as constants for the lattice strain fits of the sodium bearing experiments. Ionic radii in [6]-fold coordination were taken from Shannon (1976). The values of the lattice strain parameters D_0, r_0 and E are displayed in Table 2.7. Error bars are one standard deviation.

Clinopyroxene/silicate melt partitioning data for tetravalent cations entering the M1 site (e.g. Ti, Sn, Zr and Hf) was well reproduced using the lattice strain function, but only for the Na_2O-free experiment (Figure 2.11). For the Na_2O bearing experiments, $D_{Ti}^{cpx/melt}$ is not affected like the other tetravalent cations by changes in Na_2O in the silicate melt. We assume that Ti is mainly in five or six-fold coordination in basaltic magmas (Farges et al., 1996), and enters the octahedral site of clinopyroxene (e.g. Fonseca

et al., 2014).

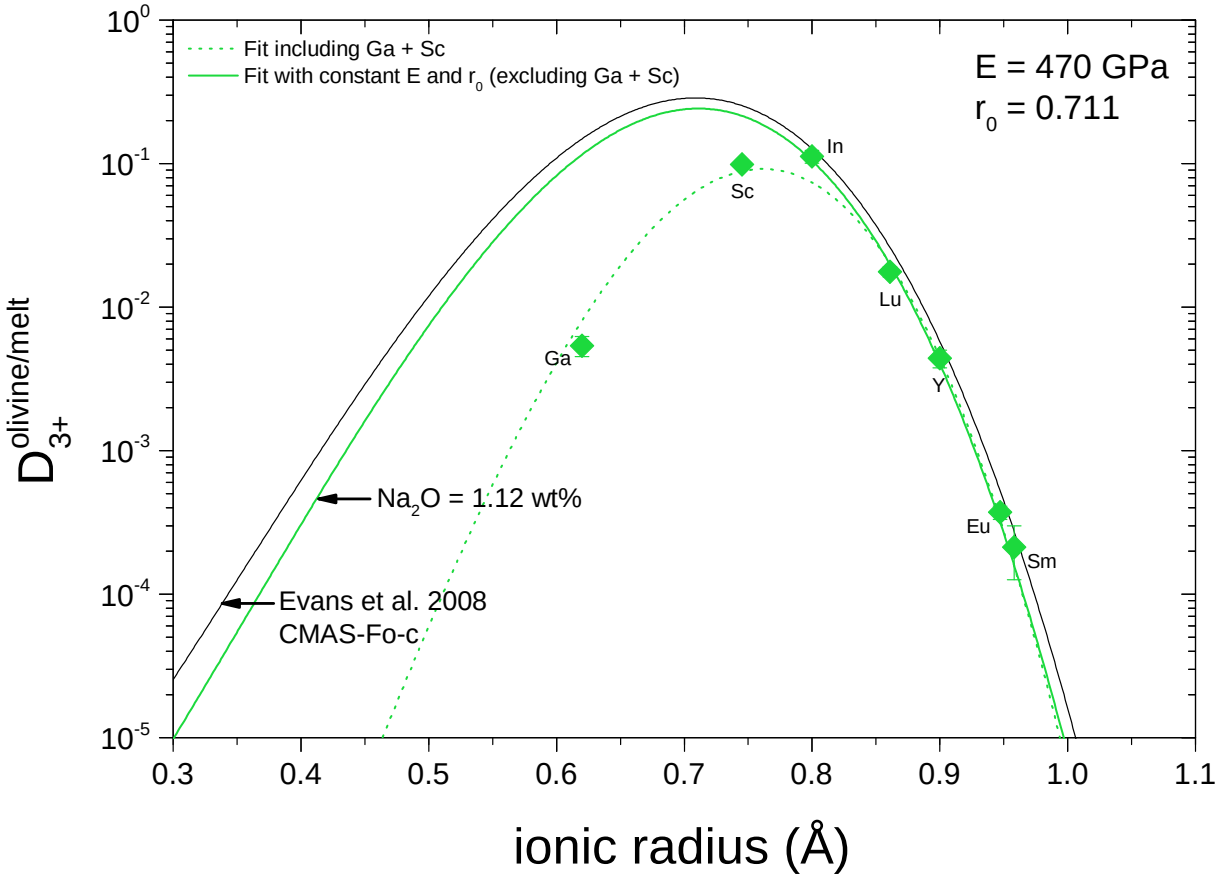

Figure 2.12: Lattice strain model fit for the M1/2 site of olivine, determined using the partitioning data of the REE+Y and In. The value of $D_{Ga}^{olivine/melt}$ shows a distinct offset to the defined lattice strain parabola, in a similar way as found for the cpx M1 site. Lattice strain parameters of all experiments are displayed as a function of $Na_2O_{(melt)}$ (wt%). Ionic radii in [6]-fold coordination were taken from Shannon (1976). Error bars are one standard deviation. The values of the lattice strain parameters D_0, r_0 and E are displayed in Table 2.7. See text for details.

The lattice strain parameters obtained when using Sn, Zr, Hf and Ti partitioning data (see dashed lines in Figure 2.11) show that E and r_0 shift in order to account for the differences in partitioning behavior obtained for Ti as a function of Na_2O_{melt} when compared to Sn, Zr and Hf (Table 2.7). As a consequence, $D_{Ti}^{cpx/melt}$ values of experiments with elevated Na_2O_{melt}

cannot be considered in the lattice strain fits. The fitting parameters E and r_0 were fixed for all CMAS + xNa_2O experiments to the values obtained from the lattice strain fit of the sodium free experiment (W1-2), as these values are not expected to change as a function of Na_2O_{melt} (see continuous lines in Figure 2.11). It is worth pointing out that $D_{Ga}^{crystal/melt}$ is always offset to lower values when compared to what is predicted from the lattice strain fits (see Figures 2.10 and 2.12). This distinct behavior of $D_{Ga}^{cpx/melt}$ seems to be unrelated to the Na_2O_{melt} content, and was noticed in previous studies (Adam and Green, 2006; Dygert et al., 2014), but not discussed in greater detail. To explain this phenomenon, it could be assumed that Ga^{3+} enters the M2 site, or even the tetrahedral site of cpx, or that it is forming a specific melt complex with a major element, which still needs to be investigated in greater detail. Olivine can be used to investigate if melt composition is influencing the crystal/silicate melt partitioning of trace elements, since its crystal chemistry is not affected by major element changes in the silicate glass. Fits of the $D_i^{olivine/melt}$ data to the lattice strain function (Blundy and Wood, 1994) can reproduce results of $Na_2O_{(melt)}$-bearing experiments (Figure 2.12).

However, the lattice strain fit based on crystal/silicate melt partitioning of Ga, Sc, In and the REE + Y has to be evaluated in order to isolate crystal and melt compositional effects. First of all, when compared to relatively recent literature data (cf. Mallmann and O'Neill, 2013; Evans et al., 2008) the obtained Young's modulus (E) of the lattice strain fit that includes Ga, Sc, in addition to the REE + Y partitioning data shows a distinct offset from previously reported values ($\approx$ 200 GPa). The stiffness (high E value) of the olivine M1/M2 site in the experiments, is mainly controlled by the position of $D_{Ga}^{olivine/melt}$. Secondly, in previous partitioning studies, it was noticed that Sc substitution into olivine deviates from the mechanism of

substitution of the REE (Evans et al., 2008).

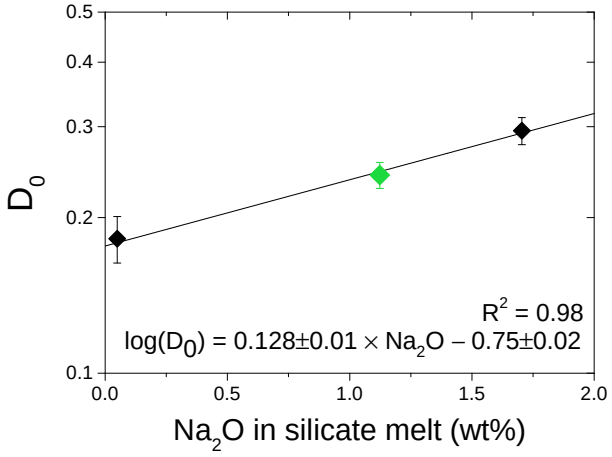

Figure 2.13: Variations in D_0 for the M1/2 sites of olivine are displayed as a function of $Na_2O_{(melt)}$. The symbol colored in light green is the representative D_0 value of the lattice strain parabola depicted in Figure 2.12.

Taking this into account, we have excluded Ga and Sc partitioning data from the data that were used to obtain the lattice strain fitting parameters. In order to obtain valid lattice strain parameters, the REE + Y and In olivine/melt partitioning data of the Na_2O-free experiment (W1-2) was fitted to the lattice strain function (Equation 2.5) using a fixed E-value derived from the experimental results of Evans et al. (2008), i.e. 470 GPa. The obtained value of r_0 of the Na_2O-free experiment can be used as a constant together with the E-value from the literature to derive values of D_0 for all experiments. The linear correlation of D_0 with Na_2O_{melt} obtained (Figure 2.13) is in agreement with that observed for trivalent cations entering the M2 site of cpx (Figure 2.7). This indicates that melt composition is more likely than crystal chemistry to be responsible for the observed changes in $D_{Ga}^{olivine/melt}$ as a function of Na_2O_{melt}.

2.5 Concluding remarks

Results presented here lead to the separation of crystal and melt compositional effects on trace element partitioning between clinopyroxene, olivine and silicate melt. Namely, increasing $^{[4]}$Al into the cpx structure, while eliminating the effect of changes in degree of melt polymerization, will result in an increase of the $D_{REE+Y}^{cpx/melt}$, supporting previous findings (e.g Lundstrom et al., 1994; Gaetani and Grove, 1995; Lundstrom et al., 1998; Schösnig and Hoffer, 1998; Blundy et al., 1998; Hill et al., 2000). By isolating crystal chemistry and melt structure effects, we show that cpx/silicate melt partitioning of Sn, Ba, In and Ga also increase as a function of $^{[4]}$Al, which was not accomplished in previous studies. There is still a need for further investigations to fully resolve the effect of Na_2O_{melt} on the crystal/silicate melt trace element partitioning. Results also indicate that Na may act to break "REE-Al complexes" in the melt (e.g. Schösnig and Hoffer, 1998), causing an increase in the activity coefficient of trace elements and consequently, $D_i^{crystal/melt}$. This becomes particularly important because most experimental datasets of crystal/silicate melt trace element partitioning dealt with simplified systems, with less than 0.5 wt% of Na_2O in the melt (e.g. Gaetani and Grove, 1995; Hill et al., 2000; Mallmann and O'Neill, 2009), while in natural samples, such as the mid-ocean ridge basalts, this element may be present in average concentrations of 2.8 wt% (Gale et al., 2013), but can be as high as 6 wt% (Jenner and O'Neill, 2012). Moreover, it is important to consider all the parameters that may be affecting the observed $D_i^{crystal/melt}$ values, in order to have meaningful results when applying the lattice strain model theory (Blundy and Wood, 1994), as exemplified, for instance, by the misfit of $D_{Ga,Ti,Al}^{crystal/melt}$.

Chapter 3

The effect of titanium on the partitioning behaviour of high-field strength elements between silicates, oxides and lunar basaltic melts with applications to the origin of mare basalts

3.1 Introduction

Titanium is generally considered to be a minor element in the Bulk Silicate Earth (BSE: 1265 μg/g Palme and O'Neill, 2014), with an average of 1.6 wt. % TiO_2 for mid-ocean ridge basalts (Gale et al., 2013) and a maximum reported concentration of 5.5 wt. % (Arndt et al., 1995). On the Moon, however, mare basalts show a bimodal distribution with respect to their TiO_2 contents, and are subdivided into low- and high-Ti groups, the latter of which can reach concentrations as high as 16 wt. % of TiO_2 (e.g., Marvin and Walker, 1978; Meyer, 2012). The main hypotheses that are invoked to

account for this extreme TiO_2 enrichment include: 1) the assimilation of Fe-Ti bearing minerals when low-Ti basaltic magmas ascended to the Moons surface (e.g., Liang and Hess, 2006; Liang et al., 2007; Münker, 2010; Dygert et al., 2013) or; 2) mantle overturn after crystallization of a magma ocean, with addition of ilmenite from late-crystallizing mafic cumulates to early, ultramafic harzburgite cumulates, generating a mixed cumulate source (e.g. Ringwood and Kesson, 1976; Beard et al., 1998). Despite distinct theories for their origin, lunar basalts are thought to be partial melts of a peridotite mantle. As such, understanding their formation may contribute to a better understanding of planetary evolution processes, like the differentiation of the Moon, lunar mantle dynamics, composition and phase stability (Bence et al., 1980; Shearer and Papike, 1993). Therefore, it is crucial to have precise knowledge of how major and trace elements fractionate under different conditions. In particular, it is necessary to understand how the melt composition, namely at high TiO_2 contents, may affect trace element partitioning during lunar differentiation and mantle melting.

A variety of factors affect the partitioning of trace elements between crystals and silicate melts. These include crystal composition and structure (Blundy and Wood, 1994); pressure and temperature (e.g. Adam and Green, 1994); the oxidation state of the magma (e.g. Borisov, 2012; Mallmann et al., 2015); melt structure and composition (e.g. Mysen, 1990; Prowatke and Klemme, 2005; Dygert et al., 2013). Of all these factors, the effect of melt composition is the least well-constrained, despite of its potential importance in affecting trace element behavior during magmatic processes (Watson, 1976; Ryerson and Hess, 1978). The TiO_2 melt content has been shown to affect the exchange of Fe and Mg between olivine and silicate melt (D_{ol-liq}^{Fe-Mg} Longhi et al., 1978; Jones, 1988; Xirouchakis et al., 2001). As TiO_2 contents increase, D_{ol-liq}^{Fe-Mg} decreases, mostly due to the formation of

Fe-Ti-O melt species (e.g., Ferropseudobrookite) which bind Fe and prevent it from substituting into other phases like olivine (Xirouchakis et al., 2001). In this regard, Longhi et al. (1978) expected that this effect would show and influence not only on the partitioning behavior of network forming cations, but also elements that are geochemically similar to Ti, i.e., the extended High-field Strength Elements group (HFSE Nb, Ta, Hf, Zr, as well as Mo and W), U and Th. In this sense, Dygert et al. (2013) demonstrated that $D_{HFSE}^{oxide/melt}$ decreases with increasing TiO_2 in the melt. However, this effect was observed only for melt TiO_2 lower than ca. 7 wt. %. Of particular interest is the behavior of Mo and W, due to the fact that they are simultaneously refractory and moderately siderophile and, hence, are important tracers for planetary evolution including studies of core formation processes (Kleine et al., 2004; O'Neill et al., 2008). Furthermore, both Mo and W, as well as U, are thought to change oxidation state under reducing conditions (e.g., O'Neill and Eggins, 2002; Danielson et al., 2011), which has been shown to dramatically affect their trace element partitioning behavior (Fonseca et al., 2014). Additionally, variations in oxidation state are known to affect phase stability in the lunar mantle sources of mare basalts (Krawczynski and Grove, 2012; Brown and Grove, 2015), which supports the necessity of further study.

Several studies have been carried out on the partitioning of the HFSE between Fe-Ti oxides (e.g. ilmenite, rutile and armalcolite) and basaltic melts (e.g. McCallum and Charette, 1978; Klemme et al., 2006; Dygert et al., 2013). Nevertheless, a scarcity of data exists for how the HFSE partition between silicates (ol, cpx and opx) and lunar mare basaltic melts as a function of melt composition, namely their TiO_2 content. To address this gap in our knowledge, several experiments have been carried out to investigate the partitioning behavior of the HFSE, Mo, W, U and Th between silicates

and realistic lunar basaltic melts.

3.2 Experimental Methods

3.2.1 Starting Materials

Starting compositions were based on the work of Longhi (1987) and Mallmann and O'Neill (2009) (Table 3.1). At one atmosphere, the base mixture of each composition, which contains around 1 wt. % TiO_2, results in silicate melt, olivine (forsterite) and an additional phase, either cpx (1), opx (5), chromite or Cr-diopside (7) and plagioclase or Al-spinel (8) (see Mallmann and O'Neill, 2009). Several compositional series were carried out in either the CMAS+TiO_2 or the CFMAS+TiO_2 systems, modifying the base compositions by adding ca. 1 to 20 wt. % TiO_2. In four series, Fe was only added in trace amounts (ca. 0.1 to 0.5 wt. %), while in a fifth series, FeO contents similar to those observed in lunar basalts (ca. 20 wt. % - Meyer, 2012) were added to the starting compositions. The rationale behind this strategy was to test whether a Fe-Ti complex was indeed responsible for the reported differences in HFSE behavior (Dygert et al., 2013). Moreover, the CMAS+TiO_2 system was chosen as an analogue for lunar basalts to avoid, at an initial stage, any potential redox interaction between FeO and TiO_2 during quenching (Borisov et al., 2013). In addition, the CMAS+TiO_2 system is thought to be a good proxy for most known basaltic compositions as it stabilizes major mineral phases of the upper mantle (Liu and O'Neill, 2007). The proportion SiO_2/TiO_2 for the compositions with 5, 10 and 20 wt. % TiO_2 was established in relation to the binary anorthite-diopside as in O'Neill et al. (2008), while the ratio between other major elements and SiO_2 remained constant in order to decrease the effect of other variables.

Table 3.1: Major element compositions (wt. %) of starting materials and expected liquidus phases.

Starting composition	CaO[a]	MgO	Al_2O_3	SiO_2	TiO_2	P_2O_5[b]	Cr_2O_3[c]	FeO[d]	Total	Expected liquidus phase***
T1+0% TiO_2	18.28	26.30	5.23	48.87	-	0.50	0.48	0.50	100.16	ol + cpx
T1+1% TiO_2*	17.91	25.83	5.11	47.86	1.08	0.49	0.44	0.48	99.20	ol + cpx
T1+2% TiO_2	17.73	25.57	5.05	47.64	2.17	0.49	0.47	0.49	99.61	ol + cpx
T1+3% TiO_2	17.55	25.31	5.00	47.40	3.33	0.48	0.45	0.48	100.00	ol + cpx
T1+5% TiO_2	17.29	24.90	4.95	46.29	5.15	0.46	0.44	0.42	99.90	ol + cpx
T1+10% TiO_2	16.42	23.62	4.70	43.90	10.02	0.44	0.42	0.44	99.96	ol + cpx
T1+20% TiO_2	14.65	21.06	4.20	39.16	19.80	0.40	0.40	0.46	100.13	ol + cpx + arm
T5+0% TiO_2	9.75	29.07	6.86	52.80	-	0.49	0.48	0.51	99.96	ol + opx
T5+1% TiO_2*	9.58	28.62	6.78	51.87	0.97	0.49	0.44	0.49	99.24	ol + opx
T5+2% TiO_2	9.55	28.48	6.72	51.74	2.26	0.48	0.43	0.50	100.16	ol + opx
T5+3% TiO_2	9.45	28.19	6.65	51.22	3.08	0.48	0.47	0.49	100.03	ol + opx
T5+5% TiO_2	9.22	27.46	6.58	49.92	5.51	0.47	0.45	0.47	100.08	ol + opx
T5+10% TiO_2	8.70	26.01	6.07	47.17	10.59	0.43	0.42	0.46	99.85	ol + opx
T5+20% TiO_2	7.70	22.96	5.41	41.74	21.67	0.39	0.35	0.37	100.59	ol + opx + arm
T7+0% TiO_2	18.10	26.04	5.18	48.38	-	0.49	1.50	0.50	100.19	ol + Cr-cpx + chr
T7+1% TiO_2*	17.73	25.52	5.06	47.34	0.95	0.48	1.47	0.49	99.04	ol + Cr-cpx + chr
T7+2% TiO_2	17.74	25.52	5.08	47.41	1.97	0.48	1.47	0.49	100.16	ol + Cr-cpx + chr
T7+3% TiO_2	17.56	25.26	5.02	46.93	3.04	0.48	1.46	0.49	100.22	ol + Cr-cpx + chr
T7+5% TiO_2	17.15	24.68	4.97	46.06	5.07	0.46	1.41	0.47	100.27	ol + Cr-cpx + chr
T7+10% TiO_2	16.27	23.40	4.68	43.47	9.99	0.43	1.35	0.44	100.03	ol + Cr-cpx + chr
T7+20% TiO_2	14.53	20.90	4.16	38.84	19.61	0.38	1.20	0.39	100.01	ol + Cr-cpx + arm
T8+0% TiO_2	12.96	19.81	23.57	44.33	-	0.11	0.11	0.12	101.01	ol + an OR spl
T8+1% TiO_2*	12.68	19.40	23.00	43.36	1.01	0.11	0.11	0.13	99.80	ol + an OR spl
T8+2% TiO_2	12.55	19.21	22.77	42.93	2.15	0.11	0.11	0.13	99.95	ol + an OR spl
T8+3% TiO_2	12.43	19.01	22.54	42.50	3.00	0.11	0.11	0.13	99.82	ol + an OR spl
T8+5% TiO_2	12.24	18.71	22.26	41.86	4.58	0.10	0.10	0.07	99.92	ol + an OR spl
T8+10% TiO_2	11.65	17.82	21.28	39.98	9.23	0.09	0.09	0.10	100.24	ol + an OR spl
T8+20% TiO_2	10.50	16.10	19.17	36.00	18.10	0.11	0.08	0.11	100.17	ol+arm
FT1	17.91	8.43	5.13	47.87	1.03	0.49	0.47	17.83	99.16	ol + cpx
FT1+5% TiO_2	17.29	8.14	4.95	46.22	5.06	0.46	0.44	17.19	99.75	ol + cpx
FT1+10% TiO_2	16.42	7.73	4.70	43.90	10.02	0.44	0.42	16.32	99.95	ol + cpx
FT1+20% TiO_2	14.65	6.89	4.19	39.16	19.73	0.40	0.38	14.58	99.98	ol + cpx + arm
ST1+5% TiO_2**	20.14	14.28	7.60	48.23	5.18	0.29	0.12	3.98	99.83	cpx
ST1+10% TiO_2**	20.09	13.31	7.50	46.47	8.71	0.26	0.11	2.86	99.32	cpx

*Starting (base) compositions based on the work of Fonseca et al. (2014), Mallmann and O'Neill (2009), O'Neill et al. (2008) and Longhi (1978)

**Average based on the microprobe analysis (n = 5 / phase) and modal proportion of each phase on the experiments (cpx + silicate glass)

***Not all runs produced all the expected liquidus phase (For details see Results section). Abbreviations according to Whitney and Evans (2010) - Ol: olivine; Cpx: Clinopyroxene, Cr-cpx: Chrome-diopside, Opx: Orthopyroxene, Chr: Chromite, Arm: Armalcolite, Sp: Al-Spinel, An: Anorthite

[a]added as $CaCO_3$; [b]added as $(NH_4)H_2PO_4$ and P_2O_5 in solution (5% HNO_3); [c]added as $Cr(NO_3)_3$; [d]added as Fe_2O_3. See text for details.

High-purity oxide powders (SiO_2, MgO, Al_2O_3, Fe_2O_3 and TiO_2) were ground with $CaCO_3$ under acetone in an agate mortar until homogeneized. Chromium was added as Specpure plasma standard solution of 10,000 g/mL

$Cr(NO_3)_3$ in 5 % HNO_3 and P was added as 1,000 μg/mL solution in 5 % HNO_3. Starting powder mixes were subsequently dried, pressed into pellets and placed in a corundum crucible inside a vertical tube furnace to decarbonate overnight in air at 1 bar and 950 °C. All pills were then re-ground under acetone and trace elements were added to the powders, in amounts of 500 to 1,000 μg/g, as oxides (Nb, Ta, Zr, Hf) as well as using 1,000 μg/mL PlasmaCal standard solutions in HNO_3 (U and Th) and H_2O (Mo and W). Barium (as $BaCO_3$ - 1,000 μg/g) and Mn (as MnO ca. 1 wt. %) were also added to some of the starting compositions. Barium was added as a tracer for evaluating the presence of melt inclusions in the crystals during LA-ICP-MS analysis (e.g., Lundstrom et al., 1994; Mollo et al., 2013). Manganese was added for use as an internal standard during LA-ICP-MS analysis (following Dygert et al., 2013). Crystal seeds were added to some starting compositions (labeled S, i.e. seeded) to promote crystal growth at run conditions. These seeds consist of pyroxene grains (Wo: 50 %, En: 34 % and Fs: 16 %) collected at the summit of Vesuvius, Italy. Finally, two extra mixtures were produced using as a starting point the composition labeled T1, with 0 % and 10 % TiO_2 and doped with rare-earth elements (La, Nd, Sm, Y and Lu) in addition to the HFSE, to constrain the crystal lattice strain model for olivine.

3.2.2 Experimental setup

Loops were made from either Pt or Re wire for experiments carried out using Fe-poor and Fe-rich compositions, respectively. Sample powders were mixed with water and polyethylene glycol to form a slurry that was placed on the loops. The metal loops + slurry were then hung in the hot spot of a furnace and fused at high-temperature. Loops were then suspended inside a vertical tube muffle furnace at temperatures between 1350 and 1400 °C,

i.e., around 50 °C to 100 °C above the expected supraliquidus and under redox conditions imposed by a gas atmosphere (CO-CO_2 - see Supplementary Material). Each sample remained at supraliquidus conditions for 3 to 5 hours to ensure that powders were completely molten and homogenized. Cooling ramps were chosen, via trial and error, to maximize crystal growth, so that they were suitable for LA-ICP-MS analysis, to avoid any chemical zonation and to mitigate the development of skeletal crystals. To address the potential role that fO_2 plays in affecting the partitioning behavior of elements like Mo, W, U, and Ti in the experiments, fO_2 was varied between the value of air (i.e., around log fO_2 = -0.7) and to ca. two orders of magnitude more reducing than the iron-wstite redox equilibrium (ΔIW-2, Myers and Eugster, 1983). These low fO_2 values for are in agreement to what is expected for the lunar mantle, which varies from IW+0.2 to -2.5 (Papike, 2005). Oxygen fugacity of each experiment was established by mixing CO-CO_2 in different proportions using Mykrolis mass flow controllers. The amount in SCCM (Standard Cubic Centimeters per Minute) required for the equilibrium gas species fugacities at 1 bar was calculated using an Excel macro as described in Kress et al. (2004) at the target temperature of each run. The effective values of fO_2 inside the furnaces were checked and calibrated using a CaO-Y_2O_3-stabilized ZrO_2 electrolite cell (see Chase, 1998; Laurenz et al., 2010). The determined fO_2 values were found to be within 0.6 log-bar units of the calculated values.

A significant challenge in carrying out experiments with FeO-bearing silicate melts is the loss of Fe into a metal wire or capsule (Borisov and Palme, 2000). To avoid this issue we pre-saturated Pt loops with Fe by pre-equilibrating them with a FeO-rich silicate melt (a K-rich lava from the Eastern Mediterranean - Kirchenbaur et al., 2012) at the relevant fO_2 of the experiment. Under more reducing conditions than FMQ (O'Neill,

1987), Fe-rich experiments were carried out in loops fashioned from Re wire, which shows only limited uptake of Fe (see Fonseca et al., 2007). Temperature monitoring during the experiments was done by an internal type B ($Pt_{70}Rh_{30}$ - $Pt_{94}Rh_6$) thermocouple and checked against the melting point of gold (1064 °C), which was measured to be always within 5 °C of the set temperature (cf. Laurenz et al., 2010, 2013). After reaching the nominal temperature, each experiment was kept in the furnace for 36 to 96 hours to maximize the approach to equilibrium. For Pt loops, quenching was performed in air by quickly removing the sample chandelier from the top of the furnace that has a water cooling system designed to keep the maximum temperature at 60 °C. Whenever rhenium loops were used, experiments had to be quenched in water, as the opening of the furnace to air almost immediately oxidized the Re wire, causing the experimental charge to drop. Quenched loops were recovered, mounted in epoxy resin and polished for analyses.

3.3 Analytical Techniques

Major (CaO, MgO, Al_2O_3, SiO_2, and TiO_2) and minor elements (P_2O_5, MnO, FeO, Na_2O and Cr_2O_3) were analyzed using a JEOL JXA 8900 electron microprobe (Steinmann Institute, University of Bonn) in Wavelength Dispersive mode (WDS), employing 15 kV acceleration voltage and 15 nA beam current. Crystals and glasses were measured with an electron beam defocused to 5 m. Peak to background calibrations were performed in a basaltic glass from the Juan de Fuca ridge (VG2), as well as in apatite, rutile and San Carlos olivine. Compositional X-ray maps were also produced for select, cross-sections of cpx to check for chemical equilibrium or the presence of any compositional zonation (Supplementary Material).

Trace element concentrations were acquired using a Resonetics Resolution M50-E 193 nm Excimer Laser Ablation apparatus coupled to a Thermo Scientific XSeries II Q-ICP-MS at the Steinmann Institute, University of Bonn. Laser spot sizes ranged between 33 and 73 m and were picked depending on crystal size and/or prevalence of melt inclusions (for details see Fonseca et al., 2014). Laser frequency was set at 15 Hz and energy fluence rate at 6 J/cm^2 when the spot size was $\geq$ 58 μm. For smaller spot sizes (33–44 μm) a lower frequency was used (10 Hz), to avoid drilling through the crystal into the silicate glass. Count rates for the following isotopes were measured: ^{29}Si, ^{43}Ca, ^{31}P, ^{46}Ti, ^{47}Ti, ^{52}Cr, ^{55}Mn, ^{90}Zr, ^{91}Zr, ^{93}Nb, ^{95}Mo, ^{98}Mo, ^{137}Ba, ^{138}Ba, ^{177}Hf, ^{178}Hf, ^{181}Ta, ^{182}W, ^{184}W, ^{195}Pt, ^{232}Th and ^{238}U. Count rates were then normalized to count rates for an isotope of an element of known concentration (internal standard), which was ^{43}Ca for plagioclase, cpx and glass, ^{29}Si for olivine, opx and glass, ^{27}Al for spinel, and finally ^{46}Ti for titanite, ilmenite and armalcolite. Normalized count rates were then converted to concentrations using the count rates of spots carried out on the NIST SRM 612 glass as the external standard, using preferred values of Jochum et al. (2011), following the methodology of Longerich et al. (1996). When more than one isotope for the same element was monitored, the relative natural abundance of each isotope was well reproduced, indicating that isobaric interferences were negligible.

Results presented in the following section are based on 70 experiments performed in the Experimental Petrology laboratory of the Steinmann Institute for Geosciences, University of Bonn, Germany. Run conditions of each experiment are shown in Table 3.2. Major and trace element compositions for each phase of all runs, as well as the stoichiometry of the crystals are listed in the Supplementary Tables.

Table 3.2: Experimental conditions for each experiment and products.

Run	*Starting materials*	*Loop*	*log fO* $_2$	*Δ relative to redox buffer* [a]	*Cooling ramp (°C/min)*	*Temp. (°C)*	*Duration (h)* [b]	*Run products* [c]
1	T1+1%	Pt	-0.7	air	0.05	1295	5 + 72	cpx+ol+glass
8	T5+20%	Pt	-0.7	air	0.05	1285	5 + 96	opx+arm+glass
10	T1+20%, T8+20%	Pt	-0.7	air	0.05	1240	5 + 72	ol+arm+glass; arm+an+glass
11	T7+1%, T5+20%	Pt	-0.7	air	0.03	1280	5 + 80	cpx+glass; opx+arm+glasss
12	T7+20%	Pt	-0.7	air	0.05	1273	5 + 96	ol+arm+glass
15	T8+20%	Pt	-7.6	FMQ = 0.0	0.05	1270	3 + 48	arm+glass
20	T1+1%, T5+10%	Pt	-7.3	FMQ = 0.0	0.05	1300	5 + 96	cpx+ol+glass; opx+glass
21	T7+10%	Pt	-7.4	FMQ + 0.1	0.05	1280	3 + 72	cpx+chr+glass
22	T1+20%, T7+20%, T8+20%	Pt	-7.7	FMQ + 0.1	0.04	1250	3 + 80	ol+arm+glass; arm+pgt+glass; arm+glass
23	T1+10%, T8+1%	Pt	-7.7	FMQ = 0.0	0.02	1260	3 + 72	cpx+glass; ol+glass
24	T5+1%, T7+1%	Pt	-7.3	FMQ = 0.0	0.02	1300	3 + 72	opx+glass; cpx+chr+glass
25	T8+1%	Pt	-7.7	FMQ + 0.1	0.06	1250	3 + 96	spl+glass
27	T8+10%, T7+20%	Pt	-8.2	FMQ - 0.1	0.05	1230	3 + 72	an+glass; cpx+pgt+arm+glass
28	T5+5% , T5+10%	Pt	-0.7	air	0.06	1280	3 + 96	opx+glass; opx+glass
30	T5+5%, T7+5%	Pt	-7.4	FMQ + 0.1	0.03	1280	3 + 80	opx+glass; cpx+chr+ol+glass
31	T1+20%, ST1+5%, ST1+10%, T8+5%	Pt	-7.7	FMQ = 0.0	0.03	1260	3 + 60	cpx+arm+rt+glass; cpx+glass; cpx+glass; an+ol+glass
34	T1+0%, T5+0%, T1+2%, T5+2%, T1+3%, T5+3%	Pt	-7.3	FMQ = 0.0	0.04	1300	3 + 96	cpx+ol+glass; opx+pgt+glass; cpx+ol+glass; opx+glass; cpx+ol+glass; opx+glass
35	T7+0%, T8+0%, T7+2%, T8+2%, T7+3%, T8+3%	Pt	-7.4	FMQ + 0.1	0.04	1280	5 + 96	cpx+chr+glass; an+ol+glass; cpx+chr+ol+glass; spl+glass; cpx+chr+ol+glass; spl+glass
36	T1+5%	Pt	-7.6	FMQ = 0.0	0.04	1270	3 + 96	cpx+ol+glass
38	T1+0%, T1+1% T1+2%, T1+3%, T1+5%	Pt	-12.6	IW - 1.6	0.04	1300	3 + 96	cpx+ol+glass; ol+glass; cpx+pgt+glass; ol+glass; ol+glass
40	T5+0%, T5+1%, T5+2%, T5+3%, T5+5%	Pt	-12.9	IW - 1.8	0.04	1300	5 + 72	opx+glass; opx+glass; opx+glass ; opx+glass; opx+glass
41	T1+10%, T1+20%, T5+10%, T5+20%	Pt	-13.0	IW - 1.6	0.05	1250	5 + 48	cpx+pgt+glass; cpx+pgt+arm+glass; opx+glass; opx+arm+glass
42	FT1+5%, FT1+10%, FT1+20%	Re	-15.1	IW - 1.8	0.05	1100	3 + 36	cpx+glass; cpx+ilm+glass; cpx+ttn+arm+glass
43	FT1+1%, FT1+5%	Re	-13.7	IW - 1.5	0.05	1200	3 + 60	cpx+glass; cpx+glass
44	T1+0%, T1+3%, T1+5%	Pt	-0.7	air	0.05	1305	3 + 96	cpx+ol+glass; cpx+ol+glass; ol+glass
45	T1+3%, T1+5%	Pt	-12.6	IW - 1.7	0.05	1290	3 + 72	cpx+ol+glass; cpx+glass
46	T7+5%, T7+10%	Pt	-12.7	IW - 1.6	0.05	1280	3 + 72	ol+glass; cpx+ol+glass
47	T1+0%+REE	Re	-12.6	IW - 1.6	0.04	1300	3 + 48	cpx+glass
48	T1+10%+REE	Re	-12.7	IW - 1.6	0.05	1280	3 + 36	cpx+ol+glass

[a] Air: top and bottom of the furnace were not sealed during the experiment to produce an oxidized environment and have only the more oxidized species of each element present; for experiments performed with oxygen fugacities relevant to Earth's mantle the value is given relative to the FMQ: Fayalite-Magnetite-Quartz mineral redox buffer as described by O'Neill (1987); for experiments performed with oxygen fugacities relevant to the lunar mantle the value is given relative to the IW: Iron Wüstite mineral redox buffer as described by Myers and Eugster (1983).

[b] Time spent at supraliquidus (50 to 100 °C above target temperature) + Time spent at the desired equilibrium temperature

[c] Mineral assemblages in each experiment are separated by ";" relatively to column "Starting Materials"; Abbreviations according to Whitney and Evans (2010) - cpx: clinopyroxene; ol: olivine; opx: orthopyroxene; pgt: pigeonite; rt: rutile; arm: armalcolite; spl: Al-spinel; an: anorthite; chr: chromite; ilm: ilmenite; ttn: titanite

3.4 Results

3.4.1 Run Products

With the exception of spinel and ilmenite, most mineral phases that were present as run products ranged between hundreds of micrometers to millimeter in size, whereas the silicate melt always quenched to a homogeneous glass (Figures 3.1a-f). As expected, a major control on the size of the different minerals that crystallized in each experiment was the cooling rate. However, TiO_2 content also proved to be an important factor in determining crystal size, as crystals were larger and less skeletal at higher melt TiO_2 contents, possibly reflecting the depolymerizing effect that TiO_2 has on silicate melts at high TiO_2 contents (Mysen and Neuville, 1995). Moreover, results from the experiments confirm that increasing the TiO_2 content of silicate melts leads to a decrease of its solidus by ca. 1 °C / wt. %, as previously observed by Liu and O'Neill (2007). Changes in fO_2 did not affect significantly the order in which mineral assemblages crystallized. For the most part, run products were homogeneous with respect to their major element composition. There were exceptions, however, as Fe-bearing clinopyroxenes were typically zoned, whereas Fe-free clinopyroxenes showed only incidental zonation in a couple of experiments. In the case of zoned minerals, large enough homogeneous areas, along the rims of the crystal, in direct contact with silicate melt were measured. The different starting materials aimed at crystallizing a wide range of clinopyroxene compositions, depending on their initial content of Cr_2O_3, TiO_2 and FeO. As such, diopside, Cr-diopside, Ti-diopside, augite, and Ti-augite occurred as experimental run products. Clinopyroxene crystals were typically large (Fig. 3.1c-d), sometimes exceeding 1 mm in size, which allowed the use of large laser spot sizes (58 to 73 μm) during trace element analysis.

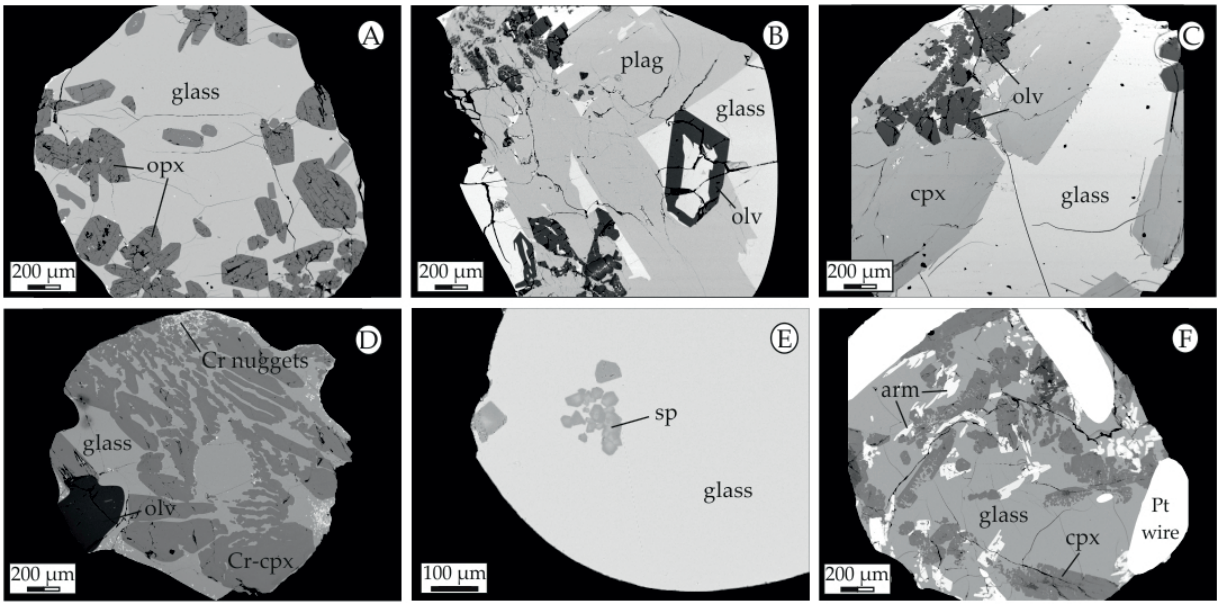

Figure 3.1: Back-scattered electron images of typical experimental run products: A) Euhedral to subhedral orthopyroxene (composition T5); B) Plagioclase (anorthite) large and euhedral crystals formed during experiments (composition T8); C) Olivine (forsterite) and clinopyroxene (diopside) euhedral to subhedral crystals; D) Cr-diopside, olivine and mycrolites of chromite typical of runs labeled T7; E) Spinel crystals no greater than 30 μm and with zonation, not adequate for laser analyses; F) Armalcolite and cpx crystals typical of high-Ti experiments showing some melt inclusions but also areas large enough to set adequate laser spots. See text for details of run products.

Almost all pyroxene compositions produced in the experiments had only a token Ca-Tschermak, i.e. no higher than 0.09 atoms per formula unit (apfu), reflecting the compositional range of lunar clinopyroxene (Kushiro and Nakamura, 1970; Papike et al., 1974). The exceptions were the seeded experiments, which showed ^{IV}Al in the cpx between 0.14 and 0.15 apfu, due to the Al_2O_3 content of the seeds. Orthopyroxene (Fig. 3.1a) are homogeneous ($\geq$ 99 % enstatite) and euhedral, ranging from slightly smaller than 100 μm at low TiO_2 to up to a mm in length at high TiO_2.

Olivine crystals mirrored opx, in that their crystal size depended on TiO_2 content. However, because most trace elements are more incompatible in

olivine when compared to ortho- or clinopyroxene, not all compositions yielded crystals that were large enough to detect these elements via LA-ICP-MS. As a result, the partitioning database for olivine is slightly more restricted than the one produced for the pyroxenes. Spinel (Fig. 3.1e) crystals were of minute size (smaller than 30 micrometers across) and often zoned. Anorthite was present as large crystals (up to a millimeter) (Fig. 3.1b). Rutile was present as an accessory phase in only two experiments.

For TiO_2 contents larger than 10 wt. % in the silicate glass, armalcolite was a typical run product. Armalcolite crystals are often acicular (Fig. 3.1f), which also turned out to be a challenge for their analyses with the laser. However, the generally higher compatibility of the HFSE allowed for a clear "melt-free" signal even though smaller spot sizes were used (33-44 μm). Iron-free experiments resulted in karrooite armalcolite ($MgTi_2O_5$). Iron-rich experiments with bulk TiO_2 of 10 wt. % or higher resulted in either skeletal ilmenite, or Fe-rich armalcolite in equilibrium with cpx. As more TiO_2 was added (see experiment FT1 + 20 wt. % TiO_2), the equilibrium mineral assemblage became titanite, armalcolite, and Ti-rich cpx. These crystals have a general formula $Mg_{0.28}Fe^{2+}_{0.64}Al_{0.04}Cr^{2+}_{0.02}Ca_{0.02}Ti^{3+}_{0.03}Ti^{4+}_{1.97}O_5$, very similar in composition to the type-1 armalcolite described in lunar basalts by Anderson et al. (1970) and Haggerty (1973). Microprobe analysis of these crystals reveal a cation deficiency in their stoichiometry (see Supplementary Material), related to a small amount of Ti^{3+} substituting into their M2 site (Stanin and Taylor, 1980). Enrichments of Al (0.34 to 0.38 apfu) and Cr (0.06 to 0.20 apfu) are found on the armalcolites from mixtures numbered "T7" and "T8", respectively.

3.4.2 Crystal/silicate melt partitioning of Zr, Hf, Nb, Ta and Th

Partition coefficients for the homovalent HFSE (Zr, Hf, Nb, and Ta), and Th derived from the experimental results are given in Table 3.3n average of the $D_M^{silicates/melt}$ for each experiment with the same initial TiO_2 content at different fO_2 is plotted against the TiO_2 content in the melt for clinopyroxene, orthopyroxene, and olivine in Figures 3.2, 3.3, and 3.4 respectively. The general trend $D_M^{cpx/melt} > D_M^{opx/melt} > D_M^{ol/melt} \approx D_M^{an/melt}$ is observed for silicates. Our results show that the partitioning behavior of Zr, Hf, Ta, Th and, to a lesser extent Nb, between cpx and silicate melt has a clear negative correlation with the amount of TiO_2 in the melt (Figure 3.2), decreasing by over an order of magnitude for melt TiO_2 contents between 0 and ca. 16 wt. %. Iron-rich or Cr-rich experiments (FT1 and T7, respectively) show the same trend and almost identical values to the Fe- and Cr-poor series. The values observed for $D_{Zr}^{cpx/melt}$ range from 0.048 to 0.007; $D_{Hf}^{cpx/melt} = 0.14$ to 0.02; $D_{Nb}^{cpx/melt} = 0.0047$ to 0.0009, $D_{Ta}^{cpx/melt} = 0.004$ to 0.0004 and $D_{Th}^{cpx/melt} = 0.005$ to 0.0004. Both seeded experiments (ST1) yielded slightly higher values for all partition coefficients, albeit in a non-systematic fashion. For orthopyroxene, $D_M^{opx/melt}$ is shown to be insensitive to melt TiO_2 for the homovalent HFSE.

Olivine/melt partition coefficients, regardless of the bulk composition of the experiment, show a slightly negative correlation between $D_M^{ol/melt}$ and TiO_2 in the silicate melt from 0 to ca. 5 wt. % TiO_2, after which values become constant. The highest $D_{Zr}^{ol/melt}$ observed is 0.00046 for low-Ti experiments, while the lowest is 0.00011 in high-Ti experiments (> 5 wt. % TiO_2 in the silicate glass). For $D_{Hf}^{ol/melt}$, $D_{Nb}^{ol/melt}$ and $D_{Ta}^{ol/melt}$ the same is observed, with values ranging from 0.00082 to 0.00016; 0.00013 to 0.000042; and 0.00013 to 0.000016, respectively. Since Th concentrations in olivine

were very low, $D_{Th}^{ol/melt}$ with relatively high uncertainties were obtained. In an effort to improve counting statistics, the results of experiments carried out with the same TiO_2 contents were averaged out (Figure 3.4). Interestingly, if one considers only the average values, $D_{Th}^{ol/melt}$, like the $D_{HFSE}^{ol/melt}$, show a similar negative trend compared to $D_{HFSE}^{cpx/melt}$ with increasing TiO_2 from 0 to ca. 5 wt. % TiO_2 in the glass, with the highest $D_{Th}^{ol/melt}$ of 5.7 x 10^{-6} at low-Ti experiments and lowest of 1.6 x 10^{-6} for the high-Ti experiments.

Even though only a relatively smaller number of experiments have been carried out with plagioclase present as a run product, $D_{HFSE}^{an/melt}$ and $D_{Th}^{an/melt}$ show no significant change for different contents of TiO_2. Average values are 0.00036, 0.00022, 0.00033, 0.00024 and 0.00019 for $D_{Zr}^{an/melt}$, $D_{Hf}^{an/melt}$,$D_{Nb}^{an/melt}$, $D_{Ta}^{an/melt}$ and $D_{Th}^{an/melt}$ respectively. Only one experiment contained titanite as a liquidus phase (FT1+20 % TiO_2), which yielded single values for $D_{HFSE}^{ttn/melt}$ of 0.8, 1.5, 1.08 and 4.67 for Zr, Hf, Nb and Ta, respectively, and 0.32 for $D_{Th}^{ttn/melt}$.

Experiments in this study cover a wide range of TiO_2 contents in silicate melt in the presence of armalcolite and a limited dataset for ilmenite (one experiment) and spinel (three experiments). Armalcolite/melt partition coefficients (Table 3.3) show that the homovalent HFSE, with the exception of Th, are all compatible into the Mg-rich end-member of this phase, and that it is possible to distinguish three distinct patterns on the $D_{HFSE}^{arm/melt}$ from the results of this study (Figure 3.5). Mineral/melt partition coefficients for Al-rich armalcolites (T8) are higher than those for Mg-rich (T1, T5 and T7) crystals, and iron-rich armalcolite (FT1) shows the lowest overall $D_{HFSE}^{arm/melt}$ (Table 3.3).

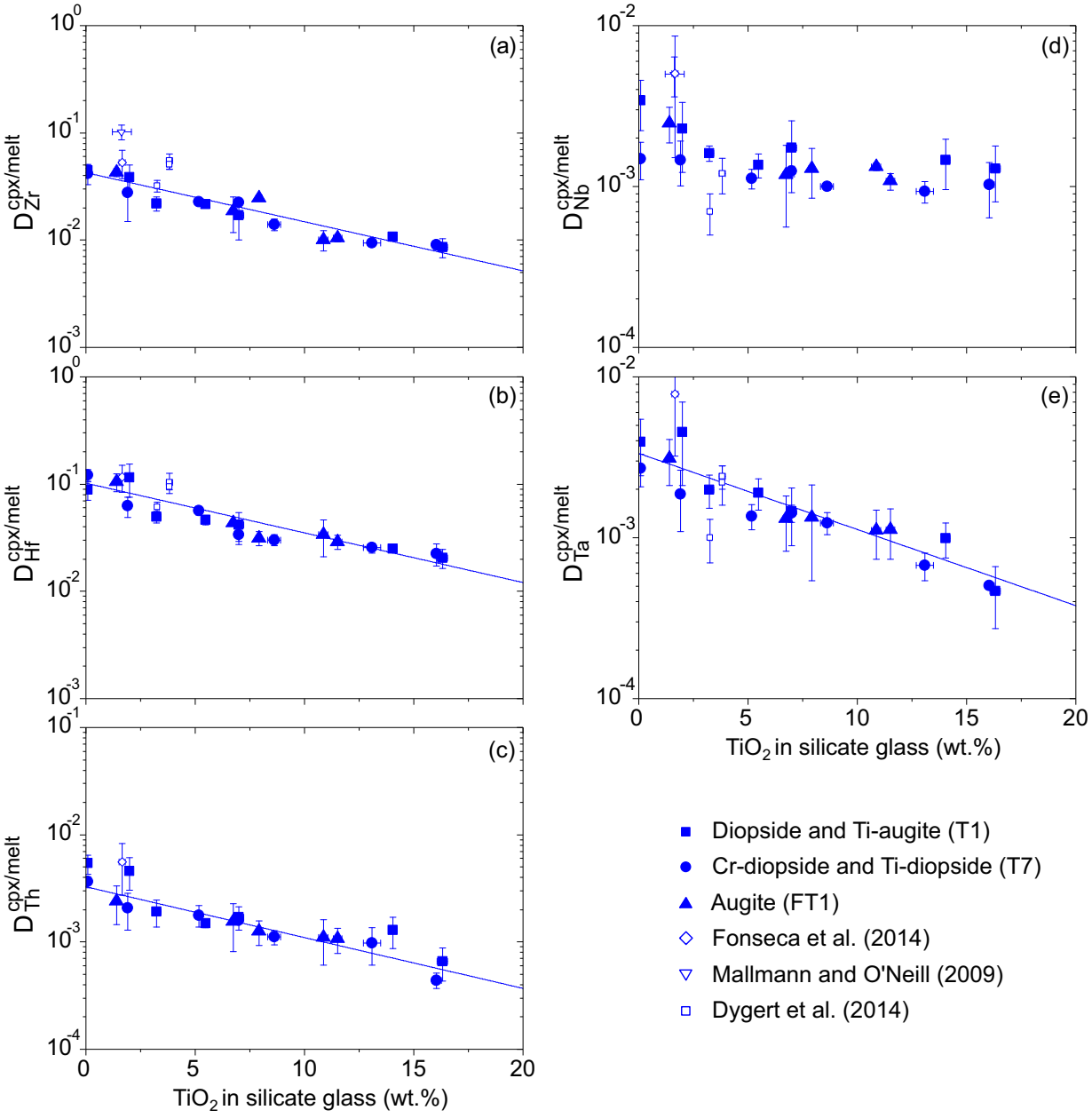

Figure 3.2: Average partition coefficients for the homovalent HFSE between cpx and silicate melt plotted against the different contents of TiO_2 in the silicate glass. Error bars are 1σ of the standard deviation of averaged values and analytical uncertainties. (a) $D_{Zr}^{cpx/melt}$, (b) $D_{Hf}^{cpx/melt}$, (c) $D_{Th}^{cpx/melt}$, (d) $D_{Nb}^{cpx/melt}$ and (e) $D_{Ta}^{cpx/melt}$. Seeded experiments are not plotted. Literature data are average values from Mallmann and O'Neill (2009); Dygert et al. (2014); Fonseca et al. (2014). Blue lines represent linear fits of the data using instrumental weighing of the error.

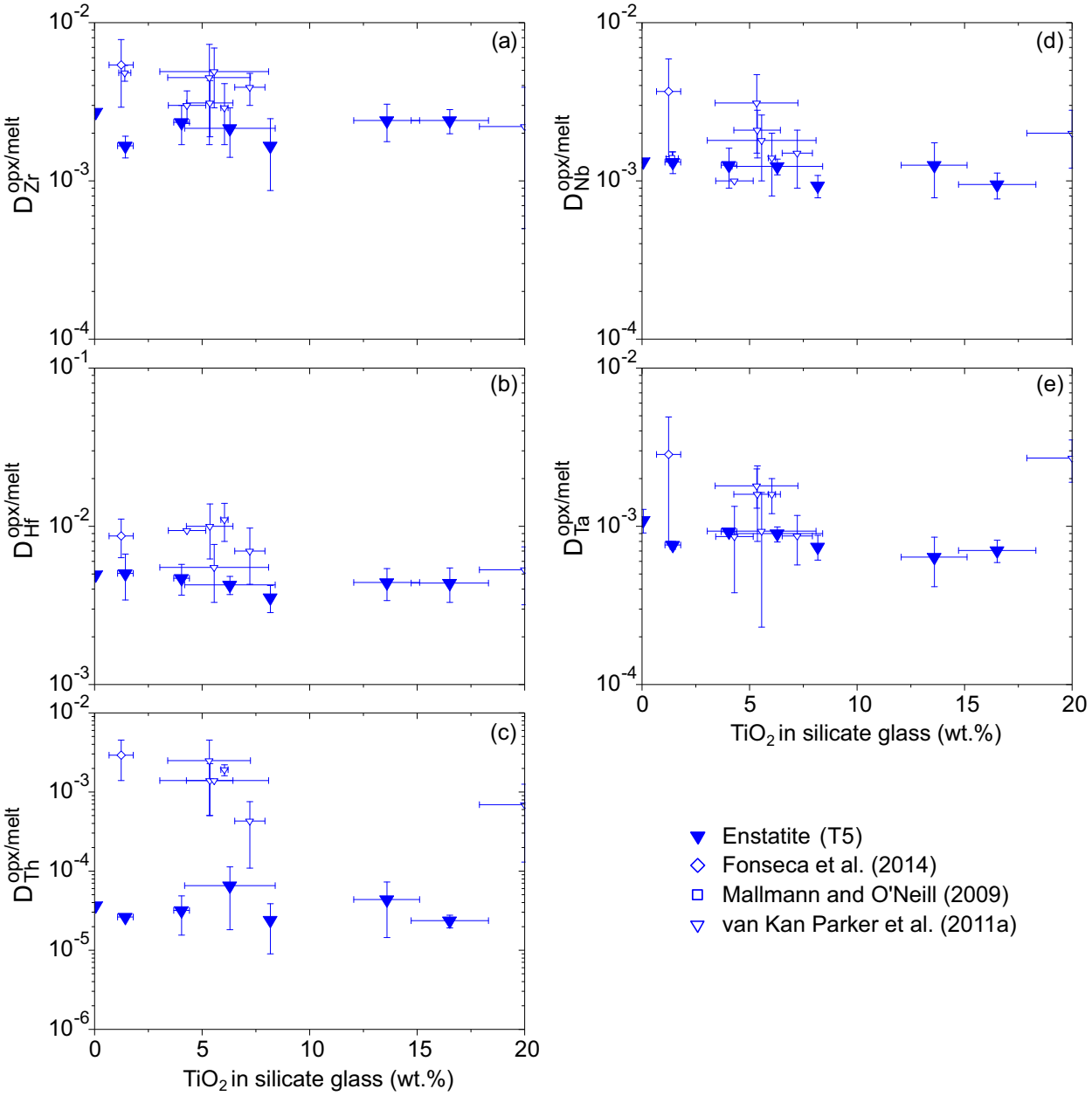

Figure 3.3: Average partition coefficients for the homovalent HFSE between opx and silicate melt plotted against the different contents of TiO_2 in the silicate glass. Error bars are 1σ of the standard deviation of averaged values and analytical uncertainties. (a) $D^{opx/melt}_{Zr}$, (b) $D^{opx/melt}_{Hf}$, (c) $D^{opx/melt}_{Th}$, (d) $D^{opx/melt}_{Nb}$ and (e) $D^{opx/melt}_{Ta}$. Literature data are average values from Mallmann and O'Neill (2009); van Kan Parker et al. (2011b); Fonseca et al. (2014). The partition coefficients obtained for the highest value of TiO_2 in the silicate glass by van Kan Parker et al. (2011b), which is 28.3 wt. %, is represented at the intersection of the horizontal axis at 20 wt. % TiO_2.

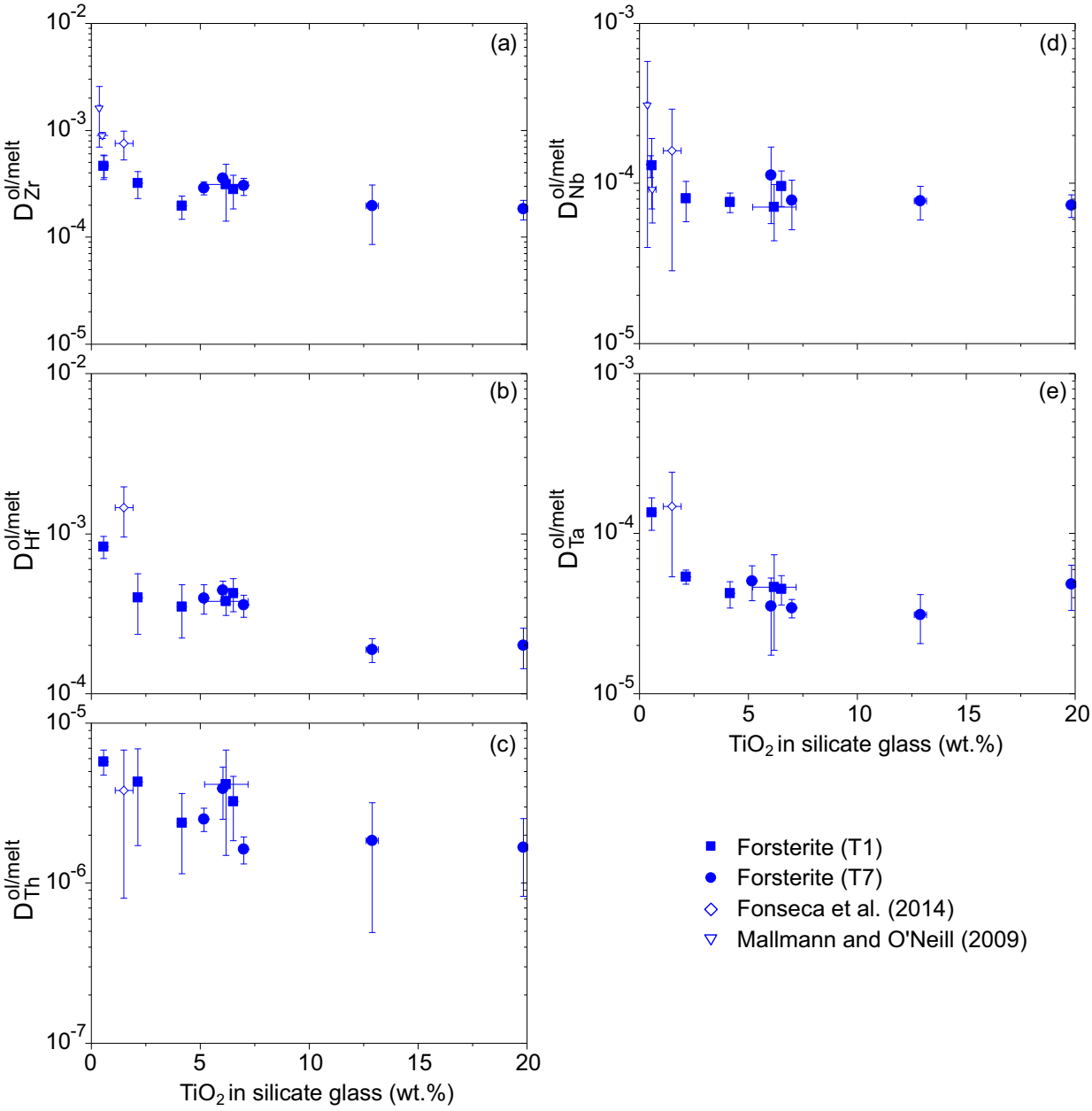

Figure 3.4: Average partition coefficients for the homovalent HFSE between olivine and silicate melt plotted against the different contents of TiO_2 in the silicate glass. Error bars are 1σ of the standard deviation of averaged values and analytical uncertainties. (a) $D^{ol/melt}_{Zr}$, (b) $D^{ol/melt}_{Hf}$, (c) $D^{ol/melt}_{Th}$, (d) $D^{ol/melt}_{Nb}$ and (e) $D^{ol/melt}_{Ta}$. Literature data are average values from Mallmann and O'Neill (2009) and Fonseca et al. (2014).

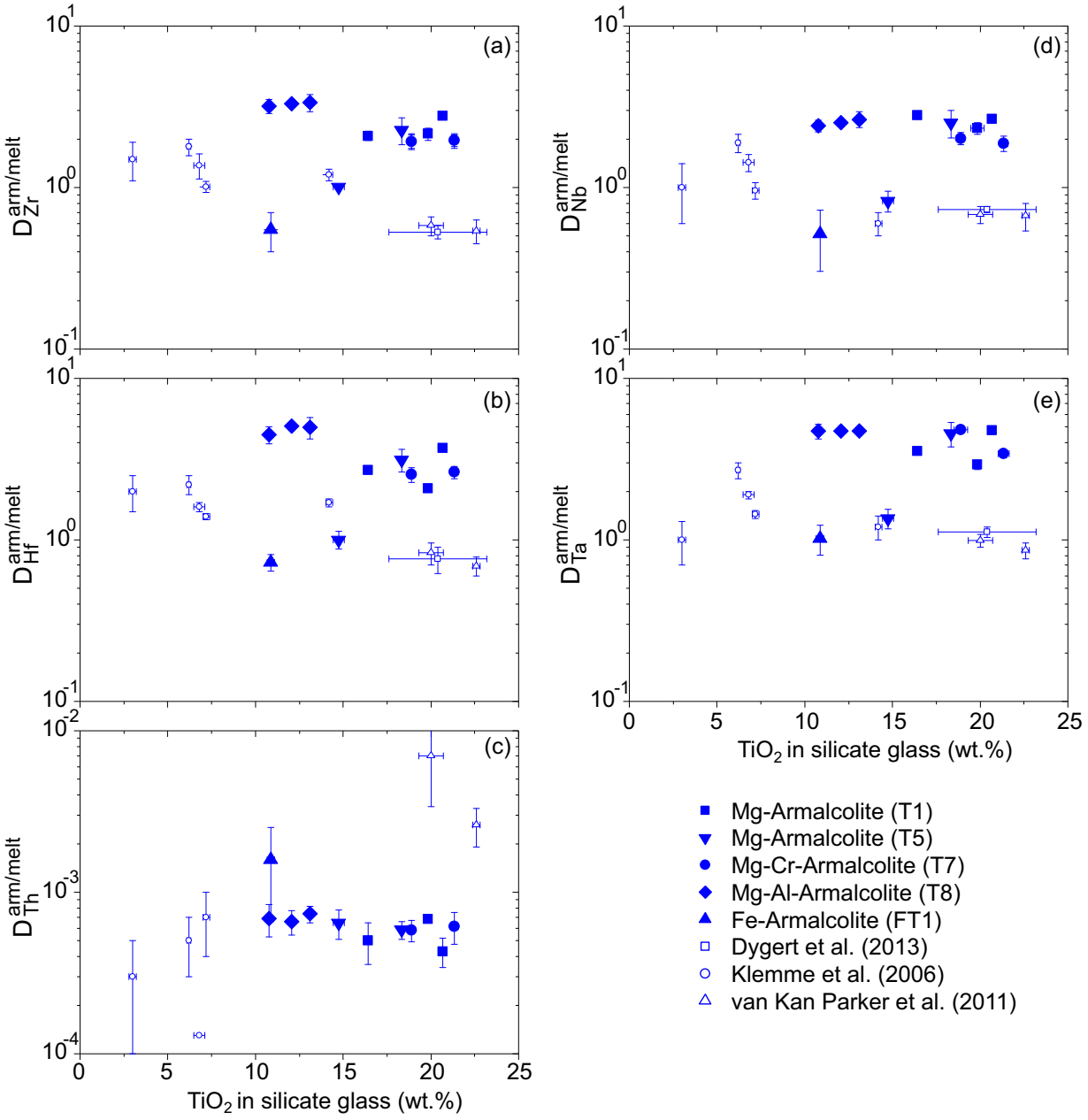

Figure 3.5: Partition coefficients for the homovalent HFSE between armalcolite and silicate melt plotted against the different contents of TiO_2 in the silicate glass. Error bars are 1σ of the standard deviation. (a) $D^{arm/melt}_{Zr}$, (b) $D^{arm/melt}_{Hf}$, (c) $D^{arm/melt}_{Th}$, (d) $D^{arm/melt}_{Nb}$ and (e) $D^{arm/melt}_{Ta}$. Literature data are taken from Klemme et al. (2006); van Kan Parker et al. (2011); Dygert et al. (2013).

3.4.3 Crystal/silicate melt partitioning of Ti, Cr, Mo, W, and U

As expected, the partition coefficients of heterovalent Ti, Cr, Mo, W and U between cpx, opx, olivine and the silicate melt varied systematically with fO_2, as shown in Table 3.3 and Figure 3.6. The $D_{Ti}^{cpx/melt}$ values for both iron-free and iron-bearing cpx range between 0.12 and 0.27. A small increase is observed from experiments performed at oxidized (air or FMQ) to reduced conditions (IW -1.8), over the entire range of TiO_2 in the silicate melt in this study. Following the same trend of the homovalent HFSE, $D_{Ti}^{cpx/melt}$ is higher for the seeded experiments, with an average value of 0.3. Chromium partitioning between cpx and silicate melt appears to be affected by the TiO_2 content in the melt under conditions more oxidized than FMQ, with values ranging from ca. 24 (low-Ti) to ca. 3 (high-Ti) for both Cr-rich or Cr-poor starting compositions, in agreement with the observations of Dygert et al. (2013). Under conditions more reduced than FMQ (i.e. at IW $<$ -1.5), $D_{Cr}^{cpx/melt}$ becomes relatively small and appears to be unaffected by the TiO_2 in the melt, with values ranging from 1.4 to 5.4 regardless of whether the bulk composition had Fe or not. Seeded experiments, however, exhibit higher $D_{Cr}^{cpx/melt}$ than observed in any other experiment, with values ranging between 10.1 and 8.2. The values for $D_{U}^{cpx/melt}$ in the more reduced experiments show only a marginal negative correlation with the TiO_2 content in the glass (Fig. 3.6c), ranging from 0.0025 (low-Ti) to 0.0010 (high-Ti). No visible correlation is seen for $D_{U}^{cpx/melt}$ with the TiO_2 in the silicate glass at experiments performed under more oxidized conditions (air and FMQ). The highest $D_{U}^{cpx/melt}$ reported here are also found in the seeded experiments, with 0.0035 and 0.0047.

Table 3.3: Distribution coefficients obtained for each crystalline phase.

Experiment	Temp. (° C)	Δ relative to buffer	D_{Ti}	±	D_{Cr}	±	D_{Zr}	±	D_{Nb}	±	D_{Mo}	±	D_{Hf}	±	D_{Ta}	±	D_{W}	±	D_{Th}	±	D_{U}	±
	Cpx/melt																					
T1 + 0% Ti	1300	IW - 1.6	-	-	3.78	(5)	0.040	(3)	0.0047	(10)	0.066	(24)	0.080	(7)	0.0029	(3)	0.02456	(96)	0.0068	(12)	0.00231	(68)
T1 + 0% Ti	1300	FMQ = 0.0	-	-	24.08	(47)	0.049	(5)	0.0021	(6)	0.008	(3)	0.097	(18)	0.0050	(18)	0.00009	(1)	0.0040	(3)	0.00175	(13)
T1 + 1% Ti	1295	air	0.20	(2)	7.65	(18)	0.038	(7)	0.0016	(5)	-	-	0.087	(19)	0.0028	(9)	0.000031	(1)	0.0033	(9)	0.00022	(5)
T1 + 1% Ti	1300	FMQ = 0.0	0.18	(3)	11.12	(42)	0.039	(9)	0.0030	(10)	0.014	(6)	0.142	(37)	0.0063	(27)	0.0001432	(3)	0.0058	(12)	0.00089	(21)
T1 + 2% Ti	1300	FMQ = 0.0	0.23	(1)	7.82	(14)	0.023	(3)	0.0013	(1)	0.010	(3)	0.055	(6)	0.0021	(2)	0.000077	(2)	0.0018	(2)	0.00069	(21)
T1 + 2% Ti	1300	IW - 1.6	0.21	(4)	5.37	(11)	0.021	(2)	0.0019	(1)	0.295	(62)	0.044	(3)	0.0018	(4)	0.00805	(19)	0.0020	(5)	0.00256	(55)
T1 + 3% Ti	1300	FMQ = 0.0	0.18	(1)	9.15	(9)	0.022	(1)	0.0014	(2)	0.007	(3)	0.046	(4)	0.0019	(4)	0.00012	(1)	0.0015	(1)	0.00090	(3)
T1 + 5% Ti	1270	FMQ = 0.0	0.19	(1)	2.68	(5)	0.018	(5)	0.0017	(4)	0.010	(1)	0.041	(8)	0.0015	(4)	0.000091	(4)	0.0016	(2)	0.00066	(16)
T1 + 5% Ti	1290	IW - 1.7	0.21	(2)	4.50	(4)	0.016	(5)	0.0017	(7)	0.341	(134)	0.042	(10)	0.0014	(4)	0.0209	(103)	0.0018	(3)	0.00212	(39)
T1 + 10% Ti	1260	FMQ = 0.0	0.14	(2)	3.80	(3)	0.010	(1)	0.0016	(3)	0.0140	(2)	0.0222	(4)	0.0011	(3)	0.000178	(1)	0.0016	(3)	0.00096	(8)
T1 + 10% Ti	1250	IW - 1.6	0.17	(2)	2.19	(2)	0.011	(1)	0.0014	(4)	1.235	(521)	0.027	(1)	0.0008	(1)	0.0478	(197)	0.0009	(2)	0.00131	(43)
T1 + 20% Ti	1260	FMQ = 0.0	0.17	(3)	3.07	(10)	0.007	(1)	0.0010	(3)	0.045	(10)	0.021	(2)	0.0004	(1)	0.0000498	(3)	0.0009	(2)	0.00052	(7)
T1 + 20% Ti	1250	IW - 1.6	0.19	(1)	1.42	(2)	0.010	(1)	0.0016	(4)	2.418	(1494)	0.020	(3)	0.0006	(2)	0.0336	(194)	0.0004	(1)	0.00116	(72)
T7 + 0% Ti	1280	FMQ + 0.1	-	-	6.96	(4)	0.042	(9)	0.0015	(4)	0.005	(2)	0.121	(16)	0.0027	(6)	0.000058	(1)	0.0036	(4)	0.00092	(21)
T7 + 1% Ti	1280	air	0.24	(3)	3.36	(5)	0.034	(10)	0.0013	(2)	-	-	0.060	(11)	0.0018	(7)	0.000062	(1)	0.0024	(8)	0.00056	(26)
T7 + 1% Ti	1300	FMQ = 0.0	0.15	(3)	5.12	(2)	0.022	(8)	0.0017	(5)	0.010	(6)	0.065	(7)	0.0019	(3)	0.00019	(1)	0.0018	(3)	0.00111	(36)
T7 + 2% Ti	1280	FMQ + 0.1	0.20	(2)	5.03	(5)	0.023	(2)	0.0011	(2)	0.0041	(2)	0.056	(5)	0.0014	(2)	0.000035	(1)	0.0018	(4)	0.00107	(13)
T7 + 3% Ti	1280	FMQ + 0.1	0.23	(2)	4.03	(3)	0.023	(1)	0.0012	(1)	0.0052	(3)	0.034	(7)	0.0014	(2)	0.000038	(1)	0.0016	(1)	0.0010	(6)
T7 + 5% Ti	1280	FMQ + 0.1	0.13	(3)	4.10	(3)	0.014	(2)	0.0010	(1)	-	-	0.030	(4)	0.0012	(2)	0.000078	(5)	0.0011	(2)	0.00065	(18)
T7 + 10% Ti	1280	FMQ + 0.1	0.13	(1)	4.18	(5)	0.0094	(5)	0.0009	(1)	0.006	(3)	0.025	(3)	0.0007	(1)	0.00030	(2)	0.0010	(4)	0.0011	(6)
T7 + 20% Ti	1230	FMQ - 0.1	0.12	(1)	2.99	(4)	0.009	(1)	0.0010	(4)	0.009	(1)	0.022	(5)	0.00050	(2)	0.00072	(3)	0.0004	(1)	0.00110	(30)
FT1+1% Ti	1200	IW - 1.5	0.29	(5)	5.39	(9)	0.043	(4)	0.0025	(6)	0.149	(51)	0.105	(20)	0.0031	(10)	0.00108	(6)	0.0024	(9)	0.00208	(31)
FT1+5% Ti	1200	IW - 1.5	0.23	(3)	4.77	(7)	0.019	(7)	0.0012	(6)	0.309	(50)	0.043	(2)	0.0013	(5)	0.00635	(20)	0.0015	(7)	0.00168	(26)
FT1+5% Ti	1100	IW - 1.8	0.20	(1)	3.97	(6)	0.025	(1)	0.0013	(4)	0.338	(84)	0.031	(5)	0.0013	(8)	0.00830	(48)	0.0013	(3)	0.00121	(57)
FT1+10%Ti	1100	IW - 1.8	0.27	(3)	3.11	(4)	0.010	(1)	0.0011	(1)	0.302	(112)	0.029	(5)	0.0011	(4)	0.00391	(19)	0.0011	(3)	0.00139	(32)
FT1+20%Ti	1100	IW - 1.8	0.23	(7)	3.80	(8)	0.010	(2)	0.0013	(1)	0.489	(187)	0.034	(13)	0.0011	(4)	0.00566	(16)	0.0011	(5)	0.00096	(32)
ST1 + 5% Ti	1260	FMQ = 0.0	0.34	(3)	10.09	(27)	0.070	(7)	0.0024	(6)	0.025	(1)	0.261	(98)	0.0053	(5)	0.000075	(1)	0.0045	(5)	0.00467	(168)
ST1 + 10% Ti	1260	FMQ = 0.0	0.31	(5)	8.24	(9)	0.148	(32)	0.0032	(12)	0.017	(2)	0.227	(43)	0.0129	(36)	0.00026	(1)	0.0083	(23)	0.00348	(79)
T1+0% Ti + REE	1300	IW - 1.6	-	-	0.98	(12)	0.030	(9)	0.0018	(7)	0.319	(16)	0.042	(18)	0.0025	(9)	0.0421	(236)	0.0018	(7)	0.0040	(12)
T1+10% Ti + REE	1280	IW - 1.6	0.23	(1)	0.72	(7)	0.013	(2)	0.0014	(3)	0.881	(232)	0.029	(2)	0.0010	(3)	0.0852	(276)	0.0008	(3)	0.0013	(4)
	Opx/melt																					
T5 + 0% Ti	1300	FMQ = 0.0	-	-	3.51	(17)	0.0028	(8)	0.0013	(26)	0.01	(0.3)	0.0050	(10)	0.00123	(2)	0.00109	(2)	0.000036	(13)	0.00031	(22)
T5 + 0% Ti	1300	IW - 1.8	-	-	8.68	(20)	0.0027	(3)	0.0014	(5)	0.69	(19)	0.0049	(12)	0.00096	(1)	0.00361	(12)	0.000038	(15)	0.00071	(6)
T5 + 1% Ti	1300	IW - 1.8	0.09	(4)	6.27	(10)	0.0018	(6)	0.0015	(5)	0.75	(25)	0.0039	(8)	0.00079	(1)	0.00595	(19)	0.000026	(9)	0.00051	(10)
T5 + 1% Ti	1300	FMQ = 0.0	0.06	(1)	1.715	(3)	0.0015	(3)	0.0012	(3)	-	-	0.0062	(6)	0.00073	(1)	0.00074	(2)	0.000026	(7)	0.00029	(4)
T5 + 2% Ti	1300	IW - 1.8	0.09	(1)	1.92	(1)	0.0028	(3)	0.0015	(5)	2.69	(103)	0.0055	(4)	0.000947	(4)	0.01480	(94)	0.000044	(9)	0.00091	(10)

Experiment	Temp. (° C)	Δ relative to buffer	D_{Ti}	±	D_{Cr}	±	D_{Zr}	±	D_{Nb}	±	D_{Mo}	±	D_{Hf}	±	D_{Ta}	±	D_{W}	±	D_{Th}	±	D_{U}	±
	Opx/melt																					
T5 + 2% Ti	1300	FMQ = 0.0	0.06	(1)	2.64	(11)	0.0019	(6)	0.0010	(2)	0.03	(1)	0.0040	(9)	0.00090	(2)	0.00096	(2)	0.000020	(9)	0.00036	(25)
T5 + 3% Ti	1300	IW - 1.8	0.08	(1)	2.16	(3)	0.0016	(2)	0.0011	(1)	-	-	0.0039	(8)	0.00083	(2)	0.01785	(54)	0.000032	(11)	0.00055	(8)
T5 + 3% Ti	1300	FMQ = 0.0	0.06	(1)	2.78	(4)	0.0027	(11)	0.0013	(1)	0.020	(3)	0.0047	(11)	0.00097	(2)	0.001323	(4)	0.000100	(72)	0.00034	(21)
T5 + 5% Ti	1280	FMQ + 0.1	0.05	(1)	1.90	(2)	0.00256	(3)	0.00125	(1)	-	-	0.0047	(1)	0.001163	(2)	0.001255	(4)	0.00018	(3)	0.00026	(1)
T5 + 5% Ti	1280	air	0.06	(1)	1.07	(3)	0.0020	(3)	0.0008	(1)	-	-	0.0035	(5)	0.00086	(1)	0.00118	(2)	0.000026	(7)	0.00007	(4)
T5 + 5% Ti	1280	IW - 1.8	0.07	(1)	1.09	(1)	0.0014	(6)	0.0011	(1)	2.29	(97)	0.0036	(4)	0.000629	(4)	0.01388	(62)	0.000022	(12)	0.00040	(5)
T5 + 10% Ti	1300	FMQ = 0.0	0.06	(1)	1.74	(1)	0.0029	(6)	0.0017	(9)	0.01	(1)	0.0054	(14)	0.00086	(1)	0.00105	(1)	0.000032	(7)	0.00028	(17)
T5 + 10% Ti	1280	air	0.049	(5)	3.12	(7)	0.0017	(3)	0.0007	(1)	-	-	0.0035	(3)	0.00064	(1)	0.00105	(3)	0.000022	(8)	0.00002	(1)
T5 + 10% Ti	1250	IW - 1.6	0.12	(2)	2.835	(5)	0.0026	(4)	0.0014	(3)	2.36	(25)	0.004282	(5)	0.000416	(3)	0.01526	(23)	0.000077	(19)	0.00055	(11)
T5 + 20% Ti	1285	air	0.077	(5)	1.95	(5)	0.0028	(10)	0.0010	(2)	-	-	0.0056	(11)	0.00082	(2)	0.00169	(2)	0.000021	(5)	0.00010	(8)
T5 + 20% Ti	1280	air	0.07	(1)	1.90	(3)	0.0024	(13)	0.0007	(2)	-	-	0.0040	(8)	0.00067	(2)	0.00143	(5)	0.000022	(9)	0.00007	(4)
T5 + 20% Ti	1250	IW - 1.6	0.06	(1)	1.02	(1)	0.0020	(5)	0.0011	(3)	3.11	(158)	0.0036	(6)	0.00060	(1)	0.05652	(180)	0.000028	(15)	0.00039	(3)
	Ol/melt																					
T1+0% Ti	1305	air	-	-	1.21	(1)	0.0005	(12)	0.00013	(6)	-		0.00083	(13)	0.00014	(3)	0.00004	(2)	0.0000058	(10)	0.0000015	(8)
T1+1% Ti	1300	IW - 1.6	0.011	(6)	2.17	(4)	0.0004	(7)	-		0.444	(192)	0.00052	(11)	0.00006	(4)	0.00506	(106)	0.0000061	(9)	0.0000126	(45)
T1+1% Ti	1300	FMQ = 0.0	0.015	(7)	2.23	(2)	0.0003	(11)	0.00008	(2)	0.0047	(2)	0.00028	(12)	0.00005	(2)	0.00003	(1)	0.0000025	(5)	0.0000023	(16)
T1+2% Ti	1300	FMQ = 0.0	0.006	(2)	1.22	(2)	0.0002	(5)	0.00008	(1)	0.0066	(1)	0.00035	(13)	0.00004	(1)	0.00003	(2)	0.0000024	(12)	0.0000024	(4)
T1+3% Ti	1300	FMQ = 0.0	0.005	(2)	1.27	(2)	0.0001	(8)	0.00004	(1)	0.0069	(5)	0.00031	(9)	0.00002	(1)	0.00003	(1)	0.0000026	(5)	0.0000024	(3)
T1+3% Ti	1305	air	0.004	(3)	1.36	(3)	0.0004	(13)	0.00010	(3)	-	-	0.00045	(17)	0.00007	(4)	0.00003	(1)	0.0000072	(4)	0.0000021	(10)
T1+3% Ti	1300	IW - 1.6	0.006	(3)	0.97	(1)	0.0004	(12)	0.00008	(1)	-	-	0.00037	(11)	0.000053	(4)	0.00453	(44)	0.0000026	(6)	0.0000119	(43)
T1+5% Ti	1300	IW - 1.6	0.007	(2)	0.94	(1)	0.0003	(7)	0.00009	(3)	0.671	(386)	0.00054	(13)	0.00003	(2)	0.00393	(263)	0.0000046	(10)	0.0000108	(32)
T1+5% Ti	1270	FMQ = 0.0	0.008	(6)	1.00	(2)	0.0002	(8)	0.00012	(3)	0.0070	(3)	0.00036	(12)	0.00005	(3)	0.00004	(2)	0.0000034	(16)	0.0000017	(4)
T1+5% Ti	1305	air	0.003	(2)	0.84	(2)	0.0003	(12)	0.00008	(2)	-	-	0.00038	(11)	0.00005	(3)	0.00004	(2)	0.0000018	(4)	0.0000020	(7)
T1+20% Ti	1250	air	0.004	(2)	0.67	(2)	0.0003	(19)	0.00008	(2)	-	-	0.00027	(10)	0.00004	(1)	0.00003	(1)	0.0000028	(10)	0.0000037	(26)
T7+2% Ti	1280	FMQ + 0.1	0.005	(3)	0.65	(1)	0.0003	(4)	-	-	0.0041	(2)	0.00040	(8)	0.00005	(1)	0.00004	(1)	0.0000025	(4)	0.0000016	(1)
T7+3% Ti	1280	FMQ + 0.1	0.005	(1)	0.63	(1)	0.0003	(5)	0.00008	(3)	0.0082	(1)	0.00036	(6)	0.000034	(4)	0.00004	(1)	0.0000016	(3)	0.0000029	(6)
T7+5% Ti	1280	FMQ + 0.1	0.006	(2)	0.406	(5)	0.0003	(8)	-	-	0.0110	(1)	0.00049	(14)	0.000023	(5)	0.00003	(1)	0.0000049	(3)	0.0000023	(17)
T7+5% Ti	1280	IW - 1.6	0.004	(4)	1.12	(1)	0.0004	(16)	0.00011	(6)	-	-	0.00040	(17)	0.00005	(3)	0.00565	(261)	0.0000029	(19)	0.0000120	(29)
T7+10% Ti	1280	IW - 1.6	0.009	(1)	0.94	(1)	0.0003	(1)	0.00006	(1)	-	-	0.00021	(10)	0.00004	(1)	-	-	0.0000028	(16)	0.0000134	(29)
T7+10% Ti	1280	FMQ + 0.1	0.009	(1)	0.47	(1)	0.0001	(5)	0.00009	(2)	0.0078	(2)	0.00017	(9)	0.00002	(1)	0.00003	(1)	0.0000009	(8)	0.0000027	(17)
T7+20% Ti	1250	FMQ + 0.1	0.006	(3)	0.72	(1)	0.0002	(4)	0.00007	(1)	-	-	0.00020	(6)	0.00005	(2)	0.00004	(1)	0.0000017	(8)	0.0000023	(16)
T1+10% Ti + REE	1280	IW - 1.6	0.007	(2)	0.52	(6)	0.0002	(1)	0.00010	(2)	0.304	(120)	0.00047	(1)	0.00001	(1)	0.00727	(372)	0.0000040	(3)	0.0000035	(2)
	Arm/melt																					
T1 + 20% Ti	1250	FMQ + 0.1	3.89	(4)	30.89	(14)	2.15	(6)	2.32	(4)	0.77	(2)	2.08	(1)	2.92	(18)	0.059	(3)	0.00068	(3)	0.00669	(31)
T1 + 20% Ti	1240	air	3.81	(8)	70.69	(16)	2.77	(7)	2.67	(1)	-	-	3.69	(2)	4.76	(22)	0.10	(1)	0.00063	(13)	0.00469	(47)

Experiment	Temp. (° C)	Δ relative to buffer	D_{Ti}	±	D_{Cr}	±	D_{Zr}	±	D_{Nb}	±	D_{Mo}	±	D_{Hf}	±	D_{Ta}	±	D_{W}	±	D_{Th}	±	D_{U}	±
	Arm/melt																					
T1 + 20% Ti	1250	IW - 1.6	5.27	(5)	15.51	(1)	2.09	(9)	2.80	(1)	4.15	(16)	2.69	(1)	3.54	(17)	0.50	(24)	0.00050	(15)	0.00722	(207)
T7 + 20% Ti	1273	air	3.62	(4)	50.06	(11)	1.95	(16)	1.88	(2)	-	-	2.63	(2)	3.41	(32)	0.14	(3)	0.00061	(14)	0.00367	(57)
T7 + 20% Ti	1250	FMQ + 0.1	3.91	(18)	35.26	(6)	1.93	(22)	2.02	(2)	0.79	(1)	2.54	(3)	4.81	(39)	0.10	(2)	0.00058	(9)	0.00993	(217)
T5 + 20% Ti	1285	air	4.27	(3)	53.94	(16)	2.27	(43)	2.52	(5)	0.47	(1)	3.15	(5)	4.55	(78)	0.15	(2)	0.00059	(7)	0.00413	(148)
T5 + 20% Ti	1250	IW - 1.6	5.60	(12)	5.56	(0.3)	1.01	(3)	0.83	(1)	5.00	(19)	1.00	(1)	1.36	(19)	0.08	(1)	0.00065	(13)	0.00323	(99)
T8 + 20% Ti	1270	FMQ = 0.0	5.62	(10)	75.01	(21)	3.35	(39)	2.64	(3)	0.88	(1)	4.98	(8)	4.71	(6)	0.11	(2)	0.00073	(9)	0.00512	(22)
T8 + 20% Ti	1240	air	6.74	(4)	64.59	(21)	3.19	(32)	2.41	(2)	0.78	(3)	4.49	(5)	4.72	(49)	0.14	(1)	0.00068	(16)	0.00475	(30)
T8 + 20% Ti	1250	FMQ + 0.1	6.00	(9)	31.08	(4)	3.31	(14)	2.51	(1)	0.73	(1)	5.09	(2)	4.73	(17)	0.13	(2)	0.00066	(11)	0.00685	(36)
FT1+20%	1100	IW - 1.8	6.79	(17)	10.34	(2)	0.55	(15)	0.51	(1)	4.18	(11)	0.73	(1)	1.02	(23)	0.10	(2)	0.00159	(93)	0.01098	(192)
	An/melt																					
T8 + 0% Ti	1280	FMQ + 0.1	-	-	0.008	(3)	0.0003	(1)	0.00024	(8)	0.0042	(5)	0.00028	(1)	0.00020	(3)	0.00004	(2)	0.00018	(3)	0.000032	(14)
T8 + 5% Ti	1260	FMQ = 0.0	0.022	(5)	0.022	(1)	0.0005	(2)	0.00038	(5)	-	-	0.00028	(1)	0.00025	(4)	0.00012	(6)	0.00032	(10)	0.000047	(24)
T8 + 10% Ti	1230	FMQ - 0.1	0.022	(2)	0.014	(3)	0.0003	(1)	0.00040	(19)	0.0028	(15)	0.00014	(1)	0.00031	(4)	0.00011	(8)	0.00015	(5)	0.000067	(47)
T8 + 20% Ti	1240	air	0.028	(3)	0.103	(28)	-	-	0.00033	(9)	-	-	0.000176	(2)	0.00023	(3)	0.00005	(2)	0.00013	(3)	0.000013	(6)
	Spl/melt																					
T8 + 1% Ti	1250	FMQ + 0.1	0.05	(2)	38.28	(12)	1.5E-03	(6)	0.00040	(1)	-	-	0.00059	(25)	0.00044	(2)	0.00040	(1)	0.00034	(2)	0.00086	(51)
T8 + 2% Ti	1280	FMQ + 0.1	0.076	(5)	46.27	(22)	1.2E-03	(5)	0.00121	(3)	-	-	0.00071	(16)	0.00039	(2)	0.00097	(53)	0.00026	(2)	0.00048	(35)
T8 + 3% Ti	1280	FMQ + 0.1	0.06	(1)	331.21	(115)	-	-	0.00042	(1)	-	-	0.000362	(5)	0.000082	(3)	0.000016	(3)	0.00003	(4)	0.00002	(1)
	Ilm/melt																					
FT1+10%	1100	IW - 1.8	4.7	(9)	12.0	(23)	0.89	(29)	1.46	(23)	5.91	(85)	0.76	(16)	1.72	(33)	0.96	(73)	0.08	(2)	0.05	(1)
	Ttn/melt																					
FT1+20%	1100	IW - 1.8	3.7	(8)	5.11	(1)	0.83	(2)	1.08	(9)	6.96	(20)	1.52	(2)	4.67	(7)	0.185	(3)	0.32	(3)	0.30	(3)

Standard deviation is given as 1σ of the mean value, with only the last significant number rounded up showed in parenthesis. For the exact value obtained for each partition coefficient and standard deviation please download the spreadsheet available online. Abbreviations according to Whitney and Evans (2010) - Ol: olivine; Cpx: Clinopyroxene, Opx: Orthopyroxene, Chr: Chromite, Arm: Armalcolite, Spl: Al-Spinel, An: Anorthite, Ttn: Titanite, Ilm: Ilmenite. *For partition coefficients of the rare-earth elements (REE) between crystal and silicate melt in these two experiments please see the Supplementary Material

The mineral/melt partition coefficients of Mo and W show a marked difference in experiments carried out under reducing conditions when compared to oxidizing conditions (Fig. 3.6a,b). At ca. IW-1.8, $D_{Mo}^{cpx/melt}$ and $D_{W}^{cpx/melt}$ show a fairly constant increase from 0.06 to 0.29 and 0.001 to 0.008, respectively, with increasing TiO_2 in the silicate glass from 0 to 2.5 wt. % TiO_2, from which point they become relatively constant at higher TiO_2 contents of the melt. The observed behavior of Mo and W with TiO_2 content of the melt is also mirrored in the ol/melt and opx/melt systems, which will be detailed below.

Orthopyroxene/melt partition coefficients for heterovalent elements are generally lower than $D_{M}^{cpx/melt}$. Values for $D_{M}^{opx/melt}$ do not show any clear correlation with the TiO_2 content in the silicate melt at oxidized experiments. $D_{Ti}^{opx/melt}$ increases from oxidized to reduced experiments with minimum and maximum values from 0.05 to 0.12. At IW -1.5 or lower, $D_{Cr}^{opx/melt}$ decrease from 8.7 (low-Ti) to 1.0 (high-Ti). $D_{Mo}^{opx/melt}$ and $D_{W}^{opx/melt}$ are shown to increase from 0.7 to 2.7 and from 0.0036 to 0.014 and mirror the same positive correlation observed for the cpx/melt experiments. Uranium partitioning between opx and silicate melt is shown to be insensitive to the TiO_2 in the silicate glass. However, $D_{U}^{opx/melt}$ changes with fO_2, with maximum value of 0.0009 at the more reduced experiments and minimum of 2 x 10^5 under oxidizing conditions. Olivine/melt partition coefficients for the heterovalent elements do not show any clear dependence on the TiO_2 content of the silicate melt, with the exception of $D_{Cr}^{ol/melt}$. Like with cpx and opx, changes in oxygen fugacity are shown to affect the $D_{M}^{ol/melt}$. $D_{Ti}^{ol/melt}$ shows only a small difference from reducing to oxidizing conditions, with maximum and minimum values ranging from 0.015 to 0.004. The partitioning of Cr between olivine and silicate melt for the more reduced experiments (IW -1.5 or lower) decreases slightly from 2.1 at low-Ti to 1.1 at ca. 5 wt. % TiO_2 in

the glass, after which they remain constant. Olivine crystals from Cr-rich liquids at FMQ have an average value of $D_{Cr}^{ol/melt} = 0.7$, slightly lower than in Cr-poor experiments at all conditions of oxygen fugacities. In Cr-poor experiments, Cr behaves as a compatible element, with an average value of $D_{Cr}^{ol/melt} = 1.2$. Molybdenum, W and U are incompatible elements in olivine over the entire range of fO_2 and TiO_2 in this study. However, as in the case of opx and cpx-bearing experiments, $D_{Mo}^{ol/melt}$, $D_{W}^{ol/melt}$ and $D_{U}^{ol/melt}$ show a substantial difference between experiments carried out under oxidizing conditions and those at reducing conditions (Fig. 3.6g-i). At fO_2 larger than FMQ, $D_{Mo}^{ol/melt}$, $D_{W}^{ol/melt}$ and $D_{U}^{ol/melt}$ are constant regardless of TiO_2 content, with average values of 0.007 and 3.5 x 10^{-5} and 2.2 x 10^{-6}, respectively. At reducing conditions (i.e., around IW-1.8), $D_{Mo}^{ol/melt}$, $D_{W}^{ol/melt}$ and $D_{U}^{ol/melt}$ are TiO_2 insensitive, but higher than in the oxidized experiments, with average values of 0.55, 0.0047 and 1.2 x 10^{-5}, respectively.

The partitioning of Ti, Cr, Mo, W and U between plagioclase and silicate melt seems to be insensitive to the TiO_2 content in the silicate glass, although the experimental dataset for this phase is restricted. In contrast, experiments under oxidizing conditions (i.e., air) show differences in the vaue of $D_{M}^{an/melt}$ for the heterovalent elements, with the exception of Ti, with $D_{Ti}^{an/melt}$ exhibiting a constant value of ca. 0.03 over the entire range of TiO_2 in the silicate glass. Chromium has a higher $D_{Cr}^{an/melt}$ value (0.10) for the oxidized experiment (T8+20 % TiO_2) when compared to the experiments performed at ca. FMQ, at which $D_{Cr}^{an/melt}$ is about an order of magnitude lower. Only two experiments, performed at FMQ, yielded $D_{Mo}^{an/melt}$ values (0.0028 and 0.0042). Because Mo is highly volatile in air (Schryer and Walberg, 1966), no data were obtained for fO_2 more oxidized than FMQ.

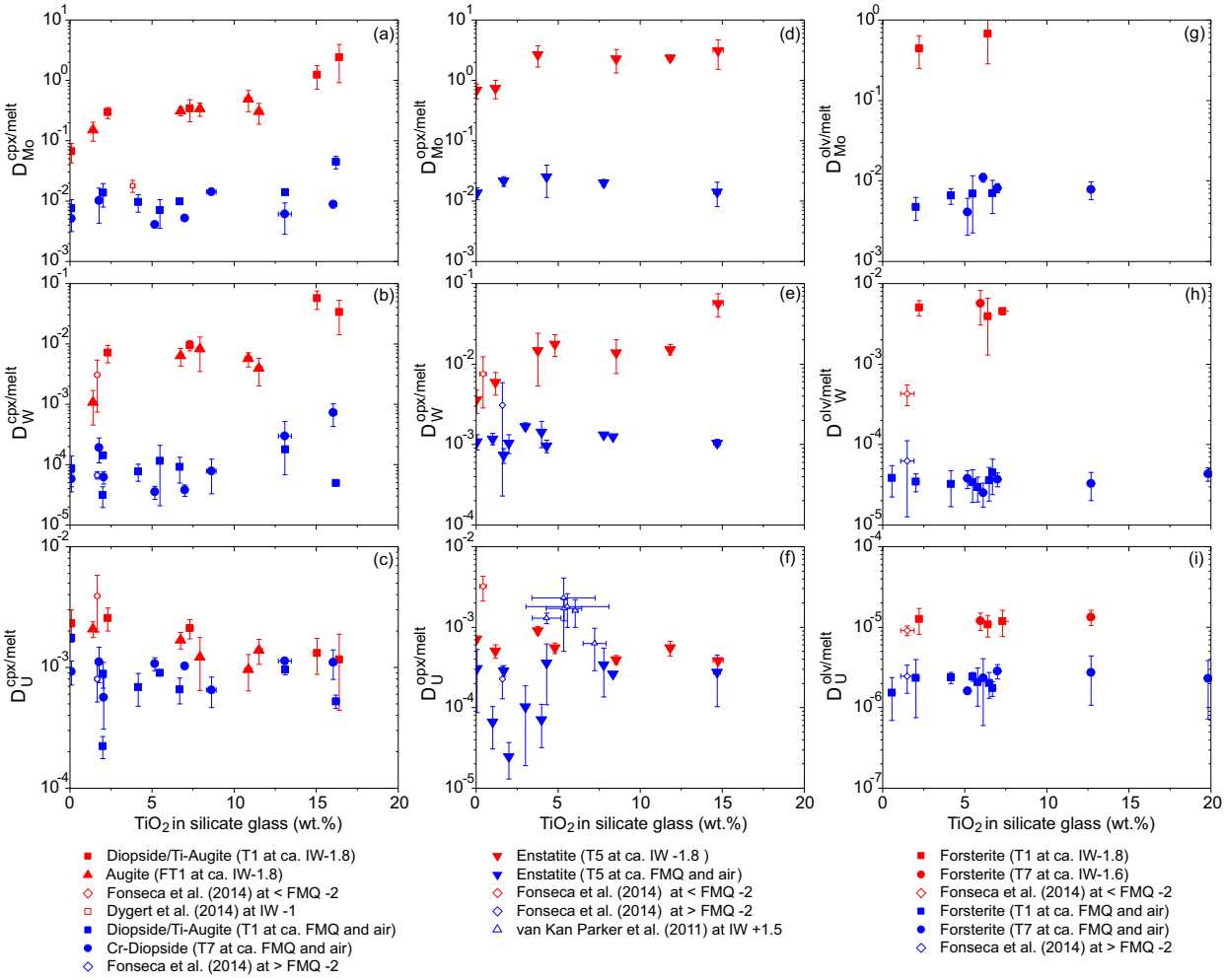

Figure 3.6: Crystal/silicate melt partition coefficients for heterovalent elements plotted against TiO_2 in the silicate glass. Experiments depicted here were conducted at different oxygen fugacities (see text and legend for details). (a) $D^{cpx/melt}_{Mo}$, (b) $D^{cpx/melt}_{W}$, (c) $D^{cpx/melt}_{U}$, (d) $D^{opx/melt}_{Mo}$, (e) $D^{opx/melt}_{W}$, (f) $D^{opx/melt}_{U}$, (g) $D^{ol/melt}_{Mo}$, (h) $D^{ol/melt}_{W}$ and (i) $D^{ol/melt}_{U}$. Error bars are 1σ of the standard deviation. Literature data are taken from average values at specific intervals of oxygen fugacity for Mallmann and O'Neill (2009) and Fonseca et al. (2014); and absolute values for van Kan Parker et al. (2011b) and Dygert et al. (2013).

At the range of oxygen fugacities (FMQ and air) of the plagioclase experiments, $D^{an/melt}_{W}$ and $D^{an/melt}_{U}$ do not significantly change, with average values of 8.2 x 10^{-5} and 4.0 x 10^{-5}, respectively. Chromium and Mo are shown to be compatible in titanite, with $D^{ttn/melt}_{Cr}$ and $D^{ttn/melt}_{Mo}$ of 5.11 and

6.96, respectively. On the other hand, W and and U are slightly incompatible in titanite, with $D_W^{ttn/melt}$ and $D_U^{ttn/melt}$ of 0.18 and 0.30, respectively.

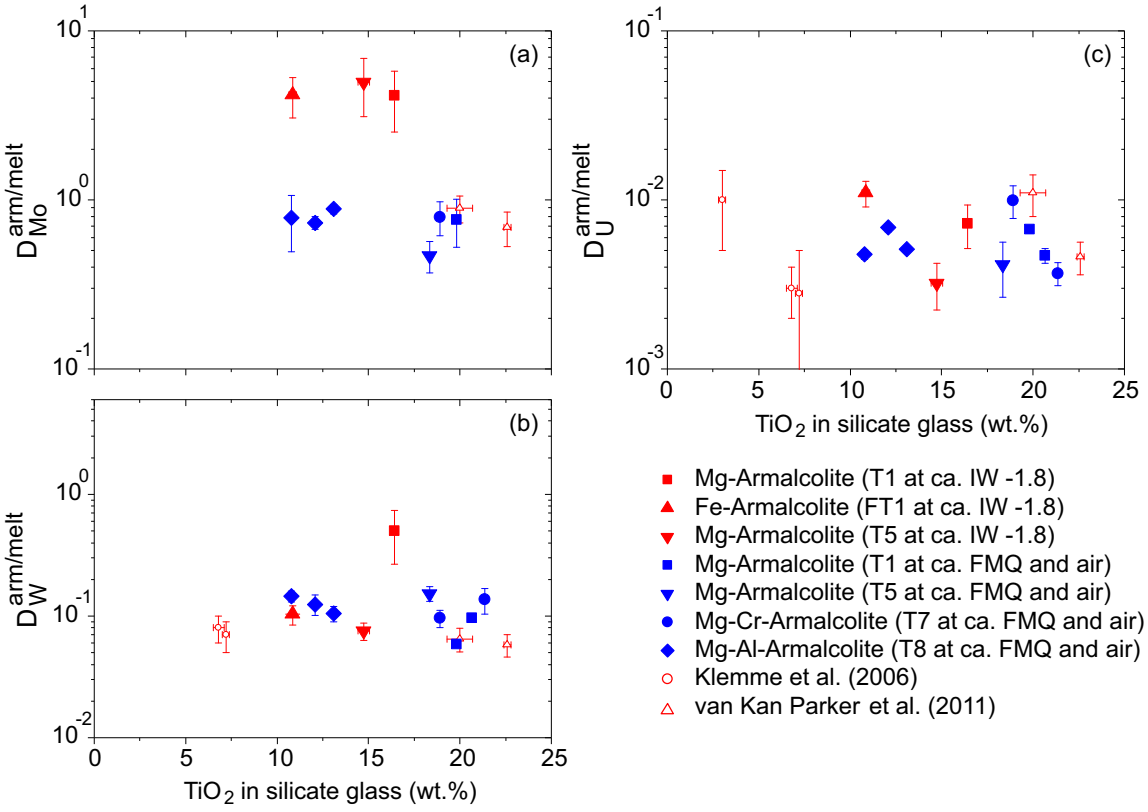

Figure 3.7: Partition coefficients for heterovalent elements between armalcolite and silicate glass plotted against TiO_2 in the silicate glass. Experiments depicted here were conducted at different oxygen fugacities (see text and legend for details). (a) $D_{Mo}^{arm/melt}$, (b) $D_W^{arm/melt}$ and (c) $D_U^{arm/melt}$. Error bars are 1σ of the standard deviation. Literature data are taken from Klemme et al. (2006) and van Kan Parker et al. (2011).

No clear correlation between TiO_2 in the silicate glass with either $D_M^{arm/melt}$ or $D_M^{spl/melt}$ for heterovalent elements was observed. Chromium is strongly compatible with all types of armalcolite, but shows lower values in reduced experiments ($D_{Cr}^{arm/melt} = 5$ to 15) than in their oxidized counterparts ($D_{Cr}^{arm/melt} = 31$ to 75). The behavior of Mo ranges from being highly compatible in armalcolite under reducing conditions to slightly incompatible at

more oxidizing conditions, with $D_{Mo}^{arm/melt}$ ranging from ca. 5 to 0.5 (Fig. 3.7a). Mg-rich armalcolite at IW -1.6 has the highest value of $D_{W}^{arm/melt}$ = 0.5, while the addition of Fe, Cr or Al into the mineral structure do not seem to affect the $D_{W}^{arm/melt}$, which has an average value of 0.1 (Fig. 3.7b). Uranium behaves as an incompatible element in armalcolite and its partitioning is insensitive to changes in fO_2, with $D_{U}^{arm/melt}$ averaging at about 0.007 (Fig. 3.7c).

3.5 Discussion

3.5.1 The effect of melt TiO_2 contents on the partitioning of the HFSE between silicates, armalcolite and lunar basaltic melts

Few studies have reported HFSE partitioning data that reect realistic compositions for lunar mare basalts (Dygert et al., 2013; van Kan Parker et al., 2011,b), i.e. accounting for the extreme TiO_2 enrichment in some of these rocks. Owing to the importance that Fe-Ti-rich oxides might have in affecting the behavior of the HFSE during partial melting (e.g., Münker, 2010; Dygert et al., 2013), it is not surprising that most studies have focused their efforts on these phases. However, there is a paucity of data pertaining to how the TiO_2 content of a silicate melt affects the partitioning behavior of the HFSE, Mo, W, U and Th between the more abundant silicate phases and silicate melts. As Longhi et al. (1978)first pointed out, it is not ideal to extrapolate partition coefficients obtained for a specific system to another with a different melt composition, given the fact that trace elements may be affected similarly as $D_{Fe-Mg}^{ol/melt}$ between low-Ti to high-Ti basalts. Within this framework, O'Neill and Eggins (2002) demonstrated

that the partition coefficient has to be affected by changes in temperature (as well as pressure), crystal chemistry (the "stoichiometric control") and, most importantly, by changes in the activity coefficient of a given trace element oxide species in the crystal and in the melt. The formation of melt complexes involving a major element and the trace element of interest in the melt will change the activity coefficient of the trace element, therefore it will affect its overall partitioning behavior. Such phenomena have been since demonstrated. For example, Dygert et al. (2013) have shown that $D_{HFSE}^{ilm/melt}$ decreases from low-Ti magmas to ca. 6 wt. % TiO_2 in the silicate melt, which may be explained by the association between HFSE and Fe-Ti-O complexes present in the melt that results in lower activity coefficients of the HFSE melt species and, consequently, the $D_{HFSE}^{crystal/melt}$. Of all the major silicate phases present in the lunar mantle, olivine has the largest potential for investigating whether or not the possible interactions between the HFSE and TiO_2 in the silicate melt affects their partitioning behavior. The reason is simple: olivine accepts only limited Ti in its structure, as such, any change in $D_{HFSE}^{ol/melt}$ has to be a result of a melt compositional effect. From our results, the observed drop in $D_{Hf,Ta}^{ol/melt}$ (Fig. 3.4) appears to validate this expectation, as values become lower from 0 to ca. 5 wt. % TiO_2 in the melt, in similar fashion to the observed by Dygert et al. (2013) for $D_{HFSE}^{ilm/melt}$. Since olivine in our experiments crystallized from a Fe-poor liquid ($FeO_t <$ 0.5 wt. %) it can speculated that this melt component may also be formed with a structure akin to magnesium titanates, such as $MgTi_2O_5$ or $MgTiO_3$. The reason why such an effect is only noticeable at low TiO_2 in the melt can be that at higher TiO_2 contents the silicate melt is not structurally affected by further addition of titanium (Dygert et al., 2013).

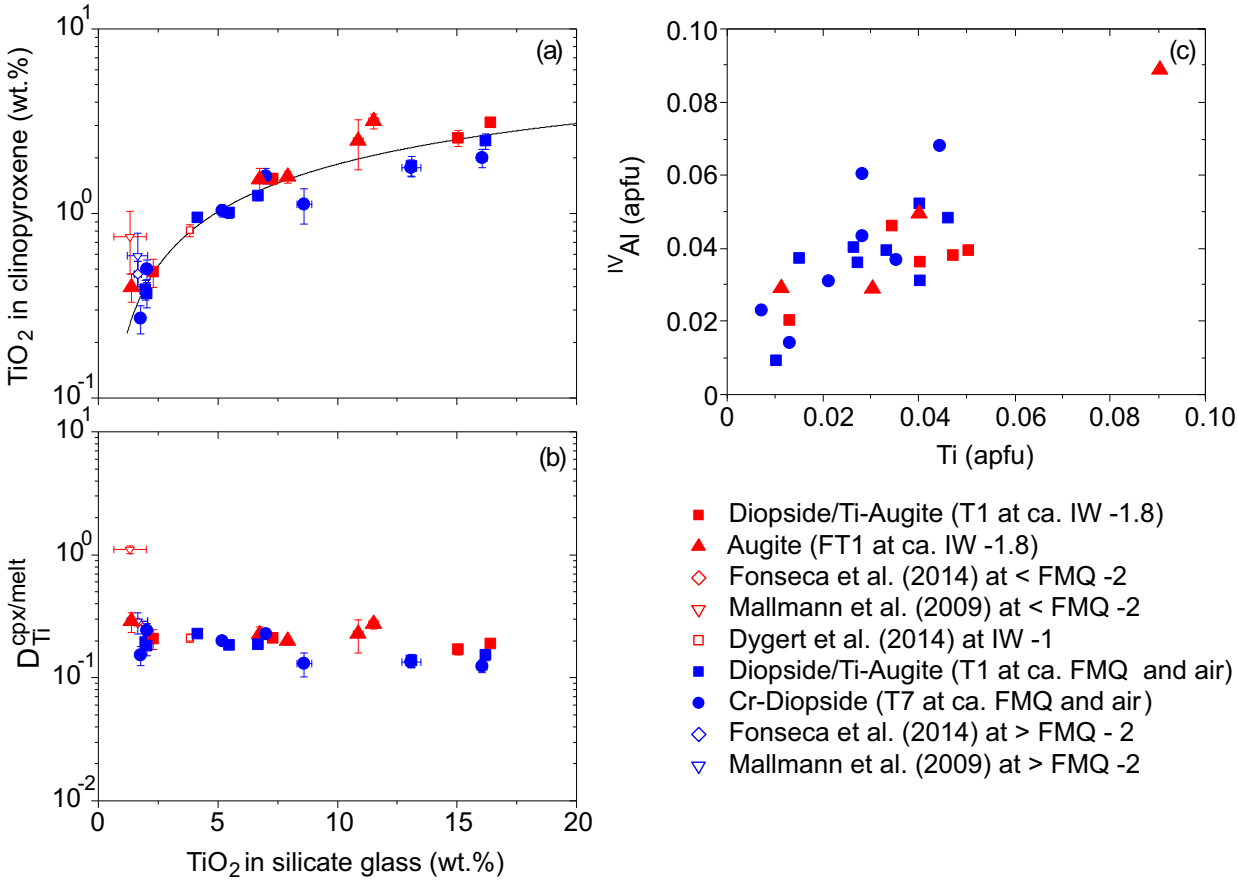

Figure 3.8: (a) TiO_2 content in the cpx (wt. %) plotted against the TiO_2 in the silicate melt (wt. %). (b) $D_{Ti}^{cpx/melt}$ plotted against the TiO_2 in the silicate melt (wt. %). Error bars are 1σ of the standard deviation. Literature data are average values at a specific interval of oxygen fugacity from Fonseca et al. (2014), Mallmann and O'Neill (2009) and Dygert et al. (2014). (c) ^{IV}Al (atoms per formular unit apfu) plotted against Ti (apfu) in the M1 site of cpx.

Interestingly, $D_{HFSE}^{opx/melt}$ appears to be insensitive to the TiO_2 content in the silicate glass, in agreement to the work of van Kan Parker et al. (2011b). One reason for this is that the solubility of TiO_2 in orthopyroxene (up to 1.4 wt. %) when compared to the olivine (up to 0.11 wt. %). Alternatively, this could be the result of different degrees of melt polymerization between compositions that yielded cpx and olivine (more depolymerized), and those that yielded opx (more polymerized). The near constant $D_{HFSE}^{opx/melt}$ could

indicate that in more polymerized liquids the formation of melt species involving both Ti and the HFSE is more difficult. However, this is unlikely as opx-bearing compositions only have slightly lower NBO/T (ca. 0.8) compared to ol- and cpx-bearing ones (greater than 1.0), not reaching values of less than 0.5, where the shift in partition coefficient values due to melt polymerization is expected to happen (cf., Gaetani, 2004). Nevertheless, the data for opx, specially for $D_{Th}^{opx/melt}$, shows an improvement in contrast to the literature (Fig. 3.3 and 3.6), with relatively more precise values for $D_{HFSE}^{opx/melt}$ when compared to the work of Mallmann and O'Neill (2009), van Kan Parker et al. (2011b), and Fonseca et al. (2014). This can be attributed to the larger crystal size (greater than 100 μm) obtained in our experiments, when compared to what is reported in the literature. It is also possible that melt inclusion "contamination", ubiquitous in experimental works, may have occurred in previous studies, which even in very small proportions can lead to an overestimation of the $D_{HFSE}^{opx/melt}$.

Although the dataset is limited for plagioclase, no significant change of $D_{HFSE}^{pl/melt}$ was observed as a function of TiO_2 in the melt. The experiments, however, do not represent well the interval between 0 and 5 wt. % TiO_2, where melt complexation with Ti is thought to significantly affect trace element partitioning behavior. The data for Zr, Hf, Nb and Ta in the present study show lower values of $D_{HFSE}^{an/melt}$ (10^3 to 10^4), compared to de Vries et al. (2012), Tepley et al. (2010), and Fonseca et al. (2014), who reported values between 10^2 to 10^3. A possible explanation is the large size of crystals obtained in this study, which allowed avoiding the incorporation of melt inclusions during LA-ICP-MS. Another likely explanation is the high An# content of plagioclase crystals, which typically display lower $D_M^{pl/melt}$ for most trace elements than more albite-rich plagioclase (e.g., Bindeman and Davis, 2000; Tepley et al., 2010). Nevertheless, it is worth pointing out that

lunar plagioclases from mare basalts are Na-poor, presumably because the crystallization of the lunar anorthositic crust removed the bulk of the Na_2O content of the lunar magma ocean (Shearer et al., 2006; Crawford, 1976).

Clinopyroxene, being the major silicate phase in the lunar mantle most accepting Ti in its structure, shows a strong negative correlation between $D_{HFSE}^{cpx/melt}$ and melt TiO_2 (Fig. 3.2 and 3.5). Major changes in crystal chemistry in cpx make it almost impossible to disentangle the effects of crystal chemistry and/or melt composition. Therefore, a detailed explanation for this specific phase and a comparison with literature data is presented in the following section. Relative to elemental ratios fractionation between olivine, pyroxenes, armalcolite and silicate melt, only those involving W at more reduced conditions (i.e. ca. IW -1.8) are affected by the TiO_2 content in the melt, while Nb/Ta, Zr/Hf and U/Th are constant within error (Supplementary Material).

Regarding the partitioning behavior of the HFSE between armalcolite and silicate melt, the studies of Klemme et al. (2006), van Kan Parker et al. (2011), and Dygert et al. (2013) cover the entire range of compositions for lunar armalcolites, thus allowing a direct comparison between our data and those reported in these studies. Klemme et al. (2006) stabilized armalcolite at relatively low melt (3.0 wt. %), albeit with SiO_2 contents as high as 68 wt. %, which is considerably higher than observed in basalts. The $D_{HFSE}^{arm/melt}$ for Fe-rich armalcolite is in good agreement with the data of van Kan Parker et al. (2011) and Dygert et al. (2013), with the exception of $D_{Mo}^{arm/melt}$, which can be explained by the more reduced conditions achieved in our work (IW -1.8) when compared to the ΔIW +1.5 imposed by graphite-lined Pt capsules in the work of van Kan Parker et al. (2011). Considering only the data for Fe-rich armalcolite from our experiments and those found in the literature, it is possible to observe a slightly negative trend between $D_{HFSE}^{arm/melt}$

and $D_{Cr}^{arm/melt}$, and the TiO_2 in the silicate melt (Figs. 3.5 and 3.7), with the exception of $D_{Th}^{arm/melt}$, which appears to increase with TiO_2 content of the melt. The partition coefficients for Zr, Hf, Nb and Ta between Mg-rich armalcolite and silicate melt are higher in our experiments than previously reported in the literature. This can be explained by the fact that without Fe or Ti^{3+}, there are more sites for the HFSE to enter into the crystal structure, which deserves further attention, even though iron-free armalcolites are not realistic for lunar mantle conditions, which have Mg# between 60 and 70 (e.g., Haggerty, 1973; Thacker et al., 2009).

3.5.2 The effect of pyroxene crystal chemistry on the behaviour of trace elements in lunar basaltic melts

Clinopyroxene shows the highest $D_{Ti}^{cpx/melt}$ values among the major lunar mantle silicate phases (i.e. opx, olivine, pigeonite and plagioclase). Unsurprisingly, cpx is the silicate phase that most accepts Ti into its structure, with TiO_2 contents up to 3 wt. %, proportional to the TiO_2 in the silicate melt (Fig. 3.8a). Titanium clinopyroxene/melt partition coefficients are constant, regardless of the TiO_2 content of the silicate melt, which indicates that this element does not deviate from Henry's law behavior even for TiO_2 concentrations in silicate melt as high as 20 wt. % (Fig. 3.8b).

Titanium, as well as the HFSE, substitutes mainly into the M1 site of the cpx. The charge balance mechanism associated with this substitution is the exchange between $^{M1}Ti^{4+}$ by $2Al^{3+}$, as already noted for lunar pyroxenes by Papike (2005). Experimental results of this study showed that from 8.0 wt. % TiO_2 (Fig. 3.8a) in the silicate melt, a cation deficiency in the tetrahedrally coordinated site of cpx develops, as Si and Al are insufficient to maintain charge balance in that site. This charge imbalance is resolved with

the introduction of Ti in tetrahedral coordination. However, because Ti has a much higher ionic radius than Si, only a relative small amount of Ti atoms are allowed into the tetrahedral site. The strong negative correlation of $D_{HFSE}^{cpx/melt}$ with TiO_2 content in the basaltic glass (Fig. 3.2) is also explained by the addition of Ti into the M1 site of the cpx. To better constrain this mechanism, we applied the lattice strain model of Blundy and Wood (1994). Since no major crystal chemistry changes were observed for olivine and opx, we refer to the lattice strain fitting parameters for tetravalent elements into these phases reported by Fonseca et al. (2014). The slightly lower $D_{Mo,W}^{opx/melt}$ at reduced conditions (ca. IW1.8) in low-Ti experiments (up to 2 wt. % TiO_2) compared to high-Ti experiments can be explained by the fact that W and Mo may compete with Ti for sites in the silicate melt. This process would lead to an increase in the activity coefficient of Mo and W at higher melt TiO_2 (O'Neill et al., 2008). In the case of olivine, the high $D_{Mo}^{ol/melt}$ of ca. 0.6 observed at the most reduced experiments can be used to indirectly determine that Mo^{4+} is predominant at IW-1.8. The parabola constrained for rare-earth elements and other trivalent cations substituting into olivine is much less stiff than the one for tetravalent cations, indicating that the global partition coefficient of Mo should be lower if Mo^{3+} was dominant (see Supplementary Material). The HFSE and Mo substitute into the M1 site of clinopyroxene in VI-fold coordination and, as such, should be affected by the substitution of Ti into the same site. It is then interesting to verify in what way the different lattice strain parameters change over the range of TiO_2 contents in the silicate melt. To that effect, $D_{HFSE-Mo}^{cpx/melt}$ derived over a range of silicate melt TiO_2 contents, were fitted to the Lattice Strain Model(Brice, 1975; Blundy and Wood, 1994) using non-linear least squares regression through direct weighing of the error. Four fits were produced, at 2, 5, 10 and 20 wt. % silicate melt TiO_2, and the results of

each fit were excellent as shown by the very small chi-nu squared values associated with each fit (Table 3.4). Ionic radii were taken from Shannon (1976). Tetravalent cations entering the M2 site (U^{4+} and Th^{4+}) or pentavalent cations entering the M1 site (Nb and Ta) were not constrained by the model because insufficient data were available to constrain the lattice strain functions for those sites and valences in any meaningful fashion. Partitioning data derived for experiments at 2, 5, 10 and 20 wt. % TiO_2 were fitted to Lattice Strain Model equation, the results of which are depicted in Fig. 3.9. From these parabolas, it becomes clear that the M1 site lattice strain parameters change with increasing TiO_2 content in the silicate glass (Fig. 3.9). As TiO_2 contents in the silicate glass increase, so do D_0 and the Young's modulus of the M1 site, which increase exponentially after ca. 7 wt. % TiO_2 in the glass (Figs. 3.9b,c). Molybdenum is known to change its oxidation state from Mo^{4+} to Mo^{6+} in magmatic systems (e.g., Holzheid et al., 1994; O'Neill and Eggins, 2002). Our fit assume that, at the most reduced experiments, Mo is present entirely as Mo^{4+}, in agreement with the findings of Danielson et al. (2011) who stated that only below IW -2 does Mo^{3+} become significant. In our experiments, Mo has an ionic radius close to the ideal r_0 at all TiO_2 contents, indicating that it is likely to be mainly present as Mo^{4+} at ca. IW1.8, in agreement with the recent observations made by Righter et al. (2016). The changes observed in the parameters of the lattice site (Fig. 3.9) mean that Mo^{4+} in VI-fold coordination, which has a $r_i \approx r_0$ will substitute more easily into the M1 site of cpx. However, because E also increases as a result of the site elasticity becoming stiffer (Fig. 3.9c), the M1 site of cpx becomes less likely to incorporate Zr and Hf, whose partition coefficients between cpx and silicate melt decrease (Fig. 3.2 and 3.9a) with increasing bulk TiO_2.

Table 3.4: Results for non-linear least squares fitting of the cpx/melt partitioning data for Ti^{4+}, Zr^{4+}, Hf^{4+} and Mo^{4+} (M1 - VI fold coordination) to the Lattice Strain Model.

Experiment	Temp. (° C)	Δ IW	r_0	σ	E (GPa)	σ	D_0	σ	X_v^{2*}
T1 + 2% Ti	1300	-1.6	0.6386	0.0002	1960	34	0.309	0.001	1.3E-08
T1 + 5% Ti	1290	-1.7	0.6408	0.0004	2265	61	0.354	0.002	1.1E-07
T1 + 10% Ti	1250	-1.6	0.6504	0.0004	5350	89	1.235	0.002	1.6E-08
T1 + 20% Ti	1250	-1.6	0.6507	0.0006	6806	142	2.419	0.008	6.8E-08

*Reduced chi-nu square calculated based on direct weighing of the error

From the fit we can predict the partition coefficient of any 4+ cation entering the M1 site of cpx. This is especially important for those heterovalent cations that exhibit more than one oxidation state at the conditions in which the experiments were carried out - i.e. W. For example, Fonseca et al. (2014) showed that even a small amount of W^{4+} is enough to change the overall compatibility of these elements into cpx, opx and olivine at reduced conditions. Given that $D_W^{cpx/melt}$ increases with TiO_2 content of silicate melt, it is important to assess whether this increase may also be due to the presence of a higher proportion of W^{4+} in the bulk W content of the system. For example, O'Neill and Eggins (2002) have shown that the association between CaO and MoO_3 in silicate melt leads to a shift in the Mo^{4+}-Mo^{6+} transition to lower fO_2. Given this observation, it is entirely within the realm of possibility that a similar shift in the W^{4+}-W^{6+} transition takes place as a result of the association between TiO_2 and W oxides species in silicate melt. A clinopyroxene/melt partition coefficient at fixed fO_2 for the fictive W^{4+} cation can be calculated from the fitted lattice strain parameters based on the ionic radius of W^{4+} in VI-fold coordination (0.66 $\mathring{A}$) (Fig. 3.9), using a simple mass balance equation, as follows:

$$\begin{aligned} D_{W_{measured}}^{cpx/melt} = & D_{W^{6+}}^{cpx/melt} \ (X_{W^{6+}}/(X_{W^{4+}} + X_{W^{6+}})) \\ & + D_{W^{4+}}^{cpx/melt} \ (X_{W^{4+}}/(X_{W^{4+}} + X_{W^{6+}})) \end{aligned} \tag{3.1}$$

Where X_M is the atomic fraction of each W cation. Based on the knowledge that W is exclusively hexavalent at fO_2 higher than FMQ, and that $D_{W^{6+}}^{cpx/melt}$ is essentially zero (ca. 10^{-5}), we can simplify equation (3.1) to obtain the ratio between W^{4+} and W_{Total}:

$$\frac{X_{W^{4+}}}{\sum W} = D_{W_{measured}}^{cpx/melt} / D_{W^{4+}}^{cpx/melt} \tag{3.2}$$

Using equation (3.2) combined with the $D_{W^{4+}}^{cpx/melt}$ values obtained for each interval of TiO_2 content in the silicate melt and estimated from the fits of the lattice strain model, we can calculate the overall ratio between the two oxidation states of W. Low-Ti basalts (from 0 to 7 wt. % TiO_2) have a constant ratio W^{4+}/W_{Total} of 0.0003, while the same ratio for high-Ti basalts (T1+10 % and 20 % TiO_2) decrease to 0.00015 and 2.31 x 10^5, respectively, according to what was observed from the lattice site parameters. On the basis of different W^{4+}/W_{Total} values with increasing TiO_2 in the silicate glass, we hypothesize that the bulk Ti content of the system may affect the redox transition of W^{4+} to W^{6+} shifting it to lower fO_2, which deserves to be further investigated. However, as can be seen from the discussion above, the competing effects responsible for changes in the partitioning of trace elements between minerals and melts are extremely difficult to deconvolute even in simplified systems.

Literature data for $D_{HFSE}^{cpx/melt}$ shows that the ^{IV}Al content affects the compatibility of the REE and HFSE, by facilitating their substitution through a charge balance mechanism (see Hill et al., 2000; Dygert et al., 2014). The bulk Al introduced in the cpx lattice is essentially being used to balance the substitution of Ti^{4+} into the M1 site. Given that lunar pyroxenes are Al-poor, there is little tetrahedrally-coordinated Al left to balance the substitution of other tetravalent cations, like Th and U^{4+}, as well as the

HFSE. Therefore $D_{Th}^{cpx/melt}$ and melt TiO_2 (Fig. 3.2) are negatively correlated. $D_{U^{4+}}^{cpx/melt}$ also show a negative but less pronounced correlation with TiO_2, which may be due to some U^{6+} still being present at the most reduced experiments, at ca. IW -1.8.

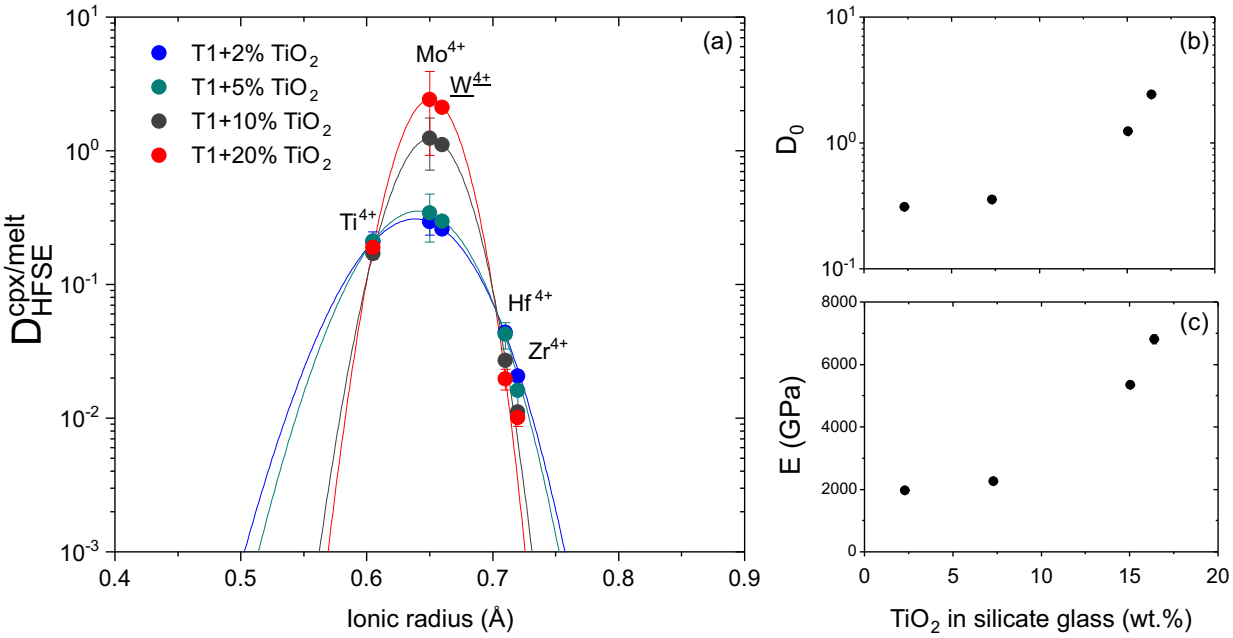

Figure 3.9: (a) Observed cpx/melt partition coefficients for Ti^{4+}, Mo^{4+}, Hf^{4+} and Zr^{4+} cations entering the M1 site of clinopyroxene plotted against ionic radius in VI-fold coordination. Ionic radii taken from Shannon (1976) with uncertainty of 0.05 $\AA$. The LevenbergMarquardt algorithm was used to adjust the parameters for the minimum chi-square values, based on direct weighing of the error. Lines represent least-squares fits of the data as a function of TiO_2 in the melt to the equation of Blundy and Wood (1994). Error bars are 1σ of the standard deviation. The predicted partition coefficient for W^{4+} is also shown with open symbols, since it was not measured but actually estimated from the lattice strain fit. Crystal lattice parameters are obtained through the fitting of the lattice strain model to different TiO_2 contents in the silicate glass (b) D_0 ;(c) E (GPa).

Taking this fact into account, the differences observed between our results and those of Dygert et al. (2014) can be reconciled. In another study, Bennet et al. (2004) performed experiments in the NCMAS system and

concluded that the introduction of Na into clinopyroxene led to an increase in $D^{cpx/melt}_{REE,HFSE}$. The same authors performed one experiment enriched in TiO_2 (6 wt. %) but did not note any difference from the CMAS system, although their conclusion is based on only one experiment with much higher Al_2O_3 both in cpx and silicate glass. The TiO_2 content in Fe-free cpx of Bennet et al. (2004) is ca. 4 wt. %, with 6.8 wt. % in the glass. Given that their experiments were done with more Al_2O_3 than achieved by experiments reported in this study, it is clear that the amount of ^{IV}Al facilitates the substitution of Ti and the HFSE into the M1 site of cpx, due to an increase in the net charge of the site (Hill et al., 2000). Mollo et al. (2013) also observed that $D^{cpx/melt}_{Ti}$ are strongly affected by the content of tetrahedrally coordinated Al in this mineral structure. Therefore, since most of the experiments show only a narrow range of variation in ^{IV}Al (Fig. 3.8c), it is not surprising that $D^{cpx/melt}_{Ti}$ are constant (Fig. 3.8b). The introduction of large amounts of Ti causes a distortion in the cpx crystal structure, manifested in higher values of E (Fig. 3.9c). The same is expected to occur in lunar pyroxenes, which are generally Al-poor (Papike, 2005). Nevertheless, seeded experiments which show higher ^{IV}Al also have generally higher $D^{cpx/melt}_{HFSE}$ that are well in agreement with the data of Mollo et al. (2013).

3.5.3 Partial melting of the LMO cumulates and generation of lunar mare basalts

The ^{182}Hf-^{182}W decay system has been widely applied to date core formation processes in planetary bodies (e.g., Kleine et al., 2002; Schoenberg et al., 2002). The application of the Hf-W system to date the differentiation of planetary bodies like the Moon and the Earth requires knowledge about the bulk Hf/W values of their silicate portion. To apply this system to the

Moon, the Hf/W ratio of the lunar mantle is calculated by using average mare basalt values for U/W or Th/W and chondritic Hf/Th or Hf/U, assuming that U, Th, and W behave similarly during partial melting (e.g., Palme and Rammensee, 1981; Righter and Shearer, 2003; Touboul et al., 2007; Münker, 2010). This assumption is seemingly supported by apparently near constant U/W and Th/W in terrestrial basalts (see O'Neill and Jenner, 2012). However, recently Fonseca et al. (2014) have shown that the partitioning behavior of W and U is redox sensitive, leading to a fractionation of the two elements from one another and from the homovalent HFSE and Th during partial silicate melting on the Moon. To address this issue and to exemplify an application of the new experimental dataset of partition coefficients, we performed simple aggregate modal fractional melting models of a model lunar mantle to reproduce the trace elements pattern of low and high-Ti mare basalts. Specifically, we focus on how trace elements are affected as a function of the TiO_2 content in the silicate melt and the Fe-Ti oxide phase present in the lunar mantle.

The Lunar Magma Ocean (LMO) crystallization sequence of Snyder et al. (1992) was recreated using trace element concentrations in the bulk LMO reported by Münker (2010) and Fonseca et al. (2014), and applying the new partition coefficients reported here. The maximum TiO_2 content reached during the crystallization of the LMO is 5 wt. % and the expected fO_2 of the lunar mantle is $\approx$ IW -1.5 (e.g., Snyder et al., 1992; Papike, 2005), so only D values from experiments that reflect those conditions were used (e.g., T1 + 5% Ti – 1290 °C – IW -1.7). For simplicity we only report results on the basis of the LMO model of Snyder et al. (1992) because the models of Elkins-Tanton et al. (2002) and Elardo et al. (2011) produces only marginally different results for Th/W, Hf/W and U/W (Fonseca et al., 2014). Furthermore, recent experimental work by Rapp and Drap-

per (2013) have provided support for the theoretical LMO crystallization model of Snyder et al. (1992). The LMO sequence of Snyder et al. (1992) is divided into five solidification phases, starting with the crystallization of olivine and opx (from 0 to 78 wt. % solidified) and ending with the crystallization of pigeonite, plagioclase, cpx and ilmenite. Trapped interstitial residual liquid (TIRL) is assumed to occur in different proportions in association with the different lunar mantle cumulates (see Sprung et al., 2013). An average of the partition coefficients between crystal and silicate melt for Zr, Hf, Nb, Ta, U, Th and W obtained in experiments at IW -1.8 was used for olivine, plagioclase and opx, because these change only slightly along the entire range of melt TiO_2 investigated. As in previous studies, $D_M^{opx/melt}$ were used as a proxy for pigeonite. Because pigeonite is essentially a low Ca clinopyroxene, partition coefficients for trace elements are only slightly different than those reported for opx (e.g., Righter and Shearer, 2003; van Westrenen et al., 2000). For clinopyroxene, $D_{HFSE}^{cpx/melt}$ obtained from the run T1+10 % TiO_2 at IW 1.6 was used for the models that aimed at reproducing the ratios observed in high-Ti basalts, since this experiment has TiO_2 content similar to that of the high-Ti basalts sampled during the Apollo 11 and 17 missions. For the low-Ti basalts the model assumed $D_{HFSE}^{cpx/melt}$ from low-Ti experiments at ca. IW 1.8. Ilmenite/melt partition coefficients were an average from high-Ti experiments of Dygert et al. (2013), which resulted in better fits than when using the partitioning data of Klemme et al. (2006) and our own single datum. One of the most accepted theories for the origin of high-Ti basalts is a mixed cumulate source that results from a mantle overturn, where ilmenitebearing cumulates sink towards the center of the Moon and partially melt (e.g., Ringwood and Kesson, 1976; Hess and Parmentier, 1995; Beard et al., 1998). Based on this hypothesis, the ratios between Hf, Th, W and U of both low and high-Ti basalts from Apollo 11,

12, 15 and 17 can only be reproduced (Fig. 3.10) by assuming different amounts of TIRL and the presence of metal in all source regions (assuming $D_W^{metal/silicate}$ of 6.2 from Righter et al., 2010). Differences between aggregate modal fractional melts trends are the proportion between the lunar cumulates ol–opx (1,2), ol–pgt–pl (3), cpx–pl–pgt (4) and pgt–pl–cpx–ilm (5) in the bulk hybridized mantle source (Supplementary Tables). The values used for the plots and selected partition coefficients for the models are given in the Supplementary Material. The Lu–Hf–Sm–Nd isotopic systematics of Apollo 17 high-Ti basalts (Sprung et al., 2013) may be used to constrain the proportion between various model cumulates in the melting lunar mantle source. By doing this we estimated a source for the aggregate fractional melting model "D" (Supplementary Material), which reproduces well the Hf/W, Th/W and U/W of Apollo 17 high-Ti basalts (Fig. 3.10a,b). The assumption of a mantle source of harzburgite composition (model "H") can also reproduce the trace element ratios of lunar low-Ti mare basalts, with the presence of metal only necessary to modify the required degree of melting of the source. It is worth pointing out that the presence of residual metal in the source of mare basalts is in agreement with the reduced fO_2 condition expected for the lunar mantle (Sato, 1976; Nicholis and Rutherford, 2009; Wade and Wood, 2016) and the depletion in Ni observed for lunar olivine, specifically associated with high-Ti basalts (Karner et al., 2006). Moreover, the normally low platinum group elements (PGE) content of mare basalts (Righter et al., 2000) also indicate a source that comprises residual metal. A modelled lunar mantle source that does not consider the presence of residual metal is not able to reproduce the observed fractionation of the Hf/W observed in most high-Ti basalts (Apollo 11 and 17) through the aggregate modal fractional melting models performed in this study (e.g. model "I").

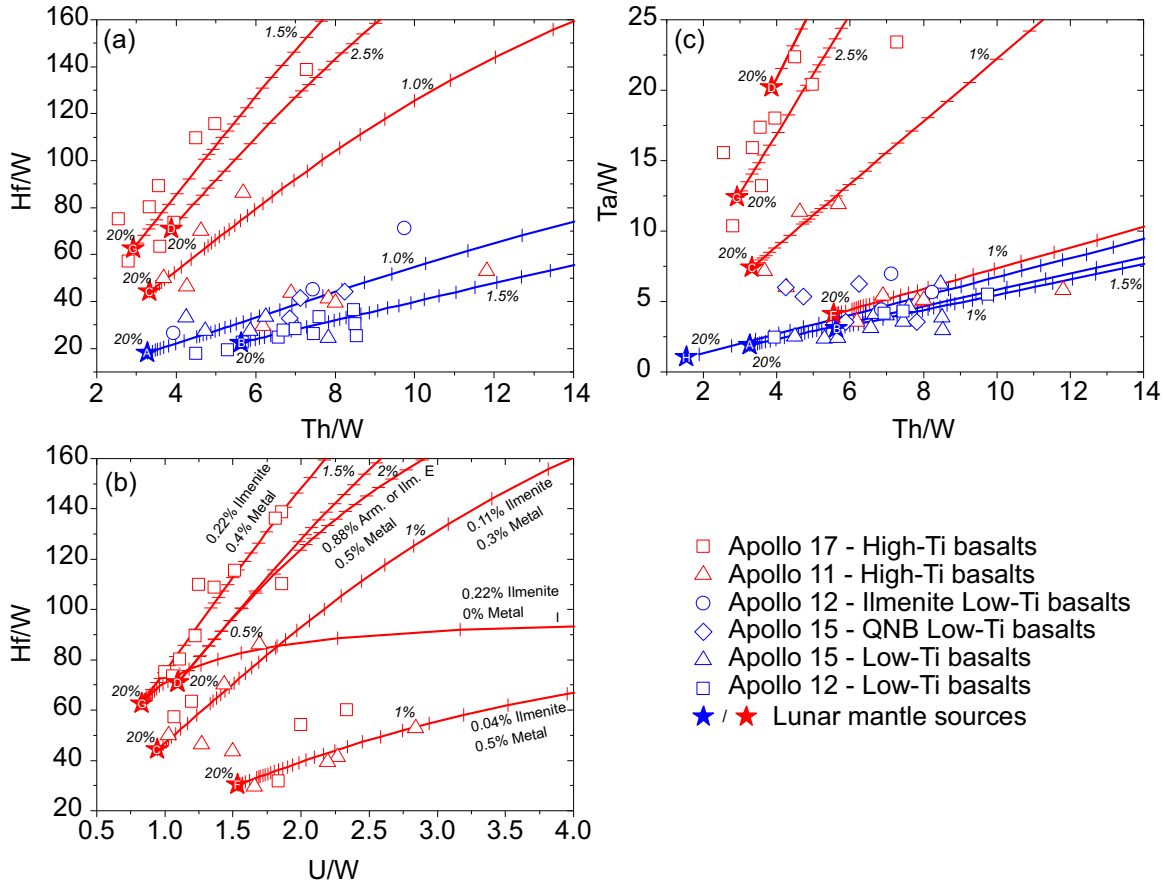

Figure 3.10: Aggregate modal fractional melting models plotted together with sampled low and high-Ti lunar mare basalts data from Apollo 11, 12, 15 and 17 missions. Lunar dataset for Hf and W acquired with isotope dilution or neutron activation method was used whenever possible (Wänke et al., 1970, 1971, 1974; Lee et al., 1997; Münker et al., 2003; Kleine et al., 2005; Münker, 2010). In the other cases, the lunar dataset for trace elements was acquired with various analytical techniques (Neal, 2001; Meyer, 2012). Modelled trends and values used for plots are given in the Supplementary Material. Trajectories indicate the composition of aggregate modal fractional melts for degrees of melting given by tick marks and indicated in %. Stars represent composition of the model mantle source. (a) Hf/W vs. Th/W; (b) Hf/W vs. U/W and (c) Ta/W vs. Th/W. Differences between aggregate modal fractional melts trends are the proportion between the lunar cumulates ol-opx (1,2), ol-pgt-pl (3), cpx-pl-pgt (4), pgt-pl-cpx-ilm (5), residual metal and trapped interstitial residual liquid (TIRL) in the bulk hybridized mantle source, which are shown in the Supplementary Material. See text for details.

The other major conclusion is that at least one Fe-Ti oxide phase must be involved in the generation of high-Ti basalts (Fig. 3.10b). The modelled trends are highly sensitive to the proportion of Fe-Ti oxide in the source, clearly illustrating the importance of this phase for the bulk HFSE in lunar melts (e.g., Münker, 2010; Dygert et al., 2013). Literature data normally consider this Fe–Ti oxide to be ilmenite, based on LMO evolution models (e.g., Hess and Parmentier, 1995; Snyder et al., 1992; Elkins-Tanton et al., 2002; Dygert et al., 2013). As more ilmenite is added to the mantle source, the higher the Hf/W and the lower the Th/W and U/W values of the modeled lunar basalts become, in agreement with the data obtained for natural mare basalts from Apollo 11 and 17 missions (Fig. 3.10a,b).

Interestingly, since all our experiments were done at one atmosphere and most with Mg-rich compositions, armalcolite was a common liquidus phase at TiO_2 contents higher than 10 wt. % in the silicate glass, in agreement with the findings of Thacker et al. (2009). Partition coefficients for W, Th and U between armalcolite and silicate melt are slightly lower than the ones observed for ilmenite (Table 3.3). To test if the presence of armalcolite at the hybridized mantle source would change the modeled trends, we replaced the modal proportion of ilmenite in the source by armalcolite, using the $D_M^{arm/melt}$ from experiment FT1 + 20 % Ti at IW 1.8. The results of this substitution are not significantly different for degrees of partial melting higher than ca. 3 %, and can be seen from model curve "E" (Fig. 3.10b). However, at partial melting degrees lower than 3 % the model using armalcolite as residual phase has less fractionated trends, with lower Hf/W, Ta/W and U/W. Reproducing the Ta/W, as well as Nb/W of high-Ti basalts proved to be especially problematic, showing an offset to higher values when compared to natural Apollo 17 samples (Fig. 3.10c - "D"). To be able to have a good fit even for the lowest Ta/W values observed in high-

Ti basalts from Apollo 17, a source that comprised a mixture of sequences 1+2 and 5 (model "G") was required (Fig. 3.10c). However, this model source is not compatible with the Hf-Nd isotope systematics of Apollo 17 high-Ti mare basalts (Sprung et al., 2013). It can be seen that when our partitioning data is combined with literature data and used to model lunar compositions, most trace element ratios can be reproduced within uncertainty. However, this is not always the case, as exemplified by the difficulty found in reproducing the Ta/W and Nb/W ratios of high-Ti basalts, when isotope-constrained modal silicate abundances are assumed. The enrichment in TiO_2 through assimilation of ilmenite-cumulates during the ascent of a low-Ti basaltic magma (e.g., Wagner and Grove, 1997; Liang and Hess, 2006) was considered unlikely by Fonseca et al. (2014), since they were not able to reproduce the Hf/W trends of Apollo 17 high-Ti basalts. Therefore, the assimilation mechanism was not considered in this study. The lack of agreement between modal fractional melting models in this study and the actual mare basalts further illustrates a greater need for high-resolution isotope dilution data for HFSE, Mo, W, Th and U in lunar samples, which would make comparison between experimental and natural datasets more robust.

3.6 Concluding remarks

Two important conclusions arise from the experimental results and the melting model carried out here. First, metal saturation in the mantle sources of mare basalts is a necessity, if W is to fractionate from the HFSE, as well as U and Th. Second, the only way to reproduce the trace element ratios of high-Ti basalts is to assume that some Fe-Ti oxide phase was present at the mantle source, as suggested previously by Dygert et al. (2013) and

in agreement with δ ^{49}Ti measurements of lunar lithologies (Millet et al., 2016). Our study has two limitations. The first is the difficult of performing LA–ICP–MS analyses of concentrations for very incompatible elements, such as U and Th in olivine, and the second is the scarcity of empirical data regarding lunar mare basalts, which may lead to a biased view of the TiO_2 contents in the Moon (cf. Giguere et al., 2000). Nevertheless, our findings in conjunction with literature data, could be applied quite reliably to the petrogenesis of lunar mare basalts and can hopefully provide a better understanding of the evolution of the Moon. Moreover, our data corroborates the hypothesis that the choice of partition coefficients between crystals and silicate melt is not trivial and that changes in oxygen fugacity and crystal/melt composition need to be taken into account (e.g., O'Neill and Eggins, 2002; Gaetani, 2004; Borisov, 2012; Dygert et al., 2013; Mallmann and O'Neill, 2013; Fonseca et al., 2014).

Chapter 4

Redox dependent behaviour of molybdenum during magmatic processes in the terrestrial and lunar mantle: Implications for the Mo/W of the bulk silicate Moon

4.1 Introduction

Molybdenum is a transition metal that has at least four known oxidation states in basaltic melts (Mo^{3+}, Mo^{4+}, Mo^{5+}, Mo^{6+}), ranging from mainly Mo6+ in terrestrial magmatism to the most reduced Mo^{3+} and even Mo^{0} during planetesimal accretion (Holzheid et al., 1994; Danielson et al., 2011; Ma et al., 2014; Hin et al., 2015; Righter et al., 2016). Carbonaceous (CI) chondrites and the Bulk Silicate Earth (BSE) have estimated Mo contents of 0.96 and 0.047 μg/g, respectively (Sims et al., 1990; Fitton, 1995; Palme and O'Neill, 2014), representing the highest total abundance amongst the refractory siderophile and chalcophile elements in the solar system (see Palme and O'Neill, 2014). Most of the interest shown in the planetary sciences for Mo

stems from its refractory behaviour during accretion processes as well as its moderately siderophile character during planetary differentiation. Because Mo may provide important constraints for core formation models, significant effort has been made on studying its partitioning behavior between metal and silicate liquids (Righter et al., 1997; Wood et al., 2006; Holzheid and Palme, 2007; Righter, 2011; Burkemper et al., 2012; Wade et al., 2012). Recent experimental studies have also shown that mass-dependent stable isotope fractionation of $\delta^{98/95}$Mo may occur as a result of high-temperature (up to 3000 °C) equilibrium between metal and silicate liquid, where the heavier isotope is incorporated preferentially into the silicate melt rather than the liquid metal (Hin et al., 2013). More recently, magmatic processes, such as crustal and hydrothermal assimilation, fractional crystallization and partial melting have also been invoked to explain observed mass-dependent Mo isotope fractionation between meteorites, terrestrial and lunar samples (e.g., Dauphas et al., 2002, 2004; Burkhardt et al., 2011, 2014; Greber et al., 2015; Bezard et al., 2016; Voegelin et al., 2016; Willbold and Elliott, 2016; Liang et al., 2017).

Surprisingly, given the obvious potential of Mo as a tracer for various high-temperature geochemical processes, only a very limited number of experimental studies have investigated the partitioning of Mo between the major silicate phases in the upper mantle of the Earth and the Moon (e.g., olivine and pyroxene) and silicate melts (e.g., Dunn and Sen, 1994; Hill et al., 2000; Adam and Green, 2006; Wijbrans et al., 2015). Among these studies, none systematically covered a broad range of oxygen fugacity conditions relevant to planetary formation. To fill this gap we carried out a series of experiments to investigate the partitioning of Mo between silicate minerals (pyroxene, olivine and plagioclase) and silicate melts as a function of composition and oxygen fugacity. Our experimental results cover a broad

range of fO_2, ranging from average expected values for terrestrial mantle reservoirs, such as mid-ocean ridge basalts (MORB – around the Fayalite–Magnetite–Quartz - FMQ - redox equilibrium), ocean island basalts (OIB – ca. FMQ +0.5), the most oxidized source (ca. FMQ +1.6) for island arc (IAB) basalts (Christie et al., 1986; Ballhaus, 1993; Eggins, 1993; Rhodes and Vollinger, 2005; Mallmann and O'Neill, 2007), and the extremely reduced conditions (about an order of magnitude below the Fe–FeO redox equilibrium - IW–1, i.e. ca. FMQ –4.5) expected for the lunar mantle (Papike, 2005; Nicholis and Rutherford, 2009).

4.2 Methods

4.2.1 Starting compositions and experimental setup

Five compositions in the CaO–MgO–Al_2O_3–SiO_2 system were prepared (see Supplementary Material). The first two compositions (WM–1 and HSM–1) were designed based on Mallmann and O'Neill (2009) and Hill et al. (2000), to produce ^{IV}Al-poor and ^{IV}Al-rich clinopyroxene crystals, respectively. The third and fourth (OPM–3 and OLM–1) were based on the average of compositions used by Mallmann and O'Neill (2013) and Evans et al. (2008), which essentially represent the first appearance of olivine (forsterite) in the subsystem forsterite-enstatite-diopside at 1400 °C. For this composition, the proportions of SiO_2, MgO and CaO were modified according to model results from the MELTS software (Gualda and Ghiorso, 2015) to achieve crystallization of orthopyroxene or olivine in equilibrium with silicate melt at set target temperatures and fO_2. To facilitate crystal growth, TiO_2 was added at ca. 5 wt. % to the opx and olivine compositional series due to its melt depolymerisation effect, which enhances crystal growth without significantly affecting the pyroxene and olivine/melt partition co-

efficients or the phase stability regime at one atmosphere (Leitzke et al., 2016). The fifth mixture (M8) aimed to crystallize An–plagioclase in equilibrium with silicate glass at 1280 °C and was based closely on the Al–rich starting composition of Mallmann and O'Neill (2009).

High-purity oxide powders (SiO_2, MgO, Al_2O_3, Fe_2O_3, TiO_2, MnO and Cr_2O_3) and P (1,000 μg/mL solution in 5% HNO_3) were ground with $CaCO_3$ under acetone in an agate mortar. Mixes were subsequently dried, pressed into pellets and placed in a quartz crucible inside a furnace to decarbonise overnight at 900 °C. Pellets were then re-ground under acetone and trace elements were added in concentrations from 500 to 1000 μg/g. A large group of trace elements (Sc, V, Sr, Y, Zr, Nb, Ba, La, Nd, Sm, Eu, Hf, Ta, W, Th and U) was also investigated to better constrain the mechanisms of their substitution into the minerals. Trace elements were added as powders (Sc_2O_3, $SrCO_3$, V_2O_5, Y_2O_3, ZrO_2, Nb_2O_5, La_2O_3, Lu_2O_3, HfO_2, Ta) as well as using 1,000 μg/mL solutions in HNO_3 (Eu, Sm, Nd, U and Th) and H_2O (Mo and W). Barium (as $BaCO_3$ 1000 μg/g) was added as a tracer for evaluating the presence of melt inclusions in crystals during laser ablation–inductively coupled plasma–mass spectrometry (LA–ICP–MS) analysis, since this elements is strongly incompatible in pyroxene and olivine (e.g. Lundstrom et al., 1994; Mollo et al., 2013).

The cpx series were divided into three separate sets of experiments; one doped with Mo and W simultaneously, and the other two with either Mo or W, in addition to the other trace elements. The reason for that was to observe if a melt complex between W and Mo (O'Neill and Eggins, 2002) could potentially affect the partitioning behaviour of these elements in the silicate melt. The only simplification from natural systems to our starting compositions is the small amount of Fe, as the use of Pt wire leads to significant Fe-loss, especially at low fO_2.

Table 4.1: Summary of run conditions for each experiment.

Starting materials	log fO_2	Δ relative to redox buffer FMQ[a]	Cooling ramp (°C/min)	Temp. (°C)	Duration (h)[b]	Run products[c]	CO - CO_2[d]
WM1+W, WM1+Mo+W	-5.58	1.9	0.04	1300	3 + 96	ol+cpx+glass; cpx+glass	5 - 310
WM1+W, WM1+Mo+W, WM1+Mo	-6.33	1.0	0.04	1300	3 + 98	ol+cpx+glass; ol+cpx+glass; ol+cpx+glass	5 - 175
WM1+W, WM1+Mo+W, WM1+Mo	-7.30	0.0	0.05	1300	3 + 72	ol+cpx+glass; ol+cpx+glass; ol+cpx+glass	10 - 160
WM1+W, WM1+Mo+W, WM1+Mo	-8.42	-1.1	0.05	1300	3 + 78	ol+cpx+glass; ol+cpx+glass; ol+cpx+glass	15 - 95
WM1+Mo	-9.35	-2.1	0.04	1300	3 + 75	ol+cpx+glass	50 - 80
WM1+W, WM1+Mo+W	-10.34	-3.0	0.04	1300	3 + 62	cpx+glass, ol+cpx+glass	70 - 40
WM1+W, WM1+Mo+W	-11.56	-4.2	0.05	1300	3 + 60	cpx+glass, ol+cpx+glass	100 - 15
HSM1+Mo+W, HSM1+W, HSM1+Mo	-6.38	1.8	0.04	1220	3 + 96	cpx+glass, pl+cpx+glass, cpx+glass	4 - 310
HSM1+Mo+W, HSM1+W, HSM1+Mo	-7.18	1.0	0.04	1220	3 + 84	cpx+glass, pl+cpx+glass, pl+cpx+glass	7 - 400
HSM1+Mo+W, HSM1+Mo	-8.23	-0.1	0.05	1220	3 + 76	pl+cpx+glass, pl+cpx+glass, cpx+glass	20 - 200
HSM1+Mo+W	-9.40	-1.2	0.04	1220	3 + 80	pl+cpx+glass	25 - 190
HSM1+Mo+W, HSM1+Mo	-10.34	-2.2	0.04	1220	3 + 88	cpx+glass, cpx+glass	80 - 90
HSM1+Mo+W, HSM1+W	-11.30	-3.1	0.04	1220	3 + 96	cpx+glass, cpx+glass	90 - 25
HSM1+Mo, HSM1+W	-12.38	-4.2	0.05	1220	3 + 60	cpx+glass, pl+cpx+glass	100 - 8
OPM3, OLM1	-5.58	1.9	0.03	1300	3 + 98	opx+glass, ol+glass	5 - 310
OPM3, OLM1	-6.33	1.0	0.03	1300	3 + 77	opx+glass, ol+glass	5 - 175
OPM3, OLM1	-7.30	0.0	0.03	1298	3 + 64	opx+glass, ol+glass	10 - 160
OPM3, OLM1	-8.42	-1.1	0.03	1300	3 + 83	opx+glass, ol+glass	15 - 95
OPM3, OLM1	-9.35	-2.1	0.04	1300	3 + 72	opx+glass, ol+glass	50 - 80
OPM3, OLM1	-10.34	-3.0	0.04	1300	3 + 84	opx+glass, ol+glass	70 - 40
OPM3	-11.47	-4.1	0.04	1300	3 + 96	opx+glass	70 - 10
OLM1, M8	-12.98	-5.5	0.04	1280	3 + 72	cpx+glass, ol+pl+glas	140 - 4
OLM1, M8	-10.85	-3.5	0.04	1280	3 + 72	cpx+glass, ol+pl+glass	70 - 20

[a] FMQ: Fayalite-Magnetite-Quartz mineral redox buffer as described by O'Neill (1987)

[b] Time spent at supraliquidus (50 to 100 °C above target temperature) + Time spent at the desired equilibrium temperature

[c] Mineral assemblages in each experiment are separated by ";" relatively to column "Starting Materials"; Abbreviations according to Whitney and Evans (2010) - cpx: clinopyroxene; ol: olivine; opx: orthopyroxene; pl: plagioclase.

[d] Gas mixture proportions in SCCM (Standard Cubic Centimeter per Minute)

The amount of Fe from the starting compositions is expected to have little effect on trace element partitioning behaviour. Recent studies have noted that $D_M^{cpx/melt}$ differ little between iron-free and iron-rich experimental charges (Leitzke et al., 2016). Moreover, analysing the partitioning behaviour of trace elements during mantle melting using Fe-poor starting compositions is reasonable (e.g. Mallmann and O'Neill, 2009) because both primitive and depleted mantle reservoirs have Mg# higher than 80 % (e.g., Palme and O'Neill, 2014).

Experiments were carried out using the classic wire loop technique. This method uses loops of a metal (Pt or Re in this study), on which a slurry made from sample powders, H_2O and polyethylene glycol is attached. The metal loops + slurry are then hung inside a one-atmosphere vertical tube furnace at temperatures between 1350 and 1400 °C, i.e., around 50 to 100 °C above the liquidus of each composition (Supplementary Material). The temperature of the furnace had to be lowered to 800 °C with the gas mixture on before starting the experiments performed with Re–wire, in order to avoid oxidation and volatilization of the wire. Each sample remained at supra–liquidus conditions for 3 hours to ensure that the powders were completely molten and homogenized. Cooling ramps (0.03 to 0.05°/min) were chosen to maximize crystal size (at least 100 μm) for LA–ICP–MS analysis and the temperature was lowered to the nominal value of the experiment, where it remained for 48 to 96 hours to ensure chemical equilibrium (Table 4.1). Oxygen fugacity was imposed by mixing CO–CO_2 in different proportions using Mykrolis mass flow controllers. The CO–CO_2 proportions required for the equilibrium gas species fugacities at 1 bar were calculated using an Excel macro as described in Kress et al. (2004). The effective values of fO_2 inside the furnaces were checked and calibrated using a CaO-Y_2O_3–stabilized ZrO_2 electrolite cell. Measured fO_2 values were within 0.2

log–bar units of the calculated values. Temperature was monitored using a type B ($Pt_{70}Rh_{30}$ - $Pt_{94}Rh_6$) thermocouple. Quenching of the samples was carried out in air by removing the sample holder from the top of the furnace, which has a water cooling system that keeps the temperature at ca. 25 °C. Quenched loops were recovered, mounted in epoxy resin and polished for chemical analysis.

4.2.2 Analytical Techniques

Major and minor elements (CaO, MgO, Al_2O_3, SiO_2, TiO_2, MnO and FeO) were analysed by using a JEOL JXA 8900 electron microprobe. Measurements were carried out in Wavelength Dispersive mode (WDS), employing 15 kV accelerating voltage, 15 nA beam current. Crystals and glasses were measured with an electron beam defocused to 5 μm. Peak to background calibrations were performed on a basaltic glass from the Juan de Fuca ridge (VG2), as well as on rutile and San Carlos olivine. Values presented for this study consist of averages of five to ten measurements carried out on each phase.

Trace element concentrations were analysed using a Resonetics Resolution M50-E 193 nm Excimer Laser Ablation apparatus coupled to a Thermo Scientific XSeries II Quadrupole–ICP–MS. Laser spots ranged in size between 58 to 100 μm, and were chosen depending on crystal size and/or absence of melt inclusions. Whenever the time-resolved analysis showed evidence for melt contamination, the sample was re-measured until a minimum of five to ten measurements that were free of melt inclusions was obtained (for details see Fonseca et al., 2014). The laser frequency was set to 15 Hz with fluence measured at 6-7 J/cm^2. Count rates for the following isotopes were measured: ^{29}Si, ^{43}Ca, ^{31}P, ^{45}Sc, ^{46}Ti, ^{47}Ti, ^{51}V, ^{52}Cr, ^{55}Mn, ^{88}Sr, ^{89}Y, ^{90}Zr, ^{91}Zr, ^{93}Nb, ^{95}Mo, ^{98}Mo, ^{137}Ba, ^{138}Ba, ^{139}La, ^{146}Nd, ^{147}Sm, ^{151}Eu,

^{153}Eu, ^{175}Lu, ^{177}Hf, ^{178}Hf, ^{181}Ta, ^{182}W, ^{184}W, ^{232}Th and ^{238}U. Count rates were internally normalized to the count rate of an isotope of an element of known concentration acquired by electron microprobe (internal standard, e.g. ^{29}Si or ^{43}Ca). Then, they were converted to concentrations using the methodology described by Longerich et al. (1996) with the NIST SRM 610 and 612 used as the external standards (Jochum et al., 2011). When more than one isotope for the same element was monitored, the relative natural abundance of each isotope was well reproduced, indicating that isobaric and molecular interferences were negligible. Although a number of potentially interfering species are known to affect Mo–masses during ICP–MS analysis (e.g., ^{58}Ni^{40}Ar and ^{58}Fe^{40}Ar interfere on ^{98}Mo), such interferences were insignificant in this study because there were negligible Fe and Ni in the bulk compositions (Supplementary Material).

At lower fO_2 the presence of metallic nano-nuggets is known to affect LA–ICP–MS measurements of Mo in silicate phases (e.g., Wijbrans et al., 2015). To mitigate this problem, only analyses where these nuggets could be filtered out from the time-resolved spectra were used. This approach has proven successful in determining true solubility and partitioning systematics of siderophile elements in silicate systems (e.g., Mallmann and O'Neill, 2007; Wijbrans et al., 2015). At oxygen fugacities above the FMQ mineral redox buffer (O'Neill, 1987), Mo is partially lost due to its volatile behavior (Schryer and Walberg, 1966). At lower oxygen fugacities Mo diffuses into the metallic wire, turning LA–ICP–MS analysis of silicate phases challenging due to its low concentrations (0.1 – 1 μg/g Mo), which are close to the detection limit. Despite these issues, the lack of any apparent isobaric interference, and the good agreement amongst $D_{Mo}^{crystal/melt}$ values under similar fO_2 from experiments that were done on Pt and Re–wire, i.e., with different Mo contents (Mo diffuses more strongly into Pt than Re wire), strongly sug-

gests that the Mo data quality in this study is sound, and that equilibrium was reached.

Results presented in the following section are based on 48 experiments performed in the Experimental Petrology laboratory of the Steinmann Institute for Geosciences, University of Bonn, Germany. Run conditions of each experiment are shown in Table 4.1. Major and trace element compositions for each phase of all runs are listed in the Supplementary Material.

4.3 Results

4.3.1 Run Products

All experiments yielded silicate glass and, depending on the initial composition, euhedral to subhedral crystals of olivine, plagioclase, clino– and orthopyroxene. The cooling rate after reaching supraliquidus temperatures was a major factor controlling the size of the crystals, which are typically larger than 100 μm (Figure 4.1ac). Changes in fO_2 did not affect the mineral paragenesis in any of the starting compositions. For composition M8, anorthite crystals were large and euhedral, enabling accurate trace element analysis. However, plagioclase crystals present as secondary phases in experiments based on the composition HSM–1 were small in size and displayed acicular habit. Therefore, conducting LA–ICP–MS analysis on plagioclase grains in these experiments was not possible, leading to a limited dataset for $D_M^{pl/melt}$. The target temperature chosen for OLM–1 was a critical factor in controlling the phase assemblage and the size of the different crystals. A lower target temperature (1280 °C) produced large clinopyroxene crystals and small olivine grains, whereas a higher temperature (1300 °C) yielded large olivine grains but no clinopyroxene (Table 4.1). The small major element compositional variability of plagioclase, pyroxene and olivine crystals

from individual experiments (see Supplementary Material) suggests that runs likely achieved chemical equilibrium, and on the rare occasions where limited chemical zonation was present those portions of the grains were excluded from the analysis.

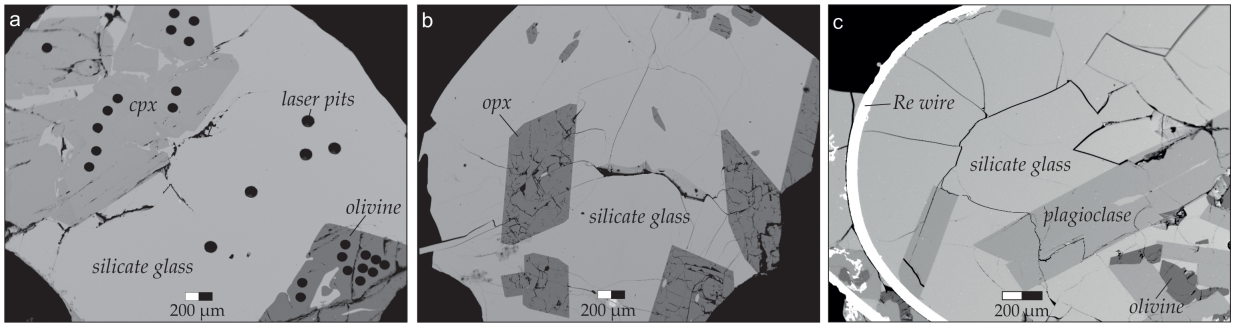

Figure 4.1: Back-scattered electron images of typical experimental run products: A) Large euhedral to subhedral clinopyroxene (diopside) and olivine (forsterite) crystals in equilibrium with silicate glass; B) Euhedral orthopyroxene (enstatite) crystals in equilibrium with silicate glass; C) Euhedral plagioclase (anorthite) and olivine (forsterite) crystals in chemical equilibrium with silicate glass.

4.3.2 Crystal-silicate melt partitioning of heterovalent minor and trace elements (P, Cr, Ti, V, Mo, W, Eu and U)

Calculated crystal/melt partition coefficients (Table 4.2 and Supplementary Material) show that fO_2 affects the compatibility of Cr, Ti, V, Mo, W, Eu and U in the pyroxenes and olivine. The element most strongly affected by changes in fO_2 is Mo, which becomes more compatible under reducing conditions (Fig. 4.2). Values for $D_{Mo}^{cpx/melt}$ increased from 0.0013 to 2.1 from oxidized, i.e. above FMQ, to more reduced conditions, i.e. below FMQ–4 (Fig. 4.2a). An increase in the same order of magnitude also occurs for $D_{Mo}^{opx/melt}$ and $D_{Mo}^{ol/melt}$ (Fig. 4.2b,c). No partitioning data were derived for conditions more oxidized than FMQ+2, given that Mo was below detection limits in all experimental run products due to its strongly volatile

behaviour under these conditions. The attainment of chemical equilibrium is a major concern in crystal/silicate melt partitioning studies using the same experimental approach as ours (e.g., Mollo et al., 2013; Fonseca et al., 2014; Wijbrans et al., 2015). We can assess the achievement of chemical equilibrium in our experiments by the fact that $D_{Mo}^{crystal/melt}$ obtained in experiments at the same conditions of fO_2 and temperature, but with different run duration, metallic wire (Pt and Re), and concentration, show values that are the same within error. Moreover, volatile loss of Mo would be more severe in silicate melt compared to any liquidus phases present in the experiments. Because of this, $D_{Mo}^{crystal/melt}$ are expected to increase at conditions more oxidized than FMQ, where Mo is expected to become partially loss to volatilization. Our results, however, show the opposite, with lower $D_{Mo}^{crystal/melt}$ occurring at higher fO_2. As such, the $D_{Mo}^{crystal/melt}$ values obtained should reflect equilibrium conditions.

The compatibility of Mo into cpx appears to be promoted slightly by the presence of a Ca-Tschermak component in clinopyroxene. In contrast, chromium and Eu behave differently, as their compatibility in both, cpx and opx, decreases at lower fO_2 (Supplementary Material), in agreement with McKay et al. (1994) and Wadhwa (2001). Titanium, V, W, and U become more compatible in all silicates with increasingly reducing conditions, which is congruent with previous findings (e.g., Mallmann and O'Neill, 2009; Fonseca et al., 2014).

Table 4.2: Selected crystal/silicate melt partition coefficients.

Starting comp.	Δ FMQ	D_V	σ	D_{Cr}	σ	D_{Mo}	σ	D_{Eu}	σ	D_{Hf}	σ	D_W	σ	D_{Th}
Cpx/silicate melt														
HSM1+Mo+W	1.8	0.26	0.01	28.5	11.3	0.002	0.001	0.29	0.01	1.14	0.07	0.00014	0.00008	0.027
	1.0	0.67	0.05	39.8	18.2	0.005	0.001	0.30	0.01	1.08	0.05	0.00021	0.00018	0.037
	-0.1	0.78	0.11	34.4	18.0	0.010	0.004	0.23	0.02	1.00	0.08	0.00015	0.00004	0.034
	-1.2	4.42	1.13	21.0	12.4	0.04	0.01	0.17	0.01	1.00	0.11	0.00015	0.00008	0.027
	-2.2	8.51	3.49	12.1	8.0	0.25	0.05	0.15	0.01	1.45	0.13	0.0014	0.0011	0.051
	-3.1	10.22	3.35	9.8	3.9	1.2	0.7	0.10	0.01	1.54	0.45	0.0051	0.0018	0.049
HSM1+Mo	-3.1	11.43	5.28	9.0	3.8	1.2	0.6	0.11	0.01	1.08	0.14	-	-	0.035
	-4.2	13.43	3.41	6.7	1.7	2.2	1.1	0.12	0.02	1.27	0.16	-	-	0.045
	1.0	0.64	0.03	21.6	7.2	0.006	0.001	0.33	0.02	0.90	0.04	-	-	0.029
	1.8	0.32	0.01	19.4	7.1	0.004	0.002	0.31	0.02	1.00	0.02	-	-	0.024
	-0.1	1.21	0.15	18.9	8.1	0.008	0.004	0.22	0.01	0.98	0.04	-	-	0.029
	-2.2	10.72	5.06	12.2	3.0	0.19	0.08	0.21	0.04	1.11	0.11	-	-	0.039
OLM-1	-3.5	6.03	1.09	3.5	0.7	0.56	0.08	0.04	0.01	0.04	0.02	0.0011	0.0004	0.0011
	-5.5	7.70	1.50	2.9	0.3	0.54	0.20	0.035	0.003	0.03	0.00	0.0054	0.0024	0.0010
	-1.1	0.81	0.13	3.7	0.5	0.013	0.003	0.08	0.01	0.03	0.01	0.00008	0.00002	0.0011
WM1+Mo+W	1.9	0.11	0.02	10.3	2.9	0.0013	0.0006	0.14	0.01	0.09	0.03	0.000033	0.000018	0.0021
	1.0	0.15	0.01	7.1	1.4	0.003	0.001	0.12	0.01	0.08	0.01	0.00006	0.00002	0.0035
	-1.1	0.98	0.07	5.7	0.9	0.008	0.002	0.08	0.01	0.04	0.01	0.00006	0.00002	0.0014
	-3.0	2.89	0.43	2.4	0.4	0.23	0.11	0.018	0.002	0.05	0.02	0.0026	0.0014	0.0018
	-4.3	3.01	0.41	1.9	0.4	0.45	0.08	0.018	0.002	0.06	0.01	0.0081	0.0023	0.0033
	0.0	0.40	0.05	9.3	2.6	0.005	0.001	0.11	0.01	0.06	0.02	0.000053	0.000016	0.0015
WM1+Mo	-1.1	1.19	0.14	3.2	0.4	0.016	0.007	0.09	0.02	0.05	0.01	-	-	0.0015
	1.0	0.21	0.04	6.5	1.8	0.003	0.001	0.09	0.02	0.07	0.03	-	-	0.0029
	0.0	0.35	0.07	5.7	1.0	0.0036	0.0004	0.11	0.01	0.06	0.01	-	-	0.0014
	-2.1	2.07	0.28	3.0	0.3	0.06	0.04	0.039	0.003	0.04	0.01	-	-	0.0030
Opx/silicate melt														
OPM-3	1.9	0.11	0.02	2.00	0.28	0.009	0.001	0.00093	0.00016	0.0049	0.0013	0.0010	0.0002	0.00002
	1.0	0.14	0.03	1.44	0.22	0.008	0.001	0.00069	0.00010	0.0041	0.0007	0.0011	0.0001	0.00003
	0.0	0.16	0.01	1.31	0.15	0.026	0.008	0.00065	0.00006	0.0038	0.0005	0.0010	0.0001	0.00002
	-1.1	0.36	0.06	1.14	0.24	0.14	0.01	0.00049	0.00008	0.0033	0.0007	0.0023	0.0007	0.00004
	-2.1	0.58	0.14	0.88	0.24	0.32	0.27	0.00012	0.00007	0.0045	0.0005	0.0025	0.0015	0.00002
	-3.0	0.58	0.07	1.23	0.08	0.63	0.34	0.00012	0.00002	0.0043	0.0007	0.0090	0.0036	0.00002
	-4.1	1.43	0.38	1.28	0.18	0.53	0.19	0.00016	0.00006	0.0048	0.0015	0.028	0.010	0.00006
Olivine/silicate melt														
OLM-1	1.9	0.013	0.001	0.52	0.02	0.006	0.002	0.00018	0.00005	0.00035	0.00010	0.000024	0.000017	0.0000031
	1.0	0.027	0.001	0.41	0.02	0.006	0.002	0.00017	0.00004	0.00049	0.00016	0.000056	0.000032	0.0000045
	0.0	0.081	0.008	0.42	0.02	0.013	0.005	0.00017	0.00002	0.00058	0.00011	0.000090	0.000046	0.0000016
	-2.1	0.25	0.17	0.64	0.11	0.064	0.022	0.00011	0.00008	0.00032	0.00006	0.00028	0.00013	0.0000059
	-3.0	0.41	0.12	0.88	0.15	0.28	0.07	0.00008	0.00003	0.00043	0.00012	0.0049	0.0023	0.0000018
	-1.1	0.12	0.01	0.50	0.11	0.032	0.007	0.00018	0.00005	0.00050	0.00045	0.000099	0.000047	0.0000036
Pl/silicate melt														
M8	-3.5	0.039	0.004	0.014	0.003	0.039	0.010	0.80	0.04	0.00025	0.00006	0.00010	0.00004	0.00016
	-5.5	0.13	0.03	0.020	0.005	0.046	0.023	1.02	0.10	0.00033	0.00027	0.0049	0.0022	0.00021

Uncertainties (σ) are propagated from the mean value and standard deviation in each phase (Supplementary Tables 2 and 3). This table is also provided as a digital file in the supplementary
3b), where D values for all trace elements added to the starting mixtures are given, as well as for the compositions without Mo.

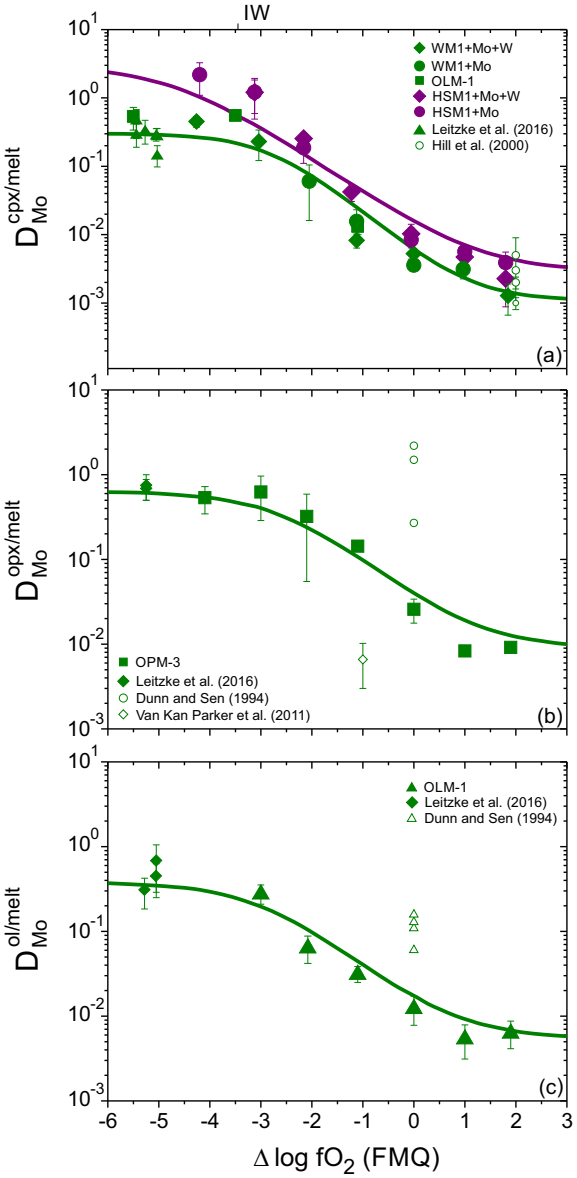

Figure 4.2: Partition coefficients of Mo as a function of fO_2 (given in Δ relative to the FMQ redox buffer) between ^{IV}Al–rich (HSM–1) and ^{IV}Al–poor (WM–1) clinopyroxene (a), orthopyroxene (b), olivine (c) and silicate melt. Lines represent best fits of the partitioning data to equation (4.6). Fitted parameters are given in Table 4.3. Error bars are one standard deviation. Literature partitioning data for Mo is selected from Dunn and Sen (1994), Hill et al. (2000), van Kan Parker et al. (2011b) and Leitzke et al. (2016). Data from previous studies produced at unconstrained fO_2, these parameters were either estimated based on $D_V^{crystal/melt}$ in the experiments (Mallmann and O'Neill, 2009, 2013), or the approximated buffer assembly mentioned in the text.

4.3.3 Crystal-silicate melt partitioning of homovalent minor and trace elements (Sc, Ba, Sr, La, Nd, Sm, Lu, Y, HFSE and Th)

Calculated crystal/melt partition coefficients for Sc, Ba, Sr, rare-earth elements (REE – La, Nd, Sm, Lu), Y, high-field strength elements (HFSE – Zr, Hf, Nb, Ta), and Th (Table 4.2 and Supplementary Material) show no dependence on fO_2, confirming their homovalent nature at the conditions relevant to planetary processes (Papike, 2005). In agreement with the results obtained by Hill et al. (2000) and Mollo et al. (2013), $D_M^{cpx/melt}$ are higher in experiments where cpx has the highest ^{IV}Al contents (composition HSM–1). Moreover, the general trend $D_M^{cpx/melt} > D_M^{opx/melt} > D_M^{ol/melt}$ is also observed (Supplementary Material).

4.4 Discussion

4.4.1 The effect of fO_2 on the partitioning of Mo between pyroxene, olivine and silicate melt

Recent studies of the behaviour of Mo in magmatic systems have focused on its moderately siderophile nature (e.g., Farges et al., 2006; Greber et al., 2015; Righter et al., 2010, 2016). It has been suggested that Mo was preserved in roughly chondritic abundances throughout the accretion of protoplanetary bodies, and that some amount of Mo may have remained in the silicate portion of terrestrial planets after metal segregation and core formation (O'Neill et al., 2008; Righter et al., 2016). It is important to note that the ratio between Mo and its geochemical twin W is higher in chondrites (10 ± 1) than in the bulk-silicate Earth (BSE), where this value is approximated to 2.4 ± 1.3 (Palme and O'Neill, 2003, 2014). This indicates

that Mo and W fractionated from each other during core formation on the Earth (O'Neill et al., 2008). In the Moon, however, Mo/W is calculated at ca. 0.2 (O'Neill, 1991), and the bulk Mo content observed in lunar basalts (between 0.01 and 0.1 μg/g) is lower than what is observed in terrestrial basalts (0.4 μg/g) or CI-chondrites (0.9 μg/g) (Newsom, 1984a; Gale et al., 2013). It can thus be surmised that the more reducing conditions operating during mantle melting and core formation in planetary bodies like the Moon and Mars (e.g., Wadhwa, 2001), will affect the relative partitioning behaviour of Mo and W.

Molybdenum is expected to change its oxidation state from 6+ to 4+ at IW–1, which has been well constrained from its metal–silicate partitioning behavior and on Mo solubility in silicate melts (e.g., Holzheid et al., 1994; O'Neill and Eggins, 2002; Righter et al., 2016). However, experimental data are still scarce regarding the partitioning of Mo at fO_2 conditions prevalent during the fractionation of a magma ocean. Therefore, it is important to constrain the partitioning of Mo between the most abundant silicate phases in the terrestrial and lunar mantle and silicate melts. To do so, we applied a parametrization similar to Mallmann and O'Neill (2007, 2009), which takes into account the contributions that the different oxidations states of Mo (4+ and 6+) have on its crystal/melt partition coefficients. The reaction describing the change in Mo oxidation state in silicate melts is:

$$Mo^{4+}O_2 + \frac{1}{2}\,O_2 = Mo^{6+}O_3 \tag{4.1}$$

The equilibrium constant (K) for this homogeneous reaction is:

$$K = (X_{Mo^{6+}O_3}.\gamma_{Mo^{6+}O_3})/(X_{Mo^{6+}O_3}.\gamma_{Mo^{6+}O_3}.(fO_2)^{1/2}) \tag{4.2}$$

where X is the mole fraction of each Mo oxide species dissolved in the silicate melt, γ is the activity coefficient of each Mo oxide component in the silicate melt, and fO_2 is oxygen fugacity. Assuming that for low concentrations, γ are constant for a given composition (Henry's Law), the equilibrium constant for reaction (4.1) can be simplified to:

$$K' = ([Mo^{6+}O_3]/[Mo^{4+}O_2]).(fO_2)^{-1/2} \tag{4.3}$$

where $K' = K(\gamma_{Mo^{4+}O_2}/\gamma_{Mo^{6+}O_3})$. Note that the conversion factor from mole fractions to concentrations (in square brackets) cancels out between the numerator and denominator. The Mo concentration in a crystalline phase will be given by the sum of Mo^{4+} and Mo^{6+}, each with its own thermodynamic component:

$$\begin{aligned} Mo^{4+}_{crystal} &= [Mo^{4+}O_2] + \Sigma[NO_x] \\ Mo^{6+}_{crystal} &= [Mo^{6+}O_3] + \Sigma[MO_x] \end{aligned} \tag{4.4}$$

where $\Sigma[NO_x]$ and $\Sigma[MO_x]$ are the major-element oxide components of the "stoichiometric control" needed to form the Mo components in the crystalline phase (e.g., O'Neill and Eggins, 2002). The bulk crystal/melt partition coefficient of Mo is defined as:

$$D^{crystal/melt}_{\Sigma Mo} = \frac{(Mo^{4+}_{crystal} + Mo^{6+}_{crystal})}{([Mo^{4+}O_2]_{melt} + [Mo^{6+}O_3]_{melt})} \tag{4.5}$$

Substituting expression (4.3) into (4.5) yields the following sigmoidal functional expression (Mallmann and O'Neill, 2007, 2009), which can be used to fit our data (Table 4.3) and describes the sole effect of fO_2 on the bulk

Mo partitioning between crystals and silicate melt:

$$D_{\Sigma Mo}^{crystal/melt} = \frac{D_{Mo^{4+}}^{crystal/melt}.(K')^{-1}.(fO_2)^{-1/2} + D_{Mo^{6+}}^{crystal/melt}}{1 + (K')^{-1}.(fO_2)^{-1/2}} \quad (4.6)$$

Equation (4.6) shows that at constant temperature and fixed melt major element composition, $D_{\Sigma Mo}^{crystal/melt}$ as a function of fO_2 will depend on three parameters: 1) $D_{Mo^{6+}}^{crystal/melt}$, i.e. the value obtained at the oxidizing plateau; 2) $D_{Mo^{4+}}^{crystal/melt}$, i.e. the value obtained at the reduced plateau, and 3) the equilibrium constant of equation (4.3). It is important to note that the stoichiometry of reaction (4.1) will control the shape of the fitted curve by the power to which fO_2 is raised, which in this case is 0.5, representing a two-electron exchange.

Table 4.3: Non-linear least squares fits to Equation (4.6)

Crystal	K'^{-1}	$^{a}D_{Mo}{}^{4+}$	$^{b}D_{Mo}{}^{6+}$	n	χ^2
Clinopyroxene (WM1)	1.5E-06	0.3	0.001	17	1.7
Clinopyroxene (HS1)	3.4E-07	2.9	0.003	12	5.0
Orthopyroxene	1.2E-05	0.7	0.009	8	0.2
Olivine	7.4E-06	0.5	0.006	9	0.3

[a] Constrained from the fitting of the data to the Lattice strain Model for tetravalent cations

[b] Constrained from average values at the oxidizing plateau (Table 2)

It is clear that each oxidation state forms a different component in the crystalline phase controlled by the stoichiometry of the crystal (e.g., $CaMo^{4+}Al_2O_6$), which in turn, is controlled by the major element composition and activities in the silicate melt (cf., O'Neill and Eggins, 2002). To exclude the melt compositional effects on $D_{Mo}^{cpx/melt}$ from our study, we have compared and fitted our data from experiments that had the same start-

ing composition and constant temperature (Table 4.1), and therefore, any change on $D_{Mo}^{crystal/melt}$ should be solely due to changes in fO_2. Previous studies reported that Mo^{4+} is the predominant oxidation state below IW–1 (O'Neill and Eggins, 2002; Danielson et al., 2011; Righter et al., 2016). Non-linear least square fits to equation (4.6) show good evidence for a two-electron-change (i.e., MoO_3 MoO_2) along the fO_2 series carried out in this study, with a general $X^2 < 2$. The only exception is the ^{IV}Al-rich clinopyroxene compositional series (HS1) where melt complexes between Mo and CaO may be involved, which could shift the redox transition between Mo^{4+} and Mo^{6+} (O'Neill and Eggins, 2002). Nevertheless, both values are close to what would be expected from a two-electron exchange, reinforcing the view that redox equilibrium of Mo was reached in our experiments.

4.4.2 Crystal chemistry and trace element partitioning

To better understand how Mo substitutes into the crystallographic sites of cpx, opx, olivine, and plagioclase, the observed $D_{HFSE}^{crystal/melt}$ were fitted to the lattice strain function (Brice, 1975; Blundy and Wood, 1994):

$$D_M^{crystal/melt} = D_0 \; exp\left[\frac{-4\pi E_s N_A[\frac{r_0}{2}(r_M - r_0)^2 + \frac{1}{3}(r_M - r_0)^3]}{RT}\right] \qquad (4.7)$$

where r_0 is the size of the lattice site with the least strain possible, r_M is the ionic radius of the cation, E_s is the apparent Young's modulus of the site when $r_0 \neq r_M$, N_A is the Avogrado's constant, R is the universal gas constant and T is the temperature in Kelvin. Fits to equation (4.7) were made assuming that Mo^{4+} is exclusively present at the most reduced conditions achieved in our experiments, i.e., that the redox change takes place at around IW at 1 bar (cf., Holzheid et al., 1994; Farges et al., 2006;

Danielson et al., 2011; Righter et al., 2016).

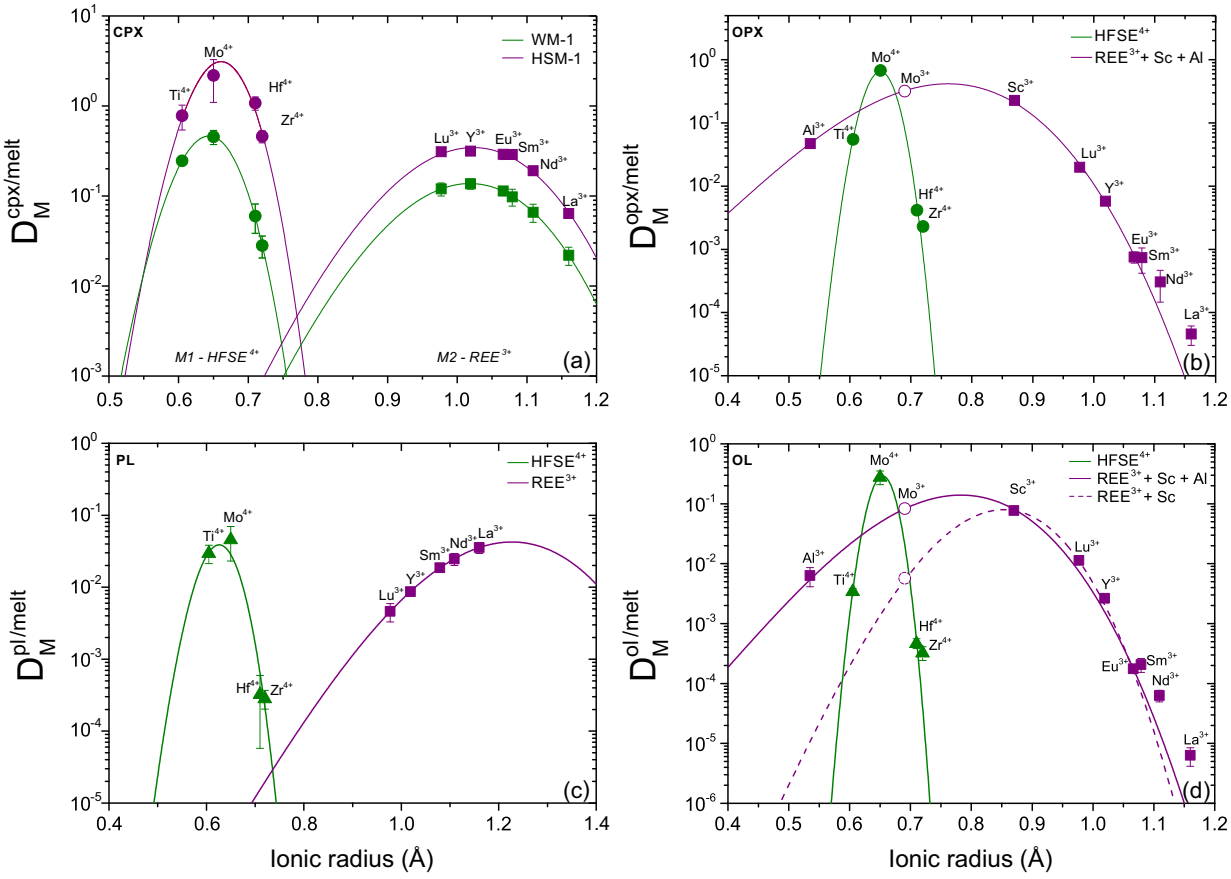

Figure 4.3: Observed crystal-silicate melt partition coefficients for Ti^{4+}, Mo^{4+}, Hf^{4+} and Zr^{4+}, Sc^{3+}, Al^{3+} and REE^{3+} cations entering the M1 and M2 sites of cpx (a), opx (b), plagioclase (c), and olivine (d) plotted against ionic radius in VI–fold (HFSE, Mo and Al) and VIII–fold (REE and Sc) coordination. Ionic radii were taken from Shannon (1976) with an assumed uncertainty of 0.005 $\mathring{A}$. The Levenberg-Marquardt algorithm was used to adjust the parameters for the minimum chi-square values, weighted by the error. Lines represent least-squares fits of the data to the equation (4.7) according to Blundy and Wood (1994). Error bars are one standard deviation. Excellent values of X_v^2 indicate the goodness of the fits (see Supplementary Material). The predicted partition coefficient for Mo^{3+} is shown with open symbols, as it was not measured but estimated from the lattice strain fits for trivalent cations.

From the results of the fits (Supplementary Material), it is clear that adding Al to the clinopyroxene crystal structure raises $D_{HFSE,REE}^{cpx/melt}$ values

(cf., Hill et al., 2000), with a less pronounced effect on $D_{Mo}^{cpx/melt}$. Partition coefficients indicate that the HFSE substitute into the smaller octahedral (M1) sites of these crystals, whereas the trivalent REEs substitute into the larger octahedral (M2) sites of pyroxene and olivine (Fig. 4.3). Scandium appears to have a misfit into the M2 site of cpx, but it fits perfectly on the same site of opx and olivine, as already noticed by Mallmann and O'Neill (2013). Lattice strain parameters obtained by olivine/melt partitioning data for HFSE and REE indicate a generally stiffer crystallographic site when compared to the pyroxenes. Assuming that the substitution mechanism of Sc and Al may not be the same as the REE into olivine, as suggested in previous studies (e.g., Evans et al., 2008; Mallmann and O'Neill, 2013), we fitted the observed partitioning data from olivine to Equation (4.7) considering two different scenarios: one including all observed values of $D_{M^{3+}}^{ol/melt}$ and another excluding Al.

The most significant difference is the stiffness of the octahedral crystallographic site, which becomes higher when Al data are excluded from the fits, with an E (Young's modulus) value of ca. 470 GPa, in agreement with the parameters obtained by Evans et al. (2008). This observation indicates that the substitution mechanism of Al is not the same for the REE, or that the substitution of Al in the mineral lattices is affected by other variables, such as the deviation from Henry's law or melt compositional effects. In this regard, Evans et al. (2008) suggested that unlike other large trivalent cations (REE, Sc and Y), Al substitutes into forsteritic olivine by replacing both Mg and Si in the octahedral and tetrahedral sites, respectively. According to Evans et al. (2008), this coupled substitution will result in a local short-range order of the crystal expressed by the reaction $AlO_{1.5}^{melt} + 0.25Mg_2SiO_4^{olivine} = 0.5MgAl_2O_4^{olivine} + 0.25SiO_2^{melt}$.

It should be noted that lattice strain fits were only obtained when par-

titioning data for enough cations with the same valence were available (at least four), in order to provide meaningful fit parameters. The main difference between both cpx starting compositions is the amount of Al_2O_3 in the starting mixture, which impacts the glass composition and how much Al is present in tetrahedral coordination in the clinopyroxene, which in our experiments ranges between 0.01 and 0.24 ^{IV}Al apfu. In this regard, our results mostly agree with the findings of Hill et al. (2000, 2011), who have shown that the elastic strain of the M1 site increases as a result of higher average cation charge, which is favoured by substituting Si^{4+} for Al^{3+}. Nevertheless, the results of Hill et al. (2000) for $D_{Mo,W}^{crystal/melt}$ are at odds with ours, given that they report a decrease in Mo and W partition coefficients between cpx and silicate melt as a function of ^{IV}Al, while our data shows the opposite. When compared to the work of Dunn and Sen (1994), our results for $D_{Mo}^{crystal/melt}$ are generally lower than the ones reported for their more oxidized experiments (≈FMQ), but are in good agreement with those carried out at more reducing conditions (≈FMQ–2). Moreover, some of the compositions of Dunn and Sen (1994) represent more evolved magmas such as andesites, whose more polymerized nature should drive $D_{Mo}^{crystal/melt}$ towards higher values (Gaetani, 2004).

Molybdenum, and to a lesser extent W, show similar values for their crystal-silicate melt partition coefficients for cpx, opx and olivine, while $D_{HFSE}^{crystal/melt}$ follows the trend $D_{HFSE}^{cpx/melt} > D_{HFSE}^{opx/melt} > D_{HFSE}^{ol/melt}$, in agreement to previous studies done under similar experimental conditions (Mallmann and O'Neill, 2009; Fonseca et al., 2014). The reason for this is that the ionic radii of W^{4+} and Mo^{4+} in VI-fold coordination are very close to the r_0 of all phases (Supplementary Material). Furthermore, the substitution mechanism for Mo in cpx is probably as $CaMo^{4+}Al_2O_6$, i.e., similar to the expected substitution mechanism of other tetravalent cations, such as Ti^{4+}

and Re^{4+} (e.g., Mallmann and O'Neill, 2007; Leitzke et al., 2016). For opx and olivine the substitution mechanism must be a direct exchange of Mo^{4+} for $2Mg^{2+}$. The stiffness of the M1 site, represented by the Young's modulus (E) in GPa follows the expected increase from cpx to opx and olivine (Supplementary Material). The predicted value of $D_{Mo^{3+}}^{crystal/melt}$ based on lattice strain model fits of trivalent cations is always lower than the measured $D_{Mo}^{crystal/melt}$, which is used as an evidence for the absence of Mo^{3+} in our experiments (Fig. 4.3b,d). This was expected since the transition to this oxidation state probably takes place at conditions more reduced than IW–3 (Danielson et al., 2011), which is still one order of magnitude lower than the range of fO_2 covered in our work.

4.4.3 The behavior of Mo during fractional crystallization and mantle partial melting

The most important implication of our work is illustrated when bulk values for $D_{Mo}^{crystal/melt}$ are calculated for different mantle source compositions over a range of fO_2 (Fig. 4.4a). During partial melting of terrestrial upper mantle (i.e. lherzolite), Mo is mainly hexavalent and shown to behave as a strongly incompatible element (bulk $D_{Mo}^{crystal/melt} \approx 10^{-3}$) at fO_2 conditions relevant to IAB, OIB and MORB mantle sources (i.e., around FMQ – see Christie et al., 1986; Ballhaus, 1993; Eggins, 1993; Rhodes and Vollinger, 2005; Mallmann and O'Neill, 2007). Under more reducing conditions, like those prevalent throughout lunar magma ocean crystallization and lunar mantle melting (i.e. around IW–1.5; see Snyder et al., 1992; Elardo et al., 2011), Mo^{4+} is the predominant Mo redox species, which leads Mo to behave more compatibly, especially when considering the potential presence of ^{IV}Al-rich residual cpx in the mantle source (Fig. 4.4a). Interestingly, the presumably more compatible nature of Mo leads to the fractionation of the

Mo/W ratio during lunar mantle melting, as Mo is progressively retained in the mantle source relative to W, which still behaves broadly incompatible (Fig. 4.4b). In contrast, during partial melting of Earth's mantle, both Mo and W are incompatible elements, and thus Mo/W is not expected to become significantly fractionated under most conditions of melting (Fig. 4.4b).

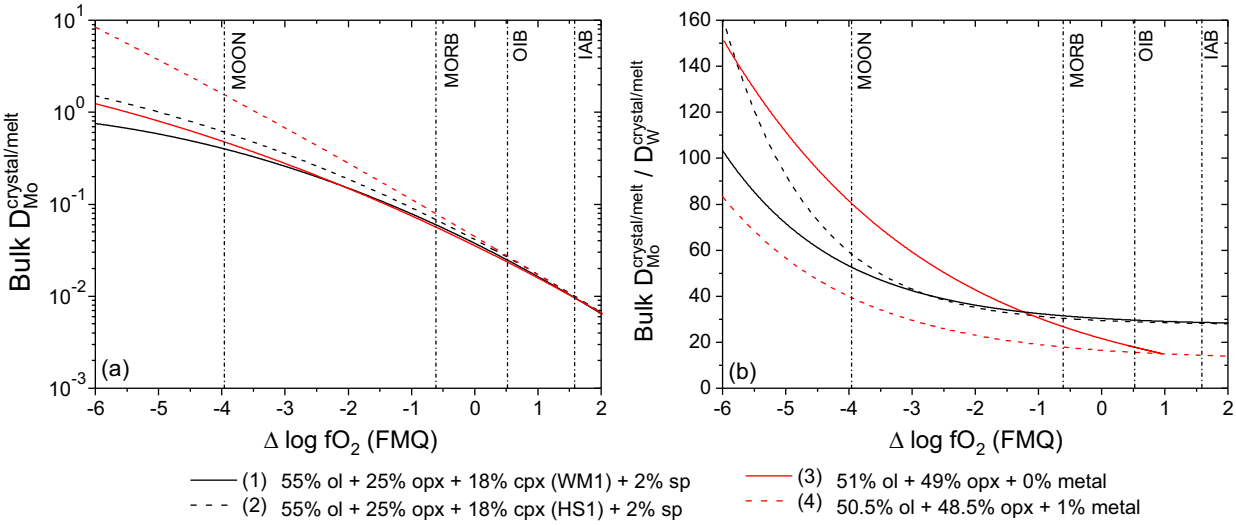

Figure 4.4: (a) Modelled bulk $D_{Mo}^{crystal/melt}$ showing the partitioning behavior of Mo during lunar and terrestrial mantle partial melting as a function of fO_2. Lines represent each of the modelled mantle sources. (b) Modelled bulk $D_{Mo}^{crystal/melt}/D_{W}^{crystal/melt}$ as a function of fO_2 for different mantle source of partial melting. Spinel/silicate melt partition coefficients as a function of fO_2 were taken from the work of Wijbrans et al. (2015). Metal/silicate melt partitioning values are from Hillgren (1991), whose work covered a broad range of fO_2. Mineral proportions in the mantle source for spinel–lherzolite were approximated using the same approach as Mallmann and O'Neill (2007) and the algorithm developed by Ghiorso et al. (2002). For the lunar mantle source, we used a simple mixture of sequences 1 and 2 of Snyder et al. (1992), varying the amount of residual metal between 0 and 1 wt. %. Vertical lines are approximations of the expected redox environment in each one of the terrestrial reservoirs (Christie et al., 1986; Ballhaus, 1993; Eggins, 1993; Rhodes and Vollinger, 2005; Mallmann and O'Neill, 2007), as well as the extremely reduced conditions expected for lunar mantle, at IW –0.5 (Papike, 2005; Nicholis and Rutherford, 2009).

Another factor that potentially enhances the fractionation of Mo from W during lunar mantle melting is the likely presence of a residual Fe-Ni alloy phase in lunar mantle sources. Such a residual alloy has been inferred to be a requirement to reproduce Hf/W and Ta/W ratios of most lunar mare basalt compositions (e.g., Fonseca et al., 2014; Leitzke et al., 2016) as well as from the depletion of Ni in lunar olivine (Karner et al., 2000). As such, partial melting in a metal saturated lunar mantle will be characterized by a significantly lower bulk $D_{Mo}^{crystal/melt}/D_{W}^{crystal/melt}$, when compared to metal–free systems (Fig. 4.4b). Hillgren (1991) covered a broad range of fO_2 in their experiments (ΔFMQ –0.9 to –4.7), and equilibrated metallic Ni with silicate melt in order to test the hypothesis of core formation in the Moon as proposed by O'Neill (1991). Our observations for metal-bearing sources consider the findings of Hillgren (1991), which showed that at more reduced conditions $D_{Mo}^{metal/silicatemelt}$ increases, contributing to an increase of the bulk $D_{Mo}^{crystal/melt}$ by three orders of magnitude along the entire range of fO_2 covered in this study (Fig. 4.4a).

Lunar samples are depleted in siderophile elements when compared to the BSE (e.g., Wänke et al., 1983; Day and Walker, 2015). It is well accepted that the Moon was formed from a giant impact of a Mars–sized body with the proto–Earth, which ejected enough terrestrial mantle material into orbit to accrete and form the Moon (e.g., Cameron and Canup, 1998; Canup and Asphaug, 2001). Therefore, to explain the depletion of siderophile elements in the Moon relative to the Earth, it has been assumed that some metal was segregated in the lunar mantle to form a lunar core, with estimates ranging between 0.15 and 5.55 wt. % of the bulk Moon (e.g., Newsom, 1984a; Rai and van Westrenen, 2014; Steenstra et al., 2016), or that just a small amount (0.02 wt. %) of late veneer material was mixed into the lunar mantle (Day and Walker, 2015; Kruijer and Kleine, 2016). Regardless of

which hypothesis is invoked, geochemical models typically assume that Mo and W are always incompatible in silicate phases during metal segregation and subsequent partial melting of the lunar mantle, in similar fashion to partial melting of Earths mantle. A typical estimate of the Mo/W of the bulk silicate Moon (BSM) is ca. 0.1 (see Newsom, 1986; O'Neill, 1991), i.e., one order of magnitude lower than the same value for the BSE (i.e., ≈ 2.4 – see Palme and O'Neill, 2003) and two orders of magnitude lower than in CI-chondrites (i.e., 10 – see Sims et al., 1990; Fitton, 1995; McDonough and Sun, 1995; König et al., 2011). This difference can be reconciled if one considers the effect of lower fO_2, which increases the bulk partition coefficient of Mo relative to W during lunar mantle melting (Fig. 4.4b).

4.4.4 Estimating the Mo/W of the bulk silicate Moon

A plethora of isotope measurements of lunar samples in recent times have reinforced the view that the bulk silicate Moon and BSE are isotopically similar (Melosh, 2014). Among these findings, similarities in terrestrial and lunar samples have been reported between the isotope composition of W (Touboul et al., 2007; Kruijer et al., 2015), H (Saal et al., 2013), Ti (Zhang et al., 2012), Cr (Lugmair and Shukolyukov, 1998; Bonnand et al., 2016), Fe (Sossi and Moynier, 2017), while O isotopes show a variation that possibly reflects the contribution of the impactor Theia (Herwartz et al., 2014). Considering the majority of similarities between isotopic compositions, it is difficult to envisage a scenario whereupon the Moon inherits a substantial amount of material from the impactor, which most likely would have been isotopically distinct to the Earth (e.g., Herwartz et al., 2014). Instead, the Moon could have been derived from material of the terrestrial mantle after core formation (i.e., BSE), a hypothesis that was already advocated by Ringwood and Kesson (1977) when analysing siderophile and volatile

elements in the Moon. In an effort to better constrain the Mo/W value during early magmatic processes in the Moon and to assess to which extent the lower lunar Mo/W relative to terrestrial and chondritic reservoirs estimated by Newsom (1986) is significant, we modelled the Mo–W behavior in a crystallizing Lunar Magma Ocean using the fractional crystallization sequence of Snyder et al. (1992).

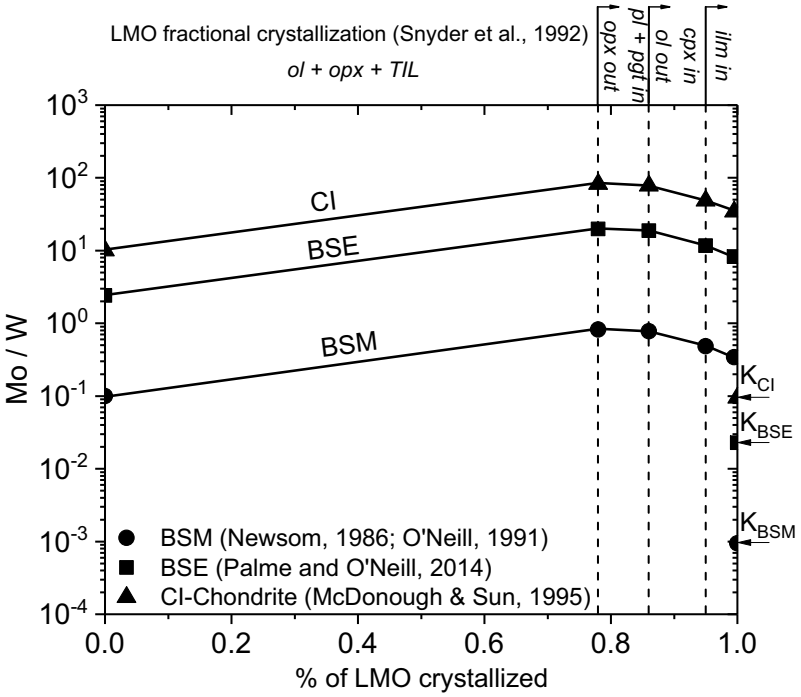

Figure 4.5: Compositional evolution of Mo/W in the residual lunar magma ocean during its crystallization according to the model of Snyder et al. (1992), assuming IW –1.5, 2% trapped interstitial residual liquid in the cumulates (cf., Snyder et al., 1992; Schönbächler et al., 2005; Münker, 2010). BSM: "canonical" bulk silicate Moon; BSE: bulk silicate earth (primitive mantle). The "K" marks on the right vertical axis are KREEP estimates considering each one of the scenarios. See text for discussion. All data included in the three different models are given in the Supplementary Material.

The last 0.5% of LMO crystallization is represented by the last residue of a magma enriched in incompatible trace elements called KREEP, which stands for K, REE and P (Warren and Wasson, 1979). A well-established

approach to constrain the functionality of the LMO crystallization model is to reproduce the trace element ratios exhibited by lunar KREEP samples i.e. the last vestige of the lunar magma ocean (cf. McKay and Weill, 1976; Warren, 1988). Unfortunately, to the best of our knowledge, KREEP values for Mo are not well constrained, with only one lunar sample (15386) being analysed for both Mo and W, with a Mo/W of 0.15 ± 0.04 (Neal and Kramer, 2003). Therefore, we adopted a different approach to estimate the Mo/W of the bulk silicate Moon, by using a reverse modelling based on the Mo/W range observed in lunar mare basalts, which are direct products of lunar mantle partial melting (e.g., Grove and Krawczynski, 2009). As a tracer for fractionation trends, we chose the Mo/Hf value since Hf is also a tetravalent element under the conditions relevant to lunar magmatism, but shows an exclusively lithophile behaviour during core formation in planetary bodies.

Three different scenarios have been considered to estimate the initial Mo content of the bulk silicate Moon and its evolution during the LMO fractionation (Fig. 4.5). In a first scenario an initial Mo/W of 0.1 is considered (i.e. "canonical" BSM; cf. Newsom, 1986; O'Neill, 1991), and the initial Hf and W concentration in the bulk silicate Moon as modelled by Münker (2010) and Fonseca et al. (2014). The second and third scenarios consider that an LMO with a BSE-like and chondritic Mo/W, i.e., 2.4 and 10, respectively, (using values from Palme and O'Neill, 2014). It is worth pointing out that Mo concentration estimates in the literature have an uncertainty of 40 % (see Palme and O'Neill, 2014), and recently Liang et al. (2017) has suggested a higher Mo concentration for the primitive upper mantle, showing that this is still a debatable topic. Trapped instantaneous liquid (TIL) was assumed (2 4 %) for all models, to account for the major element variation observed in lunar mare basalts (e.g., Warren and Taylor, 2014), as well

as 2% of entrained plagioclase to account for their Al content (cf. Snyder et al., 1992; Schönbächler et al., 2005; Münker, 2010). A lunar magma ocean equilibrated at ≈ IW –1.5 was assumed throughout the entire modelling, in agreement with the current estimates of oxygen fugacity for the lunar mantle (Papike, 2005; Nicholis and Rutherford, 2009). We also assume that a small amount (0.1 %) of residual metal may be required at the lunar mantle source to reproduce the values observed for high-Ti basalts (Fig. 4.6). The presence of residual metal in the lunar mantle source of high-Ti basalts is in agreement with the extremely reduced nature of the lunar mantle (e.g., Nicholis and Rutherford, 2009). Crystal/silicate melt partition coefficients for pyroxene, plagioclase, and olivine were selected taking into account the variation of TiO_2 exhibited by lunar mare basalts (cf., Leitzke et al., 2016) and the effect of fO_2 on the behavior of both Mo and W (see Supplementary Material for a complete list of values). Ilmenite/silicate melt partition coefficients are an average of the high-Ti experiments listed in Dygert et al. (2013). Liquid metal/silicate melt partition coefficients for W and Mo were taken from Righter et al. (2010) and Righter et al. (2016), respectively. The proportions of different cumulates in the hybrid lunar mantle sources as well as the amount of trapped instantaneous liquid (TIL) were constrained from the Lu-Hf and Sm-Nd isotope systematics of lunar basalts reported in Sprung et al. (2013) and are shown in Figure 4.6 and in the Supplementary Material.

Once aggregate modal fractional melting models of a hybrid lunar mantle source (Ringwood and Kesson, 1976; Beard et al., 1998) are evaluated, it becomes clear that assuming a BSE-like composition for the LMO yields the best fit to available Mo/W measurements from lunar mare basalts (Fig. 4.6a,b). Moreover, modelled degrees of partial melting (tick marks shown in Figure 4.6) show excellent agreement with estimates based on the MgO

content of both low and high-Ti basalts (ca. 10.1 wt.% and 8.1 wt.%, respectively; – see Binder, 1982; Meyer, 2012; Warren and Taylor, 2014).

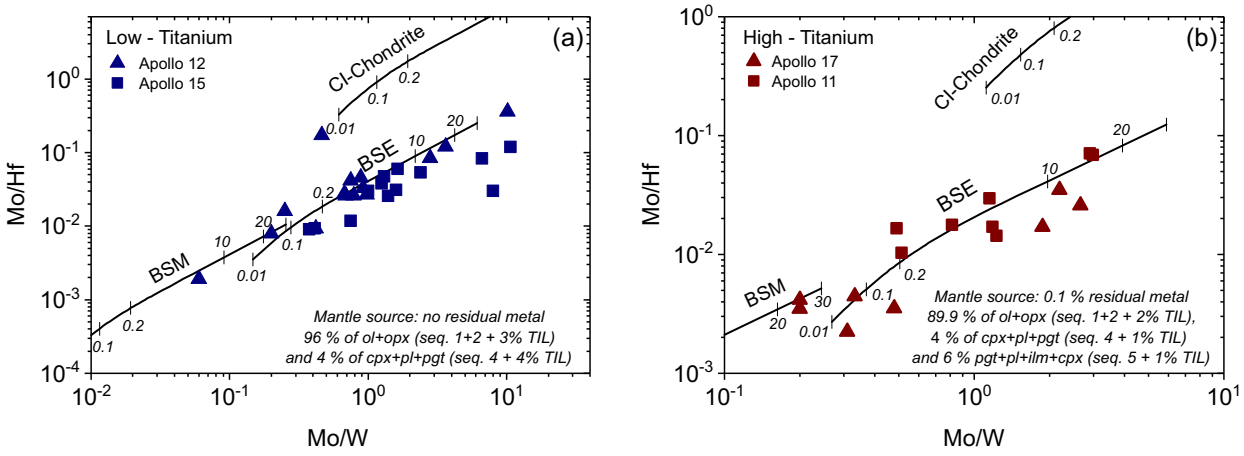

Figure 4.6: Aggregate modal fractional melting models of a hybrid lunar mantle following a mantle overturn after the crystallization of the LMO (Snyder et al., 1992). The lines represent three different scenarios, considering initial concentrations for the LMO crystallization according to estimates for bulk silicate Moon (BSM), bulk silicate Earth (BSE) and CI–chondrite. Degrees of partial melting are given by tick marks and are indicated in %. Shown are data for low (a) and high–Ti (b) lunar mare basalts from Apollo 11, 12, 15 and 17 missions. Lunar dataset for Hf, W and Mo was compiled from the literature and acquired through different techniques (Morrison et al., 1970; Taylor et al., 1971; Brunfelt et al., 1971; Klein et al., 1971; Wänke et al., 1971, 1972; Newsom, 1984a; Lee et al., 1997; Kleine et al., 2005; Neal, 2001; Münker et al., 2003; Münker, 2010). Lunar data and calculated model curves are given in the Supplementary Material.

Previous studies that aimed to constrain the Mo budget of the lunar mantle (e.g., Newsom, 1986; O'Neill, 1991) did not consider that Mo in its tetravalent state behaves almost as a compatible element during partial melting of the lunar mantle, leading to a fractionation of Mo/W in lunar basalts. The *de facto* assumption that Mo and W behave similarly during lunar mantle melting together with the lack of Mo data in the literature for lunar samples has led to an underestimation of the Mo/W of the bulk silicate Moon, which can now be easily reconciled through our new dataset

of partition coefficients coupled with new literature data for Mo/W in mare basalts (e.g., Neal, 2001).

4.5 Concluding remarks

Our results show that molybdenum undergoes a redox transition from Mo^{6+} at FMQ+2 to predominantly Mo^{4+} below FMQ–4, which is in agreement with previous studies (e.g., Righter et al., 2016). This redox transition affects the compatibility of Mo in silicates (pyroxene and olivine), with a change in $D_{Mo}^{crystal/melt}$ by three orders of magnitude over the range of fO_2 covered in this study. As a result, at extremely reducing conditions, such as those relevant to partial melting of the lunar mantle, Mo is partially retained in residual silicate phases like ortho– and clinopyroxene. As a result, Mo was likely retained in lunar mantle sources, in contrast to what occurred in Earth where Mo is a perfectly incompatible trace element (e.g., Newsom, 1984a). Once the more compatible behaviour of Mo in the lunar mantle is considered, the somewhat lower than expected lunar Mo/W ratio in mare basalts is easily explained assuming that the bulk silicate Moon composition was BSE–like. This finding is in agreement with the hypothesis that the Moon was mainly derived from terrestrial mantle material following fractionation of Earth's core (e.g., Canup, 2012; de Meijer et al., 2013). Finally, the effect of fO_2 on the behavior of Mo must be considered in any petrological models that attempt to precisely reproduce natural processes, such as mantle partial melting, by using, for instance, mass-dependent Mo isotope fractionation (e.g., Burkhardt et al., 2013), and in core formation models for planetary bodies (e.g., Rubie et al., 2003; Wade et al., 2012; Wade and Wood, 2016).

Chapter 5

Conclusions

Crystal/silicate melt partitioning of trace elements depends on several factors, such as silicate melt composition, crystal chemistry, and oxygen fugacity. Hence, performing experiments under conditions relevant to lunar magmatism, which are substantially different than those prevalent in terrestrial magmatism, are essential to model the evolution of the Moon from the Giant Impact, initial differentiation of the Lunar Magma Ocean and origin of the lunar mare basalts. For example, a specific feature of some basaltic lunar rocks is that their TiO_2 contents can reach concentrations as high as 16 wt.%. The high-field strength elements (HFSE) group, which includes Ti, provide valuable information of the processes that occurred in the lunar mantle to generate these rocks. In this regard, this study has shown that, with the exception of Nb, all $D_{HFSE}^{cpx/melt}$ have a strong negative correlation with the TiO_2 content of the silicate melt (Leitzke et al., 2016). Olivine/Silicate melt partition coefficients for Zr, Hf, Nb, Ta and Th decrease slightly from 0 to ca. 5 wt.% TiO_2, above which they remain constant up to ca. 20 wt.% TiO_2 in the silicate glass. In addition, redox sensitive elements, i.e. U, Mo, and W show clearly distinct $D_M^{silicates/melt}$ at different fO_2, implying that these elements are relatively more compatible at reduced (ca. IW -1.8) than at oxidized (FMQ and air) environments.

This redox transition affects the compatibility of Mo in silicates (pyroxene and olivine), with a change in $D_{Mo}^{crystal/melt}$ by three orders of magnitude over the range of fO_2 covered in this study. As a result, at extremely reducing conditions, such as those relevant to partial melting of the lunar mantle, Mo is partially retained in residual silicate phases like ortho– and clinopyroxene (Leitzke et al., 2017). Iron-rich and Mg-rich armalcolite show contrasting patterns of $D_M^{crystal/melt}$, with the latter exhibiting slightly higher values of partition coefficient for all analysed elements, except Th, which is equally incompatible in both end-members.

In addition to TiO_2, the Al_2O_3 and Na_2O contents of silicate melts were also shown to affect the structure of silicate melts and especially clinopyroxene crystal chemistry (Michely et al., 2017). The amount of $^{[4]}Al$ in clinopyroxene will result in an increase of $D_i^{cpx/melt}$ even after applying a correction factor to account for the effect of melt polymerization. Moreover, the positive correlation between $^{[4]}Al$ and $D_i^{cpx/melt}$ is not restricted to the REE, but also applies for Sn, Ga, In, and Ba. The addition of up to 2.6 wt% Na_2O to the silicate melt universally increases the $D_i^{cpx/melt}$ without any concomitant change in crystal chemistry or a significant effect on melt polymerization. This compositional effect is likely due to the ability of Na to break REE-Al complexes in the melt (e.g. Schösnig and Hoffer, 1998; Michely et al., 2017). Moreover, results presented here emphasize the importance of considering all variables that affect the behavior of trace elements in magmatic systems before applying the lattice strain model and derive meaningful results for the changes in the parameters of the crystallographic sites.

Applying the new dataset of crystal/silicate melt partition coefficients to lunar petrology, allowed a number of important conclusions arise, as well as explain some key geochemical differences and similarities observed in the

Earth-Moon system. First, metal saturation in the mantle sources of mare basalts is a necessity, if W is to fractionate from the HFSE, as well as U and Th, as evidenced from data obtained from the lunar sample compendium (Meyer, 2012). Second, the only way to reproduce the trace element ratios of high-Ti basalts is to assume that some Fe-Ti oxide phase was present at the mantle source, as suggested previously by Dygert et al. (2013) and in agreement with δ ^{49}Ti measurements of lunar lithologies (Millet et al., 2016). Third, once the more compatible behaviour of Mo in the lunar mantle is considered, the somewhat lower than expected lunar Mo/W ratio in mare basalts is easily explained assuming that the bulk silicate Moon composition was BSE–like. This finding is in agreement with the hypothesis that the Moon was mainly derived from terrestrial mantle material following fractionation of Earth's core (e.g., Canup, 2012; de Meijer et al., 2013).

There are two main advantage of producing crystal/silicate melt experiments in a systematic way. The first is to better understand each one of the variables governing the behavior of trace elements in magmatic systems. The second is that, as new data is acquired, for example through new remote sensing findings by spacecrafts that have recently orbited the Moon, such as the GRAIL (Gravity Recovery and Interior Laboratory, USA) and LRO (Lunar Reconnaissance Orbiter, USA), or even planned missions to land and collect new samples on the Moon (e.g., Chang'e 5, China), the geochemical models can be easily adapted to account those new findings. Moreover, the new crystal/silicate melt partitioning data can be coupled to recent experimental findings regarding the behavior of siderophile and volatile elements during formation of the lunar core (Steenstra et al., 2016, 2017) as well as updated lunar magma ocean fractional crystallization models (e.g. Elkins-Tanton et al., 2002; Elardo et al., 2011; Lin et al., 2017a,b) to perform an integrated model of lunar evolution through time.

The findings presented in this dissertation, when coupled to whole-rock trace element literature data, filled a gap regarding crystal/silicate melt partitioning data under lunar conditions, and could be applied quite reliably to the petrogenesis of lunar mare basalts, as well as lunar early evolution. Moreover, the experimental data corroborates the hypothesis that the choice of partition coefficients between crystals and silicate melt is not trivial and that changes in oxygen fugacity and crystal/melt composition need to be taken into account during geochemical modelling (e.g., van Westrenen et al., 2000; O'Neill and Eggins, 2002; van Westrenen and Draper, 2007; Borisov, 2012; Dygert et al., 2013; Mallmann and O'Neill, 2013; Fonseca et al., 2014).

–THE END–

Appendix A

Supplementary Material

A.1 Supplementary data tables

Supplementary Table 2.1 - LA-ICP-MS trace element concentrations (µg/g) of crystals and silicate glasses

Experiment	HS1		HE1		HE2		HB1		W1		W1-1			W1-2		W1-3		W1-4		W1-5		W1-6	
Phase	cpx	glass	cpx	glass	cpx	glass	cpx	glass	cpx	glass	olivine	glass	olivine	cpx	glass	cpx	glass	cpx	glass	cpx	glass	olivine	glass
Sc											74.70	756.66	66.65	583.46	725.39	914.38	554.44	1124.96	501.76	1198.54	517.51	102.05	858.09
σ											2.34	5.91	3.86	68.24	18.82	87.15	11.24	70.86	4.40	83.72	5.25	4.19	10.69
Mn											645.62	787.15	611.30	436.37	901.25	353.22	912.15	497.78	1309.13	431.40	1203.81	647.20	764.30
σ											21.54	6.79	18.52	41.60	8.95	32.03	7.95	33.10	25.95	22.64	6.30	24.11	4.57
Ni											4812.4	458.7	5688.9	888.5	647.9	567.2	394.1	555.1	364.9	540.7	396.6	3778.4	369.6
σ											135.3	10.4	111.8	63.2	9.5	25.5	27.5	21.1	12.5	22.2	14.6	117.3	5.1
Ga	598.1	838.91	655.97	1445.50	493.07	1556.35	488.02	871.89	165.00	1824.55	5.01	929.98	5.65	108.39	1150.80	166.43	1403.18	174.02	1268.92	173.11	1185.56	5.72	980.21
σ	48	41.30	27.52	42.98	26.44	66.17	59.28	23.36	15.52	24.67	0.80	8.55	0.57	13.03	18.20	18.95	15.89	7.23	24.76	7.62	8.03	0.72	9.56
Ge	102.14	42.88	3.15	1.60	144.08	56.95	62.71	38.55	2.93	1.97	7.25	1.11	5.48	1.79	1.48	6.64	2.17	7.97	2.01	12.90	2.94	19.76	1.60
σ	13.53	1.81	0.21	0.15	19.77	12.13	3.13	2.34	0.22	0.13	2.13	0.20	0.38	0.03	0.22	0.78	0.21	0.88	0.27	0.70	0.27	10.64	0.14
Y	430.51	705.33	394.84	528.63	401.58	679.90	306.33	722.18	249.39	1499.26	3.86	877.25	3.14	174.21	1095.10	259.20	1306.94	314.98	1212.15	301.04	1198.42	5.85	948.03
σ	51.21	15.10	34.08	9.06	15.21	50.59	7.12	55.33	17.24	21.64	0.28	8.11	0.21	12.46	23.86	28.27	28.87	42.29	15.42	20.11	15.14	0.44	5.13
Zr											0.26	788.43	0.22	23.15	1084.18	59.30	1248.17	103.93	1164.45	127.26	1168.92	0.26	802.88
σ											0.04	5.39	0.03	6.52	26.78	8.97	25.18	8.26	14.67	18.63	19.74	0.01	3.78
Nb														1.40	1148.24	3.02	1457.59	5.05	1329.60	6.77	1318.03		
σ														0.22	16.87	0.29	25.87	0.86	16.79	2.20	7.90		
Rh	42.07	3.62	28.21	2.07	159.31	9.18	46.13	8.20	58.10	18.56	43.39	20.23	36.08	56.09	19.58	19.10	4.48	28.98	4.79	19.95	3.81	51.85	19.16
σ	24.37	0.26	8.06	0.06	31.56	1.46	26.31	3.25	9.87	0.67	7.31	0.25	2.41	4.09	0.83	3.07	0.27	6.85	0.12	1.79	0.20	6.18	0.30
In	1252	581.50	586.92	413.62	584.75	425.06			315.12	961.60	56.88	507.51	28.04	113.65	347.09	358.79	431.68	389.42	409.09	516.23	530.54	49.82	411.66
σ	168.26	26.24	51.21	10.43	44.67	51.83			35.93	34.57	2.95	2.22	0.78	9.23	5.72	21.51	9.26	16.72	7.36	28.00	6.66	3.37	5.33
Sn	136.37	11.57	4.31	1.52	178.16	50.15	34.96	5.89	2.64	5.51				1.00	5.31	1.44	3.11	1.76	4.35	4.24	6.36		
σ	35.55	0.40	0.43	0.08	25.81	13.86	6.56	0.35	0.66	0.32				0.42	0.26	0.28	0.09	0.15	0.61	0.64	0.53		
Ba	0.27	173.27	0.22	133.43	0.14	161.14	0.22	277.13	0.04	139.33	0.004	1544.42	0.003	0.25	2040.84	0.58	3023.40	0.76	2947.45	0.65	2845.96	0.03	1906.27
σ	0.15	2.61	0.12	2.11	0.04	10.41	0.06	13.90	0.03	1.83	0.001	8.88	0.002	0.02	29.36	0.07	42.26	0.11	62.59	0.05	22.63	0.01	8.13
La	79.82396	631.65	108.40	970.06	112.76	1214.15	120.95	1455.68	3.09	118.46	0.004	832.49	0.004	26.80	1062.18	58.53	1351.25	80.48	1223.70	74.79	1226.87	0.00	882.26
σ	16.66	9.74	13.51	15.28	10.63	89.55	16.92	132.29	0.47	1.73	0.001	4.54	0.001	3.82	15.55	2.09	29.87	20.69	25.21	7.65	10.29	0.001	5.88
Sm	595.07	1077.26	0.50	0.85	640.82	1331.98	711.74	2002.82	246.47	1977.09	0.24	1107.79	0.20	171.76	1395.42	289.25	1650.32	369.38	1518.73	350.69	1534.69	0.43	1164.47
σ	75.14	20.91	0.05	0.07	30.09	96.31	92.51	138.52	21.36	24.37	0.05	9.81	0.01	17.21	6.93	28.99	32.14	50.08	21.33	24.33	19.83	0.11	16.70
Eu	677.097	1136.44	0.13	0.19	706.23	1343.00	779.70	2068.73	275.97	2033.72	0.43	1163.77	0.35	194.90	1451.98	320.71	1685.56	394.55	1566.88	379.67	1559.74	0.69	1243.15
σ	82.6	14.84	0.02	0.01	30.25	92.89	100.17	108.83	22.54	38.32	0.02	5.02	0.02	17.61	20.95	33.56	21.36	52.97	16.90	28.12	17.97	0.08	7.52
Lu	451.1891	782.61	566.77	857.45	576.76	1034.90	150.82	356.12	5.20	31.37	17.77	1005.19	15.09	185.93	1241.29	286.54	1434.78	363.71	1325.41	351.38	1347.29	26.23	1071.52
σ	47.17	24.97	58.46	16.50	22.73	138.29	20.70	28.43	0.39	0.44	0.71	6.22	0.70	16.90	18.47	26.71	36.53	46.76	25.12	23.73	15.17	1.67	9.14
Hf											0.44	907.95	0.40	55.64	1181.04	148.24	1358.45	258.27	1288.91	311.80	1347.34	0.37	944.28
σ											0.08	6.80	0.02	17.39	29.05	21.94	27.13	16.49	24.22	39.93	14.42	0.08	14.04
Ta											0.02	925.91	0.01	1.45	1301.18	4.03	1425.19	8.15	1340.27	17.29	1612.68	0.04	847.29
σ											0.01	5.23	0.01	0.51	24.17	0.90	30.47	1.63	37.59	6.74	18.13	0.03	7.78
Pt	0.59	5.79	0.18	2.95	0.07	1.75	0.33	8.15	0.09	5.28				0.21	9.17	0.45	9.99	0.87	9.78	0.93	8.73		
σ	0.27	0.34	0.01	0.08	0.02	0.19	0.08	1.68	0.03	0.25				0.05	0.39	0.10	1.79	0.20	0.45	0.16	0.55		
Th											0.001	1019.81	0.0025	2.05	1423.36	6.54	1913.38	7.93	1736.70	12.15	1759.89		865.42
σ											0.0004	139.65	0.0020	0.62	10.73	0.56	34.26	1.54	41.05	2.84	17.47		83.68
U														0.003	43.14	0.017	81.58	0.019	109.80	0.034	164.81		
σ														0.001	1.34	0.003	1.56	0.002	5.90	0.008	9.34		

Supplementary Table 3.1 - Gas mixtures (SCCM) used in the experiments in order to achieve the desired oxygen fugacity

Temp. (° C)	log fO_2	Δ FMQ	Δ IW	CO	CO_2
1230	-8.2	-0.1	3.4	10	190
1250	-7.7	0.1	3.6	10	240
1260	-7.8	0.0	3.4	15	300
1270	-7.7	0.0	3.4	15	300
1280	-7.4	0.1	3.6	10	210
1300	-7.3	0.0	3.5	10	160
1100	-15.1	-5.4	-1.8	90	4
1200	-13.5	-5.0	-1.5	110	4
1250	-12.9	-5.1	-1.6	130	4
1280	-12.6	-5.1	-1.6	140	4
1290	-12.6	-5.2	-1.7	170	4
1300	-12.3	-5.0	-1.6	150	3
1310	-12.4	-5.2	-1.8	170	3

SCCM: sccm standard cubic centimeter per minute; FMQ: Fayalite-Magnetite-Quartz redox buffer (O'Neill, 1987) and IW: Iron-wüstite redox buffer (Myers and Eugster, 1983)

Supplementary Table 3.2 - Major elements composition (cg/g) of main crystal phases and coexistent silicate glasses

Experiment	Temp. (° C)	Δ to redox buffer[a]	Phase	CaO	σ	MgO	σ	Al_2O_3	σ	SiO_2	σ	TiO_2	σ	FeO	σ	P_2O_5	σ	Cr_2O_3	σ	MnO[1]	σ	Na_2O[2]	σ	Total	NBO/T [3]	OB [3]
T1 + 0% Ti	1305	air	Cpx	22.76	(0.17)	19.60	(0.16)	1.42	(0.06)	54.32	(0.29)	bdl	bdl	0.06	(0.05)	0.01	(0.01)	0.83	(0.14)	0.21	(0.02)	n/a	-	99.21	-	-
			Ol	0.59	(0.04)	54.61	(0.32)	0.03	(0.01)	42.57	(0.23)	bdl	bdl	0.13	(0.05)	0.08	(0.02)	0.14	(0.01)	0.39	(0.05)	n/a	-	98.53	-	-
			Silicate Glass	19.32	(0.12)	15.85	(0.05)	10.46	(0.08)	50.28	(0.25)	0.56	(0.07)	0.10	(0.05)	1.16	(0.04)	0.12	(0.02)	0.46	(0.05)	n/a	-	98.33	1.21	0.601
T1 + 0% Ti	1300	FMQ = 0.0	Cpx	22.28	(0.34)	20.03	(0.44)	1.05	(0.18)	55.60	(0.21)	bdl	bdl	0.12	(0.06)	0.02	(0.02)	1.05	(0.18)	0.36	(0.07)	n/a	-	100.52	-	-
			Ol	0.54	(0.03)	54.33	(0.21)	0.05	(0.01)	43.10	(0.29)	bdl	bdl	0.24	(0.07)	0.03	(0.02)	0.06	(0.02)	0.93	(0.04)	n/a	-	99.27	-	-
			Silicate Glass	19.12	(0.02)	14.63	(0.11)	11.19	(0.07)	51.02	(0.35)	0.08	(0.04)	0.19	(0.07)	1.35	(0.03)	0.05	(0.02)	1.06	(0.05)	n/a	-	98.61	1.12	0.598
T1 + 0% Ti	1300	IW - 1.6	Cpx	22.78	(0.45)	20.80	(0.24)	1.22	(0.10)	56.16	(0.34)	bdl	bdl	0.01	(0.01)	0.03	(0.02)	0.19	(0.03)	0.19	(0.04)	n/a	-	101.39	-	-
			Ol	0.58	(0.05)	55.77	(0.18)	0.04	(0.01)	43.00	(0.39)	bdl	bdl	0.01	(0.01)	0.12	(0.06)	0.06	(0.04)	0.27	(0.04)	n/a	-	99.84	-	-
			Silicate Glass	19.63	(0.10)	15.29	(0.10)	11.54	(0.08)	53.07	(0.30)	0.08	(0.03)	bdl	bdl	0.32	(0.06)	0.07	(0.02)	0.26	(0.02)	n/a	-	100.26	1.11	0.598
T1 + 1% Ti	1295	air	Cpx	23.60	(0.45)	19.61	(0.28)	1.10	(0.03)	55.78	(0.31)	0.39	(0.05)	0.19	(0.02)	0.02	(0.01)	0.06	(0.03)	n/a	-	n/a	-	100.75	-	-
			Ol	0.86	(0.10)	53.51	(0.58)	0.20	(0.10)	43.75	(0.78)	0.02	(0.02)	0.20	(0.07)	0.08	(0.06)	0.02	(0.01)	n/a	-	n/a	-	98.64	-	-
			Silicate Glass	20.86	(0.11)	14.55	(0.10)	10.57	(0.16)	49.36	(0.28)	1.98	(0.05)	0.80	(0.05)	1.13	(0.05)	0.01	(0.00)	n/a	-	n/a	-	99.25	1.20	0.605
T1 + 1% Ti	1300	FMQ = 0.0	Cpx	23.03	(0.20)	19.31	(0.20)	1.70	(0.08)	54.52	(0.42)	0.37	(0.06)	0.16	(0.05)	0.04	(0.03)	0.77	(0.05)	n/a	-	n/a	-	99.90	-	-
			Ol	0.67	(0.02)	54.29	(0.40)	0.04	(0.02)	43.28	(0.28)	0.02	(0.02)	0.21	(0.02)	0.03	(0.02)	0.03	(0.02)	n/a	-	n/a	-	98.57	-	-
			Silicate Glass	19.26	(0.20)	15.24	(0.15)	9.88	(0.07)	50.94	(0.10)	2.02	(0.06)	0.35	(0.05)	0.96	(0.07)	0.06	(0.02)	n/a	-	n/a	-	98.71	1.16	0.599
T1 + 1% Ti	1300	IW - 1.6	Ol	0.56	(0.01)	56.35	(0.17)	0.03	(0.02)	43.47	(0.54)	0.02	(0.01)	0.02	(0.02)	0.05	(0.04)	0.02	(0.02)	0.07	0.03	n/a	-	100.58	-	-
			Silicate Glass	21.18	(0.09)	16.61	(0.15)	6.41	(0.10)	54.19	(0.48)	2.22	(0.06)	0.01	(0.01)	0.23	(0.02)	0.01	(0.01)	0.04	0.02	n/a	-	100.90	1.37	0.603
T1 + 2% Ti	1300	FMQ = 0.0	Cpx	21.95	(0.33)	19.76	(0.39)	1.55	(0.21)	54.45	(0.46)	0.95	(0.05)	0.06	(0.02)	0.04	(0.03)	0.98	(0.20)	0.45	0.06	n/a	-	100.18	-	-
			Ol	0.55	(0.03)	54.68	(0.21)	0.02	(0.01)	43.11	(0.18)	0.01	(0.01)	0.13	(0.03)	0.07	(0.02)	0.13	(0.04)	0.56	(0.09)	n/a	-	99.27	-	-
			Silicate Glass	18.24	(0.38)	15.25	(0.42)	9.02	(0.09)	49.63	(0.15)	4.16	(0.09)	0.08	(0.06)	1.11	(0.04)	0.10	(0.02)	0.92	(0.03)	n/a	-	98.51	1.15	0.597
T1 + 2% Ti	1300	IW - 1.6	Cpx	19.74	(0.69)	23.12	(0.67)	0.97	(0.20)	56.41	(0.66)	0.48	(0.08)	0.01	(0.01)	0.02	(0.01)	0.20	(0.03)	0.40	(0.05)	n/a	-	101.34	-	-
			Pgt	4.25	(0.30)	35.53	(0.27)	0.42	(0.11)	59.34	(0.39)	0.22	(0.04)	bdl	bdl	0.02	(0.02)	0.12	(0.04)	0.59	(0.09)	n/a	-	100.49	-	-
			Silicate Glass	16.25	(0.08)	13.62	(0.09)	12.27	(0.08)	53.50	(0.36)	2.31	(0.12)	bdl	bdl	0.73	(0.06)	0.07	(0.03)	0.34	(0.04)	n/a	-	99.09	0.87	0.586
T1 + 3% Ti	1305	air	Cpx	21.67	(0.22)	20.67	(0.32)	1.10	(0.23)	54.36	(0.43)	1.21	(0.22)	0.15	(0.05)	0.02	(0.02)	0.03	(0.01)	0.20	(0.04)	n/a	-	99.41	-	-
			Ol	0.47	(0.02)	54.49	(0.13)	0.04	(0.01)	42.90	(0.05)	0.02	(0.02)	0.13	(0.04)	0.11	(0.07)	0.02	(0.01)	0.29	(0.06)	n/a	-	98.47	-	-
			Silicate Glass	17.86	(0.13)	14.80	(0.25)	8.30	(0.05)	49.41	(0.59)	5.79	(0.11)	0.61	(0.02)	0.94	(0.05)	0.01	(0.01)	0.47	(0.03)	n/a	-	98.20	1.16	0.599
T1 + 3% Ti	1300	FMQ = 0.0	Cpx	21.48	(0.42)	20.41	(0.37)	1.19	(0.06)	54.85	(0.16)	1.01	(0.07)	0.13	(0.04)	0.04	(0.02)	1.15	(0.15)	0.37	(0.07)	n/a	-	100.64	-	-
			Ol	0.48	(0.02)	54.57	(0.13)	0.02	(0.02)	43.37	(0.13)	0.02	(0.02)	0.38	(0.05)	0.11	(0.07)	0.18	(0.03)	0.48	(0.02)	n/a	-	99.61	-	-
			Silicate Glass	17.15	(0.11)	15.27	(0.11)	8.29	(0.09)	50.25	(0.17)	5.47	(0.11)	0.31	(0.05)	0.85	(0.01)	0.14	(0.02)	0.83	(0.09)	n/a	-	98.56	1.12	0.595
T1 + 3% Ti	1300	IW - 1.6	Ol	0.52	(0.01)	56.09	(0.27)	0.02	(0.02)	43.85	(0.24)	0.04	(0.02)	0.03	(0.02)	0.04	(0.02)	0.08	(0.02)	0.22	(0.03)	n/a	-	100.89	-	-
			Silicate Glass	16.78	(0.08)	10.92	(0.22)	11.00	(0.13)	51.64	(0.38)	7.32	(0.20)	bdl	bdl	0.93	(0.06)	0.05	(0.03)	0.22	(0.03)	n/a	-	98.86	0.79	0.585
T1 + 5% Ti	1305	air	Ol	0.49	(0.01)	54.33	(0.19)	0.04	(0.01)	42.84	(0.13)	0.02	(0.01)	0.09	(0.06)	0.09	(0.06)	0.01	(0.01)	0.30	(0.06)	n/a	-	98.20	-	-
			Silicate Glass	20.08	(0.06)	14.79	(0.19)	6.29	(0.12)	51.03	(0.86)	6.49	(0.12)	0.13	(0.08)	0.64	(0.11)	0.22	(0.03)	0.43	(0.05)	n/a	-	100.10	1.26	0.601
T1 + 5% Ti	1270	FMQ = 0.0	Cpx	22.47	(0.18)	19.72	(0.43)	1.36	(0.39)	54.31	(0.64)	1.25	(0.08)	0.05	(0.02)	0.02	(0.01)	0.85	(0.15)	0.43	(0.09)	n/a	-	100.68	-	-
			Ol	0.50	(0.02)	55.14	(0.23)	0.04	(0.01)	43.15	(0.28)	0.02	(0.02)	0.05	(0.02)	0.06	(0.03)	0.13	(0.02)	0.73	(0.07)	n/a	-	99.82	-	-
			Silicate Glass	18.48	(0.08)	15.57	(0.20)	9.02	(1.27)	48.14	(0.19)	6.69	(0.13)	0.06	(0.05)	0.91	(0.07)	0.06	(0.05)	0.98	(0.10)	n/a	-	99.90	1.19	0.603
T1 + 5% Ti	1300	IW - 1.6	Ol	0.48	(0.02)	55.61	(0.19)	0.03	(0.01)	42.63	(0.62)	0.05	(0.01)	0.07	(0.04)	0.08	(0.07)	0.14	(0.03)	0.42	(0.06)	n/a	-	99.49	-	-
			Silicate Glass	20.00	(0.17)	14.77	(0.11)	6.33	(0.08)	50.75	(0.51)	6.41	(0.07)	0.07	(0.06)	0.60	(0.06)	0.22	(0.02)	0.50	(0.06)	n/a	-	99.63	1.26	0.601
T1 + 5% Ti	1290	IW - 1.7	Cpx	22.11	(0.25)	20.48	(0.10)	1.11	(0.19)	54.04	(0.14)	1.54	(0.11)	0.14	(0.04)	0.01	(0.01)	0.02	(0.02)	0.31	(0.02)	n/a	-	99.75	-	-
			Silicate Glass	18.21	(0.10)	14.95	(0.12)	7.77	(0.06)	47.84	(0.21)	7.31	(0.19)	0.47	(0.04)	0.75	(0.06)	0.01	(0.01)	0.50	(0.04)	n/a	-	97.81	1.20	0.603
T1 + 10% Ti	1260	FMQ = 0.0	Cpx	19.55	(1.07)	22.51	(0.87)	0.77	(0.07)	55.07	(0.28)	1.81	(0.23)	0.01	(0.01)	0.01	(0.01)	0.71	(0.09)	n/a	-	n/a	-	100.79	-	-
			Silicate Glass	16.17	(0.04)	15.25	(0.16)	6.11	(0.11)	47.42	(0.43)	13.11	(0.10)	0.03	(0.03)	0.46	(0.04)	0.25	(0.04)	n/a	-	n/a	-	98.73	1.12	0.597
T1 + 10% Ti	1250	IW - 1.6	Cpx	20.06	(0.91)	22.73	(0.84)	0.88	(0.09)	54.76	(0.69)	2.56	(0.26)	0.01	(0.01)	0.02	(0.02)	0.03	(0.03)	0.05	(0.03)	n/a	-	101.10	-	-
			Pgt	2.71	(0.15)	36.78	(0.29)	0.60	(0.19)	58.06	(0.51)	1.35	(0.27)	bdl	bdl	0.02	(0.01)	0.03	(0.01)	0.05	(0.03)	n/a	-	99.61	-	-
			Silicate Glass	16.25	(0.17)	13.81	(0.07)	8.08	(0.06)	46.28	(0.24)	15.05	(0.16)	bdl	bdl	0.41	(0.03)	0.02	(0.01)	0.07	(0.02)	n/a	-	99.96	0.99	0.598
T1 + 20% Ti	1250	FMQ + 0.1	Ol	0.25	(0.01)	55.74	(0.36)	0.02	(0.02)	42.69	(0.20)	0.12	(0.05)	0.06	(0.02)	0.05	(0.04)	0.08	(0.03)	n/a	-	n/a	-	99.02	-	-
			Arm	0.36	(0.07)	18.14	(0.16)	1.32	(0.03)	0.19	(0.02)	77.14	(0.37)	0.05	(0.04)	bdl	bdl	3.90	(0.21)	n/a	-	n/a	-	101.09	-	-
			Silicate Glass	15.29	(0.06)	14.77	(0.16)	5.09	(0.05)	43.28	(0.18)	19.83	(0.19)	0.06	(0.05)	0.48	(0.03)	0.19	(0.03)	n/a	-	n/a	-	99.00	1.09	0.601
T1 + 20% Ti	1260	FMQ = 0.0	Cpx	20.28	(0.79)	21.68	(0.80)	1.17	(0.04)	53.59	(0.63)	2.76	(0.44)	0.04	(0.03)	0.02	(0.01)	0.41	(0.05)	n/a	-	n/a	-	99.66	-	-
			Arm	0.12	(0.05)	18.36	(0.11)	1.89	(0.02)	0.21	(0.02)	78.26	(0.28)	0.07	(0.04)	bdl	bdl	1.21	(0.10)	n/a	-	n/a	-	100.11	-	-
			Rt	0.05	(0.03)	0.02	(0.01)	0.13	(0.02)	0.10	(0.05)	97.45	(0.66)	0.07	(0.01)	0.02	(0.02)	0.70	(0.14)	n/a	-	n/a	-	98.53	-	-
			Silicate Glass	15.74	(0.05)	11.93	(0.07)	7.60	(0.06)	45.87	(0.22)	16.20	(0.20)	0.04	(0.06)	0.74	(0.05)	0.08	(0.01)	n/a	-	n/a	-	98.17	0.89	0.593
T1 + 20% Ti	1240	air	Ol	0.26	(0.02)	55.90	(0.18)	0.01	(0.00)	43.45	(0.13)	0.07	(0.03)	0.08	(0.05)	0.09	(0.06)	0.03	(0.03)	n/a	-	n/a	-	99.87	-	-
			Arm	0.06	(0.04)	18.95	(0.21)	1.35	(0.08)	0.22	(0.03)	78.86	(1.46)	1.56	(0.05)	0.01	(0.00)	0.09	(0.03)	n/a	-	n/a	-	101.10	-	-

Supplementary Table 3.2 - Major elements composition (cg/g) of main crystal phases and coexistent silicate glasses

Experiment	Temp. (° C)	Δ to redox buffer[a]	Phase	CaO	σ	MgO	σ	Al_2O_3	σ	SiO_2	σ	TiO_2	σ	FeO	σ	P_2O_5	σ	Cr_2O_3	σ	MnO[1]	σ	Na_2O[2]	σ	Total	NBO/T [3]	OB [3]
			Silicate Glass	15.92	(0.17)	14.22	(0.14)	4.98	(0.06)	43.21	(0.11)	20.67	(0.15)	0.47	(0.08)	0.54	(0.04)	0.02	(0.02)	n/a	-	n/a	-	100.04	1.10	0.603
T1 + 20% Ti	1250	IW - 1.6	Cpx	20.73	(0.14)	22.19	(0.26)	0.95	(0.13)	54.60	(0.34)	3.10	(0.14)	0.02	(0.01)	bdl	bdl	0.04	(0.004)	n/a	-	n/a	-	101.61	-	-
			Pgt	2.76	(0.16)	37.06	(0.24)	0.45	(0.04)	59.67	(0.14)	1.39	(0.14)	0.02	(0.02)	bdl	bdl	0.02	(0.01)	n/a	-	n/a	-	101.37	-	-
			Arm	0.11	(0.09)	15.58	(0.16)	1.42	(0.05)	0.09	(0.02)	86.41	(0.43)	0.04	(0.01)	0.01	(0.01)	0.11	(0.02)	n/a	-	n/a	-	103.77	-	-
			Silicate Glass	16.29	(0.06)	13.23	(0.07)	7.16	(0.08)	47.35	(0.26)	16.41	(0.14)	bdl	bdl	0.31	(0.03)	0.01	(0.01)	n/a	-	n/a	-	100.76	0.96	0.596
T7 + 0% Ti	1280	FMQ + 0.1	Cpx	22.84	(0.15)	19.92	(0.16)	1.23	(0.11)	55.88	(0.30)	bdl	bdl	0.02	(0.02)	0.01	(0.01)	1.13	(0.19)	0.35	(0.04)	n/a	-	101.38	-	-
			Silicate Glass	18.96	(0.03)	14.49	(0.08)	12.20	(0.12)	50.26	(0.16)	0.10	(0.06)	0.02	(0.02)	1.69	(0.06)	0.18	(0.02)	1.11	(0.08)	n/a	-	99.01	1.05	0.595
T7 + 1% Ti	1300	FMQ = 0.0	Cpx	20.72	(0.16)	20.95	(0.26)	1.06	(0.05)	54.62	(0.68)	0.27	(0.05)	0.12	(0.04)	0.02	(0.02)	1.22	(0.08)	n/a	-	n/a	-	98.98	-	-
			Silicate Glass	17.21	(0.04)	16.09	(0.13)	8.92	(0.10)	53.38	(0.27)	1.77	(0.09)	0.26	(0.07)	0.67	(0.06)	0.30	(0.01)	n/a	-	n/a	-	98.60	1.13	0.591
T7 + 1% Ti	1280	air	Cpx	22.49	(0.46)	20.88	(0.36)	1.12	(0.19)	56.23	(0.19)	0.50	(0.06)	0.19	(0.04)	0.03	(0.01)	0.03	(0.02)	n/a	-	n/a	-	101.49	-	-
			Silicate Glass	17.82	(0.12)	14.94	(0.11)	10.65	(0.09)	52.91	(0.22)	2.04	(0.10)	0.94	(0.06)	1.07	(0.04)	bdl	bdl	n/a	-	n/a	-	100.38	1.06	0.593
T7 + 2% Ti	1280	FMQ + 0.1	Cpx	22.91	(0.26)	19.24	(0.16)	1.91	(0.31)	54.24	(0.61)	1.03	(0.08)	0.02	(0.02)	0.02	(0.02)	1.33	(0.22)	0.38	(0.10)	n/a	-	101.09	-	-
			Ol	bdl	bdl	54.91	(0.23)	0.02	(0.01)	43.56	(0.20)	0.03	(0.02)	bdl	bdl	0.05	(0.02)	0.14	(0.03)	0.93	(0.07)	n/a	-	99.63	-	-
			Silicate Glass	18.22	(0.04)	14.77	(0.10)	9.76	(0.12)	48.69	(0.20)	5.17	(0.10)	0.04	(0.04)	1.09	(0.03)	0.23	(0.03)	0.84	(0.10)	n/a	-	98.82	1.10	0.597
T7 + 3% Ti	1280	FMQ + 0.1	Cpx	22.13	(0.09)	19.12	(0.21)	1.67	(0.10)	52.91	(0.45)	1.60	(0.15)	bdl	bdl	0.01	(0.01)	1.25	(0.24)	0.37	(0.03)	n/a	-	99.06	-	-
			Ol	bdl	bdl	54.43	(0.05)	0.04	(0.02)	42.75	(0.12)	0.04	(0.01)	0.03	(0.02)	0.53	(0.09)	0.16	(0.02)	0.53	(0.09)	n/a	-	98.51	-	-
			Silicate Glass	17.27	(0.10)	15.02	(0.11)	8.03	(0.10)	47.59	(0.06)	7.00	(0.12)	0.03	(0.02)	1.16	(0.04)	0.27	(0.01)	0.85	(0.04)	n/a	-	97.22	1.14	0.597
T7 + 5% Ti	1280	FMQ + 0.1	Cpx	21.37	(0.62)	21.10	(0.90)	1.05	(0.35)	54.83	(0.66)	1.12	(0.24)	0.02	(0.02)	bdl	bdl	1.21	(0.33)	n/a	-	n/a	-	100.72	-	-
			Ol	0.48	(0.01)	55.86	(0.28)	0.02	(0.02)	43.43	(0.14)	0.04	(0.02)	0.04	(0.02)	0.10	(0.07)	0.16	(0.04)	n/a	-	n/a	-	100.12	-	-
			Silicate Glass	17.59	(0.07)	14.89	(0.02)	8.54	(0.02)	47.96	(0.15)	8.61	(0.30)	0.05	(0.03)	0.66	(0.03)	0.31	(0.03)	n/a	-	n/a	-	98.61	1.10	0.598
T7 + 5% Ti	1280	IW - 1.6	Ol	0.53	(0.01)	54.42	(0.15)	0.03	(0.02)	43.09	(0.32)	0.04	(0.01)	0.05	(0.01)	0.05	(0.02)	0.69	(0.10)	0.36	(0.02)	n/a	-	99.25	-	-
			Silicate Glass	20.45	(0.10)	14.64	(0.10)	6.34	(0.04)	50.98	(0.22)	5.95	(0.05)	0.03	(0.02)	0.31	(0.07)	0.56	(0.03)	0.38	(0.04)	n/a	-	99.64	1.27	0.601
T7 + 10% Ti	1280	FMQ + 0.1	Cpx	20.53	(0.93)	21.28	(0.95)	0.90	(0.24)	54.09	(0.64)	1.76	(0.18)	0.04	(0.04)	0.03	(0.02)	1.01	(0.21)	n/a	-	n/a	-	99.64	-	-
			Ol	0.45	(0.01)	54.15	(0.52)	0.04	(0.01)	42.93	(0.59)	0.06	(0.02)	0.22	(0.01)	0.10	(0.02)	0.19	(0.01)	n/a	-	n/a	-	98.13	-	-
			Silicate Glass	16.94	(0.09)	15.53	(0.01)	5.63	(0.03)	46.57	(0.19)	13.09	(0.39)	0.05	(0.01)	0.42	(0.05)	0.38	(0.05)	n/a	-	n/a	-	98.62	1.19	0.600
T7 + 10% Ti	1280	IW - 1.6	Cpx	21.58	(0.45)	21.53	(0.39)	1.07	(0.04)	54.47	(0.18)	2.76	(0.18)	0.03	(0.02)	0.02	(0.02)	0.08	(0.03)	n/a	-	n/a	-	101.54	-	-
			Ol	0.36	(0.01)	55.75	(0.26)	0.03	(0.01)	43.46	(0.17)	0.11	(0.02)	0.01	(0.01)	0.03	(0.03)	0.04	(0.03)	n/a	-	n/a	-	99.79	-	-
			Silicate Glass	16.57	(0.15)	14.83	(0.14)	7.36	(0.03)	48.23	(0.19)	12.69	(0.18)	bdl	bdl	0.16	(0.02)	0.03	(0.03)	n/a	-	n/a	-	99.87	1.07	0.598
T7 + 20% Ti	1273	air	Arm	0.10	(0.09)	18.77	(0.12)	1.25	(0.03)	0.25	(0.06)	77.23	(0.50)	1.65	(0.03)	bdl	bdl	0.03	(0.03)	n/a	-	n/a	-	99.27	-	-
			Silicate Glass	14.72	(0.04)	14.52	(0.06)	4.82	(0.03)	44.21	(0.25)	21.35	(0.20)	0.52	(0.07)	0.43	(0.03)	0.02	(0.02)	n/a	-	n/a	-	100.59	1.06	0.599
T7 + 20% Ti	1250	FMQ + 0.1	Arm	0.11	(0.07)	16.68	(0.17)	1.13	(0.08)	0.29	(0.03)	73.89	(3.39)	0.25	(0.07)	bdl	bdl	6.90	(0.23)	n/a	-	n/a	-	99.25	-	-
			Ol	0.25	(0.01)	55.74	(0.36)	0.02	(0.02)	42.69	(0.20)	0.12	(0.05)	0.06	(0.02)	0.05	(0.04)	0.08	(0.03)	n/a	-	n/a	-	99.02	-	-
			Pgt	3.33	(0.20)	35.58	(0.19)	0.34	(0.03)	58.33	(0.18)	1.18	(0.08)	0.19	(0.05)	bdl	bdl	0.46	(0.03)	n/a	-	n/a	-	99.40	-	-
			Silicate Glass	15.49	(0.09)	13.96	(0.17)	4.68	(0.10)	44.37	(0.11)	18.90	(0.18)	0.24	(0.09)	0.47	(0.06)	0.43	(0.02)	n/a	-	n/a	-	98.53	1.07	0.598
T7 + 20% Ti	1230	FMQ - 0.1	Cpx	19.73	(0.90)	22.68	(0.87)	0.76	(0.15)	54.33	(0.89)	2.00	(0.23)	0.05	(0.03)	bdl	bdl	0.94	(0.20)	n/a	-	n/a	-	100.48	-	-
			Pgt	2.85	(0.19)	36.76	(0.30)	0.53	(0.05)	59.61	(0.60)	1.19	(0.06)	0.08	(0.02)	bdl	bdl	0.50	(0.05)	n/a	-	n/a	-	101.53	-	-
			Arm	0.39	(0.08)	16.60	(0.23)	1.40	(0.08)	0.15	(0.02)	74.64	(0.78)	0.02	(0.02)	bdl	bdl	7.49	(0.40)	n/a	-	n/a	-	100.69	-	-
			Silicate Glass	15.17	(0.07)	12.40	(0.08)	6.38	(0.08)	48.30	(0.15)	16.05	(0.21)	0.04	(0.03)	0.64	(0.06)	0.27	(0.03)	n/a	-	n/a	-	99.27	0.90	0.588
ST1 + 5% Ti	1260	FMQ = 0.0	Cpx	22.64	(0.39)	17.77	(0.06)	3.79	(0.34)	51.36	(0.63)	2.66	(0.26)	2.17	(0.13)	0.03	(0.02)	0.21	(0.05)	n/a	-	bdl	bdl	100.64	-	-
			Silicate Glass	17.60	(0.05)	10.72	(0.08)	11.50	(0.13)	45.04	(0.08)	7.75	(0.11)	5.82	(0.21)	0.56	(0.01)	0.02	(0.02)	n/a	-	0.08	(0.02)	99.08	1.02	0.609
ST1 + 10% Ti	1260	FMQ = 0.0	Cpx	23.04	(0.25)	17.59	(0.25)	3.52	(0.64)	50.40	(1.05)	3.68	(0.58)	1.65	(0.09)	0.02	(0.01)	0.22	(0.05)	n/a	-	0.02	(0.01)	100.14	-	-
			Silicate Glass	18.12	(0.12)	10.46	(0.09)	10.16	(0.11)	43.85	(0.22)	12.06	(0.23)	3.67	(0.12)	0.43	(0.04)	0.04	(0.02)	n/a	-	0.09	(0.03)	98.87	0.99	0.608
T5 + 0% Ti	1300	FMQ = 0.0	Opx	0.53	(0.07)	37.45	(0.27)	0.61	(0.06)	59.84	(0.30)	bdl	bdl	0.18	(0.03)	bdl	bdl	0.61	(0.05)	0.51	(0.04)	n/a	-	99.73	-	-
			Silicate Glass	14.95	(0.18)	14.25	(0.11)	12.16	(0.13)	55.47	(0.07)	0.06	(0.02)	0.17	(0.06)	0.53	(0.04)	0.23	(0.04)	0.92	(0.11)	n/a	-	98.74	0.86	0.580
T5 + 0% Ti	1300	IW - 1.8	Opx	0.52	0.03	38.40	0.74	0.33	0.05	59.91	1.22	bdl	bdl	0.03	0.02	0.01	(0.01)	0.12	0.06	0.19	(0.04)	n/a	-	99.53	-	-
			Silicate Glass	14.93	(0.03)	14.72	(0.10)	12.46	(0.06)	57.33	(0.27)	0.04	(0.03)	0.04	(0.004)	0.12	(0.01)	0.01	(0.01)	0.05	(0.03)	n/a	-	99.71	0.85	0.580
T5 + 1% Ti	1300	FMQ = 0.0	Opx	0.56	(0.05)	37.79	(0.80)	0.44	(0.19)	60.08	(0.38)	0.11	(0.02)	0.27	(0.14)	bdl	bdl	0.20	(0.20)	n/a	-	n/a	-	99.45	-	-
			Silicate Glass	13.58	(0.14)	15.03	(0.08)	11.33	(0.05)	57.26	(0.18)	1.68	(0.07)	0.24	(0.05)	0.42	(0.04)	0.05	(0.02)	n/a	-	n/a	-	99.59	0.84	0.577
T5 + 1% Ti	1300	IW - 1.8	Opx	0.51	(0.04)	38.87	(0.36)	0.32	(0.04)	59.98	(0.63)	0.11	(0.05)	0.03	(0.01)	0.01	(0.01)	0.08	(0.03)	n/a	-	n/a	-	99.91	-	-
			Silicate Glass	15.13	(0.08)	14.83	(0.15)	12.08	(0.08)	57.02	(0.88)	1.17	(0.05)	0.03	(0.02)	0.07	(0.02)	0.02	(0.01)	n/a	-	n/a	-	100.34	0.86	0.582
T5 + 2% Ti	1300	FMQ = 0.0	Opx	0.39	(0.05)	37.38	(0.18)	0.51	(0.07)	59.34	(0.24)	0.28	(0.04)	0.20	(0.04)	0.01	(0.02)	0.52	(0.11)	0.42	(0.04)	n/a	-	99.06	-	-
			Silicate Glass	13.54	(0.02)	12.61	(0.07)	11.99	(0.03)	54.48	(0.09)	4.29	(0.10)	0.03	(0.02)	0.51	(0.04)	0.20	(0.01)	0.88	(0.05)	n/a	-	98.53	0.75	0.577
T5 + 2% Ti	1300	IW - 1.8	Opx	0.46	(0.03)	37.53	(0.39)	0.39	(0.06)	60.17	(0.47)	0.33	(0.05)	0.02	(0.02)	0.01	(0.01)	0.22	(0.04)	0.25	(0.04)	n/a	-	99.38	-	-
			Silicate Glass	13.43	(0.09)	15.55	(0.12)	10.44	(0.07)	55.30	(0.23)	3.78	(0.11)	0.01	(0.01)	0.05	(0.02)	0.12	(0.02)	0.31	(0.03)	n/a	-	98.98	0.90	0.581
T5 + 3% Ti	1300	FMQ = 0.0	Opx	0.43	(0.04)	37.67	(0.22)	0.73	(0.08)	59.26	(0.20)	0.50	(0.05)	0.09	(0.02)	0.02	(0.01)	0.67	(0.07)	0.42	(0.09)	n/a	-	99.79	-	-

Supplementary Table 3.2 - Major elements composition (cg/g) of main crystal phases and coexistent silicate glasses

Experiment	Temp. (° C)	Δ to redox buffer[a]	Phase	CaO	σ	MgO	σ	Al_2O_3	σ	SiO_2	σ	TiO_2	σ	FeO	σ	P_2O_5	σ	Cr_2O_3	σ	MnO[1]	σ	Na_2O[2]	σ	Total	NBO/T [3]	OB [3]
			Silicate Glass	12.85	(0.07)	13.33	(0.08)	11.25	(0.09)	51.55	(0.09)	7.78	(0.07)	0.09	(0.06)	0.45	(0.02)	0.23	(0.03)	0.80	(0.08)	n/a	-	98.34	0.78	0.581
T5 + 3% Ti	1300	IW - 1.8	Opx	0.36	(0.03)	37.98	(0.11)	0.37	(0.03)	60.15	(0.33)	0.40	(0.04)	0.02	(0.02)	0.01	(0.01)	0.15	(0.02)	0.25	(0.03)	n/a	-	99.70	-	-
			Silicate Glass	12.26	(0.07)	15.15	(0.08)	11.19	(0.05)	55.51	(0.12)	4.80	(0.11)	0.05	(0.02)	0.02	(0.01)	0.15	(0.02)	0.25	(0.03)	n/a	-	99.38	0.81	0.577
T5 + 5% Ti	1280	air	Opx	0.46	(0.05)	37.76	(0.19)	0.29	(0.03)	59.48	(0.41)	0.45	(0.10)	0.10	(0.03)	bdl	bdl	0.12	(0.06)	n/a	-	n/a	-	98.65	-	-
			Silicate Glass	12.30	(0.08)	14.76	(0.07)	8.98	(0.09)	52.60	(0.18)	7.59	(0.08)	0.57	(0.05)	0.55	(0.02)	0.03	(0.02)	n/a	-	n/a	-	97.37	0.89	0.580
T5 + 5% Ti	1300	IW - 1.8	Opx	0.47	(0.06)	38.39	(0.15)	0.43	(0.03)	59.95	(0.22)	0.64	(0.06)	0.08	(0.03)	0.02	(0.01)	0.31	(0.02)	0.37	(0.05)	n/a	-	100.65	-	-
			Silicate Glass	13.45	(0.05)	12.98	(0.15)	10.37	(0.08)	52.74	(0.41)	8.55	(0.11)	0.05	(0.04)	0.29	(0.02)	0.29	(0.03)	0.62	(0.07)	n/a	-	99.34	0.79	0.580
T5 + 5% Ti	1280	FMQ + 0.1	Opx	0.52	(0.02)	38.48	(0.30)	0.37	(0.05)	60.16	(0.28)	0.45	(0.05)	0.15	(0.03)	bdl	bdl	0.34	(0.06)	0.56	(0.07)	n/a	-	101.02	-	-
			Silicate Glass	12.84	(0.11)	13.80	(0.15)	9.89	(0.10)	52.41	(0.47)	8.34	(0.10)	0.17	(0.03)	0.20	(0.04)	0.28	(0.06)	1.02	(0.10)	n/a	-	98.96	0.83	0.582
T5 + 10% Ti	1300	FMQ = 0.0	Opx	0.38	(0.03)	38.05	(0.32)	0.45	(0.04)	59.13	(0.44)	0.91	(0.13)	0.03	(0.02)	0.01	(0.01)	0.44	(0.03)	n/a	-	n/a	-	99.40	-	-
			Silicate Glass	10.44	(0.04)	15.57	(0.11)	7.91	(0.10)	49.17	(0.32)	14.68	(0.21)	0.07	(0.05)	0.40	(0.01)	0.25	(0.01)	n/a	-	n/a	-	98.50	0.85	0.581
T5 + 10% Ti	1250	IW - 1.6	Opx	0.30	(0.01)	38.72	(0.35)	0.50	(0.07)	59.80	(0.44)	1.44	(0.24)	0.01	(0.01)	0.01	(0.01)	0.02	(0.01)	n/a	-	n/a	-	100.79	-	-
			Silicate Glass	12.70	(0.11)	11.26	(0.16)	10.13	(0.07)	54.23	(0.34)	11.83	(0.14)	0.01	(0.01)	0.08	(0.01)	0.01	(0.01)	n/a	-	n/a	-	100.26	0.65	0.575
T5 + 10% Ti	1280	air	Opx	0.32	(0.01)	38.39	(0.33)	0.26	(0.06)	59.50	(0.43)	0.70	(0.06)	0.09	(0.03)	0.01	(0.01)	0.03	(0.02)	n/a	-	n/a	-	99.31	-	-
			Silicate Glass	10.34	(0.05)	15.42	(0.07)	8.08	(0.07)	49.20	(0.27)	14.23	(0.22)	0.59	(0.07)	0.47	(0.02)	0.01	(0.02)	n/a	-	n/a	-	98.33	0.85	0.582
T5 + 20% Ti	1285	air	Opx	0.30	(0.01)	39.09	(0.11)	0.38	(0.02)	59.70	(0.12)	1.41	(0.09)	0.11	(0.06)	bdl	bdl	bdl	bdl	n/a	-	n/a	-	100.99	-	-
			Arm	0.02	(0.02)	19.07	(0.21)	1.65	(0.03)	0.34	(0.05)	78.35	(0.29)	1.09	(0.06)	bdl	bdl	0.13	(0.03)	n/a	-	n/a	-	100.66	-	-
			Silicate Glass	10.11	(0.04)	14.66	(0.12)	6.96	(0.10)	49.22	(0.23)	18.33	(0.09)	0.37	(0.04)	0.34	(0.02)	0.02	(0.02)	n/a	-	n/a	-	99.99	0.81	0.581
T5 + 20% Ti	1280	air	Opx	0.25	(0.01)	38.37	(1.28)	0.36	(0.05)	59.14	(0.23)	1.10	(0.14)	0.09	(0.03)	bdl	bdl	0.02	(0.02)	n/a	-	n/a	-	99.32	-	-
			Arm	0.05	(0.02)	18.78	(0.12)	1.87	(0.11)	0.29	(0.01)	77.65	(0.62)	1.42	(0.05)	bdl	bdl	0.14	(0.01)	n/a	-	n/a	-	100.20	-	-
			Silicate Glass	9.36	(0.06)	13.61	(0.11)	8.01	(0.11)	50.37	(0.20)	16.49	(0.27)	0.36	(0.04)	0.30	(0.03)	0.02	(0.02)	n/a	-	n/a	-	98.51	0.71	0.575
T5 + 20% Ti	1250	IW - 1.6	Opx	0.43	(0.04)	38.89	(0.22)	0.42	(0.06)	59.70	(0.39)	0.87	(0.10)	0.08	(0.05)	0.01	(0.01)	0.25	(0.03)	n/a	-	n/a	-	100.65	-	-
			Arm	0.12	(0.05)	16.20	(0.11)	2.29	(0.06)	0.14	(0.02)	82.56	(0.24)	0.01	(0.01)	0.01	(0.01)	1.84	(0.09)	n/a	-	n/a	-	103.17	-	-
			Silicate Glass	12.94	(0.08)	13.76	(0.08)	9.15	(0.03)	48.58	(0.27)	14.75	(0.31)	0.03	(0.02)	0.22	(0.04)	0.25	(0.03)	n/a	-	n/a	-	99.67	0.82	0.586
T8 + 0% Ti	1280	FMQ + 0.1	An	20.02	(0.07)	0.52	(0.02)	35.56	(0.04)	45.03	(0.11)	0.02	(0.02)	0.04	(0.03)	0.01	(0.01)	0.02	(0.01)	0.04	(0.03)	0.07	(0.04)	101.33	-	-
			Ol	0.24	(0.01)	54.66	(0.33)	0.16	(0.06)	42.84	(0.11)	0.02	(0.01)	0.03	(0.02)	0.20	(0.08)	0.02	(0.02)	0.75	(0.04)	0.02	(0.00)	98.94	-	-
			Silicate Glass	13.57	(0.07)	14.25	(0.12)	20.29	(0.08)	49.87	(0.12)	0.10	(0.03)	0.02	(0.02)	0.26	(0.02)	0.03	(0.03)	1.00	(0.05)	0.05	(0.02)	99.44	0.67	0.588
T8 + 1% Ti	1250	FMQ + 0.1	Spl	0.02	(0.01)	27.04	(0.16)	72.16	(0.93)	0.09	(0.02)	0.07	(0.03)	0.02	(0.01)	bdl	bdl	0.87	(0.65)	n/a	-	n/a	-	100.28	-	-
			Silicate Glass	12.91	(0.06)	13.48	(0.09)	21.88	(0.18)	51.41	(0.21)	1.33	(0.12)	0.02	(0.02)	0.19	(0.02)	0.03	(0.03)	n/a	-	n/a	-	101.25	0.54	0.582
T8 + 2% Ti	1280	FMQ + 0.1	Spl	0.03	(0.01)	27.06	(0.20)	69.66	(1.63)	0.13	(0.04)	0.19	(0.01)	0.07	(0.03)	bdl	bdl	2.44	(1.46)	0.30	(0.07)	n/a	-	99.88	-	-
			Silicate Glass	13.50	(0.07)	13.25	(0.05)	21.51	(0.11)	47.65	(0.31)	2.49	(0.06)	0.05	(0.01)	0.19	(0.03)	bdl	bdl	0.68	(0.10)	n/a	-	99.32	0.57	0.588
T8 + 3% Ti	1280	FMQ + 0.1	Spl	0.02	(0.01)	27.18	(0.16)	67.47	(1.15)	0.09	(0.01)	0.28	(0.05)	0.03	(0.04)	bdl	bdl	4.79	(1.05)	0.28	(0.04)	n/a	-	100.14	-	-
			Silicate Glass	13.03	(0.06)	14.13	(0.12)	20.39	(0.13)	46.54	(0.22)	4.35	(0.12)	0.02	(0.01)	0.21	(0.03)	bdl	bdl	0.69	(0.10)	n/a	-	99.36	0.64	0.591
T8 + 5% Ti	1260	FMQ = 0.0	An	19.78	(0.11)	0.50	(0.03)	35.73	(0.18)	45.00	(0.11)	0.15	(0.03)	0.04	(0.02)	bdl	bdl	bdl	bdl	n/a	-	n/a	-	101.20	-	-
			Ol	0.18	(0.01)	55.07	(0.22)	0.11	(0.05)	43.10	(0.24)	0.06	(0.04)	0.07	(0.03)	0.11	(0.07)	0.03	(0.02)	n/a	-	n/a	-	98.73	-	-
			Silicate Glass	12.08	(0.04)	13.51	(0.04)	18.86	(0.13)	45.68	(0.20)	6.94	(0.18)	0.06	(0.05)	0.40	(0.04)	0.02	(0.01)	n/a	-	n/a	-	97.56	0.60	0.587
T8 + 10% Ti	1230	FMQ - 0.1	An	19.92	(0.12)	0.45	(0.01)	36.32	(0.28)	44.09	(0.27)	0.21	(0.02)	0.04	(0.03)	bdl	bdl	bdl	bdl	n/a	-	n/a	-	101.02	-	-
			Silicate Glass	10.34	(0.01)	14.23	(0.12)	19.21	(0.11)	45.38	(0.23)	9.53	(0.10)	bdl	bdl	0.19	(0.01)	0.02	(0.01)	n/a	-	n/a	-	98.90	0.54	0.584
T8 + 20% Ti	1270	FMQ = 0.0	Arm	0.03	(0.03)	16.18	(0.08)	8.86	(0.04)	0.19	(0.04)	73.67	(0.78)	0.08	(0.04)	bdl	bdl	1.21	(0.16)	n/a	-	n/a	-	100.22	-	-
			Silicate Glass	11.61	(0.04)	12.13	(0.14)	18.66	(0.15)	44.08	(0.22)	13.10	(0.17)	0.03	(0.02)	0.19	(0.03)	0.04	(0.02)	n/a	-	n/a	-	99.81	0.51	0.587
T8 + 20% Ti	1240	air	Arm	0.03	(0.02)	16.16	(0.11)	9.13	(0.25)	0.12	(0.04)	72.73	(0.58)	0.69	(0.07)	0.02	(0.01)	0.91	(0.78)	n/a	-	0.04	(0.03)	99.83	-	-
			An	19.04	(0.04)	0.42	(0.03)	35.20	(0.38)	45.39	(0.13)	0.30	(0.04)	0.02	(0.02)	0.03	(0.02)	0.01	(0.01)	n/a	-	0.23	(0.03)	100.64	-	-
			Silicate Glass	11.27	(0.10)	11.88	(0.14)	18.75	(0.18)	45.09	(0.31)	10.78	(0.07)	0.12	(0.05)	0.23	(0.03)	bdl	bdl	n/a	-	0.14	(0.04)	98.27	0.50	0.584
T8 + 20% Ti	1250	FMQ + 0.1	Arm	0.02	(0.01)	15.53	(0.07)	9.99	(0.09)	0.32	(0.05)	72.49	(0.42)	0.07	(0.06)	bdl	bdl	1.98	(0.18)	n/a	-	n/a	-	100.40	-	-
			Silicate Glass	11.62	(0.03)	11.61	(0.05)	19.41	(0.20)	43.71	(0.19)	12.07	(0.16)	0.02	(0.02)	0.17	(0.04)	0.03	(0.02)	n/a	-	n/a	-	98.65	0.48	0.586
FT1+1% Ti	1200	IW - 1.5	Cpx	22.16	(0.37)	12.35	(0.22)	1.45	(0.18)	52.89	(0.17)	0.40	(0.07)	11.86	(0.66)	0.03	(0.03)	0.81	(0.11)	n/a	-	n/a	-	101.96	-	-
			Silicate Glass	15.01	(0.10)	3.80	(0.07)	7.43	(0.08)	47.60	(0.23)	1.39	(0.08)	23.82	(0.33)	0.81	(0.07)	0.18	(0.04)	n/a	-	n/a	-	100.04	1.28	0.623
FT1+5%Ti	1200	IW - 1.5	Cpx	22.57	(0.26)	13.99	(0.24)	1.47	(0.18)	52.58	(0.45)	1.52	(0.23)	8.20	(0.17)	0.02	(0.02)	1.22	(0.17)	n/a	-	n/a	-	101.59	-	-
			Silicate Glass	14.94	(0.07)	4.22	(0.04)	6.71	(0.06)	46.87	(0.16)	6.75	(0.16)	19.36	(0.27)	0.82	(0.04)	0.27	(0.02)	n/a	-	n/a	-	99.93	1.14	0.615
FT1+5%Ti	1100	IW - 1.8	Cpx	22.72	(0.17)	13.97	(0.45)	0.72	(0.10)	52.90	(0.56)	1.58	(0.11)	10.09	(0.74)	0.02	(0.01)	0.78	(0.03)	n/a	-	n/a	-	102.37	-	-
			Silicate Glass	14.52	(0.06)	3.10	(0.04)	7.14	(0.10)	45.77	(0.48)	7.91	(0.13)	21.21	(0.12)	0.83	(0.05)	0.25	(0.05)	n/a	-	n/a	-	100.73	1.10	0.618
FT1+10%Ti	1100	IW - 1.8	Cpx	22.02	(0.03)	13.16	(0.01)	2.13	(0.24)	50.66	(0.57)	3.16	(0.29)	8.55	(0.17)	0.02	(0.01)	1.18	(0.22)	0.29	(0.02)	n/a	-	101.16	-	-
			Ilm	0.16	(0.03)	4.45	(0.10)	0.20	(0.02)	0.14	(0.06)	57.37	(0.36)	38.89	(1.59)	0.03	(0.02)	1.86	(0.09)	0.76	(0.04)	n/a	-	104.02	-	-
			Silicate Glass	14.68	(0.16)	4.53	(0.06)	5.95	(0.05)	44.51	(0.23)	11.52	(0.20)	17.04	(0.10)	0.45	(0.04)	0.30	(0.03)	0.51	(0.04)	n/a	-	99.49	1.11	0.616
FT1+20%Ti	1100	IW - 1.8	Cpx	18.48	(0.87)	15.36	(0.66)	1.09	(0.38)	52.32	(1.03)	2.48	(0.75)	12.14	(0.83)	bdl	bdl	0.23	(0.07)	0.51	(0.06)	n/a	-	102.60	-	-

Supplementary Table 3.2 - Major elements composition (cg/g) of main crystal phases and coexistent silicate glasses

Experiment	Temp. (° C)	Δ to redox buffer[a]	Phase	CaO	σ	MgO	σ	Al_2O_3	σ	SiO_2	σ	TiO_2	σ	FeO	σ	P_2O_5	σ	Cr_2O_3	σ	MnO[1]	σ	Na_2O[2]	σ	Total	NBO/T [3]	OB [3]
			Arm	0.44	(0.22)	5.29	(0.13)	0.84	(0.14)	0.76	(0.60)	73.81	(1.11)	21.65	(0.40)	0.02	(0.02)	0.56	(0.05)	0.26	(0.02)	n/a	-	104.06	-	-
			Ttn	28.34	(0.29)	0.21	(0.01)	0.35	(0.03)	29.77	(0.25)	40.50	(0.34)	0.77	(0.08)	0.13	(0.04)	0.23	(0.05)	0.10	(0.03)	n/a	-	100.39	-	-
			Silicate Glass	12.59	(0.06)	4.09	(0.09)	6.77	(0.07)	45.20	(0.78)	10.87	(0.21)	19.25	(0.17)	0.63	(0.03)	0.05	(0.02)	0.57	(0.03)	n/a	-	100.00	1.04	0.614
T1+0% Ti + REE	1300	IW - 1.6	Cpx	21.68	(0.48)	20.54	(0.54)	0.62	(0.15)	55.60	(0.21)	bdl	bdl	0.36	(0.02)	0.01	(0.01)	0.38	(0.01)	0.35	(0.06)	n/a	-	99.58	-	-
			Silicate Glass	18.44	(0.47)	14.16	(0.25)	10.40	(0.29)	50.07	(1.21)	0.14	(0.02)	1.57	(0.09)	0.03	(0.01)	0.43	(0.02)	0.53	(0.05)	n/a	-	95.76	1.16	0.600
T1+10% Ti + REE	1280	IW - 1.6	Cpx	19.29	(0.53)	21.83	(0.47)	0.93	(0.04)	53.60	(0.93)	2.73	(0.14)	0.29	(0.04)	0.03	(0.03)	0.26	(0.02)	0.22	(0.06)	n/a	-	99.18	-	-
			Ol	0.34	(0.01)	54.42	(0.19)	0.02	(0.01)	43.10	(0.23)	0.08	(0.05)	0.64	(0.05)	0.02	(0.01)	0.21	(0.05)	0.27	(0.05)	n/a	-	99.09	-	-
			Silicate Glass	15.89	(0.08)	14.85	(0.05)	5.75	(0.10)	47.89	(0.59)	11.92	(0.19)	0.69	(0.04)	0.05	(0.02)	0.42	(0.06)	0.32	(0.04)	n/a	-	97.76	1.14	0.596

[a]Air: top and bottom of the furnace were not sealed during the experiment to produce an oxidized environment and have only the more oxidized species of each element present; for experiments performed with oxygen fugacities relevant to the Earth's mantle the value is given relative to the FMQ: Fayalite-Magnetite-Quartz mineral redox buffer as described by O'Neill (1987); for experiments performed with oxygen fugacities relevant to the lunar mantle the value is given relative to the IW: Iron Wüstite mineral redox buffer as described by Myers and Eugster (1983).

[1] Only analysed on the experiments which it was added to assess its use as internal standard; [2] Not added to the experiments; [3] Non-Bridging Oxygen / Silica Tethraedra and Optical Basicity calculated as described in Mills (1993); bdl: below detection limit (< 0.00 wt. %); n/a: not acquired

Supplementary Table 3.3- Trace elements LA-ICP-MS analysis (μg/g) of main crystal phases and coexistent silicate glasses

Experiment	Temp. (° C)	Δ to redox buffer[a]	Phase	Cr	σ	Zr	σ	Nb	σ	Mo	σ	Ba	σ	Hf	σ	Ta	σ	W	σ	Th	σ	U	σ
T1 + 0% Ti	1305	air	Ol	1023	(101)	0.29	(0.07)	0.23	(0.11)	bdl	bdl	1.83	(0.20)	0.81	(0.13)	0.15	(0.03)	0.09	(0.04)	0.010	(0.002)	0.003	(0.002)
			Silicate Glass	846	(41)	621.60	(16.32)	1746.33	(39.32)	17.64	(0.38)	1589.71	(46.26)	975.05	(31.76)	1108.61	(31.17)	2364.28	(59.30)	1689.39	(45.19)	2206.31	(66.63)
T1 + 0% Ti	1300	FMQ = 0.0	Cpx	8446	(1601)	33.83	(3.58)	2.23	(0.61)	0.25	(0.10)	0.20	(0.05)	68.44	(12.47)	3.02	(1.12)	0.13	(0.08)	4.54	(0.91)	2.56	(0.14)
			Silicate Glass	351	(14)	694.41	(16.10)	1047.62	(34.34)	32.48	(1.47)	1170.05	(34.77)	708.68	(23.79)	607.02	(15.60)	1513.25	(78.725)	1421.37	(39.70)	1464.14	(72.15)
T1 + 0% Ti	1300	IW - 1.6	Cpx	1649	(126)	31.51	(2.22)	1.02	(0.20)	0.25	(0.004)	0.25	(0.08)	75.02	(5.87)	2.53	(0.25)	0.02	(0.01)	14.09	(2.54)	5.99	(1.76)
			Silicate Glass	436	(45)	786	(23.12)	216.71	(15.50)	3.76	(1.34)	1271.73	(17.82)	936.37	(28.00)	867.32	(20.47)	0.84	(0.20)	2084.42	(61.39)	2597.87	(41.70)
T1 + 1% Ti	1295	air	Cpx	283	(55)	35.96	(6.607)	2.40	(0.71)	bdl	bdl	n/a	-	70.82	(15.57)	4.33	(1.401)	0.04	(0.015)	4.54	(1.206)	0.08	(0.015)
			Silicate Glass	37	(5)	938.45	(12.81)	1502.48	(19.53)	8.09	(0.69)	n/a	-	818.56	(10.60)	1537.79	(25.86)	1308.63	(23.54)	1356.76	(18.33)	360.62	(32.88)
T1 + 1% Ti	1300	FMQ = 0.0	Cpx	5995	(2280)	36.99	(8.56)	5.33	(1.88)	0.56	(0.24)	0.31	(0.289)	108.73	(28.44)	5.90	(2.51)	0.24	(0.005)	7.636	(1.597)	1.07	(0.26)
			Ol	1201	(123)	0.24	(0.10)	0.15	(0.04)	0.19	(0.06)	0.002	(0.001)	0.22	(0.09)	0.05	(0.02)	0.06	(0.01)	0.003	(0.001)	0.003	(0.002)
			Silicate Glass	539	(12)	950.90	(12.93)	1803.46	(31.75)	40.36	(0.32)	176.41	(0.87)	764.69	(9.53)	943.41	(7.56)	1702.14	(19.79)	1311.96	(13.53)	1209.61	(9.64)
T1 + 1% Ti	1300	IW - 1.6	Ol	104	(18)	0.17	(0.03)	bdl	bdl	0.21	max	0.13	(0.01)	0.26	(0.05)	0.02	(0.01)	0.01	(0.001)	0.007	(0.001)	0.02	(0.01)
			Silicate Glass	48	(1)	452.15	(8.78)	12.24	(0.51)	0.48	(0.21)	801.94	(14.37)	496.59	(11.88)	270.67	(5.88)	1.19	(0.05)	1146.45	(25.56)	1343.74	(25.86)
T1 + 2% Ti	1300	FMQ = 0.0	Cpx	6941	(1192)	25.68	(3.06)	1.84	(0.15)	0.36	(0.11)	0.20	(0.04)	50.63	(5.11)	1.97	(0.14)	0.14	(0.04)	3.35	(0.42)	1.12	(0.34)
			Ol	1085	(121)	0.22	(0.05)	0.11	(0.02)	0.24	(0.05)	0.060	(0.003)	0.32	(0.12)	0.04	(0.01)	0.06	(0.03)	0.004	(0.002)	0.004	(0.001)
			Silicate Glass	888	(56)	1109.16	(28.06)	1412.51	(22.60)	36.84	(1.18)	1473.47	(53.27)	917.15	(20.02)	923.60	(14.91)	1868.86	(45.44)	1832.27	(39.03)	1624.64	(66.22)
T1 + 2% Ti	1300	IW - 1.6	Cpx	1904	(290)	23.16	(1.92)	2.15	(0.10)	0.31	(0.03)	0.41	(0.26)	46.13	(2.51)	3.58	(0.79)	0.22	(0.05)	3.78	(0.92)	4.69	(1.01)
			Silicate Glass	355	(44)	1121.98	(35.46)	1123.70	(53.41)	1.07	(0.19)	407.92	(14.16)	1057.55	(38.91)	1961.25	(66.41)	27.83	(3.09)	1889.62	(67.83)	1835.59	(31.72)
T1 + 3% Ti	1305	air	Ol	36	(6)	0.24	(0.07)	0.08	(0.02)	bdl	bdl	0.13	(0.09)	0.32	(0.12)	0.05	(0.03)	0.02	(0.01)	0.0089	(0.0005)	0.001	(0.001)
			Silicate Glass	26	(3)	548.70	(23.11)	802.99	(19.57)	200.04	(8.28)	993.66	(18.13)	711.13	(21.38)	764.93	(22.35)	698.93	(21.93)	1228.02	(30.51)	583.53	(60.53)
T1 + 3% Ti	1300	FMQ = 0.0	Cpx	8723	(855)	13.90	(0.87)	1.22	(0.206)	0.23	(0.12)	0.19	(0.15)	31.99	(2.91)	1.36	(0.30)	0.139	(0.114)	1.718	(0.154)	1.04	(0.03)
			Ol	1210	(222)	0.08	(0.05)	0.04	(0.012)	0.23	(0.15)	0.01	(0.01)	0.22	(0.06)	0.01	(0.00)	0.041	(0.018)	0.003	(0.001)	0.003	(0.0003)
			Silicate Glass	953	(8)	644.13	(11.73)	896.35	(6.89)	33.29	(0.89)	1133.21	(3.71)	691.76	(10.06)	716.45	(11.16)	1202.01	(17.26)	1152.66	(16.97)	1159.80	(20.90)
T1 + 3% Ti	1300	IW - 1.6	Ol	520	(29)	0.17	(0.06)	0.07	(0.01)	0.47	max	0.15	(0.12)	0.20	(0.06)	0.03	(0.002)	0.010	(0.001)	0.003	0.001	0.014	(0.005)
			Silicate Glass	538	(26)	460.22	(17.75)	988.90	(21.04)	bdl	bdl	884.35	(37.76)	534.08	(21.86)	582.00	(27.87)	2.28	(0.03)	1143.82	(64.24)	1221.58	(36.21)
T1 + 5% Ti	1305	air	Ol	23	(3)	0.09	(0.03)	0.08	(0.02)	bdl	bdl	0.50	(0.42)	0.16	(0.05)	0.05	(0.03)	0.02	(0.01)	0.0020	(0.0004)	0.0015	(0.0004)
			Silicate Glass	27	(3)	255.58	(4.18)	1021.38	(12.76)	189.20	(1.90)	1500.16	(18.23)	413.05	(4.85)	932.83	(10.94)	656.65	(4.23)	1137.43	(32.56)	539.31	30.91
T1 + 5% Ti	1270	FMQ = 0.0	Cpx	490	(73)	4.73	(0.61)	2.05	(0.43)	0.34	max	0.28	(0.07)	45.52	(7.94)	1.03	(0.25)	0.19	(0.08)	1.68	(0.17)	0.991	(0.23)
			Ol	184	(20)	0.05	(0.02)	0.15	(0.03)	0.24	(0.10)	0.11	(0.001)	0.40	(0.12)	0.04	(0.02)	0.09	(0.04)	0.003	(0.002)	0.003	(0.001)
			Silicate Glass	183	(22)	265.70	(59.35)	1187.21	(53.69)	34.03	(1.97)	1189.52	(109.59)	1113.86	(98.68)	694.11	(79.82)	2031.01	(254.43)	1020.73	(110.40)	1507.71	(105.91)
T1 + 5% Ti	1300	IW - 1.6	Ol	1619	(180)	0.08	(0.02)	0.08	(0.03)	0.22	(0.09)	0.08	(0.07)	0.30	(0.07)	0.02	(0.01)	0.01	(0.01)	0.004	(0.001)	0.010	(0.003)
			Silicate Glass	1724	(34)	224.91	(8.56)	877.58	(27.59)	0.33	(0.13)	1052.32	(25.50)	561.40	(19.29)	705.78	(23.00)	3.65	(0.13)	942.88	(41.92)	930.68	(20.44)
T1 + 5% Ti	1290	IW - 1.7	Cpx	537	(43)	22.24	(6.89)	0.01	(0.00)	0.27	(0.09)	0.054	(0.029)	59.78	(13.02)	0.64	(0.14)	0.030	(0.014)	4.14	(0.78)	6.18	1.14
			Silicate Glass	119	(4)	1376.21	(76.99)	8.58	(2.36)	0.80	(0.17)	213.68	(7.05)	1413.24	(80.09)	445.73	(83.10)	1.46	(0.26)	2327.15	(116.64)	2919.66	(54.29)
T1 + 10% Ti	1260	FMQ = 0.0	Cpx	7192	(487)	4.77	(0.27)	1.45	(0.29)	0.17	max	0.13	(0.04)	4.42	(0.06)	0.62	(0.14)	0.21	(0.02)	1.51	(0.30)	0.73	(0.06)
			Silicate Glass	1895	(13)	456.23	(8.41)	934.08	(13.92)	12.48	(0.22)	94.08	(1.50)	198.71	(1.36)	543.04	(15.81)	1176.56	(8.63)	919.66	(22.32)	764.73	(10.41)
T1 + 10% Ti	1250	IW - 1.6	Cpx	320	(22)	6.84	(0.46)	0.15	(0.04)	0.27	(0.11)	0.27	(0.33)	7.18	(0.28)	0.51	(0.06)	0.03	(0.01)	1.56	(0.40)	2.30	(0.76)
			Silicate Glass	146	(3)	616.40	(14.96)	108.21	(3.13)	0.22	max	176.27	(2.83)	265.60	(5.23)	607.86	(11.38)	0.64	(0.13)	1657.69	(38.26)	1765.04	(39.42)
T1 + 20% Ti	1250	FMQ + 0.1	Arm	16609	max	668.05	max	1247.92	max	31.87	max	0.03	max	1171.04	max	2707.07	max	83.36	max	0.74	max	7.67	max
			Silicate Glass	538	(109)	311.34	(8.67)	537.20	(91.11)	41.62	(13.06)	105.87	(3.45)	562.09	(17.00)	928.17	(56.13)	1413.49	(71.845)	1088.77	(43.81)	1145.17	(53.61)
T1 + 20% Ti	1260	FMQ = 0.0	Cpx	1651	(410)	5.06	(0.58)	0.66	(0.17)	0.48	(0.10)	0.13	(0.11)	13.35	(0.21)	0.26	(0.06)	0.06	(0.003)	1.30	(0.24)	0.79	(0.10)
			Silicate Glass	538	(109)	715.24	(66.07)	669.36	(31.44)	10.78	(1.08)	167.37	(6.18)	622.81	(61.01)	711.96	(76.14)	1297.66	(42.59)	1467.53	(12.26)	1512.94	(34.13)
T1 + 20% Ti	1240	air	Ol	17	(2)	0.09	(0.05)	0.05	(0.01)	bdl	bdl	n/a	-	0.21	(0.08)	0.02	(0.01)	0.03	(0.01)	0.002	(0.001)	0.0010	(0.0007)
			Arm	1793	(124)	731.11	(15.06)	1502.79	(61.34)	bdl	bdl	n/a	-	2914.85	(120.43)	2846.07	(116.25)	114.16	(5.39)	0.449	(0.093)	1.29	(0.12)
			Silicate Glass	25	(5)	263.88	(4.32)	563.88	(8.76)	4.75	(1.13)	n/a	-	789.46	(13.20)	597.65	(11.64)	1191.04	(28.50)	710.19	(7.75)	274.61	(8.67)

Supplementary Table 3.3- Trace elements LA-ICP-MS analysis (µg/g) of main crystal phases and coexistent silicate glasses

Experiment	Temp. (° C)	Δ to redox buffer[a]	Phase	Cr	σ	Zr	σ	Nb	σ	Mo	σ	Ba	σ	Hf	σ	Ta	σ	W	σ	Th	σ	U	σ
T1 + 20% Ti	1250	IW - 1.6	Cpx	222	(26)	3.72	(0.52)	0.13	(0.03)	0.50	(0.27)	0.12	(0.10)	9.91	(1.71)	0.45	(0.15)	0.006	(0.002)	0.64	(0.19)	1.78	(1.10)
			Arm	2416	(118)	767.37	(19.85)	220.37	(3.99)	0.85	(0.21)	0.60	(0.28)	1355.32	(40.01)	2798.06	(93.25)	0.0870	(0.01)	0.75	(0.22)	11.08	(3.17)
			Silicate Glass	156	(9)	367.87	(13.50)	78.60	(3.10)	0.20	(0.06)	173.32	(3.67)	503.04	(18.89)	791.18	(27.39)	0.17	(0.08)	1502.98	(47.52)	1535.51	(40.71)
T7 + 0% Ti	1280	FMQ + 0.1	Cpx	9150	(389)	35.58	(7.65)	3.79	(0.99)	0.49	(0.19)	0.24	(0.05)	60.37	(7.71)	4.76	(1.08)	0.16	(0.04)	10.51	(1.24)	2.04	(0.46)
			Silicate Glass	1315	(55)	850.94	(30.82)	2547.66	(77.25)	96.18	(3.83)	1893.220	(21.56)	497.98	(19.13)	1765.67	(63.97)	2693.22	(18.46)	2883.95	(86.92)	2212.12	(33.05)
T7 + 1% Ti	1300	FMQ = 0.0	Cpx	10039	(269)	19.93	(7.18)	1.08	(0.29)	0.32	(0.19)	0.18	(0.11)	55.38	(5.55)	2.59	(0.37)	0.35	(0.15)	2.32	(0.41)	1.37	(0.44)
			Silicate Glass	1961	(61)	912.03	(28.60)	645.90	(20.43)	31.30	(0.99)	143.78	(2.69)	854.90	(25.15)	1341.30	(41.98)	1834.29	(43.65)	1290.72	(39.45)	1229.18	(32.94)
T7 + 1% Ti	1280	air	Cpx	129	(16)	38.00	(10.93)	1.23	(0.18)	bdl	bdl	n/a	-	58.13	(10.82)	3.56	(1.38)	0.13	(0.03)	5.41	(1.79)	0.05	(0.02)
			Silicate Glass	38	(4)	1119.89	(41.65)	977.67	(34.32)	5.10	(0.80)	n/a	-	967.48	(37.59)	1984.69	(69.45)	2044.65	(115.21)	2297.27	(81.17)	82.66	(7.29)
T7 + 2% Ti	1280	FMQ + 0.1	Cpx	9338	(924)	12.61	(0.60)	1.78	(0.24)	0.42	(0.01)	0.25	(0.11)	29.73	(2.22)	1.90	(0.32)	0.06	(0.01)	3.22	(0.70)	1.67	(0.19)
			Ol	1201	(183)	0.16	(0.02)	bdl	bdl	0.42	(0.20)	0.46	(0.37)	0.21	(0.04)	0.07	(0.02)	0.06	(0.02)	0.005	(0.001)	0.0025	(0.0002)
			Silicate Glass	1856	(72)	557.65	(29.88)	1584.90	(69.94)	102.05	(3.08)	1419.900	(49.702)	527.38	(27.78)	1391.37	(73.59)	1680.10	(80.99)	1807.35	(87.99)	1561.30	(53.60)
T7 + 3% Ti	1280	FMQ + 0.1	Cpx	8769	(567)	15.39	(0.47)	2.06	(0.15)	0.52	(0.01)	0.25	(0.04)	22.72	(4.29)	1.72	(0.203)	0.07	(0.02)	3.327	(0.161)	1.88	(0.084)
			Ol	1375	(162)	0.21	(0.04)	0.13	(0.04)	0.82	(0.10)	0.01	(0.02)	0.24	(0.04)	0.04	(0.01)	0.07	(0.01)	0.003	(0.001)	0.005	(0.001)
			Silicate Glass	2177	(55)	682.66	(24.80)	1658.40	(30.14)	100.53	(4.62)	1403.71	(27.90)	670.90	(33.21)	1211.08	(49.71)	1939.55	(68.88)	2075.92	(86.60)	1834.80	(81.97)
T7 + 5% Ti	1280	FMQ + 0.1	Cpx	8601	(235)	10.51	(1.30)	1.13	(0.06)	bdl	bdl	0.36	(0.09)	22.32	(2.57)	1.11	(0.17)	0.22	(0.13)	1.21	(0.18)	0.37	(0.10)
			Ol	850	(82)	0.26	(0.06)	bdl	bdl	0.12	(0.01)	0.003	(0.001)	0.36	(0.11)	0.02	(0.004)	0.07	(0.02)	0.0053	(0.0003)	0.0013	(0.0010)
			Silicate Glass	2097	(121)	749.00	(18.14)	1127.69	(20.64)	10.68	(0.51)	1843.66	(38.82)	742.29	(22.69)	894.77	(28.68)	2817.90	(232.72)	1087.91	(24.17)	562.61	(20.81)
T7 + 5% Ti	1280	IW - 1.6	Ol	4905	(354)	0.16	(0.07)	0.14	(0.07)	0.72	(0.19)	1.20	(0.87)	0.23	(0.10)	0.05	(0.03)	0.02	(0.01)	0.005	(0.002)	0.010	(0.003)
			Silicate Glass	4399	(68)	439.24	(10.47)	1255.81	(5.39)	bdl	bdl	1890.44	(21.09)	576.98	(11.21)	949.42	(16.66)	3.22	(0.01)	940.50	(19.59)	871.87	(18.21)
T7 + 10% Ti	1280	FMQ + 0.1	Cpx	9089	(1140)	7.81	(0.36)	0.63	(0.10)	0.16	(0.09)	0.06	(0.01)	20.53	(2.14)	0.82	(0.15)	0.46	(0.36)	1.12	(0.43)	1.12	(0.06)
			Ol	1011	(171)	0.10	(0.04)	0.06	(0.01)	0.21	(0.05)	0.30	(0.18)	0.13	(0.07)	0.03	(0.01)	0.05	(0.02)	0.001	(0.001)	0.0027	(0.0016)
			Silicate Glass	2174	(110)	827.69	(10.6)	677.99	(6.49)	26.37	(0.73)	122.161	(1.00)	806.48	(12.50)	1218.30	(67.75)	1550.55	(20.38)	1144.07	(11.209)	986.70	(13.89)
T7 + 10% Ti	1280	IW - 1.6	Ol	348	(37)	0.21	(0.01)	0.07	(0.01)	0.48	(0.26)	0.14	(0.03)	0.20	(0.09)	0.04	(0.01)	bdl	bdl	0.004	(0.002)	0.019	(0.004)
			Silicate Glass	370	(2.6)	765.27	(17.41)	1025.40	(11.76)	bdl	bdl	108.54	(1.07)	939.95	(41.53)	988.04	(11.50)	0.27	(0.13)	1450.31	(28.27)	1406.51	(19.02)
T7 + 20% Ti	1273	air	Arm	382	(68)	1094.97	(88.7)	1759.74	(207.53)	bdl	bdl	n/a	-	1450.15	(127.63)	3702.04	(344.21)	9.25	(2.17)	0.911	(0.204)	0.10	(0.01)
			Silicate Glass	7.64	(1.05)	561.83	(6.7)	938.27	(9.47)	0.59	(0.08)	n/a	-	552.32	(5.70)	1086.63	(12.32)	67.88	(1.43)	1483.72	(19.182)	26.08	(0.56)
T7 + 20% Ti	1250	FMQ + 0.1	Arm	122609	(18946)	1026.79	(101.3)	2036.25	(174.01)	36.24	(2.63)	0.928	(0.59)	1256.65	(118.03)	3359.56	(224.05)	117.71	(18.98)	0.601	(0.083)	9.05	(1.98)
			Ol	2506	(227)	0.10	(0.02)	0.07	(0.01)	bdl	bdl	0.001	(0.0001)	0.10	(0.03)	0.03	(0.01)	0.05	(0.01)	0.0017	(0.0009)	0.002	(0.001)
			Silicate Glass	3478	(120)	531.87	(28.13)	1009.70	(32.22)	45.69	(0.61)	84.17	(1.86)	495.05	(23.32)	697.91	(32.17)	1225.13	(6.26)	1034.24	(56.01)	911.66	(7.43)
T7 + 20% Ti	1230	FMQ - 0.1	Cpx	9415	(814)	5.61	(0.35)	1.49	(0.55)	0.94	max	0.161	(0.108)	17.15	(1.62)	0.48	(0.018)	1.53	(0.626)	0.67	(0.10)	1.60	(0.43)
			Silicate Glass	3146	(252)	624.27	(44.90)	1456.48	(105.32)	105.82	(14.02)	124.55	(9.93)	763.84	(165.19)	948.53	(0.03)	2117.02	(102.17)	1519.67	(98.39)	1448.45	(97.19)
ST1 + 5% Ti	1260	FMQ = 0.0	Cpx	1573	(322)	32.55	(2.88)	1.47	(0.35)	0.71	max	0.07	(0.05)	31.67	(11.79)	1.86	(0.17)	0.06	(0.00)	3.71	(0.37)	2.70	(0.96)
			Silicate Glass	156	(28)	463.79	(16.62)	607.18	(13.61)	28.34	(1.42)	170.10	(3.63)	121.17	(4.56)	350.05	(11.97)	773.86	(20.16)	814.68	(22.83)	578.88	(28.30)
ST1 + 10% Ti	1260	FMQ = 0.0	Cpx	1809	(129)	41.48	(8.47)	2.77	(0.71)	0.42	max	0.07	(0.02)	35.95	(6.49)	5.08	(1.39)	0.20	(0.09)	5.51	(1.52)	2.24	(0.46)
			Silicate Glass	219	(19)	280.50	(19.17)	878.28	(247.67)	24.01	(3.23)	170.03	(9.35)	158.59	(9.60)	393.02	(20.06)	787.00	(47.18)	665.75	(39.68)	644.50	(61.06)
T5 + 0% Ti	1300	FMQ = 0.0	Opx	5030	(2420)	1.31	(0.35)	1.45	(0.28)	0.34	(0.07)	0.17	(0.11)	3.62	(0.72)	0.70	(0.13)	1.12	(0.23)	0.04	(0.01)	0.27	(0.19)
			Silicate Glass	1435	(81)	467.51	(18.33)	1105.25	(44.54)	24.57	(1.73)	1044.77	(52.69)	717.25	(29.52)	572.32	(23.88)	1027.31	(41.74)	1123.32	(46.87)	860.95	(48.97)
T5 + 0% Ti	1300	IW - 1.8	Opx	793	(178)	1.40	(0.13)	0.20	(0.07)	9.49	(1.97)	0.19	(0.15)	3.24	(0.77)	0.43	(0.04)	0.22	(0.069)	0.06	(0.02)	0.90	(0.02)
			Silicate Glass	91	(5)	525.95	(12.34)	144.35	(1.45)	13.82	(2.49)	1064.67	(19.29)	664.56	(17.33)	450.96	(19.67)	60.56	(5.260)	1577.55	(38.11)	1269.55	(103.00)
T5 + 1% Ti	1300	FMQ = 0.0	Opx	3979	(445)	3.02	(0.67)	1.62	(0.36)	bdl	bdl	0.0016	max	2.73	(0.25)	1.40	(0.04)	1.26	(0.26)	0.05	(0.01)	0.51	(0.07)
			Silicate Glass	2321	(26)	2045.25	(168.21)	1387.93	(132.65)	14.84	(11.64)	195.72	(10.25)	440.58	(11.91)	1914.01	(213.42)	1714.11	(78.54)	1869.97	(85.20)	1756.32	(72.45)
T5 + 1% Ti	1300	IW - 1.8	Opx	502	(79)	1.18	(0.38)	0.10	(0.03)	6.21	(1.08)	0.34	(0.20)	1.64	(0.35)	0.56	(0.07)	0.08	(0.02)	0.04	(0.02)	0.98	(0.17)
			Silicate Glass	80	(3)	636.65	(22.46)	70.09	(4.97)	8.31	(2.40)	146.40	(2.99)	419.61	(9.70)	711.91	(56.81)	12.95	(1.08)	1704.65	(57.27)	1920.12	(118.89)
T5 + 2% Ti	1300	FMQ = 0.0	Opx	4276	(673)	1.02	(0.31)	1.24	(0.19)	0.31	(0.17)	0.058	(0.05)	2.79	(0.63)	0.52	(0.10)	0.79	(0.14)	0.02	(0.01)	0.32	(0.22)
			Silicate Glass	1617	(634)	542.17	(11.92)	1233.28	(15.56)	12.09	(0.81)	954.94	(23.22)	702.37	(15.36)	583.37	(18.61)	824.17	(14.34)	1187.57	(23.23)	868.08	(22.76)

Supplementary Table 3.3- Trace elements LA-ICP-MS analysis (μg/g) of main crystal phases and coexistent silicate glasses

Experiment	Temp. (° C)	Δ to redox buffer[a]	Phase	Cr	σ	Zr	σ	Nb	σ	Mo	σ	Ba	σ	Hf	σ	Ta	σ	W	σ	Th	σ	U	σ
T5 + 2% Ti	1300	IW - 1.8	Opx	1681	(53)	1.34	(0.15)	0.52	(0.17)	1.49	(0.06)	0.04	(0.02)	4.30	(0.32)	0.57	(0.02)	0.05	(0.03)	0.07	(0.01)	1.31	(0.15)
			Silicate Glass	875	(18)	479.45	(13.13)	341.95	(4.59)	0.56	(0.21)	1044.31	(19.45)	788.81	(19.59)	604.64	(7.46)	3.41	(0.74)	1542.40	(20.05)	1436.34	(21.336)
T5 + 3% Ti	1300	FMQ = 0.0	Opx	4032	(539)	1.50	(0.64)	1.54	(0.12)	0.84	(0.06)	0.82	(0.59)	3.49	(0.83)	0.93	(0.19)	2.02	(0.03)	0.17	(0.12)	0.44	(0.27)
			Silicate Glass	1452	(35)	559.97	(13.46)	1160.30	(20.91)	41.61	(4.41)	1144.53	(19.11)	746.70	(21.75)	961.61	(26.56)	1526.66	(40.93)	1664.12	(48.39)	1295.33	(24.711)
T5 + 3% Ti	1300	IW - 1.8	Opx	1200	(187)	0.87	(0.09)	0.17	(0.01)	bdl	bdl	0.01	(0.01)	2.91	(0.62)	0.56	(0.15)	0.01	(0.00)	0.05	(0.02)	0.81	(0.12)
			Silicate Glass	555	(10)	532.82	(10.63)	150.04	(11.39)	0.30	(0.03)	1036.23	(10.91)	752.41	(12.15)	682.85	(21.88)	0.78	(0.23)	1664.13	(23.02)	1461.59	(16.31)
T5 + 5% Ti	1280	air	Opx	610	(148)	0.59	(0.09)	0.55	(0.06)	bdl	bdl	0.002	max	2.70	(0.41)	0.88	(0.14)	1.18	(0.19)	0.02	(0.01)	0.03	(0.01)
			Silicate Glass	572	(13)	298.32	(3.92)	677.34	(10.91)	17.89	(0.50)	1730.88	(14.06)	773.20	(16.13)	1031.39	(26.79)	998.23	(28.31)	946.65	(17.23)	388.26	(9.50)
T5 + 5% Ti	1300	IW - 1.8	Opx	2314	(132)	0.55	(0.25)	0.86	(0.09)	4.34	(1.13)	0.09	(0.06)	3.71	(0.42)	1.42	(0.07)	1.46	(0.50)	0.04	(0.02)	0.57	(0.07)
			Silicate Glass	2129	(183)	399.61	(14.75)	813.97	(24.39)	1.90	(0.63)	2056.73	(54.74)	1033.34	(36.54)	2260.97	(78.31)	104.87	(30.65)	1668.81	(56.74)	1426.65	(34.57)
T5 + 5% Ti	1280	FMQ + 0.1	Opx	3365	(127)	1.14	max	0.82	max	bdl	bdl	0.29	max	3.31	max	1.23	max	2.33	max	0.18	max	0.15	max
			Silicate Glass	1770	(182)	443.80	(5.17)	656.84	(5.18)	5.29	(0.24)	1668.13	(30.02)	696.52	(10.44)	1055.81	(15.28)	1857.36	(54.19)	1016.55	(14.76)	569.37	(15.10)
T5 + 10% Ti	1300	FMQ = 0.0	Opx	3200	(240)	1.60	(0.31)	1.50	(0.81)	0.16	(0.07)	0.21	(0.14)	1.15	(0.30)	0.73	(0.12)	1.19	(0.12)	0.03	(0.01)	0.26	(0.16)
			Silicate Glass	1844	(24)	549.16	(6.25)	897.08	(7.01)	11.22	(0.71)	105.59	(1.09)	211.19	(2.43)	856.00	(37.32)	1138.62	(23.85)	981.96	(6.44)	925.51	(20.14)
T5 + 10% Ti	1250	IW - 1.6	Opx	994	(16)	2.55	(0.38)	0.32	(0.06)	20.50	(2.16)	0.11	(0.08)	1.70	(0.00)	0.51	(0.03)	0.55	(0.08)	0.13	(0.03)	0.86	(0.17)
			Silicate Glass	351	(1)	966.47	(24.48)	232.28	(9.34)	8.68	(0.08)	144.78	(4.33)	397.64	(0.43)	1227.97	(37.76)	36.08	(0.99)	1726.43	(76.29)	1541.41	(36.45)
T5 + 10% Ti	1280	air	Opx	217	(46)	0.84	(0.14)	0.56	(0.08)	bdl	bdl	0.003	(0.002)	0.97	(0.09)	0.65	(0.15)	1.07	(0.28)	0.02	(0.01)	0.009	(0.004)
			Silicate Glass	70	(3)	496.59	(9.21)	760.82	(11.59)	10.65	(0.37)	108.74	(2.03)	279.93	(4.21)	1023.64	(19.69)	1016.94	(19.21)	1121.61	(20.85)	362.71	(9.64)
T5 + 20% Ti	1285	air	Opx	85	(8)	0.24	(0.09)	0.64	(0.14)	bdl	bdl	n/a	-	2.12	(0.40)	0.43	(0.11)	1.45	(0.14)	0.03	(0.01)	0.0032	(0.0026)
			Arm	2345	(435)	196.06	(37.30)	1542.40	(295.02)	1.40	max	n/a	-	1190.06	(189.74)	2349.94	(400.48)	131.47	(17.91)	0.82	(0.10)	0.13	(0.05)
			Silicate Glass	43	(10)	86.36	(1.64)	613.12	(6.54)	2.98	(0.63)	n/a	-	378.20	(6.82)	515.93	(8.72)	860.61	(8.85)	1397.39	(29.60)	30.70	(0.94)
T5 + 20% Ti	1280	air	Opx	78	(12)	0.17	(0.09)	0.36	(0.10)	bdl	bdl	n/a	-	1.80	(0.37)	0.37	(0.10)	1.23	(0.44)	0.03	(0.01)	0.005	(0.003)
			Silicate Glass	41	(1)	70.67	(3.25)	480.97	(7.76)	2.54	(0.97)	n/a	-	449.59	(17.85)	548.52	(14.44)	859.87	(21.78)	1313.94	(47.15)	67.86	(1.79)
T5 + 20% Ti	1250	IW - 1.6	Opx	1905	(106.3)	1.06	(0.26)	0.92	(0.26)	1.04	(0.44)	0.03	(0.01)	1.09	(0.20)	0.67	(0.17)	0.68	(0.21)	0.05	(0.03)	0.67	(0.05)
			Arm	10377	(614.6)	542.44	(5.43)	723.50	(106.85)	1.67	(0.41)	0.32	(0.33)	306.46	(37.56)	1514.21	(212.59)	0.91	(0.13)	1.07	(0.22)	5.61	(1.71)
			Silicate Glass	1865	(36.6)	535.85	(13.28)	874.56	(13.54)	0.33	(0.10)	123.19	(2.36)	305.35	(7.51)	1114.18	(24.00)	12.01	(0.71)	1663.21	(49.85)	1738.78	(49.45)
T8 + 0% Ti	1280	FMQ + 0.1	An	1.30	(0.5)	0.24	(0.10)	0.25	(0.08)	0.27	max	182.73	(13.32)	0.08	(0.03)	0.37	(0.06)	0.07	(0.03)	0.24	(0.04)	0.040	(0.017)
			Silicate Glass	169.31	(12.4)	863.70	(72.71)	1051.16	(64.17)	62.95	(7.23)	1206.78	(42.10)	273.10	(25.46)	1842.31	(148.60)	1574.33	(106.77)	1385.96	(101.08)	1263.18	(59.24)
T8 + 1% Ti	1250	FMQ + 0.1	Spl	4524.00	max	0.24	max	0.48	(0.16)	bdl	bdl	0.10	(0.08)	0.11	(0.05)	0.19	(0.09)	0.31	(0.01)	0.33	(0.23)	0.51	(0.30)
			Silicate Glass	118.17	(37.1)	159.96	(6.30)	1184.99	(29.80)	7.75	(0.17)	113.25	(2.43)	193.05	(9.36)	422.82	(17.58)	779.75	(13.83)	983.90	(35.86)	589.90	(23.18)
T8 + 2% Ti	1280	FMQ + 0.1	Spl	10852.25	(5175.3)	0.61	max	0.99	(0.20)	1.30	max	0.32	(0.18)	0.13	(0.03)	0.46	(0.22)	0.96	(0.53)	0.24	(0.18)	0.38	(0.28)
			Silicate Glass	234.54	(20.2)	522.25	(22.62)	813.62	(23.75)	40.75	(0.96)	826.13	(8.94)	179.19	(7.85)	1167.52	(40.14)	990.45	(8.20)	934.54	(40.25)	807.86	(7.42)
T8 + 3% Ti	1280	FMQ + 0.1	Spl	22310.78	(7236.2)	bdl	bdl	0.41	(0.00)	bdl	bdl	0.01	max	0.06	max	0.08	(0.03)	0.02	max	0.02	max	0.02	(0.01)
			Silicate Glass	67.36	(8.5)	519.96	(7.79)	973.09	(12.44)	36.51	(0.33)	825.52	(7.73)	152.73	(1.93)	980.93	(15.89)	1055.09	(14.57)	924.20	(15.23)	836.22	(7.81)
T8 + 5% Ti	1260	FMQ = 0.0	An	2.54	max	0.23	(0.10)	0.76	(0.10)	bdl	bdl	254.64	(22.87)	0.18	(0.06)	0.11	(0.02)	0.11	(0.05)	0.31	(0.10)	0.012	(0.006)
			Silicate Glass	115.18	(3.5)	440.66	(18.41)	2004.31	(44.79)	9.20	(0.53)	1286.33	(23.38)	650.99	(27.09)	438.41	(14.55)	948.16	(20.90)	956.07	(36.27)	251.68	(4.46)
T8 + 10% Ti	1230	FMQ - 0.1	An	1.13	(0.2)	0.16	(0.06)	0.30	(0.11)	0.21	(0.10)	16.86	(5.38)	0.05	(0.03)	0.16	(0.02)	0.13	(0.10)	0.13	(0.04)	0.05	(0.03)
			Silicate Glass	81.40	(3.3)	552.58	(110.80)	744.54	(205.77)	72.79	(16.07)	92.66	(9.85)	349.27	(37.12)	534.62	(38.94)	1178.98	(96.86)	871.38	(106.72)	689.18	(52.38)
T8 + 20% Ti	1270	FMQ = 0.0	Arm	18225.03	(3253.9)	610.69	(71.12)	2310.38	(261.71)	28.31	(0.97)	n/a	-	1798.23	(271.56)	1597.71	(14.11)	112.42	(16.11)	0.90	(0.11)	5.85	(0.19)
			Silicate Glass	242.95	(50.9)	182.04	(2.86)	875.08	(5.74)	32.03	(1.72)	n/a	-	361.27	(8.04)	339.00	(3.29)	1069.74	(7.92)	1226.34	(23.85)	1143.98	(31.06)
T8 + 20% Ti	1240	air	Arm	1798.74	(335.9)	469.89	(41.30)	1388.44	(108.27)	1.78	(0.58)	n/a	-	2190.61	(245.99)	1507.90	(141.79)	84.14	(8.46)	0.86	(0.19)	0.44	(0.03)
			An	2.87	max	bdl	bdl	0.19	(0.05)	bdl	bdl	n/a	-	0.09	(0.01)	0.07	(0.01)	0.03	(0.01)	0.16	(0.03)	0.0012	(0.0005)
			Silicate Glass	27.85	(7.5)	147.19	(6.641)	577.03	(18.85)	2.29	(0.38)	n/a	-	487.45	(22.87)	319.78	(13.64)	580.99	(13.82)	1250.40	(50.142)	93.52	(1.56)
T8 + 20% Ti	1250	FMQ + 0.1	Arm	34511.31	(4558.9)	559.65	(12.40)	1842.23	(35.86)	21.47	(1.83)	0.22	(0.18)	2225.04	(40.05)	1647.00	(40.39)	136.31	(23.635)	0.58	(0.10)	5.48	(0.26)
			Silicate Glass	1110.53	(20.1)	169.20	(5.97)	732.97	(19.03)	29.26	(0.46)	105.99	(1.71)	437.50	(10.85)	348.55	(8.84)	1069.08	(30.03)	885.80	(30.76)	800.27	(18.25)
FT1+1% Ti	1200	IW - 1.5	Cpx	6451.28	(1086.7)	43.77	(3.62)	0.61	(0.15)	5.43	(1.77)	0.68	(0.38)	61.24	(11.58)	3.60	(1.14)	1.73	(1.01)	4.25	(1.67)	3.54	(0.52)
			Silicate Glass	1197.95	(22.5)	1025.00	(11.11)	246.84	(2.24)	36.34	(4.07)	4073.64	(104.05)	582.41	(6.44)	1158.89	(19.64)	1603.30	(46.56)	1773.19	(26.85)	1697.69	(56.42)

Supplementary Table 3.3- Trace elements LA-ICP-MS analysis (μg/g) of main crystal phases and coexistent silicate glasses

Experiment	Temp. (° C)	Δ to redox buffer[a]	Phase	Cr	σ	Zr	σ	Nb	σ	Mo	σ	Ba	σ	Hf	σ	Ta	σ	W	σ	Th	σ	U	σ
FT1+5%Ti	1200	IW - 1.5	Cpx	9927.39	(1392.2)	11.45	(4.16)	1.14	(0.60)	21.59	(3.40)	0.25	(0.11)	15.66	(0.51)	0.80	(0.30)	6.57	(2.09)	2.15	(1.03)	2.27	(0.36)
			Silicate Glass	2083	(36.0)	616.11	(8.56)	964.19	(10.39)	69.81	(2.49)	1827.97	(15.86)	362.13	(8.16)	608.16	(13.66)	1033.22	(11.03)	1388.49	(22.82)	1354.82	(22.02)
FT1+5%Ti	1100	IW - 1.8	Cpx	6996	(995)	21.24	(0.33)	1.62	(0.55)	32.38	(6.19)	0.465	(0.21)	14.92	(2.10)	0.85	(0.50)	10.40	(5.99)	2.06	(0.53)	1.90	(0.89)
			Silicate Glass	1763	(134)	859.36	(49.72)	1259.28	(58.19)	95.68	(15.32)	1873.67	(81.46)	477.13	(21.34)	634.80	(30.70)	1252.45	(62.72)	1648.84	(75.33)	1571.38	(69.77)
FT1+10%Ti	1100	IW - 1.8	Cpx	7121	(893)	5.44	(0.38)	1.34	(0.15)	27.83	(10.08)	0.04	(0.02)	20.62	(3.14)	1.54	(0.53)	4.88	(2.37)	1.43	(0.38)	1.75	(0.40)
			Ilm	27499	(5097)	461.25	(147.92)	1814.66	(281.86)	545.31	(63.20)	640.34	(262.83)	538.45	(114.99)	2355.74	(437.62)	1202.15	(902.33)	109.13	(25.97)	66.70	(13.24)
			Silicate Glass	2291	(76)	518.93	(19.07)	1244.67	(31.79)	92.20	(7.93)	1379.43	(29.88)	711.28	(26.34)	1370.63	(49.40)	1247.55	(25.86)	1339.21	(42.00)	1255.44	(25.69)
FT1+20% Ti	1100	IW - 1.8	Cpx	1445	(224)	22.45	(0.20)	0.48	(0.01)	25.32	(9.07)	0.17	(0.10)	16.99	(0.90)	1.37	(0.43)	7.62	(1.88)	2.17	(0.96)	1.87	(0.61)
			Arm	3932	(686)	1221.41	(197.96)	187.90	(38.16)	216.61	(50.81)	86.21	(55.86)	366.61	(37.86)	1254.07	(235.60)	138.74	(17.15)	3.12	(1.82)	21.31	(3.38)
			Ttn	1943	(262)	1849.47	(132.08)	393.84	(23.09)	360.90	(90.83)	53.25	(29.14)	769.14	(76.36)	5757.81	(517.08)	248.55	(30.03)	617.64	(48.01)	585.38	(49.10)
			Silicate Glass	380	(60)	2223.88	(485.47)	364.95	(19.25)	51.83	(7.05)	2237.197	(338.15)	504.73	(188.61)	1232.71	(156.10)	1346.91	(183.80)	1959.92	(206.58)	1941.43	(144.07)

Experiment	Temp. (° C)	Δ to redox buffer[a]	Phase	Cr	σ	Y	σ	Zr	σ	Nb	σ	Mo	σ	Ba	σ	La	σ	Nd	σ	Sm	σ	Lu	σ
T1+0% Ti + REE	1300	IW - 1.6	Cpx	3036	(282)	143.48	(16.89)	25.21	(7.51)	2.10	(0.79)	5.11	(1.69)	0.20	(0.04)	20.13	(3.70)	62.46	(12.43)	199.37	(28.06)	107.50	(13.33)
			Silicate Glass	3112	(258)	1114.54	(22.10)	853.75	(54.41)	1187.65	(83.32)	16.03	(6.12)	1434.25	(18.55)	1175.94	(9.08)	1090.79	(8.66)	2500.76	(47.55)	1125.03	(22.94)
T1+10% Ti + REE	1280	IW - 1.6	Cpx	2220	(72)	77.86	(3.17)	6.08	(0.83)	1.23	(0.24)	118.54	(28.76)	0.03	(0.02)	9.63	(0.40)	32.84	(1.69)	48.80	(2.01)	75.53	(2.98)
			Ol	1594	(96)	1.75	(0.23)	0.12	(0.05)	0.09	(0.01)	40.86	(15.60)	0.010	(0.005)	0.003	(0.001)	0.05	(0.01)	0.10	(0.03)	7.19	(0.46)
			Silicate Glass	3075	(299)	677.38	(13.63)	472.75	(5.84)	892.55	(7.94)	134.57	(13.94)	126.81	(1.84)	647.76	(8.14)	630.05	(7.62)	622.52	(6.13)	670.30	(5.67)

T1+0% Ti + REE	1300	IW - 1.6	Cpx	Hf	σ	Ta	σ	W	σ	Th	σ	U	σ	Sc	σ
			Silicate Glass	37.17	(15.67)	2.54	(0.84)	2.89	(1.37)	4.00	(1.48)	6.56	(1.91)	9.24	(0.82)
T1+10% Ti + REE	1280	IW - 1.6	Cpx	881.82	(66.04)	1006.86	(103.64)	68.70	(20.56)	2257.20	(22.48)	1641.21	(14.54)	7.66	(0.44)
			Ol	6.05	(0.39)	0.51	(0.14)	16.73	(3.27)	1.14	(0.39)	1.85	(0.59)	9.75	(0.78)
			Silicate Glass	0.10	(0.02)	0.005	(0.004)	1.43	(0.63)	0.006	(0.004)	0.005	(0.003)	0.81	(0.039)
				209.74	(1.65)	513.75	(6.94)	196.42	(50.76)	1411.06	(5.12)	1412.97	(38.52)	8.75	(0.63)

[a]Air: top and bottom of the furnace were not sealed during the experiment to produce an oxidized environment and have only the more oxidized species of each element present; for experiments performed with oxygen fugacities relevant to the Earth's mantle the value is given relative to the FMQ: Fayalite-Magnetite-Quartz mineral redox buffer as described by O'Neill (1987); for experiments performed with oxygen fugacities relevant to the lunar mantle the value is given relative to the IW: Iron Wüstite mineral redox buffer as described by Myers and Eugster (1983).n/a: not acquired, bdl: below detection limit

Supplementary Table 3.4 - Number of cations per formula unity of mineral phases in experiments

Experiment	Temp. (° C)	Δ to redox buffer[a]	Phase	M2 (VI)					M1 (VI)				T (IV)				End-members (%)		
				Fe^{2+}	Mn	Mg	Ca	Ti	Al	Cr	Fe^{2+}	Mg	Si	Ti	Al	Total	Wo	En	Fs
T1 + 0% Ti	1300	FMQ = 0.0	Cpx	-	0.01	0.14	0.85	-	0.03	0.03	-	0.93	1.99	-	0.01	4.00	44.43	55.57	-
T1 + 0% Ti	1305	air	Cpx	-	-	0.11	0.89	-	0.03	0.02	-	0.95	1.97	-	0.03	4.00	45.49	54.51	-
T1 + 0% Ti	1300	IW - 1.6	Cpx	-	0.01	0.13	0.86	-	0.03	0.01	-	0.96	1.98	-	0.02	4.00	44.05	55.95	-
T1 + 1% Ti	1295	air	Cpx	-	-	0.10	0.90	0.01	0.04	-	-	0.95	1.99	-	0.01	3.99	46.37	53.63	-
T1 + 1% Ti	1300	FMQ = 0.0	Cpx	-	-	0.11	0.89	0.02	0.03	0.02	-	0.93	1.96	-	0.04	4.00	46.16	53.84	-
T1 + 2% Ti	1300	FMQ = 0.0	Cpx	-	0.01	0.14	0.85	0.03	0.03	0.03	-	0.92	1.96	-	0.04	4.00	44.39	55.61	-
T1 + 2% Ti	1300	IW - 1.6	Cpx	-	0.01	0.25	0.74	0.01	0.02	0.01	-	0.96	1.98	-	0.02	4.00	38.03	61.97	-
T1 + 3% Ti	1300	FMQ = 0.0	Cpx	-	0.01	0.17	0.82	0.03	0.01	0.03	-	0.92	1.96	-	0.04	4.00	43.07	56.93	-
T1 + 3% Ti	1305	air	Cpx	-	0.01	0.16	0.84	0.03	0.01	-	-	0.96	1.96	-	0.04	3.99	42.97	57.03	-
T1 + 5% Ti	1270	FMQ = 0.0	Cpx	-	0.01	0.12	0.86	0.04	0.01	0.02	-	0.93	1.95	-	0.05	4.00	45.03	54.97	-
T1 + 5% Ti	1290	IW - 1.7	Cpx	-	0.01	0.14	0.85	0.03	-	-	-	0.96	1.95	0.01	0.05	3.99	43.69	56.31	-
T1 + 10% Ti	1260	FMQ = 0.0	Cpx	-	-	0.26	0.75	0.04	-	0.02	-	0.94	1.96	0.01	0.03	4.00	38.43	61.57	-
T1 + 10% Ti	1250	IW - 1.6	Cpx	-	-	0.24	0.76	0.04	-	-	-	0.96	1.94	0.03	0.04	4.00	38.81	61.19	-
T1 + 20% Ti	1260	FMQ = 0.0	Cpx	-	-	0.22	0.78	0.05	-	0.01	-	0.94	1.92	0.03	0.05	4.00	40.20	59.80	-
T1 + 20% Ti	1250	IW - 1.6	Cpx	-	-	0.22	0.78	0.05	-	-	-	0.95	1.93	0.04	0.04	4.00	40.17	59.83	-
T7 + 0% Ti	1280	FMQ + 0.1	Cpx	-	0.01	0.12	0.87	-	0.04	0.03	-	0.93	1.98	-	0.02	4.00	45.17	54.83	-
T7 + 1% Ti	1300	FMQ = 0.0	Cpx	-	-	0.20	0.80	0.01	0.02	0.04	-	0.93	1.98	-	0.02	4.00	41.55	58.45	-
T7 + 1% Ti	1280	air	Cpx	-	-	0.15	0.85	0.01	0.03	-	-	0.95	1.99	-	0.02	3.99	43.64	56.36	-
T7 + 2% Ti	1280	FMQ + 0.1	Cpx	-	0.01	0.11	0.88	0.03	0.02	0.04	-	0.92	1.94	-	0.06	4.00	46.11	53.89	-
T7 + 3% Ti	1280	FMQ + 0.1	Cpx	-	0.01	0.12	0.87	0.04	0.003	0.04	-	0.92	1.93	-	0.07	4.00	45.41	54.59	-
T7 + 5% Ti	1280	FMQ + 0.1	Cpx	-	-	0.18	0.82	0.03	-	0.03	-	0.94	1.95	0.002	0.04	4.00	42.12	57.88	-
T7 + 10% Ti	1280	FMQ + 0.1	Cpx	-	-	0.21	0.79	0.04	-	0.03	-	0.94	1.95	0.01	0.04	4.00	40.94	59.06	-
T7 + 10% Ti	1280	IW - 1.6	Cpx	-	-	0.18	0.82	0.04	-	-	-	0.95	1.93	0.03	0.05	4.00	41.87	58.13	-
T7 + 20% Ti	1230	FMQ - 0.1	Cpx	-	-	0.25	0.75	0.02	-	0.03	-	0.96	1.93	0.04	0.03	4.00	38.47	61.53	-
ST1 + 5% Ti	1230	FMQ = 0.0	Cpx	0.01	-	0.12	0.88	0.07	0.02	0.01	0.06	0.84	1.86	-	0.14	4.00	46.15	50.40	3.45
ST1 + 10% Ti	1230	FMQ = 0.0	Cpx	0.01	-	0.10	0.90	0.10	-	0.01	0.05	0.86	1.84	-	0.15	4.00	47.21	50.15	2.64
FT1+1%Ti	1200	IW - 1.5	Cpx	0.04	-	0.07	0.89	0.01	0.03	0.02	0.32	0.61	1.97	-	0.03	3.99	45.60	35.36	19.05
FT1+5%Ti	1200	IW - 1.5	Cpx	0.02	-	0.08	0.90	0.04	0.01	0.03	0.23	0.69	1.95	-	0.05	4.00	46.60	40.19	13.21
FT1+5%Ti	1100	IW - 1.8	Cpx	0.03	-	0.07	0.90	0.03	-	0.01	0.28	0.69	1.94	0.03	0.03	4.01	45.41	38.85	15.74
FT1+10%Ti	1100	IW - 1.8	Cpx	0.03	0.01	0.08	0.88	0.09	-	0.01	0.24	0.65	1.89	0.02	0.09	3.99	46.85	38.96	14.20
FT1+20%Ti	1100	IW - 1.8	Cpx	0.08	0.01	0.18	0.73	0.04	-	0.01	0.30	0.66	1.92	0.03	0.05	4.01	37.46	43.33	19.21
T1+0% Ti+REE	1300	IW -1.6	Cpx	-	0.01	0.15	0.83	-	0.03	0.01	0.01	0.95	2.00	-	-	3.99	42.90	56.55	0.50
T1+10% Ti+REE	1280	IW -1.6	Cpx	-	0.01	0.25	0.75	0.05	-	0.01	0.01	0.93	1.94	0.02	0.04	4.01	38.66	60.88	0.45
T5 + 0% Ti	1300	FMQ = 0.0	Opx	-	-	0.96	0.02	-	0.02	0.02	-	0.93	2.03	-	-	3.98	1.00	99.00	-
T5 + 0% Ti	1300	IW - 1.8	Opx	-	0.01	0.98	0.02	-	0.01	-	-	0.96	2.02	-	-	3.99	0.96	99.04	-
T5 + 1% Ti	1300	FMQ = 0.0	Opx	-	-	0.98	0.02	0.003	0.02	0.01	-	0.93	2.04	-	-	3.99	1.05	98.95	-
T5 + 1% Ti	1300	IW - 1.8	Opx	-	-	0.98	0.02	0.003	0.01	-	-	0.97	2.01	-	-	3.99	0.93	99.07	-
T5 + 2% Ti	1300	FMQ = 0.0	Opx	-	0.01	0.97	0.01	0.01	0.02	0.01	-	0.93	2.03	-	-	4.00	0.74	99.26	-
T5 + 2% Ti	1300	IW - 1.8	Opx	-	0.01	0.98	0.02	0.01	0.02	0.01	-	0.93	2.04	-	-	4.00	0.87	99.13	-
T5 + 3% Ti	1300	FMQ = 0.0	Opx	-	0.01	0.97	0.02	0.01	0.03	0.02	-	0.93	2.01	-	-	4.00	0.81	99.19	-
T5 + 3% Ti	1300	IW - 1.8	Opx	-	0.01	0.98	0.01	0.01	0.02	-	-	0.94	2.03	-	-	3.99	0.68	99.32	-
T5 + 5% Ti	1280	air	Opx	-	-	0.98	0.02	0.01	0.01	-	-	0.94	2.03	-	-	4.00	0.87	99.13	-
T5 + 5% Ti	1280	FMQ + 0.1	Opx	-	0.02	0.96	0.02	0.01	0.02	0.01	-	0.95	2.01	-	-	4.00	0.96	99.04	-
T5 + 5% Ti	1300	IW - 1.8	Opx	-	0.01	0.97	0.02	0.02	0.02	0.01	-	0.95	2.01	-	-	4.00	0.87	99.13	-
T5 + 10% Ti	1300	FMQ = 0.0	Opx	-	-	0.99	0.01	0.02	0.02	0.01	-	0.94	2.01	-	-	4.00	0.71	99.29	-
T5 + 10% Ti	1280	air	Opx	-	-	0.99	0.01	0.02	0.01	-	-	0.95	2.02	-	-	4.00	0.59	99.41	-
T5 + 10% Ti	1250	IW - 1.6	Opx	-	-	0.99	0.01	0.04	0.02	-	-	0.94	2.00	-	-	4.00	0.55	99.45	-
T5 + 20% Ti	1285	air	Opx	-	-	0.99	0.01	0.04	0.01	-	-	0.96	1.99	-	-	3.99	0.55	99.45	-
T5 + 20% Ti	1280	air	Opx	-	-	0.99	0.01	0.03	0.01	-	-	0.95	2.01	-	-	4.00	0.47	99.53	-
T5 + 20% Ti	1250	IW - 1.6	Opx	-	-	0.98	0.02	0.02	0.01	0.01	-	0.96	2.00	-	-	3.99	0.79	99.21	-
T1 + 2% Ti	1300	IW - 1.6	Pgt	-	0.02	0.83	0.15	0.01	0.02	-	-	0.97	2.01	-	-	4.00	7.92	92.08	-
T1 + 10% Ti	1250	IW - 1.6	Pgt	-	-	0.90	0.10	0.04	-	-	-	0.97	1.98	-	0.02	4.00	5.03	94.97	-
T1 + 20% Ti	1250	IW - 1.6	Pgt	-	-	0.90	0.10	0.04	0.02	-	-	0.95	2.00	-	-	4.00	5.08	94.92	-
T7 + 20% Ti	1250	FMQ + 0.1	Pgt	-	-	0.88	0.12	0.03	0.01	0.01	-	0.94	2.00	-	-	3.99	6.30	93.70	-
T7 + 20% Ti	1230	FMQ - 0.1	Pgt	-	-	0.90	0.10	0.03	0.02	0.01	-	0.94	2.00	-	-	3.99	5.28	94.72	-

Supplementary Table 3.4 - Number of cations per formula unity of mineral phases in experiments

Experiment	Temp. (° C)	Δ to redox buffer[a]	Phase	Si	Ti	Al	Cr	Fe^{3+}	Fe^{2+}	Mn	Mg	Ca	Total		Te	Fo	Fa	Ca-Ol
T1 + 0% Ti	1305	air	Ol	1.0	-	-	-	-	-	0.01	2.0	0.02	3.0	-	0.40	98.83	-	0.77
T1 + 0% Ti	1300	FMQ = 0.0	Ol	1.0	-	-	-	-	-	0.02	1.9	0.01	3.0	-	0.96	98.34	-	0.70
T1 + 0% Ti	1300	IW - 1.6	Ol	1.0	-	-	-	-	-	0.01	2.0	0.02	3.0	-	0.27	98.99	-	0.74
T1 + 1% Ti	1295	air	Ol	1.1	-	-	-	-	-	-	1.9	0.02	3.0	-	-	98.86	-	1.14
T1 + 1% Ti	1300	FMQ = 0.0	Ol	1.0	-	-	-	-	-	-	1.9	0.02	3.0	-	-	99.12	-	0.88
T1 + 1% Ti	1300	IW - 1.6	Ol	1.0	-	-	-	-	-	-	2.0	0.01	3.0	-	0.07	99.22	-	0.71
T1 + 2% Ti	1300	FMQ = 0.0	Ol	1.0	-	-	-	-	-	0.01	1.9	0.01	3.0	-	0.57	98.71	-	0.71
T1 + 3% Ti	1305	air	Ol	1.0	-	-	-	-	-	0.01	1.9	0.01	3.0	-	0.30	99.09	-	0.61
T1 + 3% Ti	1300	FMQ = 0.0	Ol	1.0	-	-	-	-	0.01	0.01	1.9	0.01	3.0	-	0.49	98.50	0.38	0.62
T1 + 3% Ti	1300	IW - 1.6	Ol	1.0	-	-	-	-	-	-	2.0	0.01	3.0	-	0.22	99.12	-	0.66
T1 + 5% Ti	1305	air	Ol	1.0	-	-	-	-	-	-	1.9	0.01	3.0	-	0.31	99.05	-	0.64
T1 + 5% Ti	1270	FMQ = 0.0	Ol	1.0	-	-	-	-	-	0.01	1.9	0.01	3.0	-	0.74	98.62	-	0.64
T1 + 5% Ti	1300	IW - 1.6	Ol	1.0	-	-	-	-		0.01	2.0	0.01	3.0	-	0.42	98.97	-	0.61
T1 + 20% Ti	1250	FMQ + 0.1	Ol	1.0	-	-	-	-	-	-	2.0	0.01	3.0	-	-	99.68	-	0.32
T1 + 20% Ti	1240	air	Ol	1.0	-	-	-	-	-	-	2.0	0.01	3.0	-	-	99.67	-	0.33
T7 + 2% Ti	1280	FMQ + 0.1	Ol	1.0	-	-	-	-	-	0.02	1.9	-	3.0	-	0.95	99.05	-	-
T7 + 3% Ti	1280	FMQ + 0.1	Ol	1.0	-	-	-	-	-	0.01	2.0	-	3.0	-	0.55	99.45	-	-
T7 + 5% Ti	1280	FMQ + 0.1	Ol	1.0	-	-	-	-	-	-	2.0	0.01	3.0	-	-	99.39	-	0.61
T7 + 5% Ti	1280	IW - 1.6	Ol	1.0	-	-	0.01	-		0.01	1.9	0.01	3.0	-	0.37	98.94	-	0.69
T7 + 10% Ti	1280	IW - 1.6	Ol	1.0	-	-	-	-			2.0	0.01	3.0	-	-	99.54	-	0.46
T5 + 20% Ti	1270	air	Ol	1.0	-	-	-	-	-	-	2.0	-	3.0	-	-	99.83	-	0.17
T8 + 0% Ti	1280	FMQ + 0.1	Ol	1.0	-	-	-	-	-	0.02	1.9	0.01	3.0	-	0.77	98.92	-	0.31
T8 + 5% Ti	1260	FMQ = 0.0	Ol	1.0	-	-	-	-	-	-	2.0	-	3.0	-	-	99.77	-	0.23
T1+10% Ti+REE	1280	IW -1.6	Ol	1.1	-	-	-	-	0.01	-	1.9	-	3.0	-	-	99.04	0.65	-

				Mg	Na	Fe^{2+}	Ca	Ti	Si	Al	P	Cr	K	Total		Kar	Fpsb
T1 + 20% Ti	1250	FMQ + 0.1	Arm	0.90	-	-	0.01	1.92	0.01	0.05	-	0.10	-	2.99	-	100.00	-
T1 + 20% Ti	1260	FMQ = 0.0	Arm	0.91	-	-	-	1.96	0.01	0.07	-	0.03	-	2.98	-	100.00	-
T1 + 20% Ti	1240	air	Arm	0.93	-	0.04	-	1.96	0.01	0.05	-	-	-	3.00	-	95.59	4.41
T7 + 20% Ti	1273	air	Arm	0.94	-	0.05	-	1.96	0.01	0.05	-	-	-	3.00	-	95.30	4.70
T7 + 20% Ti	1250	FMQ + 0.1	Arm	0.85	-	0.01	-	1.89	0.01	0.05	-	0.19	-	2.98	-	99.17	0.83
T7 + 20% Ti	1230	FMQ - 0.1	Arm	0.83	-	-	0.01	1.88	0.01	0.06	-	0.20	-	2.99	-	100.00	-
T5 + 20% Ti	1270	air	Arm	0.90	-	-	0.01	1.95	0.01	0.06	-	0.06	-	2.98	-	100.00	-
T5 + 20% Ti	1285	air	Arm	0.94	-	0.03	-	1.95	0.01	0.06	-	-	-	3.00	-	96.89	3.11
T5 + 20% Ti	1280	air	Arm	0.93	-	0.04	-	1.95	0.01	0.07	-	-	-	3.00	-	95.93	4.07
T8 + 20% Ti	1270	air	Arm	0.79	-	-	-	1.82	0.01	0.34	-	0.03	-	2.99	-	100.00	-
T8 + 20% Ti	1240	air	Arm	0.79	-	0.02	-	1.80	-	0.35	-	0.02	-	3.00	-	97.66	2.34
T8 + 20% Ti	1250	FMQ + 0.1	Arm	0.76	-	-	-	1.78	0.01	0.38	-	0.05	-	2.99	-	100.00	-
FT1+20%	1100	IW - 1.8	Arm	0.28	-	0.64	0.02	1.97	0.01	0.04	-	0.02	-	2.96	-	30.31	69.69
T5+20%	1250	IW - 1.6	Arm	0.78	-	-	-	2.00	-	0.09	-	0.05	-	2.92	-	100.00	-
T1+20%	1250	IW - 1.6	Arm	0.74	-	-	-	2.08	-	0.05	-	-	-	2.88	-	100.00	-

				Si	Ti	Al	Cr	Fe^{3+}	Fe^{2+}	Mn	Mg	Ca	Na	Total		An	Ab	Or
T8 + 0% Ti	1280	FMQ + 0.1	An	2.06	-	1.92	-	-	-	-	0.04	0.98	0.01	5.00	-	99.37	0.63	-
T8 + 5% Ti	1260	FMQ = 0.0	An	2.06	0.01	1.93	-	-	-	-	0.03	0.97	-	5.00	-	100.00	0.00	-
T8 + 10% Ti	1230	FMQ - 0.1	An	2.02	0.01	1.96	-	-	-	-	0.03	0.98	-	5.00	-	100.00	0.00	-
T8 + 20% Ti	1240	air	An	2.09	0.01	1.91	-	-	-	-	0.03	0.94	0.02	5.00	-	97.86	2.14	-

				Si	Ti	Al	Cr	Fe^{3+}	Fe^{2+}	Mn	Mg	Total
T8 + 1% Ti	1250	FMQ + 0.1	Spl	-	-	2.02	0.02	-	-	-	0.96	3.00
T8 + 2% Ti	1280	FMQ + 0.1	Spl	-	-	1.97	0.05	-	-	0.01	0.97	2.99
T8 + 3% Ti	1280	FMQ + 0.2	Spl	-	0.01	1.92	0.09	-	-	0.01	0.98	3.00

				Mg	Na	Fe^{2+}	Ca	Ti	Si	Al	P	Cr	K	Mn	Total
FT1+10%	1100	IW - 1.8	Ilm	0.15	-	0.76	-	1.00	-	0.01	-	0.03	-	0.06	1.95

				Mg	Na	Fe^{2+}	Ca	Ti	Si	Al	P	Cr	K	Mn	Total
FT1+20%	1100	IW - 1.8	Ttn	0.01	0.02	-	0.99	0.99	0.97	0.01	-	0.01	-	0.01	3.01

* only values higher than 0.005 apfu are shown, with the exception of Ti

Supplementary Table 3.5 - Lunar Magma Ocean (LMO) cumulates[1] proportion (%) at the hybrid lunar mantle source used for the aggregate modal partial melting models

Modeled curve (Source)	Sequence 1 +2 (ol+opx)	Sequence 3 (pl+ol+pgt)	Sequence 4 (cpx+pl+pgt)	Sequence 5 (pgt+pl+cpx+ilm)	Residual Metal
A	82.7 (0.01)	17.0 (2.0)	-	-	0.3
B	97.7 (2.00)	-	2.0 (2.0)	-	0.3
C	94.7 (0.20)	-	4.0 (2.0)	1.0 (2.0)	0.3
D	90.5 (0.01)	-	1.0 (2.0)	8.0 (2.0)	0.5
E[2]	90.5 (0.01)	-	1.0 (2.0)	8.0 (2.0)	0.5
F	95.5 (2.00)	-	4.0 (2.0)	0.4 (2.0)	0.1
G	91.6 (0.15)	-	6.0 (2.0)	2.0 (0.5)	0.4
H	98.0 (0.15)	-	-	-	2.0
I	92.0 (0.15)		6.0 (2.0)	2.0 (0.5)	-

[1]LMO sequences as modeled by Snyder et al. (1992); [2]Using armalcolite as Fe-Ti oxide in the source instead of ilmenite. Numbers in parentheses are the amount (%) of trapped interstitial liquid (TIL) in the source. Ol: olivine; opx: orthopyroxene; pgt: pigeonite; cpx: clinopyroxene; pl: plagioclase; ilm: ilmenite

Supplementary Table 3.6 - Partition coefficients and modeled aggregate modal fractional melting curves shown in Fig. 10

Model A

	D_W	D_{Nb}	D_{Ta}	D_{Th}	D_{Zr}	D_{Hf}	D_U	Mineralogical proportion (% at source)	
Olv	5.1E-03	7.5E-05	5.3E-05	6.1E-06	3.8E-04	5.2E-04	1.3E-05	Ol	46.4
Opx	6.0E-03	1.5E-03	7.9E-04	2.6E-05	1.8E-03	3.9E-03	5.1E-04	Opx	40.5
Cpx	8.1E-03	1.9E-03	1.8E-03	2.0E-03	2.1E-02	4.4E-02	2.6E-03	Cpx	-
Pig	6.0E-03	1.5E-03	7.9E-04	2.6E-05	1.8E-03	3.9E-03	5.1E-04	Pgt	3.7
Plag	1.2E-04	3.8E-04	2.5E-04	3.2E-04	5.2E-04	2.8E-04	4.7E-05	Pl	9.0
Ilm	7.5E-02	5.9E-01	9.9E-01	6.0E-04	3.0E-01	4.1E-01	3.9E-03	Ilm	-
Metal	6.2E+00	-	-	-	-	-	-	Metal	0.3

F	W	Nb	Ta	Th	Zr	Hf	U
0 (source)	0.0007768	0.0265652	0.0014795	0.0025416	0.3670685	0.0140293	0.0007397
0.001	0.032251	20.007136	1.3599282	2.5415654	227.01274	5.5449812	0.729105
0.002	0.0315967	12.474237	0.7349182	1.2707827	156.84074	4.450466	0.3697618
0.003	0.0309597	8.7223904	0.4928989	0.8471885	115.5793	3.6436699	0.2465573
0.004	0.0303394	6.6168302	0.3698523	0.6353914	89.833447	3.0396056	0.1849185
0.005	0.0297355	5.3082279	0.2958933	0.5083131	72.825743	2.5800317	0.1479348
0.006	0.0291474	4.4265449	0.2465785	0.4235942	60.992041	2.2246949	0.123279
0.007	0.0285747	3.7948165	0.211353	0.3630808	52.377867	1.9455188	0.1056677
0.008	0.0280168	3.3206005	0.1849339	0.3176957	45.863505	1.7227282	0.0924593
0.009	0.0274735	2.9516745	0.1643857	0.2823962	40.77864	1.5422495	0.082186
0.01	0.0269443	2.6565136	0.1479471	0.2541565	36.704553	1.393957	0.0739674
0.011	0.0264287	2.4150138	0.1344974	0.2310514	33.369075	1.2704829	0.0672431
0.012	0.0259265	2.2137629	0.1232893	0.2117971	30.58877	1.1664028	0.0616395
0.013	0.0254371	2.0434736	0.1138055	0.195505	28.235944	1.0776759	0.056898
0.014	0.0249602	1.8975112	0.1056765	0.1815404	26.219146	1.0012556	0.0528339
0.015	0.0244956	1.7710104	0.0986314	0.1694377	24.471222	0.9348175	0.0493116
0.016	0.0240427	1.6603223	0.092467	0.1588478	22.941778	0.8765674	0.0462296
0.017	0.0236014	1.5626563	0.0870277	0.1495038	21.592264	0.825104	0.0435102
0.018	0.0231712	1.475842	0.0821928	0.1411981	20.392695	0.7793213	0.041093
0.019	0.0227518	1.3981661	0.0778669	0.1337666	19.319395	0.7383364	0.0389302
0.02	0.022343	1.3282578	0.0739736	0.1270783	18.353426	0.7014379	0.0369837
0.021	0.0219444	1.2650075	0.070451	0.1210269	17.479453	0.6680465	0.0352226
0.022	0.0215558	1.2075071	0.0672487	0.1155257	16.684932	0.6376867	0.0336215
0.023	0.0211768	1.1550068	0.0643248	0.1105028	15.959501	0.6099646	0.0321597
0.024	0.0208072	1.1068815	0.0616446	0.1058986	15.294521	0.5845514	0.0308198
0.025	0.0204468	1.0626063	0.0591788	0.1016626	14.68274	0.5611704	0.029587
0.026	0.0200952	1.0217368	0.0569027	0.0977525	14.11802	0.5395876	0.028449
0.027	0.0197523	0.9838947	0.0547952	0.0941321	13.59513	0.5196033	0.0273953
0.028	0.0194177	0.9487556	0.0528383	0.0907702	13.10959	0.5010462	0.0264169
0.029	0.0190913	0.9160399	0.0510162	0.0876402	12.657535	0.4837689	0.025506
0.03	0.0187728	0.8855052	0.0493157	0.0847188	12.235617	0.4676433	0.0246558
0.035	0.0172917	0.7590045	0.0422706	0.0726162	10.487672	0.4008372	0.0211335
0.04	0.0159781	0.6641289	0.0369868	0.0635391	9.1767128	0.3507326	0.0184919
0.045	0.0148103	0.5903368	0.0328771	0.0564792	8.157078	0.3117623	0.0164372
0.05	0.0137695	0.5313031	0.0295894	0.0508313	7.3413702	0.2805861	0.0147935
0.055	0.0128397	0.4830028	0.0268995	0.0462103	6.6739729	0.2550782	0.0134486
0.06	0.0120068	0.4427526	0.0246579	0.0423594	6.1178085	0.2338217	0.0123279
0.065	0.0112588	0.4086947	0.0227611	0.039101	5.6472079	0.2158354	0.0113796
0.075	0.0099773	0.3542021	0.0197263	0.0338875	4.8942468	0.1870574	0.0098623
0.1	0.0076789	0.2656516	0.0147947	0.0254157	3.6706851	0.140293	0.0073967
0.2	0.0038838	0.1328258	0.0073974	0.0127078	1.8353426	0.0701465	0.0036984

Model B

	D_W	D_{Nb}	D_{Ta}	D_{Th}	D_{Zr}	D_{Hf}	D_U	Mineralogical proportion (% at source)	
Olv	5.1E-03	7.5E-05	5.3E-05	6.1E-06	3.8E-04	5.2E-04	1.3E-05	Ol	49.8
Opx	6.0E-03	1.5E-03	7.9E-04	2.6E-05	1.8E-03	3.9E-03	5.1E-04	Opx	47.9
Cpx	8.1E-03	1.9E-03	1.8E-03	2.0E-03	2.1E-02	4.4E-02	2.6E-03	Cpx	0.8
Pig	6.0E-03	1.5E-03	7.9E-04	2.6E-05	1.8E-03	3.9E-03	5.1E-04	Pgt	0.5
Plag	1.2E-04	3.8E-04	2.5E-04	3.2E-04	5.2E-04	2.8E-04	4.7E-05	Pl	0.7
Ilm	7.5E-02	5.9E-01	9.9E-01	6.0E-04	3.0E-01	4.1E-01	3.9E-03	Ilm	-
Metal	6.2E+00	0.0E+00	0.0E+00	0.0E+00	0.0E+00	0.0E+00	0.0E+00	Metal	0.3

Supplementary Table 3.6 - Partition coefficients and modeled aggregate modal fractional melting curves shown in Fig. 10

F	W	Nb	Ta	Th	Zr	Hf	U
0 (source)	0.0021994	0.1164608	0.0067721	0.0123767	1.5491442	0.0493758	0.0034341
0.001	0.0895684	85.164516	6.1271581	12.376723	857.26812	16.412467	3.3467611
0.002	0.0877868	54.030833	3.3553935	6.1883613	620.19453	13.689175	1.7159421
0.003	0.0860513	38.069883	2.2554161	4.1255742	470.49041	11.567392	1.1446804
0.004	0.0843606	28.964559	1.6928766	3.0941807	371.9515	9.8978965	0.8585239
0.005	0.0827135	23.259944	1.3544008	2.4753445	304.36761	8.5708897	0.6868194
0.006	0.0811086	19.402965	1.1286751	2.0627871	256.16635	7.505163	0.5723495
0.007	0.0795449	16.635618	0.9674364	1.7681032	220.53513	6.6403237	0.4905853
0.008	0.0780212	14.557217	0.8465069	1.5470903	193.34336	5.9311968	0.4292621
0.009	0.0765362	12.939998	0.7524506	1.3751914	172.00894	5.3437821	0.3815664
0.01	0.075089	11.646057	0.6772056	1.2376723	154.86726	4.8523235	0.3434097
0.011	0.0736785	10.587339	0.6156414	1.1251566	140.8123	4.4371773	0.3121907
0.012	0.0723036	9.7050646	0.564338	1.0313936	129.08765	4.083256	0.2861748
0.013	0.0709633	8.958522	0.5209274	0.9520556	119.1618	3.7788871	0.2641613
0.014	0.0696567	8.3186278	0.4837183	0.8840516	110.65187	3.5149723	0.2452927
0.015	0.0683829	7.7640527	0.4514704	0.8251148	103.27575	3.2843661	0.2289398
0.016	0.0671408	7.2787994	0.4232535	0.7735452	96.821295	3.0814134	0.2146311
0.017	0.0659296	6.8506347	0.3983562	0.7280425	91.126041	2.9016038	0.2020057
0.018	0.0647485	6.4700439	0.3762253	0.6875957	86.063531	2.7413126	0.1907832
0.019	0.0635966	6.1295153	0.356424	0.6514065	81.533892	2.5976044	0.180742
0.02	0.062473	5.8230395	0.3386028	0.6188361	77.457206	2.4680842	0.1717049
0.021	0.0613771	5.5457519	0.3224788	0.5893677	73.768771	2.3507837	0.1635284
0.022	0.0603081	5.2936723	0.3078207	0.5625783	70.415646	2.2440737	0.1560953
0.023	0.0592651	5.0635126	0.2944372	0.5381184	67.354097	2.1465963	0.1493086
0.024	0.0582476	4.8525329	0.282169	0.5156968	64.547677	2.0572126	0.1430874
0.025	0.0572547	4.6584316	0.2708822	0.4950689	61.96577	1.9749609	0.1373639
0.026	0.0562858	4.4792612	0.2604637	0.4760278	59.582471	1.8990242	0.1320807
0.027	0.0553402	4.3133626	0.2508169	0.4583971	57.375713	1.8287048	0.1271888
0.028	0.0544174	4.1593139	0.2418591	0.4420258	55.32658	1.7634034	0.1226463
0.029	0.0535166	4.0158893	0.2335192	0.4267835	53.418767	1.7026025	0.1184171
0.03	0.0526373	3.8820263	0.2257352	0.4125574	51.638142	1.6458529	0.1144699
0.035	0.0485428	3.3274511	0.1934873	0.3536206	44.261264	1.4107367	0.0981171
0.04	0.0449041	2.9115198	0.1693014	0.3094181	38.728606	1.2343952	0.0858524
0.045	0.0416628	2.5880176	0.1504901	0.2750383	34.425428	1.0972402	0.0763133
0.05	0.0387688	2.3292158	0.1354411	0.2475345	30.982885	0.9875162	0.0686819
0.055	0.0361788	2.1174689	0.1231283	0.2250313	28.166259	0.897742	0.0624381
0.06	0.033855	1.9410132	0.1128676	0.2062787	25.819071	0.8229302	0.057235
0.065	0.0317649	1.7917045	0.1041855	0.1904111	23.832988	0.7596279	0.0528323
0.075	0.0281768	1.5528105	0.0902941	0.165023	20.655257	0.6583442	0.045788
0.1	0.0217183	1.1646079	0.0677206	0.1237672	15.491442	0.4937581	0.034341
0.2	0.0109961	0.582304	0.0338603	0.0618836	7.7457212	0.2468791	0.0171705

Model C

	D_W	D_{Nb}	D_{Ta}	D_{Th}	D_{Zr}	D_{Hf}	D_U	Mineralogical proportion (% at source)	
Olv	5.0E-03	8.1E-05	5.4E-05	4.2E-06	3.3E-04	3.9E-04	1.3E-05	Ol	48.3
Opx	5.9E-03	1.3E-03	7.6E-04	2.6E-05	1.6E-03	5.0E-03	5.1E-04	Opx	46.4
Cpx	4.7E-02	1.4E-03	9.9E-04	1.3E-03	1.0E-02	2.4E-02	1.3E-03	Cpx	1.8
Pig	5.9E-03	1.3E-03	7.6E-04	2.6E-05	1.6E-03	5.0E-03	5.1E-04	Pgt	1.4
Plag	5.9E-04	3.4E-04	2.5E-04	1.9E-04	3.6E-04	2.2E-04	4.2E-04	Pl	1.8
Ilm	7.5E-02	5.9E-01	9.9E-01	6.0E-04	3.0E-01	4.1E-01	3.9E-03	Ilm	0.1
Metal	6.2E+00	-	-	-	-	-	-	Metal	0.3

F	W	Nb	Ta	Th	Zr	Hf	U
0 (source)	0.0011412	0.1268932	0.0084667	0.0038033	1.1587735	0.0505077	0.0010757
0.001	0.0452071	66.763565	4.1212961	3.8032921	581.37809	12.699528	1.0438331
0.002	0.044333	49.21073	3.118984	1.901646	435.63435	11.107063	0.5373851
0.003	0.0434809	37.807253	2.4414506	1.267764	338.57171	9.7801609	0.3585613
0.004	0.0426502	30.130988	1.9703916	0.950823	271.90988	8.6691302	0.2689277
0.005	0.0418402	24.776821	1.633435	0.7606584	224.68557	7.7341704	0.2151423
0.006	0.0410505	20.912108	1.3855782	0.633882	190.20384	6.9433281	0.1792853
0.007	0.0402805	18.031868	1.1983362	0.5433274	164.29502	6.2708844	0.1536731
0.008	0.0395295	15.822165	1.0533324	0.4754115	144.30695	5.6960834	0.134464

Supplementary Table 3.6 - Partition coefficients and modeled aggregate modal fractional melting curves shown in Fig. 10

0.009	0.0387972	14.082712	0.9384712	0.422588	128.51489	5.2021279	0.1195235
0.01	0.0380829	12.682316	0.8456243	0.3803292	115.77142	4.7753844	0.1075712
0.011	0.0373863	11.53275	0.7692136	0.3457538	105.2954	4.4047535	0.097792
0.012	0.0367067	10.573143	0.7053296	0.316941	96.542866	4.0811703	0.0896426
0.013	0.0360438	9.7604553	0.6511756	0.2925609	89.126577	3.7972071	0.082747
0.014	0.0353971	9.0635555	0.6047114	0.2716637	82.765024	3.546757	0.0768365
0.015	0.0347661	8.4594392	0.5644202	0.2535528	77.249491	3.3247812	0.0717141
0.016	0.0341505	7.9307773	0.5291549	0.2377058	72.422386	3.1271076	0.067232
0.017	0.0335498	7.4642845	0.4980334	0.2237231	68.162704	2.9502683	0.0632772
0.018	0.0329635	7.0496124	0.4703674	0.211294	64.376101	2.7913707	0.0597618
0.019	0.0323914	6.6785847	0.4456124	0.2001733	60.987985	2.6479919	0.0566164
0.02	0.031833	6.3446575	0.4233324	0.1901646	57.938632	2.5180955	0.0537856
0.021	0.031288	6.0425319	0.403174	0.1811091	55.179672	2.3999622	0.0512244
0.022	0.0307559	5.7678718	0.384848	0.1728769	52.671515	2.2921357	0.048896
0.023	0.0302365	5.5170949	0.3681156	0.1653605	50.381454	2.193377	0.0467701
0.024	0.0297294	5.287216	0.3527775	0.1584705	48.282229	2.1026278	0.0448213
0.025	0.0292343	5.0757274	0.3386664	0.1521317	46.350941	2.0189809	0.0430285
0.026	0.0287508	4.8805072	0.3256408	0.1462805	44.568213	1.9416556	0.0413735
0.027	0.0282787	4.6997476	0.31358	0.1408627	42.917539	1.8699772	0.0398412
0.028	0.0278177	4.5318995	0.3023807	0.1358319	41.38477	1.8033606	0.0384183
0.029	0.0273673	4.3756271	0.2919538	0.131148	39.957709	1.7412965	0.0370935
0.03	0.0269275	4.2297729	0.282222	0.1267764	38.625785	1.68334	0.0358571
0.035	0.0248756	3.6255196	0.2419046	0.1086655	33.107816	1.4430289	0.0307346
0.04	0.0230467	3.1723297	0.2116665	0.0950823	28.969339	1.2626829	0.0268928
0.045	0.0214131	2.8198486	0.188148	0.0845176	25.750523	1.1223912	0.0239047
0.05	0.0199507	2.5378637	0.1693332	0.0760658	23.175471	1.0101534	0.0215142
0.055	0.0186386	2.3071488	0.1539393	0.0691508	21.06861	0.9183215	0.0195584
0.06	0.0174587	2.1148864	0.141111	0.0633882	19.312892	0.8417948	0.0179285
0.065	0.0163951	1.9522029	0.1302563	0.0585122	17.827285	0.7770414	0.0165494
0.075	0.014564	1.6919092	0.1128888	0.0507106	15.450314	0.6734358	0.0143428
0.1	0.0112506	1.2689319	0.0846666	0.0380329	11.587735	0.5050769	0.0107571
0.2	0.0057055	0.6344659	0.0423333	0.0190165	5.7938677	0.2525384	0.0053786

Model D

	D_W	D_{Nb}	D_{Ta}	D_{Th}	D_{Zr}	D_{Hf}	D_U
Olv	5.0E-03	8.1E-05	5.4E-05	4.2E-06	3.3E-04	3.9E-04	1.3E-05
Opx	5.9E-03	1.3E-03	7.6E-04	2.6E-05	1.6E-03	5.0E-03	5.1E-04
Cpx	4.7E-02	1.4E-03	9.9E-04	1.3E-03	1.0E-02	2.4E-02	1.3E-03
Pig	5.9E-03	1.3E-03	7.6E-04	2.6E-05	1.6E-03	5.0E-03	5.1E-04
Plag	5.9E-04	3.4E-04	2.5E-04	1.9E-04	3.6E-04	2.2E-04	4.2E-04
Ilm	7.5E-02	5.9E-01	9.9E-01	6.0E-04	3.0E-01	4.1E-01	3.9E-03
Metal	6.2E+00	-	-	-	-	-	-

Mineralogical proportion (% at source)	
Ol	46.2
Opx	44.3
Cpx	2.3
Pgt	3.0
Pl	2.8
Ilm	0.9
Metal	0.5

F	W	Nb	Ta	Th	Zr	Hf	U
0 (source)	0.0027857	0.8128198	0.056228	0.0107812	5.375976	0.1976958	0.0030536
0.001	0.0726654	127.05465	5.8382823	10.781235	1247.3449	27.375765	2.9151841
0.002	0.0717527	117.17372	5.5376602	5.3906175	1103.0582	25.491297	1.5236623
0.003	0.0708546	108.31224	5.2575069	3.593745	980.96062	23.778785	1.0177653
0.004	0.069971	100.3525	4.9962676	2.6953088	877.22445	22.220679	0.7633912
0.005	0.0691016	93.191169	4.7525124	2.156247	788.72425	20.801329	0.6107154
0.006	0.0682461	86.737554	4.524926	1.7968725	712.90302	19.506773	0.5089296
0.007	0.0674043	80.911944	4.3122981	1.5401764	647.66454	18.324546	0.4362253
0.008	0.066576	75.64425	4.1135147	1.3476544	591.28661	17.243511	0.3816972
0.009	0.065761	70.872786	3.9275505	1.197915	542.35119	16.253719	0.3392864
0.01	0.0649589	66.543223	3.753461	1.0781235	499.68792	15.34627	0.3053577
0.011	0.0641696	62.607664	3.5903763	0.9801123	462.32852	14.513201	0.2775979
0.012	0.0633929	59.023856	3.437495	0.8984363	429.46986	13.74738	0.2544648
0.013	0.0626285	55.75448	3.2940784	0.8293258	400.44403	13.04242	0.2348906
0.014	0.0618762	52.766555	3.1594453	0.7700882	374.69409	12.392593	0.2181127
0.015	0.0611358	50.030899	3.0329676	0.718749	351.75431	11.792761	0.2035718
0.016	0.0604072	47.521668	2.9140658	0.6738272	331.23409	11.238309	0.1908486
0.017	0.0596901	45.215953	2.802205	0.6341903	312.80492	10.725092	0.1796222
0.018	0.0589842	43.093422	2.6968917	0.5989575	296.18959	10.249384	0.1696432

Supplementary Table 3.6 - Partition coefficients and modeled aggregate modal fractional melting curves shown in Fig. 10

0.019	0.0582895	41.136017	2.5976698	0.5674334	281.15356	9.8078312	0.1607146
0.02	0.0576057	39.327676	2.5041181	0.5390618	267.49767	9.3974128	0.1526789
0.021	0.0569326	37.654099	2.4158474	0.5133921	255.05232	9.0154077	0.1454084
0.022	0.0562701	36.102541	2.3324978	0.4900561	243.67258	8.6593608	0.138799
0.023	0.0556179	34.66163	2.2537364	0.4687493	233.23425	8.3270563	0.1327642
0.024	0.054976	33.321206	2.1792554	0.4492181	223.63049	8.016492	0.1272324
0.025	0.054344	32.072181	2.1087696	0.4312494	214.76911	7.7258574	0.1221431
0.026	0.0537219	30.906415	2.0420153	0.4146629	206.57032	7.4535141	0.1174453
0.027	0.0531094	29.816612	1.9787479	0.399305	198.96484	7.1979776	0.1130955
0.028	0.0525065	28.79622	1.9187409	0.3850441	191.89226	6.9579022	0.1090563
0.029	0.0519129	27.839349	1.8617843	0.3717667	185.29983	6.7320665	0.1052958
0.03	0.0513284	26.940698	1.8076833	0.3593745	179.14127	6.5193611	0.1017859
0.035	0.0485385	23.168812	1.5741187	0.3080353	153.58662	5.6204701	0.0872451
0.04	0.0459557	20.300726	1.3896572	0.2695309	134.39658	4.9311031	0.0763394
0.045	0.0435627	18.055426	1.2414645	0.239583	119.4655	4.3886296	0.0678573
0.05	0.0413441	16.253727	1.120486	0.2156247	107.51938	3.9520179	0.0610715
0.055	0.0392856	14.777552	1.0202502	0.1960225	97.744986	3.5936831	0.0555196
0.06	0.0373741	13.546629	0.9360689	0.1796873	89.599592	3.2946033	0.050893
0.065	0.0355976	12.504783	0.8644987	0.1658652	82.707321	3.0413377	0.0469781
0.075	0.0324071	10.837579	0.7495609	0.1437498	71.67968	2.6359204	0.0407144
0.1	0.026135	8.1281982	0.5622749	0.1078124	53.75976	1.9769579	0.0305358
0.2	0.0138904	4.0640992	0.2811402	0.0539062	26.87988	0.9884791	0.0152679

Model E

	D_W	D_{Nb}	D_{Ta}	D_{Th}	D_{Zr}	D_{Hf}	D_U	Mineralogical proportion (% at source)	
Olv	5.0E-03	8.1E-05	5.4E-05	4.2E-06	3.3E-04	3.9E-04	1.3E-05	Ol	46.2
Opx	5.9E-03	1.3E-03	7.6E-04	2.6E-05	1.6E-03	5.0E-03	5.1E-04	Opx	44.3
Cpx	4.7E-02	1.4E-03	9.9E-04	1.3E-03	1.0E-02	2.4E-02	1.3E-03	Cpx	2.3
Pig	5.9E-03	1.3E-03	7.6E-04	2.6E-05	1.6E-03	5.0E-03	5.1E-04	Pgt	3.0
Plag	5.9E-04	3.4E-04	2.5E-04	1.9E-04	3.6E-04	2.2E-04	4.2E-04	Pl	2.8
Arm	1.0E-01	5.1E-01	1.0E+00	1.6E-03	5.5E-01	7.3E-01	1.1E-02	Ilm	0.9
Metal	6.2E+00	-	-	-	-	-	-	Metal	0.5

F	W	Nb	Ta	Th	Zr	Hf	U
0 (source)	0.0027857	0.8128198	0.056228	0.0107812	5.375976	0.1976958	0.0030536
0.001	0.0721932	141.64624	5.6962451	10.781233	827.84635	19.768765	2.8254473
0.002	0.0712925	129.35736	5.4101416	5.3906175	764.42851	18.788816	1.5182891
0.003	0.0704062	118.48387	5.1430352	3.593745	707.45527	17.873076	1.017438
0.004	0.0695341	108.84316	4.893519	2.6953088	656.19363	17.016853	0.7633709
0.005	0.0686759	100.27765	4.6602963	2.156247	609.99907	16.215819	0.6107141
0.006	0.0678313	92.651235	4.4421717	1.7968725	568.30446	15.465978	0.5089295
0.007	0.0670002	85.846213	4.2380427	1.5401764	530.61043	14.76364	0.4362253
0.008	0.0661823	79.760725	4.0468928	1.3476544	496.47696	14.1054	0.3816972
0.009	0.0653773	74.306512	3.8677837	1.197915	465.516	13.488111	0.3392864
0.01	0.0645851	69.407026	3.6998498	1.0781235	437.38511	12.908868	0.3053577
0.011	0.0638055	64.995795	3.542292	0.9801123	411.7818	12.364983	0.2775979
0.012	0.0630381	61.015035	3.3943726	0.8984363	388.43871	11.853976	0.2544648
0.013	0.0622829	57.414448	3.25541	0.8293258	367.11926	11.373549	0.2348906
0.014	0.0615395	54.150204	3.1247748	0.7700882	347.61397	10.921581	0.2181127
0.015	0.0608079	51.184057	3.001885	0.718749	329.73717	10.496107	0.2035718
0.016	0.0600877	48.482591	2.8862029	0.6738272	313.32414	10.095311	0.1908486
0.017	0.0593789	46.01657	2.7772311	0.6341903	298.22859	9.7175092	0.1796222
0.018	0.0586811	43.76038	2.6745097	0.5989575	284.3205	9.3611449	0.1696432
0.019	0.0579943	41.691547	2.5776129	0.5674334	271.48417	9.0247752	0.1607146
0.02	0.0573182	39.790326	2.4861468	0.5390618	259.61653	8.7070633	0.1526789
0.021	0.0566526	38.039342	2.3997466	0.5133921	248.6257	8.4067705	0.1454084
0.022	0.0559973	36.42328	2.3180744	0.4900561	238.42965	8.1227479	0.138799
0.023	0.0553523	34.928627	2.2408171	0.4687493	228.95506	7.8539305	0.1327642
0.024	0.0547173	33.543432	2.1676847	0.4492181	220.13636	7.5993299	0.1272324
0.025	0.0540921	32.257116	2.0984079	0.4312494	211.9148	7.3580287	0.1221431
0.026	0.0534765	31.060294	2.0327372	0.4146629	204.23771	7.1291754	0.1174453
0.027	0.0528705	29.944631	1.9704411	0.399305	197.05779	6.9119791	0.1130955
0.028	0.0522738	28.902709	1.9113046	0.3850441	190.33253	6.7057048	0.1090563

Supplementary Table 3.6 - Partition coefficients and modeled aggregate modal fractional melting curves shown in Fig. 10

0.029	0.0516863	27.927916	1.8551279	0.3717667	184.02368	6.5096694	0.1052958
0.03	0.0511078	27.014348	1.8017257	0.3593745	178.09675	6.323238	0.1017859
0.035	0.0483455	23.198033	1.5707031	0.3080353	153.20095	5.515833	0.0872451
0.04	0.0457869	20.312275	1.3877047	0.2695309	134.25311	4.8752462	0.0763394
0.045	0.0434153	18.059973	1.2403515	0.239583	119.41181	4.3587994	0.0678573
0.05	0.0412154	16.25551	1.1198534	0.2156247	107.49919	3.9360822	0.0610715
0.055	0.0391732	14.778249	1.0198917	0.1960225	97.737366	3.5851685	0.0555196
0.06	0.0372761	13.5469	0.9358664	0.1796873	89.59671	3.2900536	0.050893
0.065	0.0355122	12.504888	0.8643846	0.1658652	82.706229	3.0389069	0.0469781
0.075	0.0323425	10.837594	0.7495251	0.1437498	71.679522	2.6352272	0.0407144
0.1	0.0261032	8.1281984	0.562273	0.1078124	53.759759	1.9769281	0.0305358
0.2	0.0138888	4.0640992	0.2811402	0.0539062	26.87988	0.9884791	0.0152679

Model F

	D_W	D_{Nb}	D_{Ta}	D_{Th}	D_{Zr}	D_{Hf}	D_U
Olv	5.0E-03	8.1E-05	5.4E-05	4.2E-06	3.3E-04	3.9E-04	1.3E-05
Opx	5.9E-03	1.3E-03	7.6E-04	2.6E-05	1.6E-03	5.0E-03	5.1E-04
Cpx	4.7E-02	1.4E-03	9.9E-04	1.3E-03	1.0E-02	2.4E-02	1.3E-03
Pig	5.9E-03	1.3E-03	7.6E-04	2.6E-05	1.6E-03	5.0E-03	5.1E-04
Plag	5.9E-04	3.4E-04	2.5E-04	1.9E-04	3.6E-04	2.2E-04	4.2E-04
Ilm	7.5E-02	5.9E-01	9.9E-01	6.0E-04	3.0E-01	4.1E-01	3.9E-03
Metal	6.2E+00	-	-	-	-	-	-

Mineralogical proportion (% at source)	
Ol	48.71
Opx	46.80
Cpx	1.62
Pgt	1.18
Pl	1.56
Ilm	0.04
Metal	0.10

F	W	Nb	Ta	Th	Zr	Hf	U
0 (source)	0.0024004	0.1602718	0.0098062	0.0133316	1.9981489	0.0727145	0.0036814
0.001	0.1880084	104.34056	6.799611	13.331631	1113.7178	19.732895	3.5779796
0.002	0.1807291	70.38681	4.4427421	6.6658156	803.4984	17.061508	1.8392739
0.003	0.1738212	51.160569	3.1748658	4.4438771	608.4326	14.871209	1.2271215
0.004	0.1672637	39.477423	2.4300474	3.3329078	480.45703	13.064753	0.9203608
0.005	0.1610368	31.890188	1.9559955	2.6663262	392.89556	11.565814	0.736289
0.006	0.1551219	26.664472	1.6330385	2.2219385	330.55103	10.31431	0.6135742
0.007	0.1495014	22.881852	1.4005425	1.9045187	284.51591	9.2627943	0.5259208
0.008	0.1441588	20.029693	1.2256866	1.6664539	249.40897	8.3736783	0.4601807
0.009	0.1390787	17.806659	1.0895565	1.4812924	221.87597	7.6170797	0.4090495
0.01	0.1342464	16.026768	0.9806165	1.3331631	199.7593	6.9691565	0.3681445
0.011	0.1296483	14.570033	0.8914739	1.2119665	181.62771	6.4108143	0.3346768
0.012	0.1252713	13.35594	0.8171856	1.1109693	166.50349	5.9267005	0.3067871
0.013	0.1211034	12.328585	0.7543255	1.0255101	153.70015	5.5044208	0.2831881
0.014	0.1171332	11.44798	0.7004452	0.9522594	142.72345	5.1339269	0.2629604
0.015	0.1133498	10.684783	0.6537489	0.8887754	133.20932	4.807037	0.2454297
0.016	0.1097431	10.016985	0.6128896	0.833227	124.88406	4.5170594	0.2300903
0.017	0.1063035	9.4277511	0.5768373	0.7842136	117.53807	4.2584963	0.2165556
0.018	0.1030221	8.9039873	0.5447908	0.7406462	111.00823	4.0268097	0.2045247
0.019	0.0998904	8.4353564	0.5161176	0.7016648	105.16571	3.8182368	0.1937603
0.02	0.0969004	8.0135886	0.4903117	0.6665816	99.907436	3.6296424	0.1840723
0.021	0.0940446	7.6319891	0.4669635	0.6348396	95.149942	3.4584019	0.1753069
0.022	0.0913158	7.2850805	0.4457379	0.6059832	90.824947	3.3023082	0.1673384
0.023	0.0887075	6.9683379	0.426358	0.5796361	86.876037	3.159496	0.1600628
0.024	0.0862133	6.6779905	0.4085931	0.5554846	83.256202	3.0283823	0.1533936
0.025	0.0838272	6.4108709	0.3922493	0.5332652	79.925954	2.9076166	0.1472578
0.026	0.0815438	6.1642989	0.3771628	0.512755	76.851879	2.7960423	0.141594
0.027	0.0793576	5.9359915	0.3631938	0.4937641	74.005513	2.6926643	0.1363498
0.028	0.0772636	5.7239918	0.3502226	0.4761297	71.362459	2.5966226	0.1314802
0.029	0.0752573	5.5266128	0.338146	0.4597114	68.901685	2.5071711	0.1269464
0.03	0.0733341	5.3423924	0.3268745	0.4443877	66.604962	2.4236596	0.1227148
0.035	0.0648265	4.5791935	0.2801781	0.3809037	57.089967	2.0775316	0.1051842
0.04	0.0578582	4.0067943	0.2451558	0.3332908	49.953721	1.8178587	0.0920361
0.045	0.052093	3.5615949	0.2179163	0.2962585	44.403308	1.6158776	0.0818099
0.05	0.0472754	3.2054354	0.1961247	0.2666326	39.962977	1.4542904	0.0736289
0.055	0.0432107	2.9140322	0.1782952	0.2423933	36.329979	1.3220823	0.0669354
0.06	0.0397494	2.6711962	0.1634372	0.2221939	33.302481	1.2119088	0.0613574
0.065	0.0367757	2.4657196	0.1508651	0.205102	30.740752	1.118685	0.0566376
0.075	0.0319503	2.136957	0.1307498	0.1777551	26.641985	0.969527	0.0490859

Supplementary Table 3.6 - Partition coefficients and modeled aggregate modal fractional melting curves shown in Fig. 10

0.1	0.0239999	1.6027177	0.0980623	0.1333163	19.981489	0.7271453	0.0368145
0.2	0.0120022	0.8013589	0.0490312	0.0666582	9.9907443	0.3635726	0.0184072

Model G

	D_W	D_{Nb}	D_{Ta}	D_{Th}	D_{Zr}	D_{Hf}	D_U	Mineralogical proportion (% at source)	
Olv	5.0E-03	8.1E-05	5.4E-05	4.2E-06	3.3E-04	3.9E-04	1.3E-05	Ol	46.7
Opx	5.9E-03	1.3E-03	7.6E-04	2.6E-05	1.6E-03	5.0E-03	5.1E-04	Opx	44.9
Cpx	4.7E-02	1.4E-03	9.9E-04	1.3E-03	1.0E-02	2.4E-02	1.3E-03	Cpx	2.8
Pig	5.9E-03	1.3E-03	7.6E-04	2.6E-05	1.6E-03	5.0E-03	5.1E-04	Pgt	2.2
Plag	5.9E-04	3.4E-04	2.5E-04	1.9E-04	3.6E-04	2.2E-04	4.2E-04	Pl	2.8
Ilm	7.5E-02	5.9E-01	9.9E-01	6.0E-04	3.0E-01	4.1E-01	3.9E-03	Ilm	0.2
Metal	6.2E+00	-	-	-	-	-	-	Metal	0.4

F	W	Nb	Ta	Th	Zr	Hf	U
0 (source)	0.001225	0.2211189	0.0151712	0.0035868	1.7443573	0.0765936	0.0010159
0.001	0.0384251	87.162448	4.8528044	3.586812	727.39344	16.553159	0.9787324
0.002	0.0378408	70.003608	4.078027	1.7934061	575.8928	14.770189	0.5072652
0.003	0.037268	57.343278	3.4678909	1.195604	466.42011	13.242455	0.3386118
0.004	0.0367064	47.85625	2.9831054	0.896703	385.87291	11.928987	0.2539707
0.005	0.0361558	40.633235	2.5943638	0.7173624	325.50117	10.795805	0.2031769
0.006	0.0356159	35.04505	2.2797053	0.597802	279.40287	9.8146823	0.1693141
0.007	0.0350866	30.652365	2.0225928	0.5124017	243.55385	8.962134	0.1451264
0.008	0.0345676	27.145427	1.8105083	0.4483515	215.17845	8.2185825	0.1269856
0.009	0.0340586	24.303588	1.6339236	0.3985347	192.33859	7.5676789	0.1128761
0.01	0.0335595	21.967964	1.4855446	0.3586812	173.66355	6.9957441	0.1015885
0.011	0.0330701	20.022853	1.359753	0.3260738	158.17091	6.4913094	0.0923531
0.012	0.0325901	18.383023	1.2521945	0.298901	145.14689	6.0447395	0.084657
0.013	0.0321194	16.984939	1.1594719	0.2759086	134.06573	5.6479221	0.078145
0.014	0.0316578	15.78068	1.0789173	0.2562009	124.53481	5.2940116	0.0725632
0.015	0.031205	14.733666	1.0084211	0.2391208	116.25694	4.9772184	0.0677256
0.016	0.0307608	13.815651	0.9463034	0.2241758	109.00414	4.6926338	0.0634928
0.017	0.0303252	13.004574	0.8912172	0.2109889	102.59936	4.4360863	0.0597579
0.018	0.0298979	12.28301	0.8420748	0.1992673	96.903344	4.2040219	0.056438
0.019	0.0294787	11.637056	0.7979919	0.1887796	91.80533	3.9934047	0.0534676
0.02	0.0290675	11.0555	0.7582444	0.1793406	87.216249	3.8016351	0.0507942
0.021	0.028664	10.529217	0.7222354	0.1708006	83.063747	3.6264806	0.0483755
0.022	0.0282682	10.050714	0.6894696	0.1630369	79.288481	3.4660193	0.0461766
0.023	0.0278799	9.6137821	0.6595334	0.1559484	75.841354	3.3185917	0.0441689
0.024	0.0274989	9.2132399	0.6320792	0.1494505	72.681407	3.1827616	0.0423285
0.025	0.027125	8.8447287	0.606813	0.1434725	69.774212	3.0572818	0.0406354
0.026	0.0267582	8.5045575	0.5834851	0.1379543	67.090622	2.9410669	0.0390725
0.027	0.0263982	8.18958	0.5618818	0.1328449	64.605802	2.8331693	0.0376254
0.028	0.026045	7.8970985	0.5418192	0.1281004	62.298462	2.7327594	0.0362816
0.029	0.0256983	7.6247868	0.5231388	0.1236832	60.150245	2.6391093	0.0350305
0.03	0.025358	7.3706284	0.5057028	0.1195604	58.14524	2.5515781	0.0338628
0.035	0.0237489	6.3176829	0.4334626	0.1024803	49.838781	2.188012	0.0290253
0.04	0.0222817	5.5279726	0.3792801	0.0896703	43.608933	1.9147462	0.0253971
0.045	0.0209425	4.9137534	0.3371379	0.0797069	38.763496	1.7020559	0.0225752
0.05	0.0197185	4.4223781	0.3034241	0.0717362	34.887147	1.5318653	0.0203177
0.055	0.0185985	4.0203437	0.2758401	0.0652148	31.715588	1.3926087	0.0184706
0.06	0.0175723	3.6853151	0.2528534	0.0597802	29.072622	1.2765589	0.0169314
0.065	0.0166309	3.4018293	0.2334032	0.0551817	26.836267	1.1783623	0.015629
0.075	0.0149703	2.9482521	0.2022828	0.0478242	23.258098	1.0212474	0.0135451
0.1	0.011823	2.2111891	0.1517121	0.0358681	17.443573	0.7659356	0.0101588
0.2	0.0061201	1.1055945	0.075856	0.0179341	8.7217867	0.3829678	0.0050794

Model H

	D_W	D_{Nb}	D_{Ta}	D_{Th}	D_{Zr}	D_{Hf}	D_U	Mineralogical proportion (% at source)	
Olv	5.0E-03	8.1E-05	5.4E-05	4.2E-06	3.3E-04	3.9E-04	1.3E-05	Ol	49.0
Opx	5.9E-03	1.3E-03	7.6E-04	2.6E-05	1.6E-03	5.0E-03	5.1E-04	Opx	49.0
Cpx	4.7E-02	1.4E-03	9.9E-04	1.3E-03	1.0E-02	2.4E-02	1.3E-03	Cpx	-
Pig	5.9E-03	1.3E-03	7.6E-04	2.6E-05	1.6E-03	5.0E-03	5.1E-04	Pgt	-
Plag	5.9E-04	3.4E-04	2.5E-04	1.9E-04	3.6E-04	2.2E-04	4.2E-04	Pl	-

Supplementary Table 3.6 - Partition coefficients and modeled aggregate modal fractional melting curves shown in Fig. 10

Ilm	7.5E-02	5.9E-01	9.9E-01	6.0E-04	3.0E-01	4.1E-01	3.9E-03	Ilm	-
Metal	6.2E+00	-	-	-	-	-	-	Metal	0.2

F	W	Nb	Ta	Th	Zr	Hf	U
0 (source)	0.0006303	0.0127461	0.0006553	0.0009735	0.1885852	0.0094403	0.0003092
0.001	0.0048567	9.8415525	0.6020081	0.9735499	123.11451	2.9768178	0.303013
0.002	0.0048404	6.0425977	0.3255032	0.486775	82.939989	2.5083158	0.1545519
0.003	0.0048242	4.1986455	0.2183281	0.3245166	60.239803	2.1379501	0.1030753
0.004	0.004808	3.1780071	0.1638266	0.2433875	46.465791	1.8426362	0.077307
0.005	0.0047919	2.5476755	0.1310665	0.19471	37.528847	1.6050716	0.0618456
0.006	0.0047758	2.1240581	0.1092224	0.1622583	31.376715	1.4122293	0.051538
0.007	0.0047598	1.8208143	0.0936193	0.1390786	26.924736	1.2542557	0.0441755
0.008	0.0047439	1.5932506	0.0819169	0.1216937	23.568327	1.1236594	0.0386535
0.009	0.004728	1.4162304	0.072815	0.1081722	20.952439	1.0147155	0.0343587
0.01	0.0047122	1.274609	0.0655335	0.097355	18.858067	0.9230242	0.0309228
0.011	0.0046964	1.1587357	0.0595759	0.0885045	17.14397	0.8451845	0.0281117
0.012	0.0046807	1.0621745	0.0546112	0.0811292	15.715392	0.7785516	0.025769
0.013	0.0046651	0.9804688	0.0504104	0.0748885	14.506543	0.721056	0.0237868
0.014	0.0046495	0.9104353	0.0468096	0.0695393	13.47037	0.6710677	0.0220877
0.015	0.004634	0.8497396	0.043689	0.0649033	12.572348	0.6272943	0.0206152
0.016	0.0046185	0.7966309	0.0409584	0.0608469	11.786577	0.5887047	0.0193268
0.017	0.0046031	0.7497702	0.0385491	0.0572676	11.09325	0.5544702	0.0181899
0.018	0.0045878	0.7081163	0.0364075	0.0540861	10.476958	0.5239205	0.0171793
0.019	0.0045725	0.6708471	0.0344913	0.0512395	9.9255392	0.4965096	0.0162752
0.02	0.0045573	0.6373047	0.0327667	0.0486775	9.4292622	0.4717901	0.0154614
0.021	0.0045421	0.6069569	0.0312064	0.0463595	8.9802497	0.4493926	0.0147252
0.022	0.004527	0.5793679	0.0297879	0.0442523	8.5720566	0.4290102	0.0140558
0.023	0.004512	0.554178	0.0284928	0.0423283	8.1993585	0.4103866	0.0134447
0.024	0.004497	0.5310873	0.0273056	0.0405646	7.8577185	0.393306	0.0128845
0.025	0.0044821	0.5098438	0.0262134	0.038942	7.5434098	0.3775861	0.0123691
0.026	0.0044672	0.4902344	0.0252052	0.0374442	7.2532786	0.3630715	0.0118934
0.027	0.0044524	0.4720776	0.0242717	0.0360574	6.9846387	0.3496297	0.0114529
0.028	0.0044376	0.4552176	0.0234048	0.0347696	6.7351873	0.3371464	0.0110439
0.029	0.0044229	0.4395205	0.0225978	0.0335707	6.5029395	0.3255229	0.010663
0.03	0.0044083	0.4248698	0.0218445	0.0324517	6.2861748	0.3146736	0.0103076
0.035	0.0043359	0.3641741	0.0187239	0.0278157	5.3881498	0.2697225	0.0088351
0.04	0.0042649	0.3186524	0.0163834	0.0243387	4.7146311	0.2360074	0.0077307
0.045	0.0041952	0.2832465	0.014563	0.0216344	4.1907832	0.2097844	0.0068717
0.05	0.0041269	0.2549219	0.0131067	0.019471	3.7717049	0.188806	0.0061846
0.055	0.0040599	0.2317472	0.0119152	0.0177009	3.4288226	0.1716418	0.0056223
0.06	0.0039941	0.2124349	0.0109222	0.0162258	3.1430874	0.1573383	0.0051538
0.065	0.0039297	0.1960938	0.0100821	0.0149777	2.9013115	0.1452354	0.0047574
0.075	0.0038044	0.1699479	0.0087378	0.0129807	2.5144699	0.1258707	0.004123
0.1	0.0035119	0.1274609	0.0065533	0.0097355	1.8858524	0.094403	0.0030923
0.2	0.0025901	0.0637305	0.0032767	0.0048677	0.9429262	0.0472015	0.0015461

Model I

	D_W	D_{Nb}	D_{Ta}	D_{Th}	D_{Zr}	D_{Hf}	D_U	Mineralogical proportion (% at source)	
Olv	5.0E-03	8.1E-05	5.4E-05	4.2E-06	3.3E-04	3.9E-04	1.3E-05	Ol	46.9
Opx	5.9E-03	1.3E-03	7.6E-04	2.6E-05	1.6E-03	5.0E-03	5.1E-04	Opx	45.1
Cpx	4.7E-02	1.4E-03	9.9E-04	1.3E-03	1.0E-02	2.4E-02	1.3E-03	Cpx	2.8
Pig	5.9E-03	1.3E-03	7.6E-04	2.6E-05	1.6E-03	5.0E-03	5.1E-04	Pgt	2.2
Plag	5.9E-04	3.4E-04	2.5E-04	1.9E-04	3.6E-04	2.2E-04	4.2E-04	Pl	2.8
Ilm	7.5E-02	5.9E-01	9.9E-01	6.0E-04	3.0E-01	4.1E-01	3.9E-03	Ilm	0.2
Metal	6.2E+00	-	-	-	-	-	-	Metal	-

F	W	Nb	Ta	Th	Zr	Hf	U
0 (source)	0.0012275	0.2211699	0.0151738	0.0035907	1.7451117	0.0766313	0.0010171
0.001	0.1722935	87.091395	4.8511925	3.5907062	726.58198	16.523688	0.9795059
0.002	0.1602709	69.964511	4.0770647	1.7953532	575.48504	14.747954	0.5078675
0.003	0.1493605	57.323041	3.4673565	1.1969021	466.23891	13.225839	0.3390235
0.004	0.1394471	47.847028	2.9828502	0.8976766	385.81667	11.916724	0.2542799

Supplementary Table 3.6 - Partition coefficients and modeled aggregate modal fractional melting curves shown in Fig. 10

0.005	0.1304284	40.630347	2.5942884	0.7181413	325.512	10.786906	0.2034243
0.006	0.1222131	35.045717	2.2797436	0.5984511	279.44807	9.8083781	0.1695202
0.007	0.1147199	30.654951	2.0227008	0.512958	243.61519	8.9578233	0.1453031
0.008	0.1078762	27.148979	1.8106572	0.4488383	215.24593	8.2157979	0.1271402
0.009	0.1016173	24.307557	1.6340948	0.3989674	192.40691	7.566057	0.1130135
0.01	0.0958854	21.972042	1.4857259	0.3590706	173.73002	6.9950029	0.1017121
0.011	0.0906289	20.026875	1.3599368	0.3264278	158.2343	6.4912304	0.0924656
0.012	0.0858017	18.386903	1.2523762	0.2992255	145.20675	6.0451539	0.0847601
0.013	0.0813624	16.988639	1.1596487	0.2762082	134.12202	5.6486996	0.0782401
0.014	0.0772742	15.784188	1.0790879	0.256479	124.58769	5.2950522	0.0726515
0.015	0.0735038	14.736984	1.0085846	0.2393804	116.30665	4.9784452	0.0678081
0.016	0.0700216	13.818789	0.9464596	0.2244191	109.05096	4.6939882	0.0635701
0.017	0.066801	13.007544	0.8913663	0.211218	102.64354	4.4375239	0.0598307
0.018	0.063818	12.285826	0.842217	0.1994837	96.94514	4.205509	0.0565067
0.019	0.0610513	11.639729	0.7981276	0.1889845	91.844967	3.9949162	0.0535327
0.02	0.0584813	11.058043	0.7583739	0.1795353	87.253929	3.8031523	0.0508561
0.021	0.0560909	10.531642	0.7223591	0.170986	83.099646	3.6279898	0.0484344
0.022	0.0538642	10.053029	0.689588	0.1632139	79.322757	3.4675105	0.0462328
0.023	0.0517872	9.6159975	0.6596469	0.1561177	75.874145	3.3200581	0.0442227
0.024	0.0498471	9.2153635	0.632188	0.1496128	72.712834	3.1841983	0.0423801
0.025	0.0480324	8.8467676	0.6069177	0.1436283	69.804383	3.0586858	0.0406849
0.026	0.0463327	8.5065181	0.5835858	0.1381041	67.119633	2.9424364	0.0391201
0.027	0.0447385	8.1914681	0.5619787	0.1329891	64.63374	2.8345033	0.0376712
0.028	0.0432415	7.8989193	0.5419128	0.1282395	62.325403	2.7340578	0.0363258
0.029	0.0418337	7.6265448	0.5232292	0.1238175	60.176257	2.6403723	0.0350732
0.03	0.0405083	7.3723279	0.5057902	0.1196902	58.170385	2.5528064	0.033904
0.035	0.0349117	6.3191396	0.4335375	0.1025916	49.860333	2.1890822	0.0290606
0.04	0.0306243	5.5292472	0.3793456	0.0897677	43.627792	1.9156877	0.025428
0.045	0.0272527	4.9148864	0.3371962	0.0797935	38.78026	1.7028944	0.0226027
0.05	0.0245402	4.4233978	0.3034766	0.0718141	34.902234	1.5326204	0.0203424
0.055	0.0223145	4.0212707	0.2758878	0.0652856	31.729303	1.3932952	0.0184931
0.06	0.0204571	3.6861648	0.2528971	0.0598451	29.085195	1.2771883	0.016952
0.065	0.0188844	3.4026137	0.2334435	0.0552416	26.847872	1.1789433	0.015648
0.075	0.016367	2.9489319	0.2023177	0.0478761	23.268156	1.0217509	0.0135616
0.1	0.0122754	2.2116989	0.1517383	0.0359071	17.451117	0.7663132	0.0101712
0.2	0.0061377	1.1058494	0.0758691	0.0179535	8.7255584	0.3831566	0.0050856

Supplementary Table 4.1: Major element compositions (wt. %) of starting materials and expected liquidus phases

Starting compositions	WM-1	HSM-1	OPM-3	OLM-1	M8
CaO[a]	17.91	24.33	10.03	18.22	15.33
MgO	25.57	12.08	25.54	20.75	9.70
Al_2O_3	5.13	16.61	5.56	7.08	26.56
SiO_2	47.87	43.70	52.90	48.76	46.77
TiO_2	1.00	0.97	4.30	5.00	0.05
P_2O_5[b]	0.49	0.49	0.43	0.40	0.10
Cr_2O_3	0.47	0.47	0.42	0.42	0.04
Fe_2O_3	0.49	0.49	0.43	0.47	0.05
MnO	0.50	0.50	0.64	0.50	0.20
Total	99.43	99.64	100.24	101.60	98.80
Exp. Liq. Phase	cpx+ol	cpx	opx	ol	pl

[a]added as $CaCO_3$; [b]added as P_2O_5 in solution (5% HNO_3); cpx: clinopyroxene, ol: olivine; opx: orthopyroxene; pl: plagioclase

Supplementary Table 4.2 - Average values (n=5/each phase) for major element composition (cg/g) of minerals and silicate glass in the experiments of this study

Experiment	Δ FMQ	Phase	CaO	σ	MgO	σ	Al_2O_3	σ	SiO_2	σ	TiO_2	σ	FeO	σ	MnO	σ	T.E.*	Total
HSM1+Mo+W	1.8	Cpx	25.30	0.17	15.05	0.28	7.81	0.20	49.61	0.57	0.87	0.03	0.16	0.05	0.25	0.03	1.05	100.09
		Glass	25.92	0.12	6.68	0.06	17.11	0.10	44.77	0.17	1.28	0.07	0.16	0.02	0.94	0.06	2.17	99.04
HSM1+Mo+W	1.0	Cpx	25.34	0.13	15.48	0.38	7.44	0.55	50.60	0.69	0.73	0.06	0.21	0.04	0.08	0.02	1.18	101.05
		Glass	25.36	0.06	7.92	0.13	16.53	0.09	46.87	0.16	1.11	0.05	0.41	0.01	0.31	0.03	1.51	100.01
HSM1+Mo+W	-0.1	Cpx	24.85	0.21	15.16	0.49	8.24	0.78	49.08	1.07	0.88	0.07	0.14	0.03	0.17	0.05	1.52	100.04
		Pl	19.97	0.09	0.78	0.08	34.31	0.30	45.12	0.24	0.04	0.04	0.03	0.03	0.02	0.03	-	100.27
		Glass	26.38	0.18	5.79	0.08	13.03	0.06	47.33	0.26	2.41	0.11	0.30	0.02	0.99	0.04	2.64	98.87
HSM1+Mo+W	-1.2	Cpx	24.89	0.14	15.10	0.33	7.71	0.25	49.03	0.46	0.75	0.04	0.02	0.01	0.12	0.03	1.44	99.07
		Pl	20.01	0.11	0.64	0.07	34.77	0.23	44.80	0.25	0.05	0.01	0.02	0.01	0.04	0.02	-	100.33
		Glass	26.90	0.12	6.56	0.07	12.95	0.14	46.85	0.24	2.27	0.04	bdl	-	0.65	0.08	2.35	98.53
HSM1+Mo+W	-2.2	Cpx	25.41	0.18	14.75	0.43	9.74	0.93	48.62	0.66	0.98	0.07	bdl	-	0.06	0.04	0.43	99.99
		Glass	26.64	0.08	5.50	0.07	17.73	0.14	46.31	0.16	1.02	0.03	0.01	0.004	0.07	0.05	1.59	98.88
HSM1+Mo+W	-3.1	Cpx	25.45	0.17	14.87	0.35	9.68	0.67	48.68	0.37	0.95	0.07	0.03	0.004	0.09	0.03	0.39	100.13
		Glass	28.89	0.04	5.70	0.05	17.43	0.07	43.90	0.27	0.94	0.06	0.01	0.01	0.13	0.02	1.75	98.76
HSM1+W	-4.2	Cpx	25.47	0.16	14.50	0.21	10.85	0.35	48.13	0.38	1.09	0.05	0.03	0.01	0.08	0.04	0.40	100.55
		Pl	20.35	0.10	0.86	0.08	34.31	0.15	44.60	0.21	0.04	0.01	0.01	0.004	0.02	0.01	-	100.18
		Glass	29.76	0.06	5.94	0.03	12.12	0.11	46.44	0.35	1.55	0.19	bdl	-	0.13	0.05	3.26	99.20
HSM1+W	1.0	Cpx	25.51	0.19	14.35	0.50	7.88	0.28	50.82	0.59	0.78	0.08	0.11	0.05	0.09	0.03	1.08	100.64
		Pl	20.64	0.13	0.41	0.02	34.99	0.18	44.52	0.19	0.04	0.04	0.03	0.03	0.04	0.03	-	100.67
		Glass	28.08	0.07	8.39	0.04	14.72	0.09	45.37	0.18	1.16	0.07	0.22	0.04	0.33	0.03	1.68	99.94
HSM1+W	1.8	Cpx	24.37	0.07	15.87	0.49	6.94	0.58	50.41	0.34	0.97	0.08	0.21	0.04	0.10	0.02	1.90	100.76
		Pl	20.46	0.07	0.50	0.04	35.48	0.23	44.80	0.39	0.04	0.03	0.08	0.03	0.01	0.01	-	101.38
		Glass	21.21	0.09	11.64	0.13	14.89	0.17	47.96	0.25	1.88	0.08	0.34	0.05	0.34	0.01	1.61	99.87
HSM1+W	-3.1	Cpx	25.21	0.16	14.50	0.13	9.97	0.61	48.35	0.43	1.09	0.10	0.01	0.01	0.17	0.02	0.55	99.85
		Glass	25.64	0.09	6.07	0.09	18.05	0.07	45.72	0.11	1.02	0.09	0.03	0.01	0.52	0.03	1.67	98.71
HSM1+Mo	-3.1	Cpx	25.54	0.18	14.39	0.41	10.61	0.72	48.03	0.66	1.00	0.09	0.02	0.01	0.11	0.03	0.43	100.13
		Glass	29.77	0.11	5.92	0.06	16.83	0.19	43.28	0.16	0.76	0.05	bdl	-	0.16	0.04	1.81	98.52
HSM1+Mo	-4.2	Cpx	25.79	0.14	15.03	0.40	8.92	0.79	49.06	0.57	0.90	0.09	0.02	0.01	0.07	0.02	0.42	100.21
		Glass	30.89	0.09	6.45	0.06	16.07	0.09	43.18	0.11	0.80	0.06	0.01	0.01	0.11	0.03	1.75	99.25
HSM1+Mo	1.0	Cpx	25.46	0.19	15.25	0.33	8.03	0.40	50.14	0.24	0.87	0.14	0.12	0.05	0.08	0.04	1.04	101.00
		Pl	20.33	0.07	0.64	0.06	35.00	0.20	45.37	0.19	0.05	0.02	0.05	0.02	0.03	0.01	-	101.46
		Glass	25.31	0.16	7.94	0.06	16.28	0.25	47.77	0.11	1.24	0.04	0.13	0.06	0.29	0.04	1.39	100.35
HSM1+Mo	1.8	Cpx	25.77	0.33	15.35	0.26	7.40	0.16	50.16	0.54	0.85	0.03	0.07	0.03	0.08	0.04	1.38	101.06
		Glass	27.65	0.10	6.37	0.04	17.20	0.09	44.79	0.18	1.48	0.10	0.06	0.04	0.29	0.04	1.60	99.43
HSM1+Mo	-0.1	Cpx	25.05	0.14	15.48	0.31	6.85	0.38	49.53	0.56	0.77	0.02	0.02	0.02	0.14	0.03	1.64	99.50
		Glass	27.02	0.07	6.80	0.09	16.78	0.13	44.92	0.20	1.32	0.06	0.04	0.02	0.52	0.04	1.65	99.06
HSM1+Mo	-2.2	Cpx	25.49	0.21	14.79	0.33	9.37	0.90	48.65	0.41	0.92	0.10	0.03	0.01	0.03	0.03	0.49	99.76
		Glass	31.57	0.08	6.65	0.03	15.43	0.09	41.99	0.11	0.86	0.02	0.02	0.01	0.25	0.08	1.97	98.72
WM1+Mo+W	1.9	Cpx	22.49	0.27	19.97	0.19	1.67	0.21	54.66	0.48	0.47	0.05	0.04	0.03	0.14	0.02	0.99	100.44
		Glass	17.97	0.08	14.64	0.12	10.64	0.12	50.73	0.14	1.99	0.06	0.07	0.03	0.27	0.02	2.27	98.60
WM1+Mo+W	1.0	Cpx	21.85	0.28	20.85	0.27	1.27	0.15	55.43	0.58	0.44	0.07	0.09	0.04	0.14	0.02	0.86	100.91
		Ol	0.49	0.04	55.41	0.08	0.03	0.01	43.39	0.08	0.01	0.01	0.16	0.03	0.22	0.02	-	99.71
		Glass	17.76	0.07	15.34	0.14	9.78	0.07	52.47	0.17	1.88	0.08	0.13	0.06	0.31	0.03	1.90	99.56
WM1+Mo+W	-1.1	Cpx	22.07	0.58	20.43	0.44	1.07	0.20	54.91	0.27	0.37	0.09	0.02	0.03	0.18	0.03	0.66	99.73
		Ol	0.49	0.01	54.94	0.78	0.03	0.01	42.82	0.38	0.01	0.003	0.02	0.01	0.31	0.07	-	98.63
		Glass	18.38	0.10	14.93	0.08	10.20	0.04	50.99	0.17	1.78	0.23	0.02	0.02	0.35	0.06	2.61	99.25
WM1+Mo+W	-3.0	Cpx	21.79	0.45	20.81	0.29	1.33	0.22	54.60	0.43	0.48	0.08	0.04	0.02	0.25	0.04	0.51	99.82
		Ol	0.44	0.03	55.31	0.14	0.04	0.02	42.70	0.16	bdl	-	0.03	0.02	0.34	0.05	-	98.86
		Glass	17.02	0.11	14.99	0.12	10.12	0.09	51.98	0.18	1.93	0.14	0.05	0.02	0.40	0.04	2.25	98.73
WM1+Mo+W	-4.3	Cpx	23.05	0.28	19.79	0.17	1.78	0.03	54.00	0.30	0.63	0.06	0.01	0.01	0.14	0.04	0.20	99.59
		Ol	0.59	0.03	55.38	0.42	0.03	0.02	42.41	0.24	0.03	0.01	0.04	0.004	0.19	0.04	-	98.66
		Glass	18.52	0.11	14.88	0.18	10.78	0.12	50.59	0.12	1.63	0.11	bdl	-	0.13	0.04	2.24	98.76
WM1+Mo+W	0.0	Cpx	22.27	0.32	20.45	0.17	1.24	0.11	54.04	0.41	0.41	0.03	0.17	0.01	0.24	0.05	0.98	99.79
		Ol	0.52	0.03	55.37	0.13	0.03	0.01	42.26	0.28	0.02	0.01	0.53	0.02	0.41	0.06	-	99.13
		Glass	18.36	0.13	15.47	0.12	9.25	0.03	50.55	0.10	1.86	0.11	0.62	0.05	0.50	0.02	2.18	98.80
WM1+W	1.9	Cpx	22.15	0.20	20.43	0.19	1.34	0.14	55.62	0.16	0.39	0.07	0.07	0.03	0.10	0.02	0.98	101.08
		Ol	0.46	0.03	55.75	0.18	0.03	0.01	43.60	0.16	0.03	0.01	0.10	0.04	0.23	0.03	-	100.19
		Glass	17.52	0.15	14.48	0.17	10.84	0.11	52.29	0.16	1.73	0.03	0.04	0.01	0.27	0.02	2.17	99.32
WM1+W	-3.0	Cpx	22.87	0.22	20.16	0.12	1.23	0.08	54.61	0.17	0.44	0.05	0.009	0.004	0.11	0.03	0.28	99.71

Supplementary Table 4.2 - Average values (n=5/each phase) for major element composition (cg/g) of minerals and silicate glass in the experiments of this study

Experiment	Δ FMQ	Phase	CaO	σ	MgO	σ	Al_2O_3	σ	SiO_2	σ	TiO_2	σ	FeO	σ	MnO	σ	T.E.*	Total
		Glass	18.88	0.06	14.70	0.16	10.80	0.15	49.91	0.13	1.90	0.05	0.06	0.01	0.21	0.03	2.09	98.55
WM1+W	-4.3	Cpx	22.96	0.23	20.23	0.18	1.34	0.13	54.60	0.13	0.55	0.10	0.02	0.01	0.07	0.03	0.16	99.93
		Glass	18.98	0.05	15.01	0.09	10.76	0.08	50.51	0.27	1.63	0.07	0.016	0.005	0.08	0.05	1.96	98.95
WM1+W	1.0	Cpx	22.87	0.13	19.89	0.23	1.36	0.11	54.96	0.29	0.34	0.06	0.08	0.03	0.08	0.04	0.66	100.24
		Ol	0.58	0.02	55.14	0.19	0.03	0.01	43.29	0.09	0.04	0.01	0.28	0.04	0.22	0.03	-	99.58
		Glass	19.56	0.12	15.42	0.08	9.38	0.05	50.89	0.33	1.68	0.14	0.24	0.06	0.27	0.02	2.03	99.48
WM1+W	-1.1	Cpx	22.70	0.15	19.89	0.07	1.29	0.10	54.26	0.15	0.35	0.02	0.14	0.01	0.20	0.07	0.48	99.32
		Ol	0.48	0.03	54.78	0.66	0.03	0.02	42.66	0.06	0.02	0.01	0.27	0.02	0.37	0.05	-	98.61
		Glass	18.35	0.03	14.83	0.09	10.22	0.09	49.92	0.15	2.11	0.08	0.23	0.06	0.51	0.09	2.48	98.63
WM1+W	0.0	Cpx	23.07	0.20	19.74	0.23	1.50	0.13	53.96	0.26	0.38	0.06	0.17	0.03	0.26	0.06	1.12	100.21
		Ol	0.55	0.02	55.22	0.19	0.03	0.01	42.67	0.13	0.04	0.02	0.44	0.03	0.57	0.04	-	99.53
		Glass	19.06	0.06	15.19	0.10	9.71	0.06	49.17	0.21	1.82	0.04	0.51	0.05	0.67	0.05	2.58	98.70
WM1+Mo	-1.1	Cpx	21.60	0.44	20.72	0.38	1.24	0.07	54.57	0.20	0.30	0.04	0.04	0.01	0.21	0.02	0.53	99.22
		Ol	0.42	0.02	55.12	0.22	0.04	0.02	42.81	0.18	0.02	0.01	0.09	0.02	0.39	0.07	-	98.88
		Glass	17.44	0.06	14.87	0.08	10.14	0.05	51.25	0.17	1.96	0.05	0.06	0.03	0.48	0.05	2.30	98.50
WM1+Mo	1.0	Cpx	21.97	0.19	20.76	0.24	1.14	0.09	55.59	0.47	0.30	0.06	0.11	0.04	0.14	0.03	0.90	100.90
		Ol	0.52	0.01	55.61	0.15	0.03	0.02	43.59	0.20	0.01	0.01	0.30	0.07	0.23	0.05	-	100.29
		Glass	17.99	0.07	15.76	0.10	9.21	0.04	52.31	0.17	1.62	0.12	0.35	0.03	0.28	0.05	2.00	99.51
WM1+Mo	0.0	Cpx	21.93	0.12	20.58	0.33	1.25	0.05	54.63	0.35	0.33	0.04	0.18	0.03	0.24	0.04	0.94	100.07
		Ol	0.47	0.04	55.42	0.12	0.03	0.01	42.80	0.21	0.03	0.01	0.53	0.04	0.42	0.06	-	99.68
		Glass	17.91	0.14	15.42	0.09	9.36	0.08	51.12	0.39	1.77	0.10	0.63	0.06	0.44	0.07	2.25	98.89
WM1+Mo	-2.1	Cpx	22.24	0.22	20.70	0.26	1.23	0.12	54.97	0.29	0.44	0.04	0.03	0.02	0.12	0.04	0.54	100.26
		Ol	0.50	0.04	55.63	0.16	0.02	0.01	42.92	0.19	0.02	0.01	bdl	-	0.20	0.03	-	99.29
		Glass	17.49	0.07	15.50	0.05	9.40	0.09	52.29	0.28	1.94	0.04	bdl	-	0.20	0.04	2.15	98.96
OPM-3	1.9	Opx	0.40	0.10	38.07	0.05	0.52	0.12	58.57	0.14	0.50	0.12	0.09	0.01	0.51	0.06	0.37	99.02
		Glass	12.10	0.07	14.49	0.10	9.48	0.12	50.72	0.15	8.79	0.02	0.04	0.01	1.01	0.10	2.63	99.27
OPM-3	1.0	Opx	0.41	0.03	38.04	0.24	0.45	0.09	58.89	0.08	0.55	0.11	0.04	0.02	0.50	0.03	0.29	99.17
		Glass	12.19	0.15	14.74	0.11	9.20	0.22	50.61	0.72	8.69	0.17	0.03	0.03	0.93	0.06	2.41	98.80
OPM-3	0.0	Opx	0.35	0.02	38.02	0.35	0.45	0.04	58.36	0.64	0.53	0.07	0.13	0.03	0.53	0.08	0.29	98.68
		Glass	12.05	0.11	14.70	0.04	9.13	0.08	50.68	0.37	8.85	0.08	0.10	0.04	1.00	0.10	2.33	98.84
OPM-3	-1.1	Opx	0.41	0.01	37.88	0.05	0.45	0.06	58.56	0.40	0.50	0.03	0.03	0.02	0.49	0.02	0.22	98.55
		Glass	11.89	0.07	14.94	0.04	9.82	0.07	50.65	0.32	8.80	0.15	bdl	-	0.55	0.04	2.24	98.90
OPM-3	-2.1	Opx	0.41	0.03	37.80	0.27	0.41	0.05	58.74	0.31	0.52	0.06	0.05	0.02	0.50	0.06	0.22	98.64
		Glass	12.14	0.08	15.10	0.06	9.79	0.11	49.86	0.34	8.57	0.11	0.01	0.00	0.73	0.05	2.38	98.59
OPM-3	-3.0	Opx	0.42	0.02	37.97	0.11	0.36	0.05	58.83	0.30	0.49	0.06	0.02	0.02	0.56	0.06	0.26	98.91
		Glass	12.48	0.11	14.58	0.12	9.24	0.12	50.39	0.27	8.93	0.11	bdl	-	1.04	0.05	2.26	98.92
OPM-3	-4.1	Opx	0.36	0.02	37.87	0.64	0.36	0.06	59.30	1.19	0.64	0.12	0.03	0.03	0.34	0.05	0.11	99.02
		Glass	11.62	0.14	15.11	0.15	9.48	0.03	52.97	0.22	8.35	0.26	0.01	0.01	0.34	0.03	1.98	99.86
OLM-1	1.9	Ol	0.44	0.02	55.51	0.24	0.03	0.01	42.30	0.29	0.06	0.02	0.10	0.04	0.28	0.05	0.13	98.84
		Glass	17.06	0.09	15.77	0.15	6.62	0.07	48.66	0.27	8.57	0.25	0.11	0.02	0.41	0.05	1.96	99.17
OLM-1	1.0	Ol	0.42	0.01	56.05	0.15	0.03	0.02	42.91	0.15	0.04	0.04	0.03	0.01	0.22	0.03	0.13	99.82
		Glass	18.23	0.12	16.38	0.12	5.56	0.07	49.71	0.55	7.19	0.07	0.03	0.02	0.36	0.01	1.62	99.09
OLM-1	0.0	Ol	0.41	0.02	55.52	0.19	0.05	0.02	42.28	0.24	0.04	0.03	0.15	0.02	0.29	0.04	0.17	98.90
		Glass	17.91	0.11	16.11	0.09	5.54	0.08	49.85	0.37	7.20	0.19	0.11	0.02	0.42	0.04	1.67	98.81
OLM-1	-1.1	Ol	0.42	0.03	55.22	0.30	0.04	0.01	42.47	0.34	0.04	0.03	0.05	0.02	0.26	0.02	0.15	98.64
		Cpx	18.47	0.91	24.12	0.95	0.52	0.14	55.45	0.29	1.22	0.18	0.022	0.004	0.08	0.04	1.03	100.90
		Glass	17.52	0.09	16.19	0.16	6.29	0.05	48.43	0.29	7.90	0.04	0.02	0.01	0.33	0.06	1.89	98.57
OLM-1	-2.1	Ol	0.42	0.02	55.62	0.33	0.02	0.01	43.53	0.09	0.05	0.05	0.07	0.05	0.15	0.05	0.13	99.98
		Glass	17.69	0.13	16.32	0.05	5.55	0.05	50.93	0.15	7.48	0.16	0.03	0.01	0.18	0.06	1.52	99.71
OLM-1	-3.0	Ol	0.44	0.03	55.29	0.32	0.05	0.02	42.51	0.26	0.04	0.01	0.02	0.02	0.14	0.07	0.06	98.55
		Glass	17.95	0.07	15.75	0.08	5.79	0.09	50.26	0.19	7.34	0.14	0.034	0.004	0.12	0.04	1.28	98.52
OLM-1	-3.5	Cpx	20.37	0.94	21.24	0.92	0.76	0.22	55.18	0.58	1.34	0.32	0.20	0.05	0.16	0.03	0.29	99.54
		Glass	16.30	0.32	14.61	0.15	7.61	0.21	47.97	0.35	9.62	0.11	0.61	0.06	0.33	0.08	1.54	98.60
OLM-1	-5.5	Cpx	20.20	0.95	21.35	0.83	0.77	0.20	55.56	0.54	1.67	0.22	0.03	0.02	0.06	0.03	0.14	99.77
		Glass	16.46	0.19	14.58	0.05	8.38	0.03	49.33	0.25	8.75	0.20	bdl	-	0.05	0.01	1.51	99.04
M8	-3.5	Pl	19.33	0.23	0.53	0.03	35.82	0.28	45.06	0.41	0.02	0.02	0.06	0.05	0.03	0.04	0.30	101.15
		Ol	0.21	0.01	54.76	0.40	0.12	0.03	43.02	0.24	0.04	0.02	0.23	0.02	0.54	0.03	-	98.91
		Glass	12.75	0.11	13.58	0.05	19.09	0.20	50.15	0.14	0.09	0.03	0.20	0.04	0.73	0.06	2.44	99.03
M8	-5.5	Pl	19.32	0.08	0.54	0.03	35.78	0.17	44.50	0.26	0.03	0.02	0.04	0.02	0.02	0.02	0.33	100.55

Supplementary Table 4.2 - Average values (n=5/each phase) for major element composition (cg/g) of minerals and silicate glass in the experiments of this study

Experiment	Δ FMQ	Phase	CaO	σ	MgO	σ	Al_2O_3	σ	SiO_2	σ	TiO_2	σ	FeO	σ	MnO	σ	T.E.*	Total
		Ol	0.22	0.01	54.93	0.37	0.17	0.03	42.89	0.41	bdl	-	0.03	0.02	0.39	0.05	-	98.63
		Glass	12.63	0.15	13.51	0.08	18.39	0.17	51.16	0.17	0.12	0.02	bdl	-	0.54	0.04	2.17	98.52

bdl: below detection limit (<0.01 cg/g); *T.E.: total of minor and trace elements in ppm (from LA-ICP-MS analysis excluding Ti)

Supplementary Table 4.3 - Distribution coefficients between crystals and silicate melt

Experiment	Δ FMQ	D_P	σ	D_{Sc}	σ	D_{Ti}	σ	D_V	σ	D_{Cr}	σ	D_{Sr}	σ	D_Y	σ	D_{Zr}	σ	D_{Nb}	σ	D_{Mo}	σ	D_{Ba}	σ
Cpx/melt																							
HS+Mo+W	1.8	0.027	0.009	8.88	1.41	0.62	0.03	0.26	0.01	28.5	11.3	0.063	0.003	0.31	0.02	0.49	0.03	0.017	0.004	0.002	0.001	0.00032	0.00018
HS+Mo+W	1.0	0.024	0.005	6.43	0.76	0.63	0.03	0.67	0.05	39.8	18.2	0.070	0.002	0.33	0.01	0.49	0.02	0.018	0.002	0.005	0.001	0.00035	0.00022
HS+Mo+W	-0.1	0.017	0.010	6.92	1.66	0.52	0.05	0.78	0.11	34.4	18.0	0.050	0.004	0.31	0.03	0.41	0.03	0.017	0.003	0.010	0.004	0.00015	0.00010
HS+Mo+W	-1.2	0.012	0.003	6.18	1.39	0.50	0.07	4.42	1.13	21.0	12.4	0.050	0.005	0.30	0.02	0.37	0.04	0.018	0.006	0.042	0.012	0.00011	0.00005
HS+Mo+W	-2.2	0.020	0.011	7.85	3.07	0.67	0.15	8.51	3.49	12.1	8.0	0.059	0.008	0.33	0.06	0.40	0.07	0.027	0.006	0.25	0.05	0.00020	0.00004
HS+Mo+W	-3.1	0.016	0.003	8.17	1.84	1.02	0.06	10.22	3.35	9.8	3.9	0.054	0.003	0.32	0.02	0.39	0.03	0.029	0.003	1.21	0.72	0.00016	0.00001
HS+W	-4.2	0.022	0.007	6.30	1.09	0.71	0.15	13.53	4.34	5.4	1.6	0.043	0.002	0.22	0.03	0.39	0.04	0.035	0.008	-	-	0.00020	0.00002
HS+W	1.0	0.022	0.005	7.28	2.39	0.51	0.16	0.59	0.12	26.1	6.0	0.067	0.008	0.31	0.07	0.50	0.09	0.015	0.006	-	-	0.00048	0.00014
HS+W	1.8	0.021	0.003	6.70	1.16	0.45	0.03	0.33	0.02	26.8	4.0	0.067	0.002	0.33	0.02	0.48	0.02	0.014	0.002	-	-	0.00027	0.00011
HS+W	-3.1	0.039	0.013	8.42	1.75	1.00	0.05	15.02	3.94	8.2	3.7	0.058	0.004	0.36	0.01	0.46	0.03	0.021	0.001	-	-	0.00017	0.00003
HS+Mo	-3.1	0.031	0.007	9.65	2.49	1.12	0.07	11.43	5.28	9.0	3.8	0.063	0.011	0.36	0.01	0.50	0.07	0.030	0.005	1.21	0.62	0.00021	0.00003
HS+Mo	-4.2	0.027	0.010	9.24	2.62	1.19	0.53	13.43	3.41	6.7	1.7	0.058	0.005	0.30	0.04	0.60	0.07	0.033	0.008	2.19	1.09	0.00025	0.00017
HS+Mo	1.0	0.027	0.012	5.67	0.64	0.62	0.06	0.64	0.03	21.6	7.2	0.071	0.002	0.34	0.04	0.54	0.03	0.019	0.003	0.006	0.001	0.00019	0.00004
HS+Mo	1.8	0.015	0.005	6.19	2.07	0.57	0.03	0.32	0.01	19.4	7.1	0.064	0.003	0.30	0.02	0.49	0.02	0.013	0.002	0.004	0.002	0.00033	0.00014
HS+Mo	-0.1	0.018	0.003	8.28	0.96	0.59	0.03	1.21	0.15	18.9	8.1	0.062	0.002	0.29	0.01	0.51	0.02	0.013	0.003	0.008	0.004	0.00025	0.00008
HS+Mo	-2.2	0.025	0.004	6.54	3.36	0.91	0.32	10.72	5.06	12.2	3.0	0.058	0.009	0.35	0.04	0.48	0.08	0.018	0.005	0.19	0.08	0.00020	0.00004
W1+Mo+W	1.9	0.010	0.005	1.18	0.11	0.25	0.02	0.11	0.02	10.3	2.9	0.093	0.011	0.18	0.01	0.04	0.01	0.0016	0.0006	0.0013	0.0006	0.00016	0.00004
W1+Mo+W	1.0	0.007	0.001	0.93	0.05	0.25	0.01	0.15	0.01	7.1	1.4	0.065	0.003	0.15	0.01	0.04	0.01	0.0018	0.0005	0.003	0.001	0.00014	0.00001
W1+Mo+W	-1.1	0.009	0.002	0.79	0.12	0.24	0.02	0.98	0.07	5.7	0.9	0.060	0.004	0.13	0.03	0.026	0.004	0.0015	0.0003	0.008	0.002	0.00016	0.00007
W1+Mo+W	-3.0	0.010	0.002	1.10	0.10	0.25	0.03	2.89	0.43	2.4	0.4	0.069	0.002	0.16	0.02	0.018	0.004	0.0017	0.0006	0.23	0.11	0.00010	0.00006
W1+Mo+W	-4.3	0.040	0.017	1.10	0.13	0.33	0.03	3.01	0.41	1.9	0.4	0.076	0.005	0.16	0.02	0.03	0.01	0.0029	0.0014	0.45	0.08	0.00017	0.00009
W1+Mo+W	0.0	0.013	0.006	0.86	0.09	0.19	0.02	0.40	0.05	9.3	2.6	0.069	0.005	0.13	0.01	0.03	0.01	0.0015	0.0004	0.005	0.001	0.00015	0.00002
W1+W	1.9	0.010	0.002	0.92	0.06	0.21	0.02	0.12	0.01	10.5	3.2	0.079	0.004	0.14	0.02	0.03	0.01	0.0013	0.0004	-	-	0.00014	0.00004
W1+W	-3.0	0.007	0.001	0.94	0.27	0.27	0.09	2.92	0.47	2.6	0.3	0.081	0.034	0.13	0.02	0.03	0.01	0.0016	0.0003	-	-	0.00019	0.00009
W1+W	-4.3	0.014	0.005	1.03	0.15	0.28	0.03	4.14	0.85	2.5	1.0	0.071	0.004	0.14	0.04	0.03	0.01	0.0013	0.0003	-	-	0.00020	0.00005
W1+W	1.0	0.008	0.002	0.96	0.09	0.22	0.02	0.16	0.01	7.6	2.0	0.073	0.004	0.13	0.01	0.03	0.01	0.0016	0.0005	-	-	0.00022	0.00010
W1+W	-1.1	0.007	0.001	0.82	0.07	0.19	0.02	0.85	0.08	4.1	1.1	0.066	0.007	0.12	0.01	0.029	0.005	0.0015	0.0005	-	-	0.00020	0.00006
W1+W	0.0	0.0075	0.0001	0.86	0.05	0.18	0.02	0.31	0.02	6.5	0.8	0.070	0.006	0.11	0.01	0.028	0.002	0.0014	0.0002	-	-	0.00019	0.00007
W1+Mo	-1.1	0.007	0.001	0.67	0.08	0.19	0.02	1.19	0.14	3.2	0.4	0.061	0.008	0.12	0.02	0.024	0.005	0.0012	0.0005	0.016	0.007	0.00017	0.00011
W1+Mo	1.0	0.008	0.002	0.78	0.11	0.22	0.02	0.21	0.04	6.5	1.8	0.073	0.008	0.11	0.02	0.017	0.007	0.0013	0.0003	0.003	0.001	0.00014	0.00006
W1+Mo	0.0	0.011	0.002	0.80	0.08	0.18	0.01	0.35	0.07	5.7	1.0	0.068	0.006	0.13	0.01	0.027	0.006	0.0014	0.0003	0.0036	0.0004	0.00016	0.00005
W1+Mo	-2.1	0.009	0.005	1.10	0.12	0.21	0.02	2.07	0.28	3.0	0.3	0.075	0.008	0.15	0.01	0.020	0.004	0.0016	0.0004	0.061	0.044	0.00020	0.00010
OLM-1	-1.1	0.011	0.005	0.52	0.06	0.23	0.01	0.81	0.13	3.7	0.5	0.081	0.004	0.10	0.01	0.021	0.004	0.0016	0.0007	0.013	0.003	0.00050	0.00016
OLM-1	-3.5	0.028	0.010	0.66	0.13	0.22	0.03	6.03	1.09	3.5	0.7	0.068	0.011	0.11	0.02	0.019	0.006	0.0010	0.0002	0.56	0.08	0.00018	0.00004
OLM-1	-5.5	0.079	0.035	0.67	0.05	0.23	0.03	7.70	1.50	2.9	0.3	0.071	0.006	0.12	0.01	0.014	0.002	0.0008	0.0003	0.54	0.20	0.00020	0.00016

Cpx/melt		D_{La}	σ	D_{Nd}	σ	D_{Sm}	σ	D_{Eu}	σ	D_{Lu}	σ	D_{Hf}	σ	D_{Ta}	σ	D_W	σ	D_{Th}	σ	D_U	σ
HS+Mo+W	1.8	0.067	0.006	0.195	0.012	0.27	0.01	0.288	0.015	0.301	0.015	1.140	0.074	0.065	0.014	0.00014	0.00008	0.027	0.008	0.004	0.001
HS+Mo+W	1.0	0.073	0.003	0.217	0.009	0.30	0.01	0.302	0.011	0.327	0.014	1.078	0.052	0.072	0.007	0.00021	0.00018	0.037	0.006	0.0058	0.0005
HS+Mo+W	-0.1	0.065	0.007	0.201	0.019	0.30	0.02	0.232	0.020	0.338	0.030	1.000	0.079	0.081	0.008	0.00015	0.00004	0.034	0.008	0.008	0.002
HS+Mo+W	-1.2	0.071	0.007	0.221	0.015	0.29	0.02	0.171	0.012	0.284	0.020	0.996	0.113	0.072	0.008	0.00015	0.00008	0.027	0.008	0.009	0.002
HS+Mo+W	-2.2	0.080	0.007	0.205	0.055	0.36	0.05	0.149	0.015	0.368	0.039	1.446	0.132	0.114	0.016	0.0014	0.0011	0.051	0.007	0.035	0.004
HS+Mo+W	-3.1	0.067	0.003	0.207	0.013	0.30	0.02	0.097	0.006	0.327	0.021	1.539	0.451	0.097	0.009	0.005	0.002	0.049	0.006	0.034	0.003
HS+W	-4.2	0.042	0.005	0.132	0.014	0.23	0.07	0.087	0.011	0.239	0.063	0.876	0.248	0.134	0.039	0.027	0.021	0.046	0.010	0.030	0.004
HS+W	1.0	0.063	0.016	0.161	0.045	0.26	0.04	0.275	0.034	0.256	0.056	0.944	0.340	0.069	0.014	0.0003	0.0001	0.029	0.011	0.004	0.002
HS+W	1.8	0.066	0.003	0.209	0.005	0.30	0.01	0.305	0.009	0.314	0.009	0.983	0.055	0.067	0.009	0.0002	0.0001	0.026	0.003	0.004	0.001
HS+W	-3.1	0.062	0.003	0.189	0.008	0.33	0.02	0.092	0.007	0.355	0.014	1.059	0.054	0.082	0.008	0.006	0.002	0.037	0.006	0.031	0.001

Supplementary Table 4.3 - Distribution coefficients between crystals and silicate melt

HS+Mo	-3.1	0.063	0.005	0.181	0.009	0.33	0.02	0.111	0.011	0.368	0.019	1.080	0.137	0.092	0.013	-	-	0.035	0.005	0.034	0.002
HS+Mo	-4.2	0.068	0.009	0.203	0.023	0.30	0.03	0.119	0.018	0.316	0.034	1.275	0.160	0.101	0.022	-	-	0.045	0.013	0.039	0.009
HS+Mo	1.0	0.064	0.005	0.188	0.013	0.26	0.02	0.331	0.021	0.285	0.016	0.905	0.041	0.086	0.019	-	-	0.029	0.007	0.005	0.001
HS+Mo	1.8	0.065	0.002	0.194	0.011	0.29	0.02	0.310	0.016	0.309	0.058	1.002	0.022	0.062	0.007	-	-	0.024	0.004	0.005	0.001
HS+Mo	-0.1	0.061	0.007	0.175	0.010	0.29	0.06	0.220	0.012	0.281	0.041	0.982	0.044	0.055	0.009	-	-	0.029	0.007	0.009	0.001
HS+Mo	-2.2	0.063	0.009	0.193	0.026	0.26	0.06	0.205	0.042	0.365	0.047	1.110	0.112	0.066	0.017	-	-	0.039	0.013	0.031	0.004
W1+Mo+W	1.9	0.033	0.005	0.104	0.011	0.15	0.01	0.137	0.008	0.174	0.012	0.094	0.027	0.0047	0.0024	0.00003	0.00002	0.0021	0.0010	0.0005	0.0001
W1+Mo+W	1.0	0.025	0.001	0.080	0.004	0.11	0.01	0.117	0.007	0.140	0.008	0.082	0.013	0.0034	0.0013	0.00006	0.00002	0.0035	0.0006	0.0007	0.0001
W1+Mo+W	-1.1	0.018	0.002	0.057	0.008	0.08	0.01	0.078	0.010	0.094	0.012	0.037	0.006	0.0016	0.0003	0.00006	0.00002	0.0014	0.0003	0.0010	0.0003
W1+Mo+W	-3.0	0.016	0.003	0.052	0.008	0.07	0.01	0.018	0.002	0.096	0.010	0.046	0.018	0.0012	0.0003	0.0026	0.0014	0.0018	0.0005	0.0029	0.0003
W1+Mo+W	-4.3	0.014	0.002	0.043	0.006	0.06	0.01	0.018	0.002	0.112	0.015	0.057	0.014	0.0018	0.0012	0.0081	0.0023	0.0033	0.0007	0.0049	0.0008
W1+Mo+W	0.0	0.023	0.003	0.072	0.008	0.10	0.01	0.111	0.011	0.120	0.012	0.065	0.018	0.0025	0.0011	0.00005	0.00002	0.0015	0.0004	0.0005	0.0001
W1+W	1.9	0.030	0.009	0.078	0.008	0.13	0.01	0.124	0.016	0.151	0.020	0.084	0.017	0.0028	0.0013	0.00005	0.00003	0.0026	0.0007	0.0007	0.0001
W1+W	-3.0	0.024	0.006	0.065	0.005	0.09	0.01	0.022	0.007	0.129	0.024	0.083	0.019	0.0024	0.0008	0.0020	0.0005	0.0017	0.0006	0.0024	0.0010
W1+W	-4.3	0.022	0.009	0.050	0.009	0.08	0.02	0.021	0.001	0.136	0.013	0.084	0.023	0.0047	0.0024	0.0109	0.0070	0.0032	0.0009	0.0060	0.0013
W1+W	1.0	0.025	0.002	0.077	0.007	0.11	0.01	0.113	0.012	0.126	0.014	0.081	0.021	0.0029	0.0015	0.00004	0.00001	0.0036	0.0007	0.0008	0.0002
W1+W	-1.1	0.024	0.003	0.079	0.010	0.11	0.01	0.084	0.010	0.110	0.014	0.068	0.013	0.0021	0.0008	0.00004	0.00001	0.0017	0.0005	0.0010	0.0002
W1+W	0.0	0.023	0.002	0.070	0.006	0.10	0.01	0.106	0.009	0.109	0.011	0.062	0.008	0.0021	0.0006	0.00006	0.00002	0.0016	0.0001	0.0005	0.0001
W1+Mo	-1.1	0.023	0.008	0.066	0.013	0.10	0.01	0.085	0.016	0.108	0.021	0.054	0.012	0.0015	0.0006	-	-	0.0015	0.0004	0.0011	0.0006
W1+Mo	1.0	0.022	0.004	0.057	0.014	0.09	0.02	0.092	0.021	0.105	0.022	0.068	0.025	0.0020	0.0011	-	-	0.0029	0.0006	0.0007	0.0002
W1+Mo	0.0	0.022	0.003	0.070	0.008	0.10	0.01	0.110	0.010	0.123	0.012	0.061	0.014	0.0021	0.0008	-	-	0.0014	0.0004	0.0006	0.0001
W1+Mo	-2.1	0.016	0.003	0.049	0.005	0.08	0.01	0.039	0.003	0.095	0.009	0.039	0.007	0.0011	0.0006	-	-	0.0030	0.0014	0.0019	0.0004
OLM-1	-1.1	0.016	0.002	0.053	0.007	0.08	0.01	0.083	0.008	0.093	0.010	0.034	0.009	0.0018	0.0006	0.00008	0.00002	0.0011	0.0004	0.0013	0.0006
OLM-1	-3.5	0.016	0.004	0.055	0.012	0.08	0.02	0.037	0.006	0.101	0.018	0.044	0.016	0.0012	0.0004	0.0011	0.0004	0.0011	0.0005	0.0027	0.0008
OLM-1	-5.5	0.019	0.002	0.061	0.005	0.09	0.01	0.035	0.003	0.109	0.009	0.031	0.005	0.0013	0.0006	0.0054	0.0024	0.0010	0.0001	0.0038	0.0008

Opx/melt		D_P	σ	D_{Sc}	σ	D_{Ti}	σ	D_V	σ	D_{Cr}	σ	D_{Sr}	σ	D_Y	σ	D_{Zr}	σ	D_{Nb}	σ	D_{Mo}	σ	D_{Ba}	σ
OPM-3	1.9	0.025	0.006	0.26	0.03	0.056	0.006	0.11	0.02	2.00	0.28	0.0011	0.0010	0.0061	0.0009	0.0026	0.0007	0.0013	0.0003	0.009	0.001	0.000006	0.000004
OPM-3	1.0	0.021	0.002	0.21	0.05	0.057	0.010	0.14	0.03	1.44	0.22	0.0006	0.0002	0.0057	0.0010	0.0020	0.0004	0.0011	0.0003	0.008	0.001	0.000016	0.000014
OPM-3	0.0	0.036	0.007	0.21	0.02	0.050	0.002	0.16	0.01	1.31	0.15	-	-	0.0049	0.0003	0.0020	0.0001	0.0011	0.0001	0.026	0.008	0.000002	0.000001
OPM-3	-1.1	0.030	0.002	0.20	0.02	0.048	0.005	0.36	0.06	1.14	0.24	-	-	0.0049	0.0007	0.0021	0.0005	0.0008	0.0002	0.14	0.01	0.000014	0.000008
OPM-3	-2.1	0.040	0.014	0.24	0.02	0.059	0.014	0.58	0.14	0.88	0.24	0.0009	0.0003	0.0065	0.0006	0.0027	0.0011	0.0009	0.0005	0.32	0.27	0.000021	0.000009
OPM-3	-3.0	0.054	0.027	0.26	0.03	0.060	0.007	0.58	0.07	1.23	0.08	0.0007	0.0003	0.0068	0.0009	0.0024	0.0004	0.0010	0.0002	0.63	0.34	0.000013	0.000010
OPM-3	-4.1	0.065	0.012	0.24	0.02	0.042	0.009	1.43	0.38	1.28	0.18	0.0007	0.0002	0.0070	0.0015	0.0028	0.0013	0.0009	0.0001	0.53	0.19	0.000030	0.000010

Opx/melt		D_{La}	σ	D_{Nd}	σ	D_{Sm}	σ	D_{Eu}	σ	D_{Lu}	σ	D_{Hf}	σ	D_{Ta}	σ	D_W	σ	D_{Th}	σ	D_U	σ
OPM-3	1.9	0.00007	0.00004	0.00023	0.00005	0.00055	0.00018	0.00093	0.00016	0.021	0.003	0.005	0.001	0.00085	0.00021	0.0010	0.0002	0.00002	0.00001	0.00009	0.00001
OPM-3	1.0	0.00006	0.00003	0.00022	0.00003	0.00053	0.00012	0.00069	0.00010	0.019	0.004	0.004	0.001	0.00074	0.00020	0.0011	0.0001	0.00003	0.00001	0.00016	0.00009
OPM-3	0.0	0.00005	0.00001	0.00021	0.00004	0.00053	0.00003	0.00065	0.00006	0.018	0.001	0.004	0.001	0.00066	0.00002	0.0010	0.0001	0.00002	0.00001	0.00017	0.00008
OPM-3	-1.1	0.00005	0.00003	0.00022	0.00007	0.00058	0.00010	0.00049	0.00008	0.017	0.003	0.003	0.001	0.00061	0.00015	0.0023	0.0007	0.00004	0.00002	0.00030	0.00013
OPM-3	-2.1	0.00003	0.00002	0.00062	0.00038	0.00132	0.00046	0.00012	0.00007	0.022	0.002	0.005	0.001	0.00079	0.00022	0.0025	0.0015	0.00002	0.00001	0.00069	0.00033
OPM-3	-3.0	0.00003	0.00001	0.00034	0.00009	0.00090	0.00017	0.00012	0.00002	0.023	0.003	0.004	0.001	0.00061	0.00008	0.009	0.004	0.00002	0.00002	0.00112	0.00091
OPM-3	-4.1	0.00005	0.00003	0.00041	0.00027	0.00075	0.00024	0.00016	0.00006	0.023	0.002	0.005	0.001	0.00032	0.00021	0.028	0.010	0.00006	0.00003	0.0022	0.0018

Ol/melt		D_P	σ	D_{Sc}	σ	D_{Ti}	σ	D_V	σ	D_{Cr}	σ	D_{Sr}	σ	D_Y	σ	D_{Zr}	σ	D_{Nb}	σ	D_{Mo}	σ	D_{Ba}	σ
OLM-1	1.9	0.051	0.013	0.071	0.007	0.0032	0.0003	0.013	0.001	0.516	0.019	0.00011	0.00003	0.0021	0.0002	0.00026	0.00007	0.00016	0.00007	0.006	0.002	0.000013	0.000008
OLM-1	1.0	0.062	0.030	0.077	0.004	0.0033	0.0004	0.027	0.001	0.412	0.017	0.00014	0.00003	0.0026	0.0004	0.00031	0.00011	0.00016	0.00005	0.006	0.002	0.000038	0.000026
OLM-1	0.0	0.086	0.029	0.086	0.009	0.0038	0.0005	0.081	0.008	0.420	0.016	-	-	0.0032	0.0004	0.00037	0.00005	-	-	0.013	0.005	0.000011	0.000000
OLM-1	-1.1	0.042	0.015	0.073	0.002	0.0031	0.0005	0.121	0.012	0.504	0.110	0.0001	0.0001	0.0026	0.0004	0.00030	0.00002	0.00010	0.00005	0.032	0.007	0.000017	0.000012

Supplementary Table 4.3 - Distribution coefficients between crystals and silicate melt

OLM-1	-2.1	0.090	0.012	0.092	0.033	0.0033	0.0009	0.247	0.166	0.636	0.115	0.0004	0.0002	0.0024	0.0007	0.00035	0.00014	0.00013	0.00004	0.06	0.02	0.000033	0.000012
OLM-1	-3.0	0.149	0.037	0.079	0.004	0.0039	0.0003	0.414	0.119	0.875	0.153	0.0003	0.0001	0.0027	0.0004	0.00039	0.00016	-	-	0.28	0.07	0.000011	0.000001

Ol/melt		D_{La}	σ	D_{Nd}	σ	D_{Sm}	σ	D_{Eu}	σ	D_{Lu}	σ	D_{Hf}	σ	D_{Ta}	σ	D_{W}	σ	D_{Th}	σ	D_{U}	σ
OLM-1	1.9	0.000004	0.000003	0.00008	0.00002	0.00015	0.00009	0.00018	0.00005	0.009	0.001	0.0004	0.0001	0.000006	0.000005	0.00002	0.00002	0.000003	0.000003	0.000002	0.000001
OLM-1	1.0	0.000008	0.000003	0.00005	0.00003	0.00019	0.00005	0.00017	0.00004	0.012	0.001	0.0005	0.0002	0.000065	0.000060	0.00006	0.00003	0.000004	0.000003	0.000003	0.000001
OLM-1	0.0	0.000006	0.000001	0.00007	0.00005	0.00019	0.00008	0.00017	0.00002	0.013	0.002	0.0006	0.0001	0.000032	0.000012	0.00009	0.00005	0.000002	0.000000	0.000005	0.000003
OLM-1	-1.1	0.000004	0.000002	0.00004	0.00002	0.00020	0.00013	0.00018	0.00005	0.011	0.001	0.0005	0.0005	0.000023	0.000010	0.00010	0.00005	0.000004	0.000002	0.000006	0.000002
OLM-1	-2.1	0.000009	0.000003	0.00008	0.00003	0.00026	0.00009	0.00011	0.00008	0.013	0.007	0.0003	0.0001	0.000059	0.000028	0.00028	0.00013	0.000006	0.000002	0.000010	0.000004
OLM-1	-3.0	0.000009	0.000005	0.00007	0.00004	0.00030	0.00003	0.00008	0.00003	0.012	0.001	0.0004	0.0001	0.000032	0.000014	0.00485	0.00226	0.000002	0.000001	0.000013	0.000008

Pl/melt		D_{P}	σ	D_{Sc}	σ	D_{Ti}	σ	D_{V}	σ	D_{Cr}	σ	D_{Sr}	σ	D_{Y}	σ	D_{Zr}	σ	D_{Nb}	σ	D_{Mo}	σ	D_{Ba}	σ
M8	-3.5	0.13	0.06	0.011	0.002	0.024	0.004	0.039	0.004	0.014	0.003	1.21	0.05	0.009	0.001	0.0004	0.0001	0.0003	0.0001	0.04	0.01	0.14	0.01
M8	-5.5	0.51	0.22	0.012	0.002	0.030	0.009	0.129	0.029	0.020	0.005	1.29	0.06	0.009	0.001	0.0003	0.0001	0.0007	0.0002	0.05	0.02	0.14	0.02

Pl/melt		D_{La}	σ	D_{Nd}	σ	D_{Sm}	σ	D_{Eu}	σ	D_{Lu}	σ	D_{Hf}	σ	D_{Ta}	σ	D_{W}	σ	D_{Th}	σ	D_{U}	σ
M8	-3.5	0.039	0.004	0.022	0.002	0.017	0.001	0.80	0.04	0.006	0.001	0.0002	0.0001	0.00022	0.00002	0.00010	0.00004	0.00016	0.00002	0.00007	0.00002
M8	-5.5	0.036	0.006	0.025	0.005	0.019	0.002	1.02	0.10	0.005	0.001	0.0003	0.0003	0.00025	0.00014	0.00491	0.00223	0.00021	0.00014	0.00008	0.00003

Standard deviation is given as 1σ of the mean value. Abbreviations according to Whitney and Evans (2010) - Ol: olivine; Cpx: Clinopyroxene, Opx: Orthopyroxene

Supplementary Table 4.4: Results for non-linear least squares fitting of the observed crystal/silicate melt partitioning data to the Lattice Strain Model (Blundy and Wood, 1994)

Crystal	Cations	Site	r_0 (Å)	σ	D_0	σ	E (GPa)	σ	Red. X^{2*}
Clinopyroxene (WM1)	Hf^{4+},Ti^{4+}, Zr^{4+}, Mo^{4+}	M1 (VI-fold)	0.644	0.001	0.46	0.01	2359	44	0.02
Clinopyroxene (HS1)	Hf^{4+},Ti^{4+}, Zr^{4+}, Mo^{4+}	M1 (VI-fold)	0.661	0.005	3.11	1.48	2559	916	1.95
Orthopyroxene	Hf^{4+},Ti^{4+}, Zr^{4+}, Mo^{4+}	M1 (VI-fold)	0.650	0.001	0.68	0.03	6865	368	1.00
Olivine	Hf^{4+},Ti^{4+}, Zr^{4+}, Mo^{4+}	M1 (VI-fold)	0.654	0.002	0.29	0.01	10101	560	2.56
Plagioclase	Hf^{4+},Ti^{4+}, Zr^{4+}, Mo^{4+}	M1 (VI-fold)	0.63	0.03	0.04	0.03	2938	2488	2.66
Clinopyroxene (WM1)	Lu^{3+}, Y^{3+}, Eu^{3+}, Sm^{3+}, Nd^{3+}, La^{3+}	M2 (VIII-fold)	1.018	0.001	0.14	0.01	281	5	0.05
Clinopyroxene (HS1)	Lu^{3+}, Y^{3+}, Eu^{3+}, Sm^{3+}, Nd^{3+}, La^{3+}	M2 (VIII-fold)	1.023	0.007	0.35	0.02	271	36	0.73
Orthopyroxene	Al^{3+}, Sc^{3+}, Lu^{3+}, Y^{3+}, Eu^{3+}, Sm^{3+}, Nd^{3+}, La^{3+}	M2 (VIII-fold)	0.761	0.005	0.42	0.07	239	16	2.22
Olivine	Al^{3+}, Sc^{3+}, Lu^{3+}, Y^{3+}, Eu^{3+}, Sm^{3+}, Nd^{3+}, La^{3+}	M2 (VIII-fold)	0.783	0.021	0.14	0.04	293	39	7.91
Plagioclase	Lu^{3+}, Y^{3+}, Sm^{3+}, Nd^{3+}, La^{3+}	M2 (VIII-fold)	1.227	0.003	0.042	0.002	115	2	0.01

*Goodness of fit showed by reduced chi-nu square adjusted, regressions weighted with uncertainties. $D_{Eu^{3+}}$ defined from average values at the oxidizing plateau (above FMQ). Ionic radii taken from Shannon (1976) with uncertainty of 0.005 Å.

Supplementary Table 4.5a - Lunar samples (literature data*, see text for details)

SAMPLE #	TYPE	NORM	MISSION	Mo (ppm)	W (ppm)	Hf (ppm)	Mo/W	Mo/Hf
10003,	high Ti		Apollo 11	0.18	0.22	10.20	0.82	0.018
10017,	high Ti		Apollo 11	0.99	0.34	14.00	2.92	0.071
10044,	high Ti		Apollo 11	0.12	0.23	11.70	0.51	0.010
10049,	high Ti		Apollo 11		0.32	16.90		
10050,	high Ti		Apollo 11	0.16	0.13	11.20	1.23	0.014
10057,	high Ti		Apollo 11	0.40	0.35	13.60	1.16	0.029
10058,	high Ti		Apollo 11	0.19	0.16	11.20	1.19	0.017
10069,	high Ti		Apollo 11	0.26	0.53	15.70	0.49	0.017
10084	high Ti		Apollo 11	0.70	0.23	10.20	2.99	0.069
10092,	high Ti		Apollo 11	0.06		7.56		
70011	high Ti		Apollo 17		0.12	6.50		
70135,	high Ti		Apollo 17	0.03	0.09	6.77	0.33	0.004
70215	high Ti		Apollo 17		0.09	6.33		
70275,	high Ti		Apollo 17	0.22	0.10	6.34	2.20	0.035
70315,	high Ti		Apollo 17			6.39		
71569	high Ti		Apollo 17		0.08	8.70		
72155	high Ti		Apollo 17		0.08	9.00		
74235,	high Ti		Apollo 17	0.15	0.08	8.78	1.88	0.017
74245,	high Ti		Apollo 17	0.40		7.65		
74255,	high Ti		Apollo 17	0.03	0.15	8.58	0.20	0.004
74275,	high Ti		Apollo 17	0.02	0.06	8.96	0.31	0.002
75035	high Ti		Apollo 17	0.04	0.08	11.20	0.48	0.004
78575,	high Ti		Apollo 17	0.03	0.15	7.23	0.20	0.004
78585,	high Ti		Apollo 17	0.16	0.06	6.17	2.67	0.026
78598,	high Ti		Apollo 17		0.09	8.04		
79035	high Ti		Apollo 17		0.12	7.20		
79155	high Ti		Apollo 17		0.08	8.70		
79135	high Ti		Apollo 17		0.18	5.70		
12002	low Ti	Ol	Apollo 12	0.05	0.20	3.10	0.25	0.016
12004,	low Ti	Ol	Apollo 12	0.08	0.08	2.97	0.98	0.027
12007,	low Ti	pig	Apollo 12	0.51	0.14	4.24	3.64	0.120
12009,	low Ti	OL	Apollo 12	0.15	0.17	3.26	0.88	0.046
12011,	low Ti	pig	Apollo 12	0.10	0.15	3.69	0.67	0.027
12015,	low Ti	OL	Apollo 12	0.12	0.16	2.87	0.75	0.042
12018	low Ti		Apollo 12		0.15	3.40		
12020,	low Ti	OL	Apollo 12	1.12	0.11	3.12	10.18	0.359
12021,	low Ti	pig	Apollo 12	0.12	0.13	3.62	0.92	0.033
12052	low Ti		Apollo 12	0.03	0.15	3.80	0.20	0.008
12053,	low Ti	pig	Apollo 12	0.30	0.11	3.55	2.82	0.085
12031,	low Ti	pig	Apollo 12		0.11	2.87		
12022,	low Ti	ilm	Apollo 12	0.11	0.16	4.25	0.69	0.026
12045,	low Ti	ilm	Apollo 12			4.17		
12051,	low Ti	ilm	Apollo 12	0.11	0.14	4.22	0.79	0.026
12054,	low Ti	ilm	Apollo 12		0.08	5.70		
12063,	low Ti	ilm	Apollo 12	0.04	0.10	4.29	0.42	0.009
12064,	low Ti	ilm	Apollo 12			4.10		

Supplementary Table 4.5a - Lunar samples (literature data*, see text for details)

12070	Low Ti	Soil	Apollo 12	0.03	0.50	15.60	0.06	0.002
12038	low Ti		Apollo 12	0.05	0.11	0.29	0.46	0.172
15085	low Ti	QNB	Apollo 15		0.06	2.44		
15065	low Ti	QNB	Apollo 15		0.10	3.36		
15475	low Ti	QNB	Apollo 15		0.07	2.85		
15495	low Ti	QNB	Apollo 15	0.02	0.05	2.31	0.41	0.009
15119,	low Ti	OL	Apollo 15	0.03	0.08	3.35	0.38	0.009
15256,	low Ti	OL	Apollo 15	0.32	0.03	2.69	10.67	0.119
15016,	low Ti	OL	Apollo 15	0.08	0.05	2.58	1.60	0.031
15555,	low Ti	OL	Apollo 15	0.12	0.09	2.53	1.30	0.047
15379,	low Ti	OL	Apollo 15	0.06		2.54		0.024
15529,	low Ti	OL	Apollo 15	0.12		2.63		0.046
15535,	low Ti	OL	Apollo 15	0.20		2.30		0.087
15536,	low Ti	OL	Apollo 15	0.20	0.03	2.42	6.67	0.083
15545,	low Ti	OL	Apollo 15	0.04	0.01	2.15		0.019
15546,	low Ti	OL	Apollo 15	0.10	0.01	2.83		0.035
15547,	low Ti	OL	Apollo 15	0.36		2.63		0.137
15555,	low Ti	OL	Apollo 15	0.12	0.05	2.24	2.40	0.054
15556,	low Ti	OL	Apollo 15	0.08	0.01	2.68	8.00	0.030
15556,	low Ti	OL	Apollo 15	0.18	0.11	3.02	1.64	0.060
15557,	low Ti	OL	Apollo 15	0.10	0.08	2.65	1.25	0.038
15598,	low Ti	OL	Apollo 15	0.03		2.79		0.011
15607,	low Ti	OL	Apollo 15	0.03	0.04	2.56	0.75	0.012
15622,	low Ti	OL	Apollo 15	0.12		2.53		0.047
15630,	low Ti	OL	Apollo 15	0.09		2.54		0.035
15636,	low Ti	OL	Apollo 15	0.07		2.79		0.025
15647,	low Ti	OL	Apollo 15	0.08	0.08	2.67	1.00	0.030
15668,	low Ti	OL	Apollo 15			2.77		
15672,	low Ti	OL	Apollo 15			2.39		
15674,	low Ti	OL	Apollo 15	0.21		2.79		0.075
15675,	low Ti	OL	Apollo 15	0.54		2.72		0.199
15676,	low Ti	OL	Apollo 15	0.03		2.77		0.011
15683,	low Ti	OL	Apollo 15	0.07	0.05	2.75	1.40	0.025

*Lunar dataset for Hf, W and Mo was compiled from the literature and acquired through different techniques (Morrison, 1970; Taylor et al., 1971; Brunfelt et al., 1971; Klein, 1971; Wänke et al., 1971; Wänke et al., 1972; Newsom and Palme, 1984; Lee et al., 1997; Kleine et al., 2005; Neal, 2001, Münker et al., 2003, Münker, 2010).

Supplementary Table 4.5b - Partition coefficients used for the modeling			
Low-Ti	W	Hf	Mo
Olivine/silicate melt	0.0050	0.0004	0.4700
Orthopyroxene/silicate melt	0.0059	0.0050	0.7200
Clinopyroxene/silicate melt	0.0470	0.0440	2.1800
Pigeonite/silicate melt	0.0059	0.0050	0.7200
Plagioclase/silicate melt	0.0006	0.0002	0.0390
Ilmenite/silicate melt	0.0745	0.4100	5.9100
Metal/silicate	6.2	0	330.0
High-Ti	W	Hf	Mo
Olivine/silicate melt	0.0050	0.0004	0.4700
Orthopyroxene/silicate melt	0.0059	0.0050	0.7200
Clinopyroxene/silicate melt	0.0470	0.0270	2.1800
Pigeonite/silicate melt	0.0059	0.0050	0.7200
Plagioclase/silicate melt	0.0006	0.0002	0.0390
Ilmenite/silicate melt	0.0745	0.4100	5.9100
Metal/silicate	6.2	0	330

Supplementary Table 4.5c - LMO crystallization sequence

CI-chondrite initial abundances	W	Hf	Mo	Bulk-silicate Earth (BSE) initial abundances	W	Hf	Mo	Bulk silicate Moon (BSM) initial abundances	W	Hf	Mo
seq - 1+2	0.00237	0.00104	0.83435	seq - 1+2	0.00030	0.00295	0.02511	seq - 1+2	0.000506	0.004984	0.001780
seq - 1+2 0.01% trapped melt	0.00241	0.00109	0.83437	seq - 1+2 0.01% trapped melt	0.00030	0.00308	0.02511	seq - 1+2 0.01% trapped melt	0.000515	0.005212	0.001780
seq - 1+2 0.025% trapped melt	0.00247	0.00116	0.83439	seq - 1+2 0.025% trapped melt	0.00031	0.00328	0.02511	seq - 1+2 0.025% trapped melt	0.000528	0.005553	0.001780
seq - 1+2 0.05% trapped melt	0.00258	0.00128	0.83444	seq - 1+2 0.05% trapped melt	0.00032	0.00362	0.02511	seq - 1+2 0.05% trapped melt	0.000551	0.006121	0.001780
seq - 1+2 0.075% trapped melt	0.00268	0.00140	0.83449	seq - 1+2 0.075% trapped melt	0.00034	0.00395	0.02511	seq - 1+2 0.075% trapped melt	0.000573	0.006688	0.001780
seq - 1+2 0.1% trapped melt	0.00279	0.00151	0.83453	seq - 1+2 0.1% trapped melt	0.00035	0.00429	0.02512	seq - 1+2 0.1% trapped melt	0.000595	0.007254	0.001780
seq - 1+2 0.125% trapped melt	0.00289	0.00163	0.83458	seq - 1+2 0.125% trapped melt	0.00036	0.00462	0.02512	seq - 1+2 0.125% trapped melt	0.000617	0.007820	0.001780
seq - 1+2 0.15% trapped melt	0.00299	0.00175	0.83463	seq - 1+2 0.15% trapped melt	0.00037	0.00495	0.02512	seq - 1+2 0.15% trapped melt	0.000639	0.008384	0.001780
seq - 1+2 0.2% trapped melt	0.00320	0.00199	0.83472	seq - 1+2 0.2% trapped melt	0.00040	0.00562	0.02512	seq - 1+2 0.2% trapped melt	0.000683	0.009509	0.001781
seq - 1+2 0.275% trapped melt	0.00351	0.00234	0.83486	seq - 1+2 0.275% trapped melt	0.00044	0.00661	0.02512	seq - 1+2 0.275% trapped melt	0.000749	0.011189	0.001781
seq - 1+2 0.375% trapped melt	0.00392	0.00280	0.83504	seq - 1+2 0.375% trapped melt	0.00049	0.00793	0.02513	seq - 1+2 0.375% trapped melt	0.000836	0.013416	0.001781
seq - 1+2 0.5% trapped melt	0.00442	0.00338	0.83527	seq - 1+2 0.5% trapped melt	0.00055	0.00956	0.02514	seq - 1+2 0.5% trapped melt	0.000944	0.016178	0.001782
seq - 1+2 0.75% trapped melt	0.00542	0.00452	0.83574	seq - 1+2 0.75% trapped melt	0.00068	0.01278	0.02515	seq - 1+2 0.75% trapped melt	0.001158	0.021631	0.001783
seq - 1+2 1% trapped melt	0.00640	0.00564	0.83620	seq - 1+2 1% trapped melt	0.00080	0.01595	0.02517	seq - 1+2 1% trapped melt	0.001368	0.026992	0.001784
seq - 1+2 2% trapped melt	0.01018	0.00993	0.83803	seq - 1+2 2% trapped melt	0.00127	0.02810	0.02522	seq - 1+2 2% trapped melt	0.002173	0.047556	0.001788
seq - 1+2 3% trapped melt	0.01372	0.01395	0.83984	seq - 1+2 3% trapped melt	0.00171	0.03949	0.02527	seq - 1+2 3% trapped melt	0.002929	0.066813	0.001792
seq - 1+2 4% trapped melt	0.01704	0.01773	0.84164	seq - 1+2 4% trapped melt	0.00213	0.05017	0.02533	seq - 1+2 4% trapped melt	0.003638	0.084885	0.001795
seq - 1+2 5% trapped melt	0.02016	0.02127	0.84342	seq - 1+2 5% trapped melt	0.00252	0.06021	0.02538	seq - 1+2 5% trapped melt	0.004306	0.101877	0.001799
seq - 1+2 10% trapped melt	0.03338	0.03625	0.85209	seq - 1+2 10% trapped melt	0.00417	0.10259	0.02564	seq - 1+2 10% trapped melt	0.007129	0.173592	0.001818
seq - 1+2 15% trapped melt	0.04360	0.04778	0.86039	seq - 1+2 15% trapped melt	0.00545	0.13523	0.02589	seq - 1+2 15% trapped melt	0.009310	0.228815	0.001835
seq - 1+2 20% trapped melt	0.05172	0.05694	0.86832	seq - 1+2 20% trapped melt	0.00646	0.16113	0.02613	seq - 1+2 20% trapped melt	0.011044	0.272647	0.001852
seq - 1+2 25% trapped melt	0.05834	0.06438	0.87593	seq - 1+2 25% trapped melt	0.00729	0.18219	0.02636	seq - 1+2 25% trapped melt	0.012457	0.308284	0.001869
seq - 1+2 40% trapped melt	0.07243	0.08018	0.89695	seq - 1+2 40% trapped melt	0.00905	0.22692	0.02699	seq - 1+2 40% trapped melt	0.015466	0.383973	0.001913
seq - 1+2 3% trapped melt	0.01372	0.01395	0.83984	seq - 1+2 3% trapped melt	0.00171	0.03949	0.02527	seq - 1+2 3% trapped melt	0.002929	0.066813	0.001792
seq - 1	0.00218	0.00025	0.66263	seq - 1	0.00027	0.00071	0.01994	seq - 1	0.000466	0.001196	0.001414
seq - 1 0.01% trapped melt seq-1+2	0.00222	0.00030	0.66268	seq - 1 0.01% trapped melt seq-1+2	0.00028	0.00084	0.01994	seq - 1 0.01% trapped melt seq-1+2	0.000475	0.001426	0.001414
seq - 1 0.025% trapped melt seq-1+2	0.00229	0.00037	0.66274	seq - 1 0.025% trapped melt seq-1+2	0.00029	0.00105	0.01995	seq - 1 0.025% trapped melt seq-1+2	0.000488	0.001770	0.001414
seq - 1 0.05% trapped melt seq-1+2	0.00239	0.00049	0.66285	seq - 1 0.05% trapped melt seq-1+2	0.00030	0.00138	0.01995	seq - 1 0.05% trapped melt seq-1+2	0.000511	0.002342	0.001414
seq - 1 0.075% trapped melt seq-1+2	0.00250	0.00061	0.66296	seq - 1 0.075% trapped melt seq-1+2	0.00031	0.00172	0.01995	seq - 1 0.075% trapped melt seq-1+2	0.000533	0.002913	0.001414
seq - 1 0.1% trapped melt seq-1+2	0.00260	0.00073	0.66307	seq - 1 0.1% trapped melt seq-1+2	0.00032	0.00206	0.01996	seq - 1 0.1% trapped melt seq-1+2	0.000555	0.003483	0.001415
seq - 1 0.125% trapped melt seq-1+2	0.00270	0.00085	0.66318	seq - 1 0.125% trapped melt seq-1+2	0.00034	0.00240	0.01996	seq - 1 0.125% trapped melt seq-1+2	0.000577	0.004053	0.001415
seq - 1 0.15% trapped melt seq-1+2	0.00281	0.00096	0.66329	seq - 1 0.15% trapped melt seq-1+2	0.00035	0.00273	0.01996	seq - 1 0.15% trapped melt seq-1+2	0.000599	0.004621	0.001415
seq - 1 0.2% trapped melt seq-1+2	0.00301	0.00120	0.66351	seq - 1 0.2% trapped melt seq-1+2	0.00038	0.00340	0.01997	seq - 1 0.2% trapped melt seq-1+2	0.000643	0.005754	0.001415
seq - 1 0.275% trapped melt seq-1+2	0.00332	0.00156	0.66384	seq - 1 0.275% trapped melt seq-1+2	0.00042	0.00440	0.01998	seq - 1 0.275% trapped melt seq-1+2	0.000709	0.007447	0.001416
seq - 1 0.375% trapped melt seq-1+2	0.00373	0.00202	0.66427	seq - 1 0.375% trapped melt seq-1+2	0.00047	0.00573	0.01999	seq - 1 0.375% trapped melt seq-1+2	0.000797	0.009691	0.001417
seq - 1 0.5% trapped melt seq-1+2	0.00424	0.00260	0.66482	seq - 1 0.5% trapped melt seq-1+2	0.00053	0.00737	0.02001	seq - 1 0.5% trapped melt seq-1+2	0.000905	0.012474	0.001418
seq - 1 0.75% trapped melt seq-1+2	0.00524	0.00375	0.66590	seq - 1 0.75% trapped melt seq-1+2	0.00066	0.01062	0.02004	seq - 1 0.75% trapped melt seq-1+2	0.001119	0.017968	0.001421
seq - 1 1% trapped melt seq-1+2	0.00623	0.00488	0.66699	seq - 1 1% trapped melt seq-1+2	0.00078	0.01381	0.02007	seq - 1 1% trapped melt seq-1+2	0.001329	0.023369	0.001423
seq - 1 2% trapped melt seq-1+2	0.01001	0.00921	0.67131	seq - 1 2% trapped melt seq-1+2	0.00125	0.02605	0.02020	seq - 1 2% trapped melt seq-1+2	0.002137	0.044087	0.001432
seq - 1 3% trapped melt seq-1+2	0.01355	0.01326	0.67558	seq - 1 3% trapped melt seq-1+2	0.00169	0.03752	0.02033	seq - 1 3% trapped melt seq-1+2	0.002894	0.063489	0.001441
seq - 1 4% trapped melt seq-1+2	0.01688	0.01706	0.67982	seq - 1 4% trapped melt seq-1+2	0.00211	0.04828	0.02046	seq - 1 4% trapped melt seq-1+2	0.003604	0.081696	0.001450
seq - 1 5% trapped melt seq-1+2	0.02001	0.02064	0.68402	seq - 1 5% trapped melt seq-1+2	0.00250	0.05840	0.02059	seq - 1 5% trapped melt seq-1+2	0.004273	0.098816	0.001459
seq - 1 10% trapped melt seq-1+2	0.03326	0.03572	0.70445	seq - 1 10% trapped melt seq-1+2	0.00416	0.10110	0.02120	seq - 1 10% trapped melt seq-1+2	0.007102	0.171069	0.001503
seq - 1 15% trapped melt seq-1+2	0.04349	0.04734	0.72399	seq - 1 15% trapped melt seq-1+2	0.00544	0.13398	0.02179	seq - 1 15% trapped melt seq-1+2	0.009287	0.226706	0.001544
seq - 1 20% trapped melt seq-1+2	0.05163	0.05656	0.74269	seq - 1 20% trapped melt seq-1+2	0.00645	0.16008	0.02235	seq - 1 20% trapped melt seq-1+2	0.011025	0.270867	0.001584
seq - 1 25% trapped melt seq-1+2	0.05826	0.06406	0.76061	seq - 1 25% trapped melt seq-1+2	0.00728	0.18130	0.02289	seq - 1 25% trapped melt seq-1+2	0.012441	0.306771	0.001623
seq - 1 40% trapped melt seq-1+2	0.07238	0.07999	0.81014	seq - 1 40% trapped melt seq-1+2	0.00905	0.22636	0.02438	seq - 1 40% trapped melt seq-1+2	0.015456	0.383028	0.001728
seq - 1 3% trapped melt* seq-1+2	0.01355	0.01326	0.67558	seq - 1 3% trapped melt* seq-1+2	0.00169	0.03752	0.02033	seq - 1 3% trapped melt* seq-1+2	0.002894	0.063489	0.001441
seq - 2	0.00257	0.00187	1.01510	seq - 2	0.00032	0.00530	0.03055	seq - 2	0.000548	0.008972	0.002165
seq - 2 0.01% trapped melt seq-1+2	0.00261	0.00192	1.01509	seq - 2 0.01% trapped melt seq-1+2	0.00033	0.00544	0.03055	seq - 2 0.01% trapped melt seq-1+2	0.000557	0.009198	0.002165
seq - 2 0.025% trapped melt seq-1+2	0.00267	0.00199	1.01508	seq - 2 0.025% trapped melt seq-1+2	0.00033	0.00564	0.03055	seq - 2 0.025% trapped melt seq-1+2	0.000571	0.009537	0.002165
seq - 2 0.05% trapped melt seq-1+2	0.00278	0.00211	1.01506	seq - 2 0.05% trapped melt seq-1+2	0.00035	0.00597	0.03055	seq - 2 0.05% trapped melt seq-1+2	0.000593	0.010100	0.002165
seq - 2 0.075% trapped melt seq-1+2	0.00288	0.00223	1.01504	seq - 2 0.075% trapped melt seq-1+2	0.00036	0.00630	0.03055	seq - 2 0.075% trapped melt seq-1+2	0.000615	0.010663	0.002165
seq - 2 0.1% trapped melt seq-1+2	0.00298	0.00234	1.01502	seq - 2 0.1% trapped melt seq-1+2	0.00037	0.00663	0.03055	seq - 2 0.1% trapped melt seq-1+2	0.000637	0.011224	0.002165
seq - 2 0.125% trapped melt seq-1+2	0.00309	0.00246	1.01500	seq - 2 0.125% trapped melt seq-1+2	0.00039	0.00696	0.03055	seq - 2 0.125% trapped melt seq-1+2	0.000659	0.011785	0.002165

Supplementary Table 4.5c - LMO crystallization sequence

seq - 2 0.15% trapped melt seq-1+2	0.00319	0.00258	1.01498	seq - 2 0.15% trapped melt seq-1+2	0.00040	0.00730	0.03055	seq - 2 0.15% trapped melt seq-1+2	0.000681	0.012344	0.002165
seq - 2 0.2% trapped melt seq-1+2	0.00340	0.00281	1.01494	seq - 2 0.2% trapped melt seq-1+2	0.00042	0.00795	0.03054	seq - 2 0.2% trapped melt seq-1+2	0.000725	0.013461	0.002165
seq - 2 0.275% trapped melt seq-1+2	0.00370	0.00316	1.01488	seq - 2 0.275% trapped melt seq-1+2	0.00046	0.00894	0.03054	seq - 2 0.275% trapped melt seq-1+2	0.000791	0.015128	0.002165
seq - 2 0.375% trapped melt seq-1+2	0.00411	0.00362	1.01480	seq - 2 0.375% trapped melt seq-1+2	0.00051	0.01025	0.03054	seq - 2 0.375% trapped melt seq-1+2	0.000878	0.017337	0.002165
seq - 2 0.5% trapped melt seq-1+2	0.00461	0.00419	1.01470	seq - 2 0.5% trapped melt seq-1+2	0.00058	0.01187	0.03054	seq - 2 0.5% trapped melt seq-1+2	0.000985	0.020077	0.002165
seq - 2 0.75% trapped melt seq-1+2	0.00561	0.00532	1.01450	seq - 2 0.75% trapped melt seq-1+2	0.00070	0.01506	0.03053	seq - 2 0.75% trapped melt seq-1+2	0.001199	0.025487	0.002164
seq - 2 1% trapped melt seq-1+2	0.00659	0.00643	1.01431	seq - 2 1% trapped melt seq-1+2	0.00082	0.01821	0.03053	seq - 2 1% trapped melt seq-1+2	0.001408	0.030806	0.002164
seq - 2 2% trapped melt seq-1+2	0.01036	0.01069	1.01352	seq - 2 2% trapped melt seq-1+2	0.00129	0.03026	0.03050	seq - 2 2% trapped melt seq-1+2	0.002212	0.051207	0.002162
seq - 2 3% trapped melt seq-1+2	0.01389	0.01468	1.01275	seq - 2 3% trapped melt seq-1+2	0.00174	0.04155	0.03048	seq - 2 3% trapped melt seq-1+2	0.002966	0.070313	0.002160
seq - 2 4% trapped melt seq-1+2	0.01720	0.01843	1.01198	seq - 2 4% trapped melt seq-1+2	0.00215	0.05215	0.03046	seq - 2 4% trapped melt seq-1+2	0.003674	0.088242	0.002159
seq - 2 5% trapped melt seq-1+2	0.02032	0.02195	1.01122	seq - 2 5% trapped melt seq-1+2	0.00254	0.06211	0.03043	seq - 2 5% trapped melt seq-1+2	0.004340	0.105100	0.002157
seq - 2 10% trapped melt seq-1+2	0.03352	0.03680	1.00751	seq - 2 10% trapped melt seq-1+2	0.00419	0.10416	0.03032	seq - 2 10% trapped melt seq-1+2	0.007157	0.176248	0.002149
seq - 2 15% trapped melt seq-1+2	0.04371	0.04825	1.00396	seq - 2 15% trapped melt seq-1+2	0.00546	0.13654	0.03021	seq - 2 15% trapped melt seq-1+2	0.009333	0.231035	0.002142
seq - 2 20% trapped melt seq-1+2	0.05181	0.05733	1.00057	seq - 2 20% trapped melt seq-1+2	0.00648	0.16224	0.03011	seq - 2 20% trapped melt seq-1+2	0.011064	0.274521	0.002134
seq - 2 25% trapped melt seq-1+2	0.05842	0.06471	0.99732	seq - 2 25% trapped melt seq-1+2	0.00730	0.18313	0.03001	seq - 2 25% trapped melt seq-1+2	0.012474	0.309877	0.002128
seq - 2 40% trapped melt seq-1+2	0.07248	0.08039	0.98833	seq - 2 40% trapped melt seq-1+2	0.00906	0.22751	0.02974	seq - 2 40% trapped melt seq-1+2	0.015477	0.384968	0.002108
seq - 2 3% trapped melt seq-1+2	0.01389	0.01468	1.01275	seq - 2 3% trapped melt seq-1+2	0.00174	0.04155	0.03048	seq - 2 3% trapped melt seq-1+2	0.002966	0.070313	0.002160
seq - 3 2% plag using *	0.00260	0.00111	0.92987	seq - 3 2% plag using *	0.00033	0.00315	0.02798	seq - 3 2% plag using *	0.000556	0.005333	0.001984
seq - 3 2% plag - 1% trapped melt	0.00738	0.00649	0.93529	seq - 3 2% plag - 1% trapped melt	0.00092	0.01836	0.02815	seq - 3 2% plag - 1% trapped melt	0.001575	0.031072	0.001995
seq - 3 2% plag - 2% trapped melt	0.01213	0.01184	0.94070	seq - 3 2% plag - 2% trapped melt	0.00152	0.03351	0.02831	seq - 3 2% plag - 2% trapped melt	0.002590	0.056696	0.002007
seq - 3 2% plag - 4% trapped melt	0.02157	0.02247	0.95145	seq - 3 2% plag - 4% trapped melt	0.00270	0.06359	0.02863	seq - 3 2% plag - 4% trapped melt	0.004606	0.107597	0.002030
seq - 3 2% plag - 8% trapped melt	0.04020	0.04344	0.97273	seq - 3 2% plag - 8% trapped melt	0.00502	0.12294	0.02927	seq - 3 2% plag - 8% trapped melt	0.008584	0.208031	0.002075
seq - 3 2% plag - 10% trapped melt	0.04939	0.05379	0.98326	seq - 3 2% plag - 10% trapped melt	0.00617	0.15222	0.02959	seq - 3 2% plag - 10% trapped melt	0.010546	0.257572	0.002098
seq - 3 2% plag - 15% trapped melt	0.07200	0.07925	1.00929	seq - 3 2% plag - 15% trapped melt	0.00900	0.22427	0.03037	seq - 3 2% plag - 15% trapped melt	0.015375	0.379485	0.002153
seq - 3 2% plag - 3% trapped melt	0.01686	0.01717	0.94608	seq - 3 2% plag - 3% trapped melt	0.00211	0.04858	0.02847	seq - 3 2% plag - 3% trapped melt	0.003600	0.082204	0.002018
seq - 3 plag + 0% trapped melt	0.00006	0.00015	0.06308	seq - 3 plag + 0% trapped melt	0.00001	0.00043	0.00190	seq - 3 plag + 0% trapped melt	0.000012	0.000724	0.000135
seq - 3 plag + 1% trapped melt	0.00486	0.00554	0.07850	seq - 3 plag + 1% trapped melt	0.00061	0.01567	0.00236	seq - 3 plag + 1% trapped melt	0.001038	0.026520	0.000167
seq - 3 plag + 2% trapped melt	0.00965	0.01090	0.09387	seq - 3 plag + 2% trapped melt	0.00121	0.03085	0.00283	seq - 3 plag + 2% trapped melt	0.002060	0.052200	0.000200
seq - 3 plag + 4% trapped melt	0.01915	0.02155	0.12447	seq - 3 plag + 4% trapped melt	0.00239	0.06100	0.00375	seq - 3 plag + 4% trapped melt	0.004089	0.103213	0.000266
seq - 3 plag + 8% trapped melt	0.03790	0.04257	0.18511	seq - 3 plag + 8% trapped melt	0.00474	0.12048	0.00557	seq - 3 plag + 8% trapped melt	0.008093	0.203867	0.000395
seq - 3 plag + 10% trapped melt	0.04715	0.05294	0.21514	seq - 3 plag + 10% trapped melt	0.00589	0.14982	0.00647	seq - 3 plag + 10% trapped melt	0.010068	0.253517	0.000459
seq - 3 plag + 15% trapped melt	0.06991	0.07845	0.28942	seq - 3 plag + 15% trapped melt	0.00874	0.22203	0.00871	seq - 3 plag + 15% trapped melt	0.014928	0.375698	0.000617
seq - 3 plag + 3% trapped melt	0.01441	0.01624	0.10920	seq - 3 plag + 3% trapped melt	0.00180	0.04596	0.00329	seq - 3 plag + 3% trapped melt	0.003077	0.077764	0.000233
seq - 4 2 % plag using *	0.00688	0.02929	1.21874	seq - 4 2 % plag using *	0.00086	0.08289	0.03668	seq - 4 2 % plag using *	0.001468	0.140256	0.002600
seq - 4 2 % plag - 0.1% trapped melt	0.00782	0.03031	1.21970	seq - 4 2 % plag - 0.1% trapped melt	0.00098	0.08579	0.03671	seq - 4 2 % plag - 0.1% trapped melt	0.001671	0.145161	0.002602
seq - 4 2 % plag - 1% trapped melt	0.01632	0.03948	1.22832	seq - 4 2 % plag - 1% trapped melt	0.00204	0.11174	0.03697	seq - 4 2 % plag - 1% trapped melt	0.003484	0.189080	0.002620
seq - 4 2 % plag - 2% trapped melt	0.02566	0.04958	1.23782	seq - 4 2 % plag - 2% trapped melt	0.00321	0.14031	0.03725	seq - 4 2 % plag - 2% trapped melt	0.005480	0.237411	0.002641
seq - 4 2 % plag - 4% trapped melt	0.04406	0.06946	1.25662	seq - 4 2 % plag - 4% trapped melt	0.00551	0.19657	0.03782	seq - 4 2 % plag - 4% trapped melt	0.009410	0.332617	0.002681
seq - 4 2 % plag - 8% trapped melt	0.07976	0.10803	1.29337	seq - 4 2 % plag - 8% trapped melt	0.00997	0.30574	0.03892	seq - 4 2 % plag - 8% trapped melt	0.017032	0.517338	0.002759
seq - 4 2 % plag - 16% trapped melt	0.14690	0.18065	1.36364	seq - 4 2 % plag - 16% trapped melt	0.01836	0.51124	0.04104	seq - 4 2 % plag - 16% trapped melt	0.031370	0.865065	0.002909
seq - 4 2 % plag - 3% trapped melt	0.03491	0.05957	1.24725	seq - 4 2 % plag - 3% trapped melt	0.00436	0.16858	0.03754	seq - 4 2 % plag - 3% trapped melt	0.007455	0.285255	0.002661
seq - 4 plag + 0% trapped melt	0.00012	0.00030	0.10077	seq - 4 plag + 0% trapped melt	0.00001	0.00085	0.00303	seq - 4 plag + 0% trapped melt	0.000025	0.001433	0.000215
seq - 4 plag + 0.1% trapped melt	0.00107	0.00137	0.10322	seq - 4 plag + 0.1% trapped melt	0.00013	0.00387	0.00311	seq - 4 plag + 0.1% trapped melt	0.000229	0.006546	0.000220
seq - 4 plag + 1% trapped melt	0.00966	0.01093	0.12518	seq - 4 plag + 1% trapped melt	0.00121	0.03093	0.00377	seq - 4 plag + 1% trapped melt	0.002062	0.052335	0.000267
seq - 4 plag + 2% trapped melt	0.01910	0.02145	0.14943	seq - 4 plag + 2% trapped melt	0.00239	0.06071	0.00450	seq - 4 plag + 2% trapped melt	0.004079	0.102726	0.000319
seq - 4 plag + 4% trapped melt	0.03770	0.04218	0.19746	seq - 4 plag + 4% trapped melt	0.00471	0.11938	0.00594	seq - 4 plag + 4% trapped melt	0.008052	0.201998	0.000421
seq - 4 plag + 8% trapped melt	0.07379	0.08241	0.29161	seq - 4 plag + 8% trapped melt	0.00922	0.23322	0.00878	seq - 4 plag + 8% trapped melt	0.015756	0.394635	0.000622
seq - 4 plag + 16% trapped melt	0.14166	0.15816	0.47257	seq - 4 plag + 16% trapped melt	0.01771	0.44759	0.01422	seq - 4 plag + 16% trapped melt	0.030251	0.757372	0.001008
seq - 4 plag + 3% trapped melt	0.02845	0.03187	0.17353	seq - 4 plag + 3% trapped melt	0.00356	0.09019	0.00522	seq - 4 plag + 3% trapped melt	0.006076	0.152612	0.000370
seq - 5 2 % plag using *	0.08966	0.34968	5.69385	seq - 5 2 % plag using *	0.01121	0.98961	0.17136	seq - 5 2 % plag using *	0.019147	1.674516	0.012147
seq - 5 2 % plag - 0.1% trapped melt	0.09355	0.35326	5.69244	seq - 5 2 % plag - 0.1% trapped melt	0.01169	0.99975	0.17131	seq - 5 2 % plag - 0.1% trapped melt	0.019976	1.691674	0.012144
seq - 5 2 % plag - 0.5% trapped melt	0.10899	0.36752	5.68682	seq - 5 2 % plag - 0.5% trapped melt	0.01362	1.04008	0.17114	seq - 5 2 % plag - 0.5% trapped melt	0.023274	1.759931	0.012132
seq - 5 2 % plag - 1% trapped melt	0.12810	0.38516	5.67977	seq - 5 2 % plag - 1% trapped melt	0.01601	1.09001	0.17093	seq - 5 2 % plag - 1% trapped melt	0.027355	1.844413	0.012117
seq - 5 2 % plag - 2% trapped melt	0.16567	0.41986	5.66560	seq - 5 2 % plag - 2% trapped melt	0.02071	1.18824	0.17051	seq - 5 2 % plag - 2% trapped melt	0.035378	2.010617	0.012086
seq - 5 2 % plag - 3% trapped melt	0.20240	0.45382	5.65135	seq - 5 2 % plag - 3% trapped melt	0.02530	1.28432	0.17008	seq - 5 2 % plag - 3% trapped melt	0.043221	2.173210	0.012056
seq - 5 2 % plag - 8% trapped melt	0.37402	0.61283	5.57880	seq - 5 2 % plag - 8% trapped melt	0.04675	1.73433	0.16789	seq - 5 2 % plag - 8% trapped melt	0.079870	2.934658	0.011901

Supplementary Table 4.5c - LMO crystallization sequence

seq - 5 2 % plag - 16% trapped melt	0.61109	0.83352	5.45804	seq - 5 2 % plag - 16% trapped melt	0.07639	2.35890	0.16426	seq - 5 2 % plag - 16% trapped melt	0.130493	3.991504	0.011644
seq - 5 2 % plag - 20% trapped melt	0.71439	0.93012	5.39541	seq - 5 2 % plag - 20% trapped melt	0.08930	2.63228	0.16237	seq - 5 2 % plag - 20% trapped melt	0.152553	4.454097	0.011510
seq - 5 plag + 0% trapped melt	0.00049	0.00121	0.10900	seq - 5 plag + 0% trapped melt	0.00006	0.00341	0.00328	seq - 5 plag + 0% trapped melt	0.000105	0.005777	0.000233
seq - 5 plag + 0.1% trapped melt	0.00456	0.00551	0.11171	seq - 5 plag + 0.1% trapped melt	0.00057	0.01559	0.00336	seq - 5 plag + 0.1% trapped melt	0.000974	0.026374	0.000238
seq - 5 plag + 0.5% trapped melt	0.02076	0.02262	0.12259	seq - 5 plag + 0.5% trapped melt	0.00260	0.06402	0.00369	seq - 5 plag + 0.5% trapped melt	0.004433	0.108325	0.000262
seq - 5 plag + 1% trapped melt	0.04081	0.04381	0.13622	seq - 5 plag + 1% trapped melt	0.00510	0.12398	0.00410	seq - 5 plag + 1% trapped melt	0.008714	0.209790	0.000291
seq - 5 plag + 2% trapped melt	0.08022	0.08552	0.16357	seq - 5 plag + 2% trapped melt	0.01003	0.24201	0.00492	seq - 5 plag + 2% trapped melt	0.017131	0.409514	0.000349
seq - 5 plag + 3% trapped melt	0.11876	0.12635	0.19108	seq - 5 plag + 3% trapped melt	0.01485	0.35757	0.00575	seq - 5 plag + 3% trapped melt	0.025361	0.605039	0.000408
seq - 5 plag + 8% trapped melt	0.29895	0.31799	0.33080	seq - 5 plag + 8% trapped melt	0.03737	0.89992	0.00996	seq - 5 plag + 8% trapped melt	0.063839	1.522755	0.000706
seq - 5 plag + 16% trapped melt	0.54820	0.58533	0.56223	seq - 5 plag + 16% trapped melt	0.06852	1.65650	0.01692	seq - 5 plag + 16% trapped melt	0.117063	2.802968	0.001199
seq - 5 plag + 20% trapped melt	0.65696	0.70294	0.68172	seq - 5 plag + 20% trapped melt	0.08212	1.98936	0.02052	seq - 5 plag + 20% trapped melt	0.140288	3.366202	0.001454
KREEP seq - 5 2 % plag using *	15.66054	15.76587	1.38752	KREEP seq - 5 2 % plag using *	1.95757	44.61816	0.04176	KREEP seq - 5 2 % plag using *	3.344177	75.498553	0.002960
KREEP seq - 5 2 % plag - 0.1% trapped melt	15.62507	15.73166	1.38890	KREEP seq - 5 2 % plag - 0.1% trapped melt	1.95313	44.52135	0.04180	KREEP seq - 5 2 % plag - 0.1% trapped melt	3.336604	75.334727	0.002963
KREEP seq - 5 2 % plag - 0.5% trapped melt	15.48401	15.59556	1.39441	KREEP seq - 5 2 % plag - 0.5% trapped melt	1.93550	44.13617	0.04196	KREEP seq - 5 2 % plag - 0.5% trapped melt	3.306481	74.682972	0.002975
KREEP seq - 5 2 % plag - 1% trapped melt	15.30947	15.42709	1.40134	KREEP seq - 5 2 % plag - 1% trapped melt	1.91368	43.65939	0.04217	KREEP seq - 5 2 % plag - 1% trapped melt	3.269209	73.876201	0.002989
KREEP seq - 5 2 % plag - 2% trapped melt	14.96627	15.09558	1.41529	KREEP seq - 5 2 % plag - 2% trapped melt	1.87078	42.72121	0.04259	KREEP seq - 5 2 % plag - 2% trapped melt	3.195922	72.288711	0.003019
KREEP seq - 5 2 % plag - 3% trapped melt	14.63076	14.77120	1.42938	KREEP seq - 5 2 % plag - 3% trapped melt	1.82885	41.80320	0.04302	KREEP seq - 5 2 % plag - 3% trapped melt	3.124277	70.735334	0.003049
KREEP seq - 5 2 % plag - 8% trapped melt	13.06274	13.25090	1.50195	KREEP seq - 5 2 % plag - 8% trapped melt	1.63284	37.50068	0.04520	KREEP seq - 5 2 % plag - 8% trapped melt	2.789438	63.455030	0.003204
KREEP seq - 5 2 % plag - 16% trapped melt	10.89586	11.13712	1.62582	KREEP seq - 5 2 % plag - 16% trapped melt	1.36198	31.51857	0.04893	KREEP seq - 5 2 % plag - 16% trapped melt	2.326720	53.332688	0.003468
KREEP seq - 5 2 % plag - 20% trapped melt	9.95120	10.21026	1.69153	KREEP seq - 5 2 % plag - 20% trapped melt	1.24390	28.89550	0.05091	KREEP seq - 5 2 % plag - 20% trapped melt	2.124995	48.894182	0.003609

Supplementary Table 4.5d- Aggregate modal partial melting

Assuming CI-chondrite initial abundances

	Low-Ti				High-Ti		
F	W	Hf	Mo	F	W	Hf	Mo
0.001	2.290274241	4.2662683	1.40370563	0.001	1.030864	4.536001	1.153742232
0.002	2.115491117	3.70489295	1.40325658	0.002	0.993649	4.192104	1.153736545
0.003	1.958401886	3.24177254	1.40280741	0.003	0.958203	3.88279	1.153730854
0.004	1.817001812	2.85760692	1.40235813	0.004	0.924432	3.604169	1.153725159
0.005	1.689527182	2.53713002	1.40190875	0.005	0.892249	3.352812	1.15371946
0.006	1.574425283	2.26823363	1.40145926	0.006	0.861571	3.125699	1.153713758
0.007	1.470328196	2.04128652	1.40100966	0.007	0.832317	2.920167	1.153708052
0.008	1.376029933	1.84860444	1.40055995	0.008	0.804415	2.733866	1.153702342
0.009	1.290466469	1.68403697	1.40011013	0.009	0.777794	2.56472	1.153696628
0.01	1.212698302	1.54264493	1.39966021	0.01	0.752387	2.410896	1.15369091
0.011	1.141895217	1.42044797	1.39921017	0.011	0.728131	2.270773	1.153685189
0.012	1.077322966	1.31422681	1.39876003	0.012	0.704969	2.142914	1.153679464
0.013	1.018331621	1.2213679	1.39830977	0.013	0.682842	2.026047	1.153673735
0.014	0.964345387	1.13974115	1.39785941	0.014	0.661699	1.919046	1.153668002
0.015	0.914853685	1.06760357	1.39740894	0.015	0.64149	1.820909	1.153662265
0.016	0.869403342	1.003523	1.39695835	0.016	0.622166	1.730748	1.153656525
0.017	0.827591757	0.94631774	1.39650766	0.017	0.603684	1.647772	1.153650781
0.018	0.789060903	0.89500861	1.39605686	0.018	0.586001	1.571279	1.153645032
0.019	0.753492073	0.84878062	1.39560595	0.019	0.569076	1.500641	1.15363928
0.02	0.720601272	0.80695256	1.39515493	0.02	0.552873	1.4353	1.153633524
0.021	0.690135166	0.76895246	1.39470379	0.021	0.537354	1.374758	1.153627765
0.022	0.661867531	0.73429798	1.39425255	0.022	0.522487	1.318569	1.153622001
0.023	0.635596129	0.70258057	1.3938012	0.023	0.508239	1.266334	1.153616234
0.024	0.611139962	0.67345267	1.39334974	0.024	0.494579	1.217696	1.153610462
0.025	0.588336859	0.64661729	1.39289816	0.025	0.48148	1.172336	1.153604687
0.026	0.567041342	0.62181964	1.39244648	0.026	0.468913	1.129966	1.153598908
0.027	0.547122762	0.59884014	1.39199468	0.027	0.456853	1.090328	1.153593125
0.028	0.528463642	0.57748883	1.39154278	0.028	0.445275	1.05319	1.153587338
0.029	0.510958223	0.5576007	1.39109076	0.029	0.434157	1.018342	1.153581547
0.03	0.494511174	0.53903186	1.39063863	0.03	0.423476	0.985597	1.153575752
0.035	0.425412614	0.46206009	1.38837631	0.035	0.375941	0.847977	1.153546719
0.04	0.372810166	0.40430849	1.3861112	0.04	0.336644	0.743169	1.153517587
0.045	0.33160246	0.3593864	1.38384327	0.045	0.303871	0.661043	1.153488356
0.05	0.298523856	0.32344795	1.38157252	0.05	0.276301	0.59511	1.153459024
0.055	0.271416402	0.29404363	1.37929893	0.055	0.25291	0.541075	1.153429591
0.06	0.248810244	0.26954	1.37702247	0.06	0.232899	0.49601	1.153400056
0.065	0.229675542	0.24880615	1.37474315	0.065	0.215644	0.457865	1.153370418
0.075	0.199054433	0.215632	1.37017581	0.075	0.187532	0.396822	1.15331083
0.1	0.149291166	0.161724	1.35870609	0.1	0.140982	0.297617	1.153160004
0.2	0.074645585	0.080862	1.31205446	0.2	0.070515	0.148808	1.152528078
0.3	0.049763723	0.053908	1.26404899	0.3	0.04701	0.099206	1.151843783

Assuming bulk-silicate Earth (BSE) initial abundances

	Low-Ti				High-Ti		
F	W*	Hf	Mo	F	W*	Hf	Mo
0.001	0.28628428	12.0737396	0.04224439	0.001	0.128858	12.8371	0.034721763
0.002	0.26443639	10.485021	0.04223087	0.002	0.124206	11.86385	0.034721592
0.003	0.244800236	9.17436849	0.04221736	0.003	0.119775	10.98848	0.034721421
0.004	0.227125227	8.08716176	0.04220383	0.004	0.115554	10.19997	0.034721249

Supplementary Table 4.5d- Aggregate modal partial melting

0.005	0.211190898	7.18019706	0.04219031	0.005	0.111531	9.488616	0.034721078
0.006	0.19680316	6.41920766	0.04217678	0.006	0.107696	8.845875	0.034720906
0.007	0.183791024	5.77693668	0.04216325	0.007	0.10404	8.264209	0.034720734
0.008	0.172003742	5.23163735	0.04214972	0.008	0.100552	7.736968	0.034720562
0.009	0.161308309	4.76590369	0.04213618	0.009	0.097224	7.258278	0.034720391
0.01	0.151587288	4.36575757	0.04212264	0.01	0.094048	6.82295	0.034720218
0.011	0.142736902	4.01993444	0.0421091	0.011	0.091016	6.426394	0.034720046
0.012	0.134665371	3.71932358	0.04209555	0.012	0.088121	6.064546	0.034719874
0.013	0.127291453	3.4565285	0.042082	0.013	0.085355	5.733809	0.034719702
0.014	0.120543173	3.22552097	0.04206845	0.014	0.082712	5.43099	0.034719529
0.015	0.114356711	3.02136822	0.04205489	0.015	0.080186	5.153259	0.034719356
0.016	0.108675418	2.84001719	0.04204133	0.016	0.077771	4.898098	0.034719184
0.017	0.10344897	2.67812365	0.04202777	0.017	0.075461	4.663273	0.034719011
0.018	0.098632613	2.53291637	0.0420142	0.018	0.07325	4.446793	0.034718838
0.019	0.094186509	2.402089	0.04200063	0.019	0.071135	4.246885	0.034718665
0.02	0.090075159	2.28371363	0.04198706	0.02	0.069109	4.061968	0.034718491
0.021	0.086266896	2.17617156	0.04197348	0.021	0.067169	3.89063	0.034718318
0.022	0.082733441	2.07809776	0.0419599	0.022	0.065311	3.731612	0.034718145
0.023	0.079449516	1.98833601	0.04194631	0.023	0.06353	3.583785	0.034717971
0.024	0.076392495	1.90590266	0.04193273	0.024	0.061822	3.446138	0.034717797
0.025	0.073542107	1.82995729	0.04191914	0.025	0.060185	3.317766	0.034717624
0.026	0.070880168	1.75977876	0.04190554	0.026	0.058614	3.197857	0.03471745
0.027	0.068390345	1.6947457	0.04189195	0.027	0.057107	3.085679	0.034717276
0.028	0.066057955	1.6343205	0.04187835	0.028	0.055659	2.980576	0.034717101
0.029	0.063869778	1.57803617	0.04186474	0.029	0.05427	2.881956	0.034716927
0.03	0.061813897	1.52548548	0.04185114	0.03	0.052934	2.789285	0.034716753
0.035	0.053176577	1.30765175	0.04178305	0.035	0.046993	2.399816	0.034715879
0.04	0.046601271	1.144212	0.04171489	0.04	0.04208	2.103202	0.034715002
0.045	0.041450308	1.01708037	0.04164663	0.045	0.037984	1.870784	0.034714123
0.05	0.037315482	0.91537289	0.04157829	0.05	0.034538	1.684189	0.03471324
0.055	0.03392705	0.83215727	0.04150987	0.055	0.031614	1.531267	0.034712354
0.06	0.03110128	0.76281085	0.04144136	0.06	0.029112	1.403732	0.034711465
0.065	0.028709443	0.7041331	0.04137276	0.065	0.026956	1.295781	0.034710573
0.075	0.024881804	0.61024869	0.04123531	0.075	0.023441	1.123024	0.03470878
0.1	0.018661396	0.45768651	0.04089013	0.1	0.017623	0.84227	0.034704241
0.2	0.009330698	0.22884326	0.03948615	0.2	0.008814	0.421135	0.034685223
0.3	0.006220465	0.15256217	0.03804143	0.3	0.005876	0.280757	0.034664629

Assuming BSM initial abundances

	Low-Ti				High-Ti		
F	W	Hf	Mo	F	W	Hf	Mo
0.001	0.489068979	20.4300172	0.0029945	0.001	0.220132	21.72169	0.002461259
0.002	0.451745499	17.7417409	0.00299354	0.002	0.212185	20.07486	0.002461247
0.003	0.418200403	15.5239812	0.00299259	0.003	0.204616	18.59364	0.002461235
0.004	0.388005595	13.6843149	0.00299163	0.004	0.197405	17.2594	0.002461223
0.005	0.36078445	12.1496367	0.00299067	0.005	0.190532	16.05572	0.002461211
0.006	0.336205399	10.8619638	0.00298971	0.006	0.183981	14.96814	0.002461198
0.007	0.313976334	9.77517488	0.00298875	0.007	0.177734	13.9839	0.002461186
0.008	0.293839725	8.85247196	0.00298779	0.008	0.171776	13.09175	0.002461174
0.009	0.275568361	8.0644024	0.00298683	0.009	0.166091	12.28176	0.002461162
0.01	0.258961617	7.38731374	0.00298587	0.01	0.160666	11.54514	0.00246115
0.011	0.243842208	6.80214521	0.00298491	0.011	0.155486	10.87412	0.002461137

Supplementary Table 4.5d- Aggregate modal partial melting

0.012	0.230053342	6.29348051	0.00298395	0.012	0.15054	10.26184	0.002461125
0.013	0.217456232	5.84880403	0.00298299	0.013	0.145815	9.702198	0.002461113
0.014	0.205927921	5.45791538	0.00298203	0.014	0.1413	9.189798	0.002461101
0.015	0.195359381	5.11246779	0.00298107	0.015	0.136985	8.719847	0.002461089
0.016	0.185653839	4.80560307	0.00298011	0.016	0.132858	8.28809	0.002461076
0.017	0.176725323	4.53166244	0.00297915	0.017	0.128912	7.890741	0.002461064
0.018	0.16849738	4.2859567	0.00297818	0.018	0.125136	7.524434	0.002461052
0.019	0.160901953	4.06458325	0.00297722	0.019	0.121521	7.186169	0.00246104
0.02	0.153878397	3.86427986	0.00297626	0.02	0.118061	6.87327	0.002461027
0.021	0.147372613	3.68230755	0.0029753	0.021	0.114748	6.583349	0.002461015
0.022	0.141336296	3.51635653	0.00297434	0.022	0.111573	6.314274	0.002461003
0.023	0.135726257	3.36447035	0.00297337	0.023	0.10853	6.064134	0.00246099
0.024	0.130503846	3.2249846	0.00297241	0.024	0.105613	5.831222	0.002460978
0.025	0.125634433	3.09647717	0.00297145	0.025	0.102816	5.614004	0.002460966
0.026	0.121086953	2.97772783	0.00297048	0.026	0.100132	5.411105	0.002460953
0.027	0.116833507	2.86768516	0.00296952	0.027	0.097557	5.221289	0.002460941
0.028	0.112849007	2.76543946	0.00296856	0.028	0.095085	5.043444	0.002460929
0.029	0.10911087	2.67020055	0.00296759	0.029	0.092711	4.876568	0.002460916
0.03	0.10559874	2.58127935	0.00296663	0.03	0.09043	4.719759	0.002460904
0.035	0.090843319	2.21268213	0.0029618	0.035	0.080279	4.060737	0.002460842
0.04	0.079610504	1.93612516	0.00295697	0.04	0.071887	3.558835	0.00246078
0.045	0.070810942	1.72100528	0.00295213	0.045	0.064889	3.16556	0.002460718
0.05	0.063747282	1.54890569	0.00294729	0.05	0.059002	2.849823	0.002460655
0.055	0.057958711	1.40809625	0.00294244	0.055	0.054007	2.591062	0.002460592
0.06	0.053131354	1.29075493	0.00293758	0.06	0.049734	2.375261	0.002460529
0.065	0.049045298	1.19146609	0.00293272	0.065	0.046049	2.192595	0.002460466
0.075	0.042506415	1.03260395	0.00292297	0.075	0.040046	1.900273	0.002460339
0.1	0.031879884	0.77445296	0.00289851	0.1	0.030106	1.425208	0.002460017
0.2	0.015939943	0.38722648	0.00279898	0.2	0.015058	0.712604	0.002458669
0.3	0.010626628	0.25815099	0.00269657	0.3	0.010039	0.475069	0.002457209

A.2 Supplementary figures

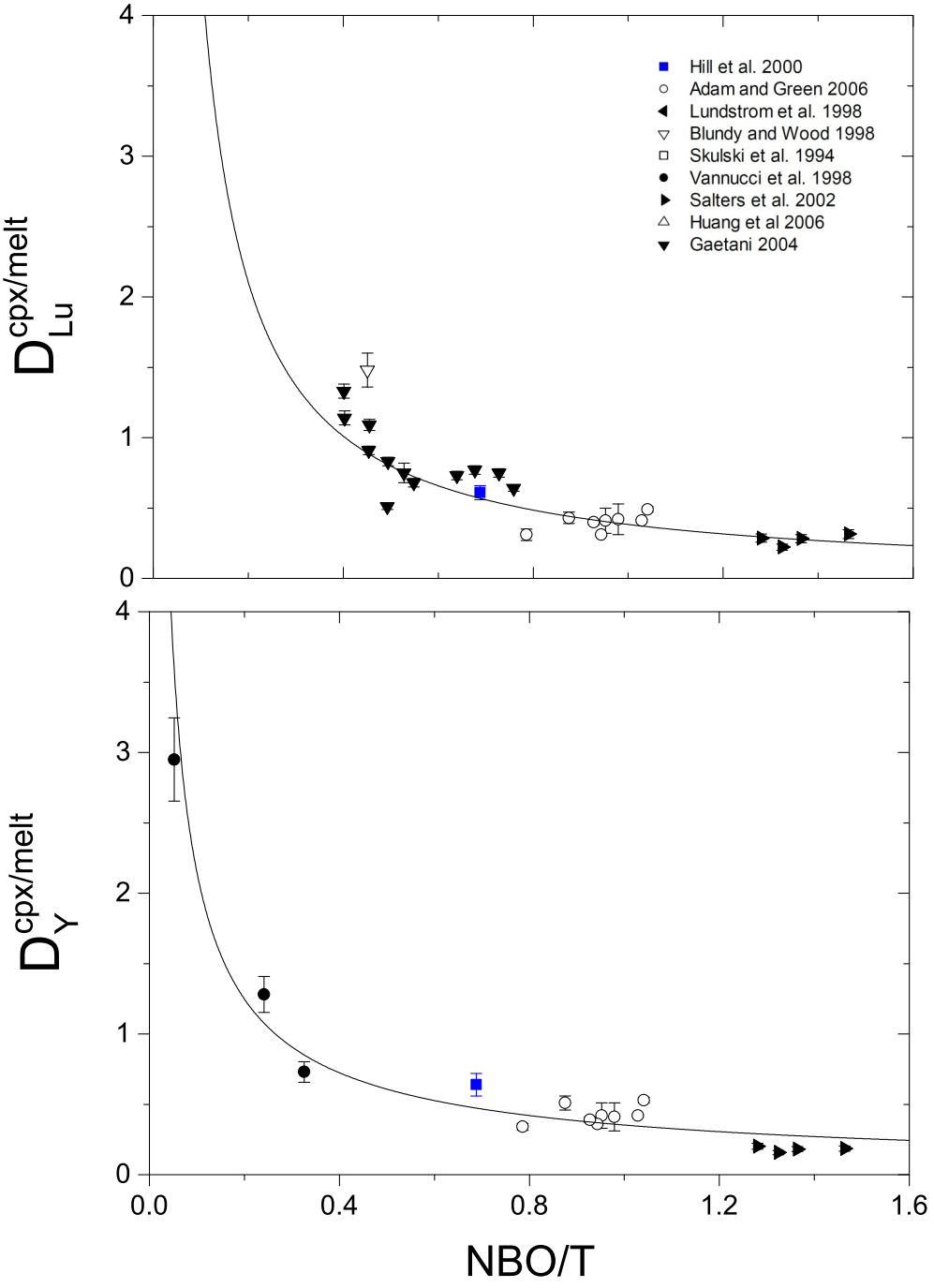

Supplementary Figure 2.1 - $D^{cpx/melt}_{Lu, Y}$ values of Lu (a) and Y (b) plotted as a function of NBO/T. Black lines represent regressions of the reported data using an exponential function. Error bars are 1σ standard deviation.

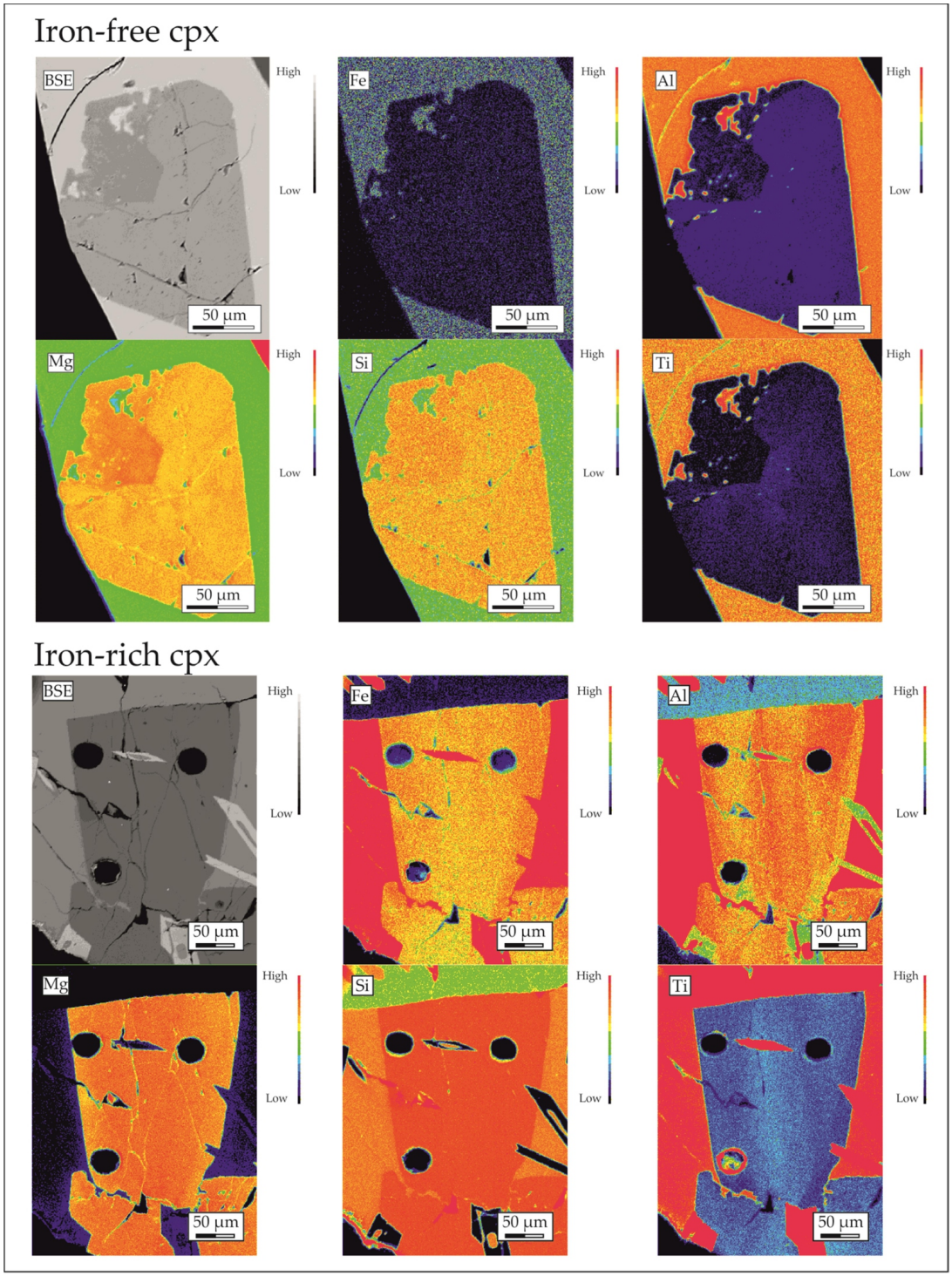

Supplementary Figure 3.1 – Back-scattered electron (BSE) images and compositional maps (Fe, Al, Mg, Si and Ti) of two clinopyroxene grains from the iron-poor (upper part) and iron-rich (lower part) compositions. When zonation was observed only clear areas close to the silicate melt were measured.

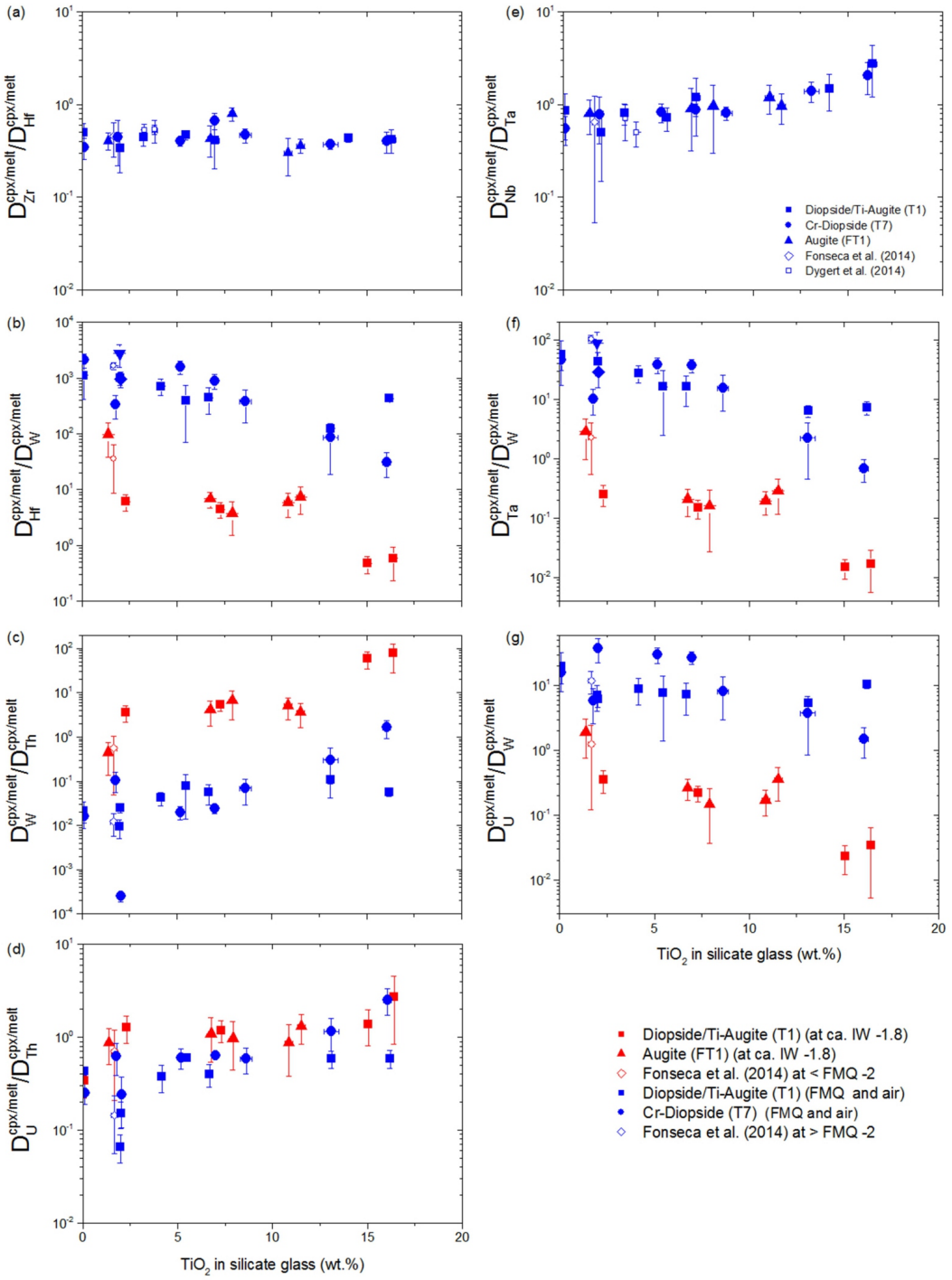

Supplementary Figure 3.2 – Trace element ratios of the calculated partition coefficients between clinopyroxene and melt plotted against the TiO_2 content in the silicate melt. (a) D_{Zr}/D_{Hf}, (b) D_{Hf}/D_W, (c) D_W/D_{Th}, (d) D_U/D_{Th}, (e) D_{Nb}/D_{Ta}, (f) D_{Ta}/D_W and (g) D_U/D_W. For the ratios Zr/Hf and Nb/Ta the average between experiments at different oxygen fugacities and same initial TiO_2 content was used, while for the rest, which involved heterovalent elements, the average values of each experiment were used.

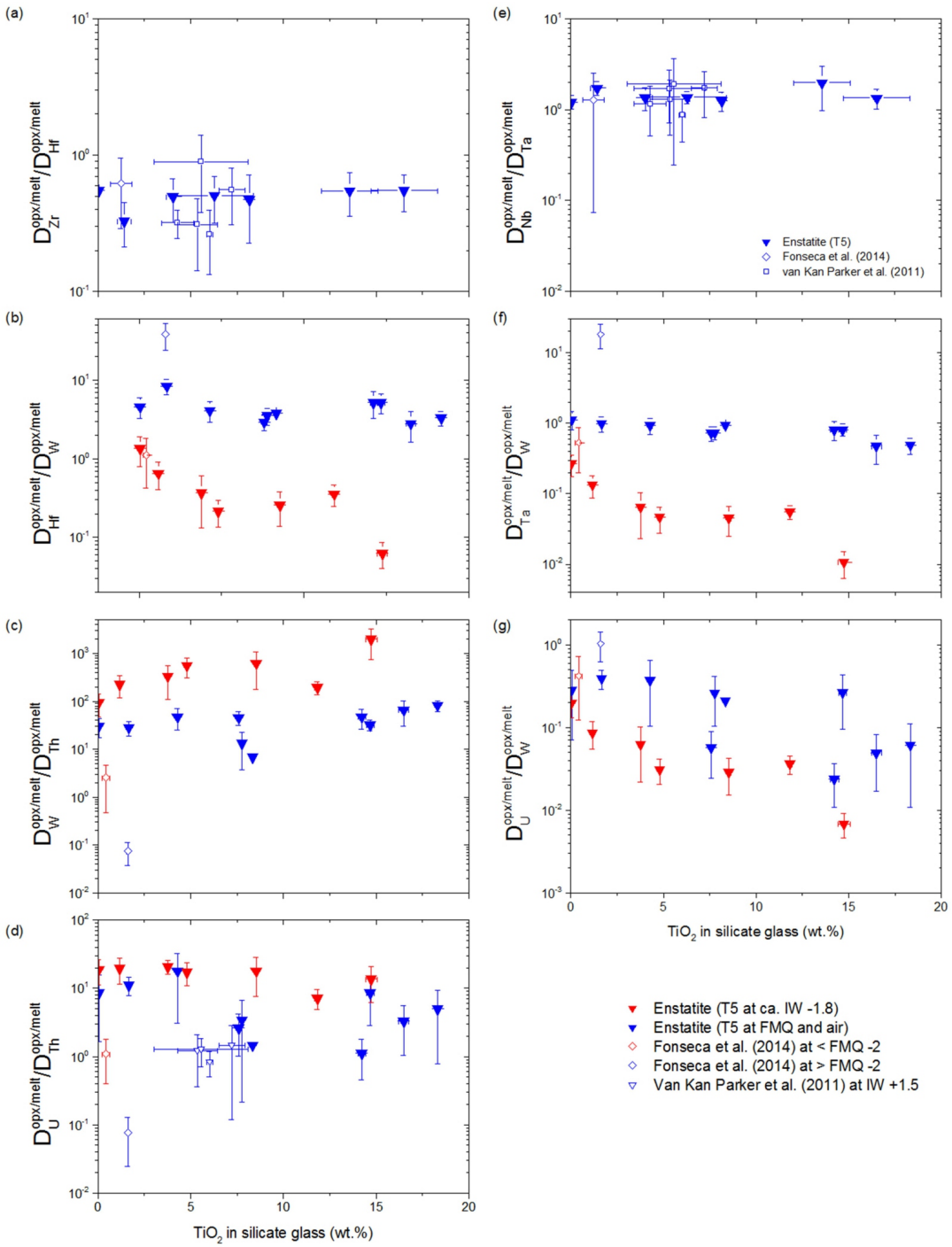

Supplementary Figure 3.3 – Trace element ratios of the calculated partition coefficients between orthopyroxene and melt plotted against the TiO_2 content in the silicate melt. (a) D_{Zr}/D_{Hf}, (b) D_{Hf}/D_W, (c) D_W/D_{Th}, (d) D_U/D_{Th}, (e) D_{Nb}/D_{Ta}, (f) D_{Ta}/D_W and (g) D_U/D_W. For the ratios Zr/Hf and Nb/Ta the average between experiments at different oxygen fugacities and same initial TiO_2 content was used, while for the rest, which involved heterovalent elements, the average values of each experiment were used.

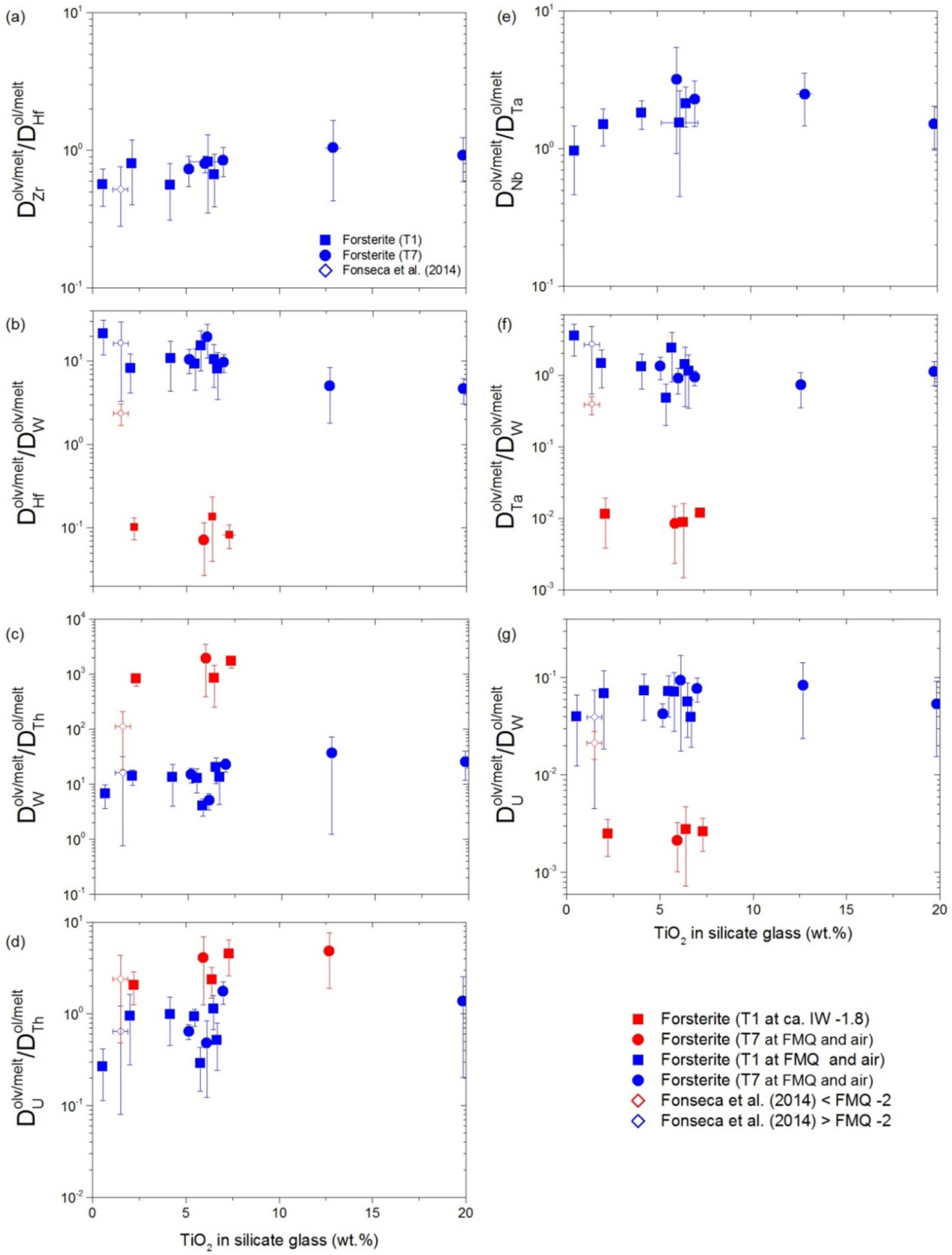

Supplementary Figure 3.4 – Trace element ratios of the calculated partition coefficients between olivine and melt plotted against the TiO_2 content in the silicate melt. (a) D_{Zr}/D_{Hf}, (b) D_{Hf}/D_W, (c) D_W/D_{Th}, (d) D_U/D_{Th}, (e) D_{Nb}/D_{Ta}, (f) D_{Ta}/D_W and (g) D_U/D_W. For the ratios Zr/Hf and Nb/Ta the average between experiments at different oxygen fugacities and same initial TiO_2 content was used, while for the rest, which involved heterovalent elements, the average values of each experiment were used.

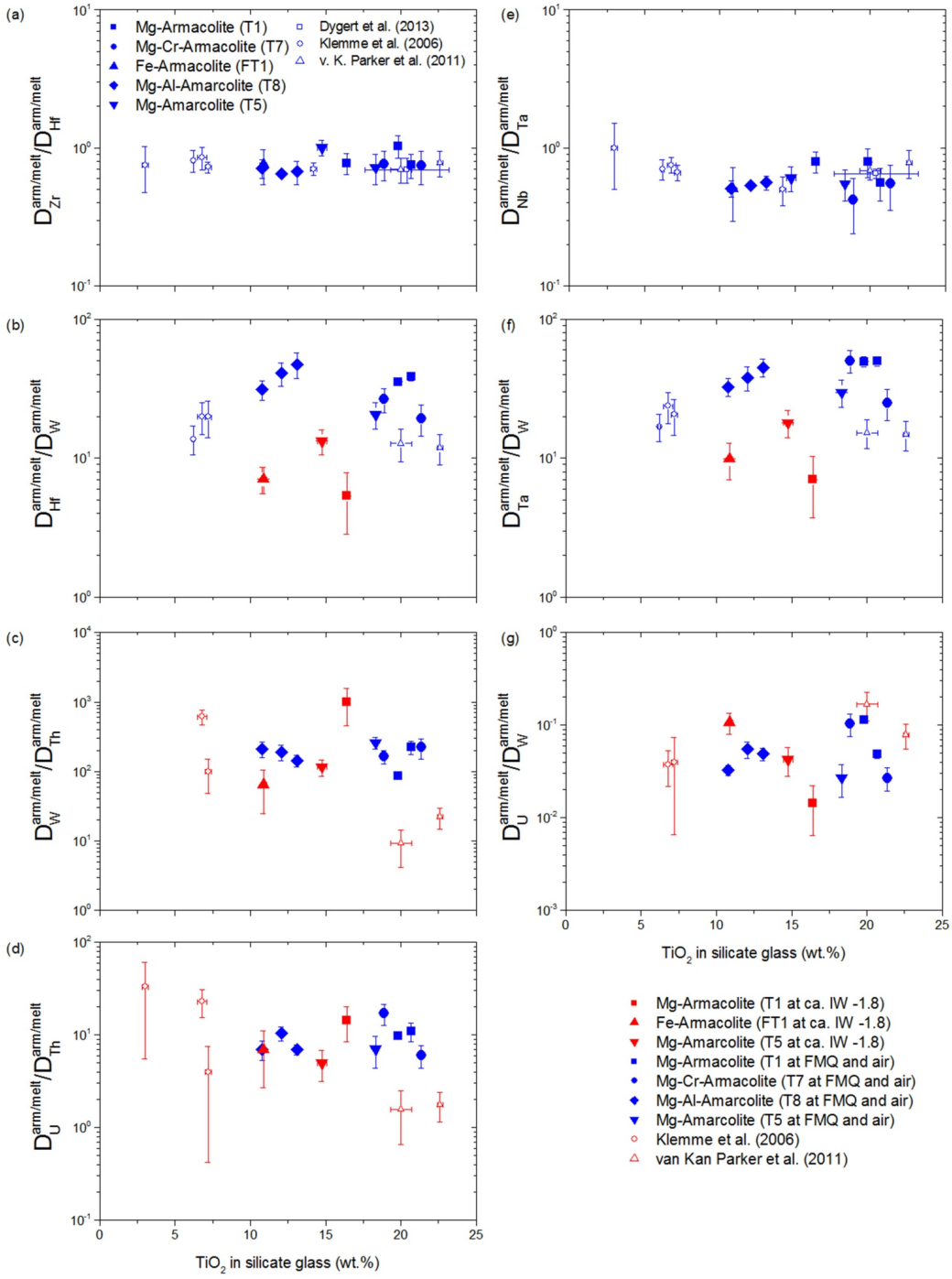

Supplementary Figure 3.5 – Trace element ratios of the calculated partition coefficients between armalcolite and melt plotted against the TiO_2 content in the silicate melt. (a) D_{Zr}/D_{Hf}, (b) D_{Hf}/D_W, (c) D_W/D_{Th}, (d) D_U/D_{Th}, (e) D_{Nb}/D_{Ta}, (f) D_{Ta}/D_W and (g) D_U/D_W.

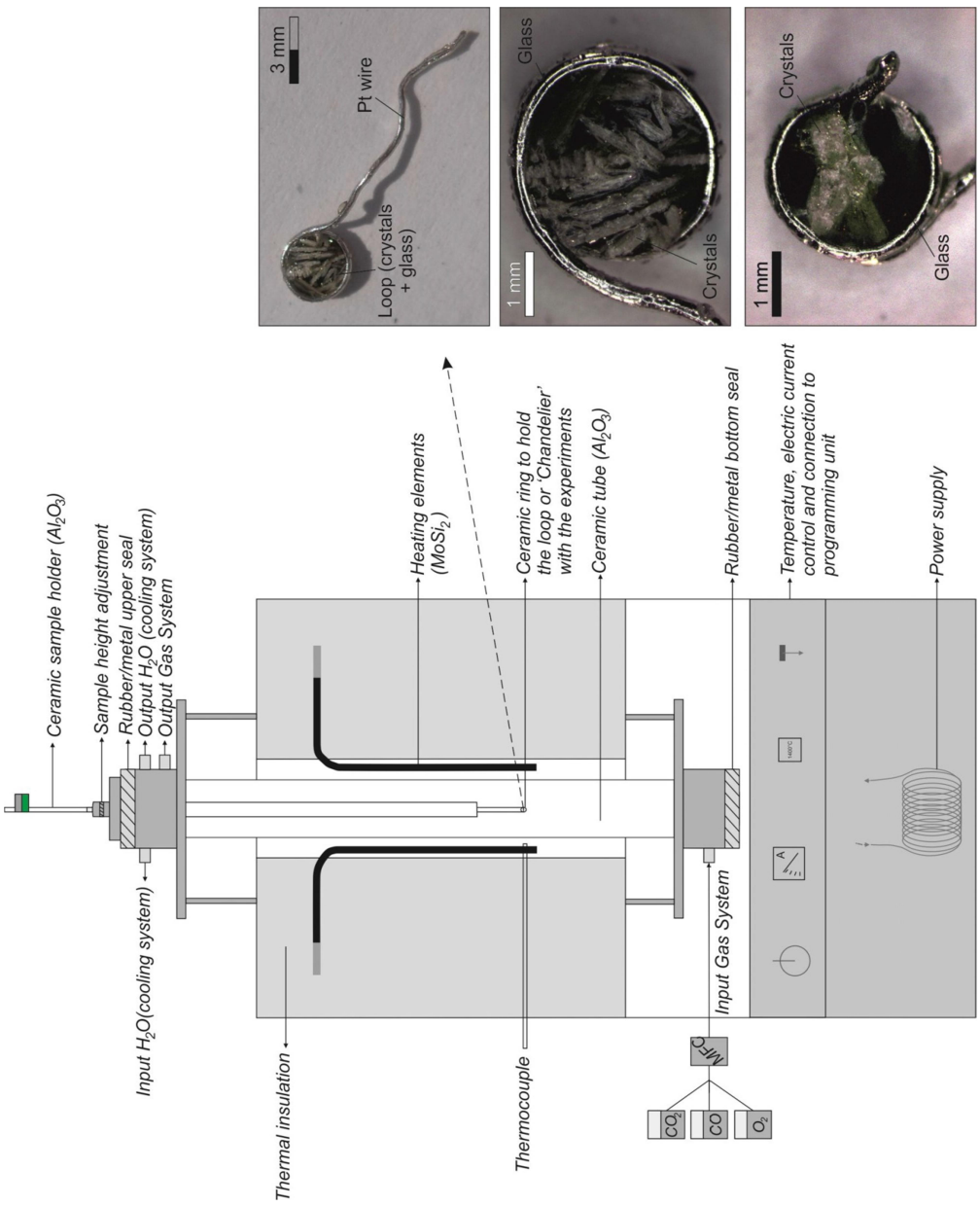

Supplementary Figure 4.1 – Sketch of the one-atmosphere vertical tube gas mixing furnace used in the experiments of this study.

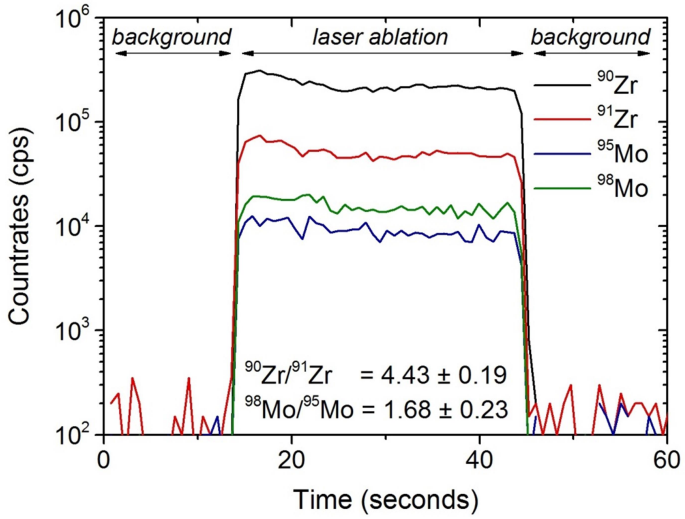

Supplementary Figure 4.2 - Example of a LA-ICP-MS spectrum for 30 seconds of ablation in silicate glass, showing that the natural abundances of both isotopes for the same element are well reproduced, indicating no isobaric interference during the analysis of either Molybdenum or Zirconium, which is also the case for other elements analysed (not shown). Natural abundances from Rosmann and Taylor (1998), which are 95Mo = 15.92 %, 98Mo = 24.13 % (i.e., 98Mo/95Mo = 1.52), 90Zr = 51.42 % and 91Zr = 11.22 % (i.e., 90Zr/91Zr = 4.58).

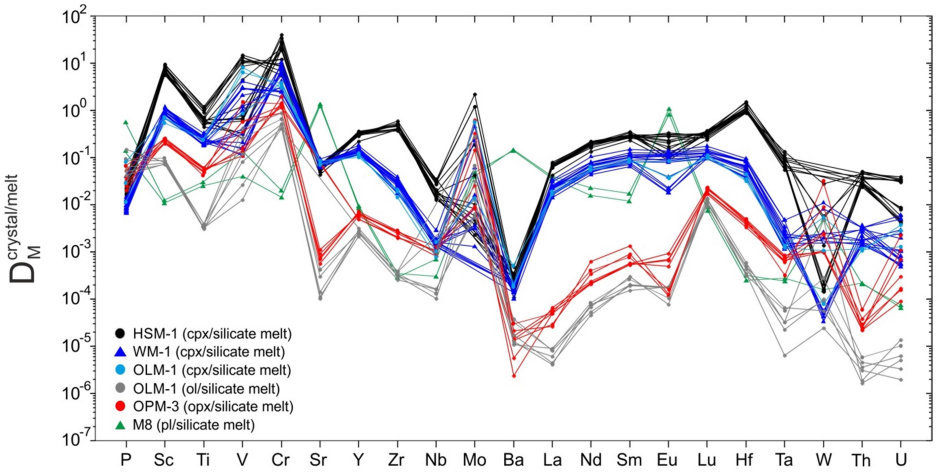

Supplementary Figure 4.3 - Multi-element variation diagram with experimentally determined partition coefficients for minor and trace elements between IVAl-rich clinopyroxene (HSM-1), IVAl-poor clinopyroxene (WM-1 and OLM-1), orthopyroxene (OPM-3), olivine (OLM-1), plagioclase (M8) and silicate melt obtained in this study.

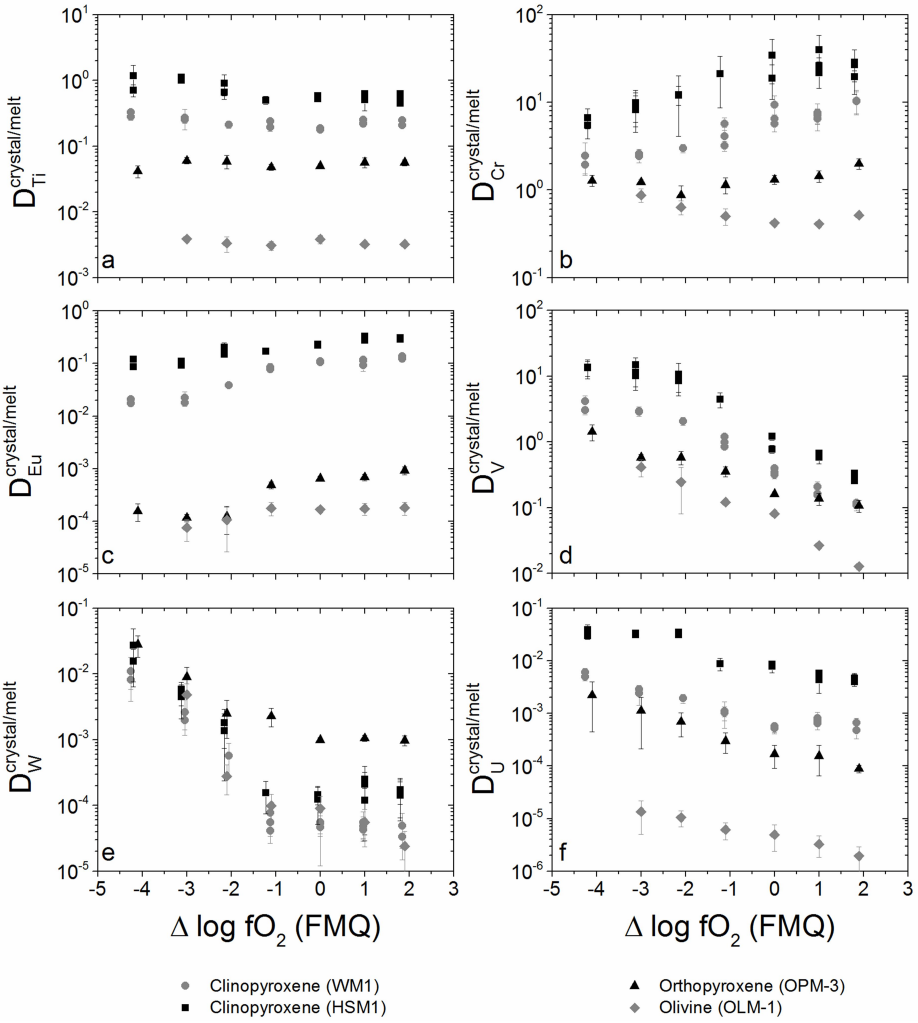

Supplementary Figure 4.4 – Partitioning of Ti (a), Cr (b), Eu (c), V (d), W (e) and U (f) between olivine, clinopyroxene, orthopyroxene and silicate melt as a function of fO_2 (given relative to the FMQ redox equilibrium). Error bars are one standard deviation.

Bibliography

Adam, J., Green, T., 2006. Trace element partitioning between mica- and amphibole-bearing garnet lherzolite and hydrous basanitic melt: 1. Experimental results and the investigation of controls on partitioning behavior. Contributions to Mineralogy and Petrology 152, 1–17.

Adam, J., Green, T. H., 1994. The effects of pressure and temperature on the partitioning of Ti, Sr and REE between amphibole, clinopyroxene and basanitic melts. Chemical Geology 117, 219–233.

Adam, J., Green, T. H., 2003. The influence of pressure, mineral composition and water on trace element partitioning between clinopyroxene, amphibole and basanitic melts. European Journal of Mineraolgy 15, 831–841.

Aigner-Torres, M., Blundy, J., Ulmer, P., Pettke, T., 2007. Laser Ablation ICP-MS study of trace element partitioning between plagioclase and basaltic melts: an experimental approach. Contributions to Mineralogy and Petrology 153, 647–667.

Amelin, Y., Krot, A. N., Hutcheon, I. D., Ulyanov, A. A., 2002. Lead isotopic ages of chondrules and calcium-aluminum-rich inclusions. Science 297, 1678–1683.

Anderson, A. T., Bunch, T. E., Cameron, E. N., Haggerty, S. E., Boyd,

F. R., Finger, L. W., James, O. B., Keil, K., Prinz, M., Ramdohr, P., Goresy, A., 1970. Armalcolite, a new mineral from the Apollo 11 samples. Proceedings of the Apollo 11 Lunar Science Conference 1, 55–63.

Arndt, N., Lehnert, K., Vasilev, Y., 1995. Meimechites - highly magnesian lithosphere-contaminated alkaline magmas from deep subcontinental mantle. Lithos 34, 41–59.

Baldwin, R. P., 1949. The face of the Moon. University of Chicago Press, Chicago, United States of America.

Ballhaus, C., 1991. Is the upper mantle metal-saturated? Earth and Planetary Science Letters 132, 75–86.

Ballhaus, C., 1993. Redox states of lithospheric and asthenospheric upper mantle. Contributions to Mineralogy and Petrology 114, 331–348.

Barboni, M., Boehnke, P., Keller, B., Kohl, I., Schoene, B., Young, E. D., McKeegan, K. D., 2017. Early formation of the Moon 4.51 billion years ago. Science Advances 3, 1–8.

Beard, B. L., Taylor, L. A., Scherer, E. E., Johnson, C. M., Snyder, G. A., 1998. The source region and melting mineralogy of high-titanium and low-titanium lunar basalts deduced from Lu-Hf isotope data. Geochimica et Cosmochimica Acta 62, 525–544.

Bence, A. E., Grove, T. L., Papike, J. J., 1980. Basalts as probes of planetary interiors: constraints on the chemistry and mineralogy of their source regions. Precambrian Research 10, 249–279.

Bennet, S. L., Blundy, J., Elliott, T., 2004. The effect of sodium and titanium on crystal-melt partitioning of trace elements. Geochimica et Cosmochimica Acta 68(10), 2335–2347.

Bezard, R., Fischer-Gödde, M., Hamelin, C., Brennecka, G. A., Kleine, T., 2016. The effects of magmatic processes and crustal recycling on the molybdenum stable isotopic composition of Mid-Ocean Ridge Basalts. Earth and Planetary Science Letters 453, 171–181.

Bezos, A., Humler, E., 2005. The Fe^{3+}/Fe_t ratios of MORB glasses and their implications for mantle melting. Geochimica et Cosmochimica Acta 69, 711–725.

Bindeman, I. L., Davis, A. M., 2000. Trace element partitioning between plagioclase and melt: Investigation of dopant influence on partition behavior. Geochimica et Cosmochimica Acta 64(16), 2863–2878.

Binder, A. B., 1982. The mare basalt magma source region and mare basalt magma genesis. Proceedings of the Lunar and Planetary Science Conference 13th, 37–53.

Blundy, J. D., Falloon, T. J., Wood, B. J., Dalton, J. A., 1995. Sodium partitioning between clinopyroxene and silicate melts. Journal of Geophysical Research 100, 15501–15515.

Blundy, J. D., Robinson, J. A. C., Wood, B. J., 1998. Heavy REE are compatible in clinopyroxene on the spinel lherzolite solidus. Earth and Planetary Science Letters 160, 493–504.

Blundy, J. D., Wood, B. J., 1994. Prediction of crystal-melt partition coefficients from elastic moduli. Nature 372, 452–454.

Blundy, J. D., Wood, B. J., 2003. Partitioning of trace elements between crystals and melts. Earth and Planetary Science Letters 210, 383–397.

Bonnand, P., Parkinson, I. J., Anand, M., 2016. Mass dependent fractionation of stable chromium isotopes in mare basalts: Implications for the

formation and the differentiation of the Moon. Geochimica et Cosmochimica Acta 175, 208–221.

Borisov, A., Behrens, H., Holtz, F., 2013. The effect of Titanium and Phosphorous on ferric/ferrous ratio in silicate melts: an experimental study. Contributions to Mineralogy and Petrology 166, 1577–1591.

Borisov, A., Palme, H., 2000. Solubilities of noble metals as derived from experiments in Fe-free systems. American Mineralogist 85, 1665–1673.

Borisov, A. A., 2012. The Ti^{4+}/Ti^{3+} ratio of magmatic melts: Application to the problem of the reduction of lunar basalts. Petrology 20, 391–398.

Bottinga, Y., Weill, D. F., 1972. The viscosity of magmatic silicate liquids. American Journal of Science 272, 438–475.

Brice, J. C., 1975. Some thermodynamic aspects of the growth of strained crystals. Journal of Crystal Growth 28, 249–253.

Brosche, P., Sündermann, J., 1978. Tidal friction and the Earth's rotation. Springer Verlag, Heidelberg, Germany.

Brown, G. M., Emeleus, C. H., Holland, J. G., Peckett, A., Phillips, R., 1972. Mineral-chemical variations in Apollo 14 and Apollo 15 basalts and granitic fractions. Proceedings of the Lunar and Planetary Science Conference 3rd, 141–157.

Brown, S. M., Grove, T. L., 2015. Origin of the Apollo 14, 15, and 17 yellow ultramafic glasses by mixing of deep cumulate remelts. Geochimica et Cosmochimica Acta 171, 201–215.

Brunfelt, A. O., Heier, K. S., Steiennes, E., 1971. Determination of 40 elements in Apollo 12 materials be neutron activation analysis. Proceedings of the Lunar and Planetary Science Conference 2nd, 1281–1290.

Buck, W. R., Toksöz, M. N., 1980. The bulk composition of the Moon based on geophysical constraints. Proceedings of the Lunar and Planetary Science Conference 11th, 2043–2058.

Burkemper, L. K., Agee, C. B., Garcia, K. A., 2012. Molybdenum metal-silicate partitioning behavior: constraining the magma ocean hypothesis for core formation. Proceedings of the Lunar and Planetary Science Conference 43rd, 2155.

Burkhardt, C., 2017. Isotopic composition of the Moon and the lunar isotopic crisis. Encyclopedia of Lunar Science Springer, 1–13.

Burkhardt, C., Hin, R. C., Kleine, T., Bourdon, B., 2013. Mass-dependent molybdenum isotope fractionation - a new tracer for core formation. Proceedings of the Lunar and Planetary Science Conference 44th, 1902.

Burkhardt, C., Hin, R. C., Kleine, T., Bourdon, B., 2014. Evidence for Mo isotope fractionation in the solar nebula and during planetary differentiation. Earth and Planetary Science Letters 391, 201–211.

Burkhardt, C., Kleine, T., Oberli, F., Pack, A., Bourdon, B., Wieler, R., 2011. Molybdneum isotope anomalies in meteorites: constraints on solar nebula evolution and origin of the Earth. Earth and Planetary Science Letters 312, 390–400.

Burnham, C. W., 1981. The nature of multicomponent aluminosilicate melts. Physics and Chemistry of the Earth 13, 197–229.

Cameron, A. G. W., Benz, W., 1991. The origin of the Moon and the single impact hypothesis. Icarus 92, 204–216.

Cameron, A. G. W., Canup, R. M., 1998. The giant impact occured during

Earth accretion. Proceedings of the Lunar and Planetary Science Conference 29th, 1062.

Cameron, A. G. W., Ward, W. R., 1976. The origin of the Moon. Proceedings of the Lunar and Planetary Science Conference 7th, 120–122.

Canup, R. M., 2004. Dynamics of lunar formation. Annual Reviews on Astronomy and Astrophysics 42, 441–475.

Canup, R. M., 2012. Forming a Moon with and Earth-like composition via a giant impact. Science 338, 1052–1055.

Canup, R. M., 2013b. Planetary science: Lunar conspiracies. Nature 504, 27–29.

Canup, R. M., Asphaug, E., 2001. Origin of the Moon in a giant impact near the end of the Earth's formation. Nature 412, 708–712.

Canup, R. M., Barr, A. C., Crawford, D. A., 2013. Lunar-forming impacts: high-resolution SPH and AMR-CTH simulations. Icarus 222, 200–219.

Chase, M. W., 1998. NIST-JANAF thermodynamic tables. National Institute of Standards and Technology, Washington DC, USA.

Chemia, Z., Dolejs, D., Steine-Neumann, G., 2015. Thermal effects of variable material properties and metamorphic reactions in a three component subducting slab. Journal of Geophysical Research, Solid Earth 1220, 6823–6845.

Christie, D. M., Carmichael, I. S. E., Langmuir, C. H., 1986. Oxidation states of mid-ocean ridge basalt glasses. Earth and Planetary Science Letters 79, 397–411.

Cottrell, E., Kelley, K. A., 2011. The oxidation state of Fe in MORB glasses and the oxygen fugacity of the upper mantle. Earth and Planetary Science Letters 305, 270–282.

Crawford, M. L., 1976. Crystallization of plagioclase in mare basalts. Proceedings of the Lunar and Planetary Science Conference 4th, 705–717.

Cuk, M., Stewart, S. T., 2012. Making the Moon from a fast-spinning Earth: A giant impact followed by resonant despinning. Science 338, 1047–1052.

Dana, J. D., 1846. On the volcanoes of the Moon. Hamlen, New Haven, United States of America.

Danielson, L. R., Righter, K., Newville, M., Sutton, S., Choi, Y., Pando, K., 2011. Molybdenum valence in basaltic melts: effects of temperature and pressure. Proceedings of the Lunar and Planetary Science Conference 42nd, 2609.

Darwin, G. H., 1879. On the bodily tides of viscous and semi-elastic spheroids, and the Ocean tides upon a yelding nucleus. Philosophical Transactions of the Royal Society of London 170, 1–35.

Dauphas, N., Burkhardt, C., Warren, P. H., Teng, F. Z., 2014. Geochemical arguments for an Earth-like Moon forming impactor. Philosophical Transactions of the Royal Society A 372, 20130244.

Dauphas, N., Davis, A. M., Marty, B., Reisberg, L., 2004. The cosmic Molybdenum-Ruthenium isotope correlation. Earth and Planetary Science Letters 226, 465–475.

Dauphas, N., Marty, B., Reisberg, L., 2002. Molybdenum evidence for inherited planetary scale isotope heterogeneities of the proto solar nebula. Astrophysics Journal 565, 640–644.

Davis, F. A., Humayun, M., Hirschmann, M. M., Cooper, R. S., 2013. Experimentally determined mineral/melt partitioning of first-row transition elements (FRTE) during partial melting of peridotite at 3 GPa. Geochimica et Cosmochimica Acta 104, 232–260.

Day, J. M. D., Brandon, A. D., Walker, R. J., 2016. Highly Siderophile Elements in Earth, Mars, the Moon, and Asteroids. Reviews in Mineralogy and Geochemistry 81, 161–238.

Day, J. M. D., Pearson, D. G., Taylor, L. A., 2007. Highly siderophile element constraints on accretion and differentiation of the Earth-Moon system. Science 315, 217–219.

Day, J. M. D., Walker, R. J., 2015. Highly siderophile element depletion in the Moon. Earth and Planetary Science Letters 423, 114–124.

de Meijer, R. J., Anisichkin, V. F., van Westrenen, W., 2013. Forming the Moon from terrestrial silicate-rich material. Chemical Geology 345, 40–49.

de Vries, J., van Westrenen, W., van der Berg, A., 2012. Radiogenic heat production on the Moon: constraints from plagioclase-melt trace element partitioning experiments. Proceedings Lunar Planetary Science Conference 43rd, 1737.

Delano, J. W., 1986. Pristine lunar glasses: criteria, data, and implications. Journal of Geophysical Research 91, 201–213.

Delano, J. W., 1990. Experimental constraints on the oxidation state of the lunar mantle. Proceedings of the Lunar and Planetary Science Conference 21st, 278–279.

Dickinson, T., Taylor, G. J., Keil, K., Bild, R. W., 1989. Germanium abundances in lunar basalts: Evidence of mantle metasomatism? Proceedings of the Lunar and Planetary Science Conference 19th, 189–198.

Duffy, J. A., 1993. A review of optical basicity and its applications to oxidic systems. Geochimica et Cosmochimica Acta 57, 3961–3970.

Dunn, T., Sen, C., 1994. Mineral/matrix partition coefficients for orthopyroxene, plagioclase, and olivine in basaltic to andesitic systems: A combined analytical and experimental study. Geochimica et Cosmochimica Acta 58, 717–733.

Dygert, N., Liang, Y., Hess, P., 2013. The importance of melt TiO_2 in affecting major and trace element partitioning between Fe–Ti oxides and lunar picritic glass melts. Geochimica et Cosmochimica Acta 106, 134–151.

Dygert, N., Liang, Y., Sun, C., Hess, P., 2014. An experimental study of trace element partitioning between Augite and Fe-rich basalts. Geochimica et Cosmochimica Acta 132, 170–186.

Eggins, S. M., 1993. Origin and differentiation of picritic arc magmas, Ambae, Vanuatu. Contributions to Mineralogy and Petrology 114, 79–100.

Elardo, S. M., Draper, D. S., Shearer, C. K., 2011. Lunar Magma Ocean crystallization revisited: Bulk composition, early cumulate mineralogy, and the source regions of the Highlands Mg-suite. Geochimica et Cosmochimica Acta 75, 3024–3045.

Elkins, L. T., Fernandes, V. A., Delano, J. W., Grove, T. L., 2000. Origin of lunar ultramafic green glasses: constraints from phase equilibrium studies. Geochimica et Cosmochimica Acta 64, 2339–2350.

Elkins-Tanton, L. T., van Orman, J. A., Hager, B. H., Grove, T. L., 2002. Re-examination of the lunar magma ocean cumulate overturn hypothesis: melting or mixing is required. Earth and Planetary Science Letters 196, 239–249.

Ellam, R. M., 1992. Lithospheric thickness as a control on basalt geochemistry. Geology 20, 153–156.

Ertel, W., O'Neill, H. S. C., Sylvester, P. J., Dingwell, D. B., 1999. Solubilities of Pt and Rh in a haplobasaltic silicate melt at 1300°C. Geochimica et Cosmochimica Acta 63, 2439–2449.

Eugster, H. P., 1957. Heterogeneous reactions involving oxidation and reduction at high-pressures and temperatures. Journal of Chemical Physics 26, 1760.

Evans, T. M., O'Neill, H. S. C., Tuff, J., 2008. The influence of melt composition on the partitioning of REEs, Y, Sc, Zr and Al between forsterite and melt in the system CMAS. Geochimimica et Cosmochimica Acta 72, 5708–5721.

Farges, F., Brown, G. E., Rehr, J. J., 1996. Coordination chemistry of Ti(IV) in silicate glasses and melts: I. XAFS study of titanium coordination in oxide model compounds. Geochimica et Cosmochimica Acta 60, 3023–3038.

Farges, F., Siewert, R., Jr., G. E. B., Guesdon, A., Morin, G., 2006. Structural environments around molybdenum in silicate glasses and melts. I. Influence of composition and oxygen fugacity on the local structure of molybdenum. Canadian Mineralogist 44, 731–753.

Fitton, J. G., 1995. Coupled molybdenum and niobium depletion in continental basalts. Earth and Planetary Science Letters 136, 715–721.

Flemming, R. L., Luth, R. W., 2002. ^{29}Si MAS NMR study of diopside-Ca-Tschermak clinopyroxenes: Detecting both tetrahedral and octahedral Al substitution. American Mineralogist 87, 25–36.

Fonseca, R. O. C., Mallmann, G., O'Neill, H. S. C., Campbell, I., 2007. How chalcophile is Rhenium? An experimental study of the solubility of Re in sulphide mattes. Earth and Planetary Science Letters 260, 537–548.

Fonseca, R. O. C., Mallmann, G., Sprung, P., Sommer, J. C., Heuser, A., Speelmanns, I. M., Blanchard, H., 2014. Redox controls on tungsten and uranium crystal/silicate melt partitioning and implications for the U/W and Th/W ratio of the lunar mantle. Earth and Planetary Science Letters 404, 1–13.

Frost, B. R., 1991. Introduction to oxygen fugacity and its petrologic importance. Reviews in Mineralogy 25, 1–10.

Frost, D. J., Mann, U., Asahara, Y., Rubie, D. C., 2008b. The redox state of the mantle during and just after core formation. Philosophical Transactions of the Royal Society 366, 4315–4337.

Frost, D. J., McCammon, C., 2008. The Redox State of Earth's Mantle. Annual Reviews of Earth and Planetary Sciences 36, 389–420.

Gaetani, G. A., 2004. The influence of melt structure on trace element partitioning near the peridotite solidus. Contributions to Mineralogy and Petrology 147, 511–527.

Gaetani, G. A., Grove, T. L., 1995. Partitioning of rare earth elements between clinopyroxene and silicate melt: crystal-chemical controls. Geochimica et Cosmochimica Acta 59, 1951–1962.

Gaffney, A. M., Borg, L. E., 2014. A young solidification age for the lunar magma ocean. Geochimica et Cosmochimica Acta 140, 227–240.

Gale, A., Dalton, C. A., Langmuir, C. H., Su, Y., Schiling, J. G., 2013. The mean composition of ocean ridge basalts. Geochemistry, Geophysics, Geosystems 14(3), 489–518.

Gerstenkorn, H., 1970. The early history of the Moon. The Moon 1, 506–507.

Ghiorso, M. S., Hirschmann, M. M., Reiners, P. W., Kress, V. C., 2002. The pMELTS: a revision of MELTS for improved calculation of phase relations and major element partitioning related to partial melting of the mantle to 3 GPa. Geochimistry, Geophysics, Geosystems 3, 1–36.

Giguere, T. A., Taylor, G. J., Hawke, B. R., Lucey, P. G., 2000. The titanium contents of lunar mare basalts. Meteoritics and Planetary Sciences 35, 193–200.

Goldreich, P., 1966. History of the lunar orbit. Reviews in Geophysics 4, 411–439.

Goldschmidt, V. M., 1937. The principles of distribution of chemical elements in minerals and rocks. Journal of the Chemical Society, 655–673.

Govindaraju, K., 1994. Compilation of working values and sample description for 383 geostandards. Geostandards Newsletter 18, 1–158.

Greber, N. D., Puchtel, I. S., Nagler, T. F., Mezger, K., 2015. Komatiites constrain molybdenum isotope composition of the Earth's mantle. Earth and Planetary Science Letters 421, 129–138.

Grove, T. L., Krawczynski, M. J., 2009. Lunar mare volcanism: where did the magmas come from? Elements 5, 29–34.

Gualda, G. A. R., Ghiorso, M. S., 2015. MELTS Excel: A Microsoft Excel-based MELTS interface for research and teaching of magma properties and evolution. Geochimistry, Geophysics, Geosystems 16, 315–324.

Gudmundsson, G., Wood, B. J., 1995. Experimental tests of garnet peridotite oxygen barometry. Contributions to Mineralogy and Petrology 119, 56–67.

Hagerty, J. J., Shearer, C. K., Vaniman, D. T., 2006. Heat-producing elements in the lunar mantle: Constraints from ion microprobe analyses of lunar volcanic glasses. Geochimica et Cosmochimica Acta 70, 3457–3476.

Haggerty, S. E., 1973. Armalcolite and genetically associated opaque minerals in the lunar samples. Proceedings of the Lunar and Planetary Science Conference 4th, 777–797.

Halliday, A. N., 2000. Hf-W chronometry and inner solar system accretion rates. Space Science Reviews 92, 355–370.

Halliday, A. N., 2008. A Young Moon-Forming Giant Impact at 70-110 Million Years Accompanied by Late-Stage Mixing, Core Formation and Degassing of the Earth. Philosophical Transactions of the Royal Society A 366, 4163–4181.

Halliday, A. N., Lee, D. C., 1999. Tungsten isotopes and the early development of the Earth and Moon. Geochimica et Cosmochimica Acta 63, 4157–4179.

Hallis, L. J., Anand, M., Greenwood, R. C., Miller, M. F., Franchi, I. A., Russell, S. S., 2010. The oxygen isotope composition, petrology and geochemistry of mare basalts: evidence for large-scale compositional variation in the lunar mantle. Geochimica et Cosmochimica Acta 74, 6885–6899.

Harper, C. L., Jacobsen, S. B., 1996. Evidence for ^{182}W in the early solar system and constraints on the timescale of terrestrial core formation. Geochimica et Cosmochimica Acta 60, 1131–1153.

Hartmann, W. K., Davis, D. R., 1975. Satellite-sized planetesimals and lunar origin. Icarus 24, 504–515.

Haskin, L. A., Warren, P. H., 1991. Lunar chemistry. Lunar Sourcebook: A User's Guide to the Moon. Cambridge University Press, 357–474.

Hawke, B. R., Head, J. W., 1978. Lunar KREEP volcanism: Geologic evidence for history and mode of emplacement. Proceedings of the Lunar and Planetary Science Conference 9th, 3285–3309.

Heiken, G. H., Vaniman, D. T., French, B. M., 1991. Lunar sourcebook: a user's guide to the Moon. Cambridge University Press, Lunar and Planetary Institute, 778p.

Hertogen, J., Janssens, M. J., Palme, H., 1980. Trace elements in ocean ridge basalt glasses: Implications for fractionations during mantle evolution and petrogenesis. Geochimica et Cosmochimica Acta 44, 2125–2140.

Herwartz, D., Pack, A., Friedrichs, B., Bischoff, A., 2014. Identification of the giant impactor Theia in lunar rocks. Science 344, 1146–1150.

Hess, P. C., 1991. The role of high field strength cations in silicate melts. Physical chemistry of magmas. Springer, New York, 152–191.

Hess, P. C., Parmentier, E. M., 1995. A model for the thermal and chemical evolution of the Moon's interior: implications for the onset of mare volcanism. Earth and Planetary Science Letters 134, 501–514.

Hiesinger, H., Head, J. W., Wolf, U., Jaumann, R., Neukum, G., 2003. Ages and stratigraphy of mare basalts in Oceanus Procellarum, Mare Nubium, Mare Cognitum, and Mare Insularum. Journal of Geophysical Research 108, 1–27.

Hill, E., Wood, B. J., Blundy, J. D., 2000. The effect of Ca-Tschermaks component on trace element partitioning between clinopyroxene and silicate melt. Lithos 53, 203–215.

Hill, E., Wood, B. J., Blundy, J. D., 2011. Clinopyroxenemelt trace element partitioning and the development of a predictive model for HFSE and Sc. Contributions to Mineralogy and Petrology 161, 423–438.

Hillgren, V. J., 1991. Partitioning behavior of Ni, Co, Mo and W between basaltic liquid and Ni-rich metal: implications for the origin of the Moon and lunar core formation. Geophysical Research Letters 18, 2077–2080.

Hin, R. C., Burkhardt, C., Schmidt, M. W., Bourdon, B., Kleine, T., 2013. Experimental evidence for Mo isotope fractionation between metal and silicate liquids. Earth and Planetary Science Letters 379, 38–48.

Hin, R. C., Burnham, A. D., Walter, M. J., Elliott, T., 2015. The influence of valence state on molybdenum isotope fractionation. Goldschmidt Abstracts, 1271.

Holzheid, A., Borisov, A., Palme, H., 1994. The effect of oxygen fugacity and temperature on solubilities of nickel, cobalt and molybdenum in silicate melts. Geochimica et Cosmochimica Acta 58, 1975–1981.

Holzheid, A., Palme, H., 2007. The formation of eucrites: constraints from metal-silicate partition coefficients. Meteoritics and Planetary Sciences 42, 1817–1829.

Huang, F., Lundstrom, C. C., McDonough, W. F., 2006. Effect of melt structure on trace-element partitioning between clinopyroxene and silicic, alkaline, aluminous melts. American Mineralogist 91, 1385–1400.

Hubbard, N. J., Gast, P. W., Meyer, C., Nyquist, L. E., Shih, C., Wiesmann, H., 1971. Chemical composition of lunar anorthosites and their parent liquids. Earth and Planetary Science Letters 13, 71–75.

Irvine, T. N., 1980. Magmatic density currents and cumulus processes. American Journal of Science 280, 1–58.

Jacobs, J., 1987. The Cores of other Planets. International Geophysics 37, 347–405.

Jacobsen, S., 2005. The Hf-W isotopic system and the origin of the Earth and Moon. Annual Reviews of Earth and Planetary Sciences 33, 531–570.

Jarosewich, E., Nelen, J., Norberg, J. A., 1980. Reference samples for electron microprobe analyses. Geostandards Newsletter 4, 43–47.

Jenner, F. E., O'Neill, H. S. C., 2012. Analysis of 60 elements in 616 ocean floor basaltic glasses. Geochemistry, Geophysics, Geosystems 13, 1525–2027.

Jochum, K. P., Weis, U., Stoll, B., Kuzmin, D., Yang, Q., Raczek, I., Jacob, D. E., Stracke, A., Birbaum, K., Frick, D. A., Günther, D., Enzweiler, J., 2011. Determination of reference values for NIST SRM 610–617 glasses following ISO guidelines. Geostandards and Geoanalytical Research 35, 397–429.

Jolliff, B. L., Gillis, J. J., Haskin, L. A., Korotev, R. L., Wieczorek, M. A., 2000. Major lunar crustal terranes: Surface expressions and crust-mantle origins. Journal of Geophysical Research 105, 4197–4216.

Jones, J. H., 1988. Partitioning of Mg and Fe between Olivine and liquids of lunar compositions: the roles of composition, pressure and Ti speciation. Proceedings of the Lunar and Planetary Science Conference 19th, 561–562.

Karner, J., Papike, J. J., Shearer, C. K., 2000. Olivine from planetary basalts: Chemical signatures that indicate planetary parentage and those that record igneous setting and process. American Mineralogist 88, 806–816.

Karner, J., Sutton, S. R., Papike, J. J., Shearer, C. K., Jones, J. H., Newville, M., 2006. Application of a new vanadium valence oxybarometer to basaltic glasses from the Earth, Moon, and Mars. American Mineralogist 91, 270–277.

Khan, A., Mosegaard, K., Rasmussen, K. L., 2000. A new seismic velocity model for the Moon from a Monte Carlo inversion of the Apollo lunar seismic data. Geophysical Research Letters 27, 1591–1594.

Kirchenbaur, M., Münker, C., Schuth, S., Gaber-Schönberg, D., Marchev, P., 2012. Tectonomagmatic Constraints on the Sources of Eastern Mediterranean K-rich Lavas. Journal of Petrology 53(1), 27–65.

Klein, C., Drake, J. C., Frondel, C., 1971. Mineralogical, petrological and chemical features of four Apollo 12 microgabrros. Proceedings of the Lunar and Planetary Science Conference 2nd, 265–284.

Kleine, T., Mezger, K., Münker, C., Palme, H., Bischoff, A., 2004. ^{182}Hf – ^{182}W isotope systematics of chondrites, eucrites, and martian meteorites: chronology of core formation and early mantle differentiation in Vesta and Mars. Geochimica et Cosmochimica Acta 68, 2935–2946.

Kleine, T., Münker, C., Mezger, K., Palme, H., 2002. Rapid accretion and early core formation on asteroids and the terrestrial planets from Hf-W chronometry. Letters to Nature 418, 952–955.

Kleine, T., Palme, H., Mezger, K., Halliday, A. N., 2005. HfW chronometry of lunar metals and the age and early differentiation of the Moon. Science 310, 1671–1674.

Klemme, S., Günther, D., Hametner, K., Prowatke, S., Zack, T., 2006. The partitioning of trace elements between ilmenite, ulvospinel, armalcolite and silicate melts with implications for the early differentiation of the Moon. Chemical Geology 234, 251–263.

Kohn, S. C., Schofield, P. F., 1994. The importance of melt composition in controlling trace-element behaviour: an experimental study of Mn and Zn partitioning between forsterite and silicate melts. Chemical Geology 117, 73–87.

König, S., Münker, C., Hohl, S., Paulick, H., Barth, A. R., Lagos, M., Pfänker, J., Büchl, A., 2011. The Earth's tungsten budget during mantle melting and crustal formation. Geochimica et Cosmochimica Acta 75, 2119–2136.

Korotev, R. L., 2005. Lunar geochemistry as told by lunar meteorites. Chemie der Erde 65, 297–346.

Krawczynski, M. J., Grove, T. L., 2012. Experimental investigation of the influence of oxygen fugacity on the source depths for high titanium lunar ultramafic magmas. Geochimica et Cosmochimica Acta 79, 1–19.

Kress, V., Ghiorso, M., Lastuka, C., 2004. Microsoft EXCEL spreadsheet-based program for calculating equilibrium gas speciation in the COHS-Cl-F system. Computers and Geosciences 30(3), 211–214.

Kruijer, T. S., Kleine, T., 2016. High-precision ^{182}W measurements on mare basalts: constraints on the origin and differentiation of the Moon. Proceedings of the Lunar and Planetary Science Conference 47th, 2132.

Kruijer, T. S., Kleine, T., Fischer-Gödde, M., Sprung, P., 2015. Lunar tungsten isotopic evidence for the late veneer. Nature 520, 534–537.

Kushiro, I., Nakamura, Y., 1970. Petrology of some lunar crystalline rocks. Proceedings of the Apollo 11 Lunar Science Conference, 607–626.

Laskar, J., Joutel, F., Robutel, P., 1993. Stabilization of the Earth's obliquity by the Moon. Nature 361, 615–617.

Laurenz, V., Fonseca, R. O. C., Ballhaus, C., 2010. Solubility of Palladium in picritic melts: 1. The effect of iron. Geochimica et Cosmochimica Acta 74, 2989–2998.

Laurenz, V., Fonseca, R. O. C., Ballhaus, C., Jochum, K. P., Heuser, A., Sylvester, P. J., 2013. The solubility of Palladium and ruthenium in picritic melts: 2. The effect of sulfur. Geochimica et Cosmochimica Acta 108, 172–183.

Lee, D. C., Halliday, A. N., Snyder, G. A., Taylor, L. A., 1997. Age and origin of the Moon. Science 278, 1098–1103.

Leitzke, F. P., Fonseca, R. O. C., Michely, L. T., Sprung, P., Münker, C., Heuser, A., Blanchard, H., 2016. The effect of titanium on the partitioning behavior of high-field strength elements between silicates, oxides and lunar basaltic melts with applications to the origin of mare basalts. Chemical Geology 440, 219–238.

Leitzke, F. P., Fonseca, R. O. C., Sprung, P., Mallmann, G., Lagos, M., Michely, L. T., Münker, C., 2017. Redox dependent behaviour of molybdenum during magmatic processes in the terrestrial and lunar mantle: Implications for the Mo/W of the bulk silicate Moon. Earth and Planetary Science Letters 474, 503–515.

LeMaitre, R. W., Streckeisen, A., Zanettin, B., LeBas, M. J., Bonin, B., Bateman, P., 2005. Igneous rocks: a classification and glossary of terms. International Union of Geological Sciences, Cambridge University Press, 252 p.

Li, J., Agee, C. B., 1996. Geochemistry of mantlecore differentiation at high pressure. Nature 381, 686–689.

Liang, Y., Cascio, M. L., Hess, P. C., 2007. Preferential assimilation of armalcolite and ilmenite during melt migration and melt-rock reaction in the lunar mantle: an experimental study. Proceedings of the Lunar and Planetary Science Conference 38th, 1075–1076.

Liang, Y., Halliday, A. N., Siebert, C., Fitton, J. G., Burton, K. W., Harvey, J., 2017. Molybdenum isotope fractionation in the mantle. Geochimica et Cosmochimica Acta 199, 91–111.

Liang, Y., Hess, P., 2006. Preferential Assimilation due to melt-rock reaction in the lunar mantle: A laboratory and ophiolite perspective. Proceedings of the Lunar and Planetary Science Conference 37th, 18–19.

Lin, R. P., Mitchell, D. L., Curtis, D. W., Anderson, K. A., Carlson, C. W., McFadden, J., Acunha, M. H., Hood, L. L., Binder, A., 1998. Lunar surface magnetic fields and their interaction with the solar wind: Results from Lunar Prospector. Science 281, 1480–1484.

Lin, Y. H., Tronche, E. J., Steenstra, E. S., van Westrenen, W., 2017a. Evidence for an early wet Moon from experimental crystallization of the lunar magma ocean. Nature Geoscience 10, 14–18.

Lin, Y. H., Tronche, E. J., Steenstra, E. S., van Westrenen, W., 2017b. Experimental constraints on the solidification of a nominally dry lunar magma ocean. Earth and Planetary Science Letters 471, 104–116.

Liu, X., O'Neill, H. S. C., 2007. Effects of P_2O_5 and TiO_2 on the partial melting of spinel lherzolite in the system CaO–MgO–Al_2O_3–SiO_2 at 1.1 GPa. The Canadian Mineralogist 45, 649–655.

Logfren, G. E., Irving, A. J., Bence, A. E., Lipman, P. W., Duke, M. B., Naldrett, A. J., Dungan, M. A., Papike, J. J., Green, J. C., Reid, A. M., Haggerty, S. E., Rhodes, J. M., Haskin, L. A., Taylor, S. R., Vaniman, D. T., 1981. Basaltic Volcanism on the Terrestrial Planets. Basaltiv Volcanism Study Project Pergamon Press, 1273 p.

Longerich, H. P., Jackson, S. E., Günther, D., 1996. Laser ablation inductively coupled plasma mass spectrometric transient signal data acquisition and analyte concentration calculation. Journal of Analytical Atomic Apectrometry 11, 899–904.

Longhi, J., 1980. A model of early lunar differentiation. Proceedings of the Lunar and Planetary Science Conference 11th, 289–315.

Longhi, J., 1987. Liquidus equilibria and solid solution in the system $CaAl_2Si_2O_8$–Mg_2SiO_4–$CaSiO_3$–SiO_2 at low pressure. American Journal of Science 287, 265–331.

Longhi, J., 2003. A new view of lunar ferroan anorthosites. Journal of Geophysical Research 108, E8.

Longhi, J., 2006. Petrogenesis of picritic mare magmas: constraints on the extent of early lunar differentiation. Geochimica et Cosmochimica Acta 70, 5919–5934.

Longhi, J., Walker, D., Hays, J. F., 1978. The distribution of Fe and Mg between olivine and lunar basaltic liquids. Geochimica et Cosmochimica Acta 42, 1545–1558.

Lugmair, G. W., Shukolyukov, A., 1998. Early solar system timescales according to ^{53}Mn-^{53}Cr systematics. Geochimica et Cosmochimica Acta 62, 2863–2886.

Lundstrom, C. C., Shaw, H. F., Ryerson, F. J., Phinney, D. L., Gill, J., Williams, Q., 1994. Compositional controls on the partitioning of U, Th, Ba, Pb, Sr and Zr between clinopyroxene and haplobasaltic melts: implications for uranium series disequilibria in basalts. Earth and Planetary Science Letters 128, 407–423.

Lundstrom, C. C., Shaw, H. F., Ryerson, F. J., Williams, Q., Gill, J., 1998. Crystal chemical control of clinopyroxene-melt partitioning in the Di-Ab-An system: Implications for elemental fractionations in the depleted mantle. Geochimica et Cosmochimica Acta 62, 2849–2862.

Luth, R. W., Virgo, D., Boyd, F. R., Wood, B. J., 1990. Ferric iron in mantle-derived garnets. Contributions to Mineralogy and Petrology 104, 56–72.

Ma, C., Beckett, J. R., Rossman, G. R., 2014. Allendeite ($Sc_4Zr_3O_12$) and hexamolybdenum (Mo, Ru, Fe), two new minerals from an ultrarefractory inclusion from the Allende meteorite. American Mineralogist 99, 654–666.

MacPherson, G. J., Thiemens, M. H., 2011. Cosmochemistry: Understanding the Solar System through analysis of extraterrestrial materials. Proceedings of the National Academy of Sciences 108, 48.

Mallmann, G., Fonseca, R. O. C., Silva, A. B., 2015. An experimental study of the partitioning of trace elements between rutile and silicate melt as a function of oxygen fugacity. Anais da Academia Brasileira de Ciências 86, 1609–1629.

Mallmann, G., O'Neill, H. S. C., 2007. The effect of oxygen fugacity on the partitioning of Re between crystals and silicate melt during mantle melting. Geochimica et Cosmochimica Acta 71, 2837–2857.

Mallmann, G., O'Neill, H. S. C., 2009. The crystal/melt partitioning of V during mantle melting as a function of oxygen fugacity compared with some other elements (Al, P, Ca, Sc, Ti, Cr, Fe, Ga, Y, Zr and Nb). Journal of Petrology 50, 1765–1794.

Mallmann, G., O'Neill, H. S. C., 2013. Calibration of an Empirical Thermometer and Oxybarometer based on the Partitioning of Sc, Y and V between Olivine and Silicate Melt. Journal of Petrology 54, 933–949.

Malvin, D. J., Drake, M. J., 1987. Experimental determination of crys-

tal/melt partitioning of Ga and Ge in the system forsterite-anorthite-diopside. Geochimica et Cosmochimica Acta 51, 2117–2128.

Marquardt, D. W., 1963. An algorithm for least-squares estimation of non-linear parameters. Journal of the Society for Industrial and Applied Mechanics 11, 431–441.

Marvin, U. B., Walker, D., 1978. Implications of a titanium-rich glass clod at Oceanus Procellarum. American Mineralogist 63, 924–929.

McCallum, I. S., Charette, M. P., 1978. Zr and Nb partition coefficients: implications for the genesis of mare basalts, KREEP and sea floor basalts. Geochimica et Cosmochimica Acta 42, 859–869.

McCammon, C., Kopylova, M. G., 2004. A redox profile of the Slave mantle and oxygen fugacity control in the cratonic mantle. Contributions to Mineralogy and Petrology 148, 55–68.

McDonough, W. F., Sun, S., 1995. The composition of the Earth. Chemical Geology 120, 223–253.

McKay, G., Le, L., Wagstaff, J., Crozaz, G., 1994. Experimental partitioning of rare earth elements and strontium: constraints on petrogenesis and redox conditions during crystallization of Antarctic angrite Lewis Cliff 86010. Geochimica et Cosmochimica Acta 58, 2911–2919.

McKay, G., Weill, D. F., 1976. Petrogenesis of KREEP. Proceedings of the Lunar and Planetary Science Conference 7th, 2427–2447.

Melosh, H. J., 2014. New approaches to the Moon's isotopic crisis. Philosophical Transactions of the Royal Society A 372(2024), 20130168.

Melosh, H. J., Kipp, M. E., 1989. Giant impact theory of the Moon's origin: First 3-D hydrocode results. Proceedings of the Lunar and Planetary Science Conference 20th, 685–686.

Meyer, C., 2012. Lunar Sample Compendium. Available at: http://curator.jsc.nasa.gov/lunar/compendium.cfm.

Mezger, K., Debaille, V., Kleine, T., 2013. Core formation and mantle differentiation on Mars. Space Science Reviews 174, 27–48.

Michely, L. T., Leitzke, F. P., Speelmanns, I. M., Fonseca, R. O. C., 2017. Competing effects of crystal chemistry and silicate melt composition on trace element behavior in magmatic systems: insights from crystal/silicate melt partitioning of the REE, HFSE, Sn, In, Ga, Ba, Pt and Rh. Contributions to Mineralogy and Petrology 172, 39.

Millet, M. A., Dauphas, N. A., Greber, N. D., Burton, K. W., Dale, C. W., Debret, B., Macpherson, C. G., Nowell, G. M., Williams, H. M., 2016. Titanium stable isotope investigation of magmatic processes on the Earth and the Moon. Earth and Planetary Science Letters 449, 197–205.

Mills, K. C., 1993. The influence of structure on the physico-chemical properties of slags. ISIJ International 33, 148–155.

Mollo, S., Blundy, J. D., Iezzi, G., Scarlato, P., Langone, A., 2013. The partitioning of trace elements between clinopyroxene and trachybasaltic melt during rapid cooling and crystal growth. Contributions to Mineralogy and Petrology 166, 1633–1654.

Moretti, R., 2005. Polymerisation, basicity, oxidation state and their role in ionic modelling of silicate melts. Annals of Geophysics 48, 583–608.

Morrison, G. H., Gerard, J. T., Kashuba, A. T., Gangadharam, E. V., Potter, A. M., Miller, G. B., 1970. Elemental abundances of lunar soil and rocks. Proceedings of the Apollo 11 Lunar Science Conference, 1383–1392.

Münker, C., 2010. A high-field strength element perspective on early lunar differentiation. Geochimica et Cosmochimica Acta 74(24), 7340–7361.

Münker, C., Pfänder, J. A., Weyer, S., Büchl, A., Kleine, T., Mezger, K., 2003. Evolution of planetary cores and the Earth-Moon system from Nb/Ta systematics. Science 301, 84–87.

Münker, C., Weyer, S., Mezger, K., Rehkämpfer, M., Wombacher, F., Bischoff, A., 2000. ^{92}Nb–^{92}Zr and the early differentiation history of planetary bodies. Science 289, 1538–1542.

Myers, J., Eugster, H. P., 1983. The system Fe-Si-O: Oxygen buffer calibrations to 1,500K. Contributions to Mineralogy and Petrology 82, 75–90.

Myers, J. D., Sinha, A. K., Marsh, B. D., 1984. Assimilation of crustal material by basaltic magmas: Strontium isotopic and trace element data from the Edgecumbe Volcanic Field, SE Alaska. Journal of Petrology 25, 1–26.

Mysen, B. O., 1990. Relationships between silicate melt structure and petrologic processes. Earth–Science Reviews 27, 281–365.

Mysen, B. O., 1990b. The Structure of Silicate Melts. Annual Review of Earth and Planetary Sciences 11, 75–97.

Mysen, B. O., 2004. Element partitioning between minerals and melt, melt composition, and melt structure. Chemical Geology 213, 1–16.

Mysen, B. O., Neuville, D., 1995. Effect of temperature and TiO_2 content on the structure of $Na_2Si_2O_5$–$Na_2Ti_2O_5$ melts and glasses. Geochimica et Cosmochimica Acta 59(2), 325–342.

Nagasawa, H., 1966. Trace element partition coefficient in ionic crystals. Science 152, 769–771.

Nave, C. R., 2016. HyperPhysics. Department of Physics and Astronomy, Georgia State University, USA, http://hyperphysics.phy-astr.gsu.edu/hbase/index.html.

Neal, C., 2001. Interior of the Moon: The presence of garnet in the primitive deep lunar mantle. Journal of Geophysical Research 106, 27865–27885.

Neal, C. R., Kramer, G. Y., 2003. The composition of KREEP: a detailed study of KREEP basalt 15386. Proceedings of the Lunar and Planetary Science Conference 34th, 2023.

Neal, C. R., Taylor, L. A., 1992. Petrogenesis of mare basalts - a record of lunar volcanism. Geochimica et Cosmochimica Acta 56, 2177–2211.

Newsom, H. E., 1984a. The abundance of Molybdenum in lunar samples: new evidence for a lunar metal core. Proceedings of the Lunar and Planetary Science Conference 15th, 605–606.

Newsom, H. E., 1984b. The lunar core and the origin of the Moon. Eos 65, 22.

Newsom, H. E., 1986. Constraints on the origin of the Moon from the abundance of molybdenum and other siderophile elements. Origin of the Moon. Lunar and Planetary Institute, Houston, USA,, 279–310.

Nicholis, M., Rutherford, M. J., 2009. Graphite oxidation in the Apollo 17 orange glass magma: implications for the generation of a lunar volcanic gas phase. Geochimica et Cosmochimica Acta 73(19), 5905–5917.

Nininger, H. H., 1943. The Moon as a source of tektites. Sky and Telescope 2, 12–15.

Norman, D. M., Borg, L. E., Nyquist, L. E., Bogard, D. D., 2003. Chronology, geochemistry, and petrology of a ferroan noritic anorthosite clast from Descartes breccia 67215: Clues to the age, origin, structure, and impact history of the lunar crust. Meteoritics and Planetary Science 38, 645–661.

Onuma, N., Higuchi, H., Wakita, H., Nagasawa, H., 1968. Trace element partitioning between two pyroxenes and the host lava. Earth and Planetary Science Letters 5, 47–51.

Öpik, E. J., 1966. The cometary origin of meteorits. Advances in Astronomy and Astrophysics 4, 301–336.

O'Neill, H. S. C., 1987. Quartz-fayalite-iron and quartz-fayalite-magnetite equilibria and the free energies of formation of fayalite and magnetite. American Mineralogist 72, 67–75.

O'Neill, H. S. C., 1991. The origin of the Moon and the early history of the Earth - a chemical model. Part 1: the Moon. Geochimica et Cosmochimica Acta 55, 1135–1157.

O'Neill, H. S. C., Berry, A. J., Eggins, S. M., 2008. The solubility and oxidation state of tungsten in silicate melts: implications for the comparative chemistry of W and Mo in planetary differentiation processes. Chemical Geology 255, 346–359.

O'Neill, H. S. C., Eggins, S. M., 2002. The effect of melt composition on trace element partitioning: an experimental investigation of the activity coefficients of FeO, NiO, CoO, MoO_2 and MoO_3 in silicate melts. Chemical Geology 186, 151–181.

O'Neill, H. S. C., Jenner, F. E., 2012. The global pattern of trace-element distributions in ocean floor basalts. Nature 49, 698–705.

O'Neill, H. S. C., Palme, H., 1998. Composition of the silicate Earth: implications for accretion and core formation. The Earth's Mantle. Cambridge University Press, 3–126.

Pahlevan, K., Stevenson, D. J., 2007. Equilibration in the aftermath of the lunar-forming giant impact. Earth and Planetary Science Letters 262, 438–449.

Palme, H., O'Neill, H. S. C., 2003. Cosmochemical estimates of mantle composition. Treatise on Geochemistry 2, 1–38.

Palme, H., O'Neill, H. S. C., 2014. Cosmochemical estimates of Mantle composition. Second edition of the Treatise on Geochemistry 2, 1–39.

Palme, H., Rammensee, W., 1981. The significance of W in planetary differentiation processes - evidence from new data on eucrites. Proceedings of the Lunar and Planetary Science Conference 12th, 949–964.

Papike, J., 2005. Comparative planetary mineralogy: Valence state partitioning of Cr, Fe, Ti, and V among crystallographic sites in olivine, pyroxene, and spinel from planetary basalts. American Mineralogist 90, 277–290.

Papike, J. J., Bence, A. E., Lindsley, D. H., 1974. Mare basalts from the

Taurus-Littrow region of the Moon. Proceedings of the Lunar and Planetary Science Conference 5th, 471–504.

Papike, J. J., Ryder, G., Shearer, C. K., 1998. Lunar samples. Reviews in Mineralogy and Geochemistry 36, 5.1–5.324.

Pearce, J. A., Harris, N. B. W., Tindle, A. G., 1984. Trace element discrimination diagrams for the tectonic interpretation of granitic rocks. Journal of Petrology 25, 956–983.

Ponader, C. W., Brown, G. E., 1998. Rare earth elements in silicate glass melt systems: I. Effects of composition on the coordination environments of La, Gd, and Yb. Geochimica et Cosmochimica Acta 53, 2893–2903.

Prowatke, S., Klemme, S., 2005. Effect of melt composition on the partitioning of trace elements between titanite and silicate melt. Geochimica et Cosmochimica Acta 69, 695–709.

Purton, J. A., Allan, N. L., Blundy, J. D., 1997. Calculated solution energies of heterovalent cations in forsterite and diopside: Implications for trace element partitioning. Geochimica et Cosmochimica Acta 61, 3927–3936.

Rai, N., van Westrenen, W., 2014. Lunar core formation: new constraints from metal-silicate partitioning of siderophile elements. Earth and Planetary Science Letters 388, 343–352.

Rapp, J. F., Drapper, D. S., 2013. Can fractional crystallization of a lunar magma ocean produce the lunar crust? Proceedings of the Lunar and Planetary Science Conference 44th, 2732–2733.

Rhodes, J. M., Vollinger, M. J., 2005. Ferric/ferrous ratios in 1984 Mauna Loa lavas: a contribution to understanding the oxidation state of Hawaiian magmas. Contributions to Mineralogy and Petrology 149, 666–674.

Righter, K., 2011. Prediction of metalsilicate partition coefficients for siderophile elements: An update and assessment of PT conditions for metalsilicate equilibrium during accretion of the Earth. Earth and Planetary Science Letters 304, 158–167.

Righter, K., Danielson, L. R., Pando, K. M., Shofner, G. A., Sutton, S. R., Newville, M., Lee, C. T., 2016. Valence and metal/silicate partitioning of Mo: Implications for conditions of Earth accretion and core formation. Earth and Planetary Science Letters 437, 89–100.

Righter, K., Drake, M. J., Yaxley, G., 1997. Prediction of siderophile element metal-silicate partition coefficients to 20 GPa and 2800 °C: the effects of pressure, temperature, oxygen fugacity, and silicate and metallic melt compositions. Physics of the Earth and Planetary Interiors 100, 115–134.

Righter, K., Pando, K. M., Danielson, L., Lee, C. T., 2010. Partitioning of Mo, P and other siderophile elements (Cu, Ga, Sn, Ni, Co, Cr, Mn, V, and W) between metal and silicate melt as a function of temperature and silicate melt composition. Earth and Planetary Science Letters 291, 1–9.

Righter, K., Shearer, C. K., 2003. Magmatic fractionation of Hf and W: constraints on the timing of core formation and differentiation in the Moon and Mars. Geochimica et Cosmochimica Acta 67, 2497–2507.

Righter, K., Walker, R. J., Warren, P. H., 2000. Significance of highly siderophile elements and osmium isotopes in the lunar and terrestrial mantles. Origin of the Earth and Moon University of Arizona Press, 291–322.

Ringwood, A. E., 1955. The principles governing trace element distribution during magmatic crystallization Part I: The influence of electronegativity. Geochimica et Cosmochimica Acta 7, 189–202.

Ringwood, A. E., 1979. Origin of the Earth and Moon. Springer, New York, United States of America.

Ringwood, A. E., Kesson, S. E., 1976. A dynamic model for mare basalt petrogenesis. Proceedings of the Lunar and Planetary Science Conference 7th, 1697–1722.

Ringwood, A. E., Kesson, S. E., 1977. Basaltic magmatism and the bulk composition of the Moon. The Moon 16, 425–464.

Röhrbach, A., Ballhaus, C., Golla-Schindler, U., Ulmer, P., Kamenetsky, V. S., Kuzmin, D. V., 2007. Metal saturation in the upper mantle. Nature 449, 456–458.

Rubie, D. C., Melosh, H. J., Reid, J. E., Liebske, C., Righter, K., 2003. Mechanisms of metal-silicate equilibration in the terrestrial magma ocean. Earth and Planetary Science Letters 205, 239–255.

Rufu, R., Aharonson, O., Peters, H. B., 2017. A multiple-impact origin for the Moon. Nature Geoscience 10, 89–94.

Ryerson, F. J., Hess, P. C., 1978. Implications of liquid–liquid distribution coefficients to mineral–liquid partitioning. Geochimica et Cosmochimica Acta 42, 921–932.

Saal, A. E., Hauri, E. H., van Orman, J. A., Rutherford, M. J., 2013. Hydrogen isotopes in lunar volcanic glasses and melt inclusions reveal a carbonaceous chondrite heritage. Science 340, 1317–1320.

Sato, M., 1976. Oxygen fugacity and other thermochemical parameters of Apollo 17 high-Ti basalts and their implications on the reduction mechanism. Proceedings of the Lunar and Planetary Science Conference 7th, 1323–1344.

Scherer, E., Münker, C., Mezger, K., 2001. Calibration of the Lutetium-Hafnium clock. Science 293, 683–687.

Schoenberg, R., Kamber, B. S., Collerson, K. D., Eugster, O., 2002. New W-isotope evidence for rapid terrestrial accretion and very early core formation. Geochimica et Cosmochimica Acta 66, 3151–3160.

Schönbächler, M., Lee, D. C., Rehkämpfer, M., Halliday, A. N., Hattendorf, B., Günther, D., 2005. Nb/Zr fractionation on the Moon and the search for extinct ^{92}Nb. Geochimica et Cosmochimica Acta 69, 775–785.

Schösnig, M., Hoffer, E., 1998. Compositional dependence of REE partitioning between diopside and melt at 1 atmosphere. Contributions to Mineralogy and Petrology 133, 205–216.

Schryer, D. R., Walberg, G. D., 1966. A theoretical and experimental investigation of the oxidation state of Molybdenum at temperature at which its trioxide is volatile. NASA Technical Report 232, 1–44.

Shannon, R. D., 1976. Revised effective ionic radii and systematic studies of interatomic distance in halides and chalcogenides. Acta Crystallographica 32, 751–767.

Shaw, D. M., 1970. Trace element fractionation during anatexis. Geochimica et Cosmochimica Acta 34, 237–243.

Shearer, C. K., Floss, C., 1999. Evolution of the Moon's mantle and crust as reflected in trace-element microbeam studies of lunar magmatism. Origin of the Earth and Moon, 339–359.

Shearer, C. K., Hess, P. C., Wieczorek, M. A., Pritchard, M. A., Parmentier, E. M., Borg, L. E., Longhi, J., Elkins-Tanton, L. T., Neal, C. R.,

Antonenko, I., Canup, R. M., Halliday, A. N., Grove, T. L., Hager, B. H., Lee, D. C., Wiechert, U., 2006. Thermal and magmatic evolution of the Moon. Reviews in Mineralogy and Geochemistry 60, 365–518.

Shearer, C. K., Papike, J. J., 1993. Basaltic magmatism on the Moon: A perspective from volcanic picritic glass beads. Geochimica et Cosmochimica Acta 57, 4785–4812.

Shearer, C. K., Papike, J. J., 1999. Magmatic evolution of the Moon. American Mineralogist 84, 1469–1494.

Shearer, C. K., Papike, J. J., 2005. Early crustal building processes on the moon: Models for the petrogenesis of the magnesian suite. Geochimica et Cosmochimica Acta 69, 3445–3461.

Shirley, D. N., 1983. A partially molten magma ocean model. Journal of Geophysical Research 88, 519–527.

Sims, K. W. W., Newson, H. E., Gladney, E. S., 1990. Chemical fractionation during formation of the Earth's core and continental crust: Clues from As, Sb, W, and Mo. Origin of the Earth 1, 291–317.

Smith, J. V., Anderson, A. T., Newton, R. C., Olsen, E. J., Wyllie, P. J., Crewe, A. V., Isaacson, M. S., Johnson, D., 1970. Petrologic history of the moon inferred from petrography, mineralogy and petrogenesis of Apollo 11 rocks. Geochimica et Cosmochimica Acta Supplement 1, 897–925.

Snyder, G. A., Taylor, L. A., Jerde, E. A., Riciputi, L. R., 1994. Evolved QMD-melt parentage for lunar highlands alkali suite cumulates: evidence from ion-probe rare-earth element analyses of individual minerals. Proceedings of the Lunar and Planetary Science Conference 25th, 1311–1312.

Snyder, G. A., Taylor, L. A., Neal, C. R., 1992. A chemical model for generating the sources of mare basalts: Combined equilibrium and fractional crystallization of the lunar magmasphere. Geochimica et Cosmochimica Acta 56, 3809–3823.

Sossi, P., Moynier, F., 2017. Chemical and isotopic kinship of iron in the Earth and Moon deduced from the lunar Mg-Suite. Earth and Planetary Science Letters 471, 125–135.

Sprung, P., Kleine, T., Scherer, E. E., 2013. Isotopic evidence for chondritic Lu/Hf and Sm/Nd of the Moon. Earth and Planetary Science Letters 380, 77–87.

Stanin, F. T., Taylor, L. A., 1980. Armalcolite: an oxygen fugacity indicator. Proceedings of the Lunar and Planetary Science Conference 11th, 117–124.

Steenstra, E. S., Lin, Y., Dankers, D., Rai, N., Berndt, J., Matveev, S., van Westrenen, W., 2017. The lunar core can be a major reservoir for volatile elements S, Se, Te and Sb. Scientific Reports 7, 14552.

Steenstra, E. S., Rai, N., Knibbe, J. S., Lin, Y. H., van Westrenen, W., 2016. New geochemical models of core formation in the Moon from metalsilicate partitioning of 15 siderophile elements. Earth and Planetary Science Letters 441, 1–19.

Suavet, C., Weiss, B. P., Cassata, W. S., Shuster, D. L., Gattacceca, J., Chan, L., Garrick-Bethell, I., Head, J. W., Grove, T. L., Fuller, M. D., 2013. Persistence and origin of the lunar core dynamo. Proceedings of the National Academy of Sciences USA, 8453–8458.

Sutton, S. R., Jones, K. W., Gordon, B., Rivers, M. L., Bajt, S., Smith, J. V., 1993. Reduced chromium in olivine grains from lunar basalt 15555: X-ray Absorption Near Edge Structure (XANES). Geochimica et Cosmochimica Acta 57, 461–468.

Taura, H., Yurimoto, H., Kurita, K., Sueno, S., 1998. Pressure dependence on partition coefficients for trace elements between olivine and the coexisting melts. Physics and Chemistry of Minerals 25, 469–484.

Taylor, G. J., 2007. Two views of the Moon's composition. Planetary Science Research Discoveries Available at: http://www.psrd.hawaii.edu/April07/Moon2Views.html.

Taylor, G. J., 2009. Ancient lunar crust: origin, composition, and implications. Elements 5, 17–22.

Taylor, G. J., Warner, R. D., Keil, K., Ma, M. S., Schmitt, R. A., 1980. Silicate liquid immiscibility, evolved lunar rocks and the formation of KREEP. Lunar Highlands Crust Pergamon Press, 339–352.

Taylor, S. R., 1975. Lunar Science: A Post-Apollo View. Pergamon Press Inc., New York, 390p.

Taylor, S. R., 1982. Planetary Science: A Lunar Perspective. Lunar and Planetary Institute, 508p.

Taylor, S. R., Jakes, P., 1974. The geochemical evolution of the Moon. Proceedings of the Lunar and Planetary Science Conference 5th, 1287–1305.

Taylor, S. R., Rudowski, R., Muir, P., Graham, A., Kaye, M., 1971. Trace element chemistry of lunar samples from the Ocean of Storms. Proceedings of the Lunar and Planetary Science Conference 2nd, 1083–1099.

Taylor, S. R., Taylor, G. J., Taylor, L. A., 2006. The Moon: a Taylor perspective. Geochimica et Cosmochimica Acta 70, 5904–5918.

Tepley, F. J., Lundstrom, C. C., McDonough, W. F., Thompson, A., 2010. Trace element partitioning between high-An plagioclase and basaltic to basaltic andesite melt at 1 atmosphere pressure. Lithos 118, 82–94.

Thacker, C., Liang, Y., Peng, Q., Hess, P., 2009. The stability and major element partitioning of ilmenite and armalcolite during lunar cumulate mantle overturn. Geochimica et Cosmochimica Acta 73, 820–836.

Thiemens, M., Leitzke, F. P., Sprung, P., Fonseca, R. O. C., Münker, C., 2017. Early differentiation of the Moon from combined high precision HFSE measurements and partitioning experiments. Proceedings of the 80th Annual Meeting of the Meteoritical Society, 1987.

Thomson, W., 1864. On the secular cooling of the Earth. Transactions of the Royal Society of Edinburgh 23, 167–169.

Touboul, M., Kleine, T., Bourdon, B., Palme, H., Wieler, R., 2007. Late formation and prolonged differentiation of the Moon inferred from W isotopes in lunar metals. Nature 450, 1206–1209.

Touboul, M., Puchtel, I. S., Walker, R. J., 2015. Tungsten isotopic evidence for disproportionate accretion to the Earth and Moon. Nature 520, 530–533.

Urey, H. C., 1952. The Planets: their origin and development. Yale University Press, New Haven, United States of America.

Urey, H. C., 1959. Primary and secondary objects. Journal of Geophysical Research 64, 1721–1737.

Urey, H. C., 1962. Origin of the tektites. Science 137, 746–748.

Urey, H. C., 1965. Meteorites and the Moon. Science 147, 1262–1265.

van Kan Parker, M., Mason, P. R. D., van Westrenen, W., 2011. Trace element partitioning between ilmenite, armalcolite and anhydrous silicate melt: Implications for the formation of lunar high-Ti mare basalts. Geochimica et Cosmochimica Acta 75, 4179–4193.

van Kan Parker, M., Mason, P. R. D., van Westrenen, W., 2011b. Experimental study of trace element partitioning between lunar orthopyroxene and anhydrous silicate melt: Effects of lithium and iron. Chemical Geology 285, 1–14.

van Westrenen, W., Blundy, J. D., Wood, B. J., 2000. Effect of Fe^{2+} on garnet-melt trace element partitioning: Experiments in FCMAS and quantification of crystal-chemical controls in natural systems. Lithos 53, 191–203.

van Westrenen, W., Draper, D. S., 2007. Quantifying garnet-melt trace element partitioning using lattice-strain theory: New crystal-chemical and thermodynamic constraints. Contributions to Mineralogy and Petrology 154, 717–730.

van Westrenen, W., Wood, B. J., Blundy, J. D., 2001. A predictive thermodynamic model of garnet–melt trace element partitioning. Contributions to Mineralogy and Petrology 142, 219–234.

Verbeek, R. D. M., 1897. Over Glaskogels van Billiton. Verslagen van der vergadering der Wissen Natuurkundig Afdeeling 5, 421–425.

Voegelin, A. R., Pettke, T., Greber, N. D., von Niederhäusern, B., Nägler,

T. F., 2016. Magma differentiation fractionates Mo isotope ratios: evidence from the Kos Plateau Tuff (Aegean Arc). Lithos 191, 440–448.

Wade, J., Wood, B. J., 2016. The oxidation state and mass of the Moon-forming impactor. Earth and Planetary Science Letters 442, 186–193.

Wade, J., Wood, B. J., Tuff, J., 2012. Metal-silicate partitioning of Mo and W at high pressures and temperature: evidence for late accretion of sulphur to the Earth. Geochimica et Cosmochimica Acta 85, 58–74.

Wadhwa, M., 2001. Redox state of Mars upper mantle and crust from Eu anomalies in Shergotite pyroxenes. Science 291, 1527–1530.

Wagner, T. P., Grove, T. L., 1997. Experimental constraints on the origin of lunar high-Ti ultramafic glasses. Geochimica et Cosmochimica Acta 61, 1315–1327.

Walker, R. J., 2009. Highly siderophile elements in the Earth, Moon and Mars: update and implications for planetary accretion and differentiation. Chemie der Erde 69, 101–125.

Walker, R. J., Horan, M. F., Shearer, C. K., Papike, J. J., 2004. Low abundances of highly siderophile elements in the lunar mantle: Evidence for prolonged late accretion. Earth and Planetary Science Letters 224, 399–413.

Wänke, H., Baddenhausen, H., Balacescu, A., Teschke, F., Spettel, B., Dreibus, G., Palme, H., Quijano-Rico, M., Kruse, H., Wlotzka, F., Begemann, F., 1972. Multi-element analysis of lunar samples and some implications of the results. Proceedings of the Lunar and Planetary Science Conference 3rd, 1251–1268.

Wänke, H., Palme, H., Baddenhausen, H., Dreibus, G., Jagoutz, E., Kruse, H., Spettel, B., Teschke, F., Thacker, R., 1974. Chemistry of Apollo 16 and 17 samples: Bulk composition, late stage accumulation and early differentiation of the moon. Proceedings of the Lunar and Planetary Science Conference 5th, 1307–1335.

Wänke, H., Rieder, R., Baddenhausen, H., Spettel, B., Teschke, F., Quijano-rico, M., Balacescu, A., 1970. Major and trace elements in lunar material. Proceedings of the Apollo 11 Lunar Science Conference, 1719–1727.

Wänke, H., Wlotzka, F., Baddenhausen, H., Balacescu, A., Spettel, B., Teschke, F., Jagoutz, E., Kruse, H., 1971. Apollo 12 samples: Chemical composition and its relation to sample locations and exposure ages, the two component origin of the various soil samples and studies on lunar metallic particles. Proceedings of the Lunar and Planetary Science Conference 2nd, 1187–1208.

Wänke, H. G., Dreibus, H., Palme, H., Rammensee, W., Weckwerth, G., 1983. Geochemical evidence for the formation of the Moon from material of the Earth's mantle. Proceedings of the Lunar and Planetary Science Conference 14th, 818–819.

Ward, P. D., 1982. Comments on the long-term stability of the Earth's obliquity. Icarus 50, 444–448.

Ward, P. D., Brownlee, D., 2000. Rare Earth: Why complex life is uncommon in the Universe. Copernicus, New York, United States of America.

Warren, P. H., 1985. The magma ocean concept and lunar evolution. Annual Review of Earth and Planetary Sciences 13, 201–240.

Warren, P. H., 1988. The origin of pristine KREEP: effects of mixing between urKREEP and the magmas parental to the Mg-rich cumulates. Proceedings of the Lunar and Planetary Science Conference 18th, 233–241.

Warren, P. H., Taylor, G. J., 2014. The Moon. Treatise on Geochemistry 2, 213–250.

Warren, P. H., Wasson, J. T., 1978. Compositional-petrographic investigation of pristine nonmare rocks. Proceedings of the Lunar and Planetary Science Conference 9th, 185–217.

Warren, P. H., Wasson, J. T., 1979. The origin of KREEP. Reviews of Geophysics 17, 73–88.

Warren, P. H., Wasson, J. T., 1980. Further foraging of pristine nonmare rocks: Correlations between geochemistry and longitude. Proceedings of the Lunar and Planetary Science Conference 11th, 431–470.

Wasserburg, G. J., Papanastassiou, D. A., Tera, F., Huneke, J. C., 1977. Outline of a lunar chronology. Philosophical Transactions of the Royal Society A 285, 7–22.

Watson, E. B., 1976. Two–liquid partition coefficients: experimental data and geochemical implications. Contributions to Mineralogy and Petrology 56, 119–134.

Weber, R. C., Lin, P. Y., Garnero, E. J., Williams, Q., Lognonné, P., 2011. Seismic Detection of the Lunar Core. Science 331, 309–312.

White, W. H., 2013. Geochemistry. Wiley, New Jersey, United States of America.

Wiechert, U., Halliday, A. N., Lee, D. C., Snyder, G. A., Taylor, L. A., Rumble, D., 2001. Oxygen isotopes and the moon-forming giant impact. Science 294, 345–348.

Wieczorek, M. A., Neumann, G. A., Nimmo, F., Kiefer, W. S., Taylor, G. J., Melosh, H. J., Phillips, R. J., Solomon, S. C., Andrews-Hanna, J. C., Asmarll, S. W., Konopivll, A. S., Lemoine, F. G., Smith, D. E., Watkins, M. M., Williams, J. G., Zuber, M. T., 2013. The crust of the Moon as seen by GRAIL. Science 339, 671–675.

Wijbrans, C., Klemme, S., Berndt, J., Vollmer, C., 2015. Experimental determination of trace element partition coefficients between spinel and silicate melt: the influence of chemical composition and oxygen fugacity. Contributions to Mineralogy and Petrology 169, 45.

Willbold, M., Elliott, T., 2016. Molybdenum isotope variations in magmatic rocks. Chemical Geology 449, 253–268.

Witt-Eickshen, G., O'Neill, H. S. C., 2005. The effect of temperature on the equilibrium distribution of trace elements between clinopyroxene, orthopyroxene, olivine and spinel in upper mantle peridotite. Chemical Geology 221, 65–101.

Wolbeck, J., Connoly, H. C., 2010. Origin of the Moon: Icy Impactor Model (IIM). Proceedings of the Annual Meeting of the Meteoritical Society 73rd, 5140.

Wolf, R., Anders, E., 1980. Moon and Earth: Compositional differences inferred from siderophiles, volatiles, and alkalis in basalts. Geochimica et Cosmochimica Acta 44, 2111–2124.

Wolf, R., Woodrow, A., Anders, E., 1979. Lunar basalts and pristine highland rocks: Comparison of siderophile and volatile elements. Lunar and Planetary Science Conference 10th, 2107–2130.

Wood, B. J., 2003. The principles controlling trace element partitioning in igneous processes. V. M. Goldschmidt Medalist Lecture (Goldschmidt Conference), A3.

Wood, B. J., Blundy, J. D., 1997. A predictive model for rare earth element partitioning between clinopyroxene and anhydrous silicate melt. Contributions to Mineralogy and Petrology 129, 166–181.

Wood, B. J., Blundy, J. D., 2001. The effect of cation charge on crystal-melt partitioning of trace elements. Earth and Planetary Science Letters 188, 59–71.

Wood, B. J., Blundy, J. D., 2014. Trace element partitioning: The influences of ionic radius, cation charge, pressure, and temperature. Treatise on Geochemistry 3, 421–448.

Wood, B. J., Walter, M. J., Wade, J., 2006. Accretion of the Earth and segregation of its core. Nature 441, 825–833.

Wood, J., 1986. Moon over Mauna Loa: A review of hypotheses of formation of Earth's Moon. Origins of the Moon, Lunar and Planetary Institute, 17–55.

Wood, J. A., Dickey, J. S., Marvin, U. B., Powell, B. N., 1970. Lunar anorthosites and a geophysical model of the moon. Geochimica et Cosmochimica Acta Supplement 1, 965.

Woodland, A. B., Koch, M., 2003. Variation in oxygen fugacity with depth

in the upper mantle beneath Kaapvaal craton, South Africa. Earth and Planetary Science Letters 214, 295–310.

Woodland, A. B., Peltonen, P., 1999. Ferric iron contents of garnet and clinopyroxene and estimated oxygen fugacities of peridotite xenoliths from the Eastern Finland Kimberlite Province. Proceedings of the International Kimberlite Conference 7, 904–911.

Xirouchakis, D., Hirschmann, M. M., Simpson, J. A., 2001. The effect of titanium on the silica content and on mineral-liquid partitioning of mantle-equilibrated melts. Geochimica et Cosmochimica Acta 65, 2201–2217.

Zhang, J., Dauphas, N., Davis, A. M., Leya, I., Fedkin, A., 2012. The proto-Earth as a significant source of lunar material. Nature Geoscience 5, 251–255.

Acknowledgments

First, I would like to thank my parents, Sandro and Maria Cristina for being the greatest examples of moral, ethics, kindness, respect and strength that I have, and for always backing me up, letting me choose my own path. My sister Juliana is also thanked for her advice and support, and for being such a good friend. I am also grateful to my other family members and long-time friends who have supported me along the way. I am grateful to God, whose blessings have made me who I am today, and who gave me the knowledge and the ability to better understand the natural world. I would like to also acknowledge Mariana de Brito, who has supported me throughout my career, shared similar goals and accepted the challenges together, encouraging me to always go ahead. In this regard, a very special gratitude goes to a group of special friends, some of whom I have met in Germany struggling with the same objectives, who will be forever in my mind and heart: Ernany Schmitz, Thaisa Guio, Mariana de Brito, Glauber Dorsch, and Rachel Werneck. Our meetings have given me the best memories in Bonn for sure and helped me to relax during times of stress.

My PhD. supervisor, Raúl O.C. Fonseca, is thanked for teaching me everything that I know about Experimental Petrology and sharing his exceptional scientific knowledge in Mineralogy, Petrology, and Geochemistry. I have been extremely lucky to have an advisor who cared so much about my work, and who responded to my queries always so promptly. I thank also the

"Moon" experts: Carsten Münker, Peter Sprung and Maxwell Thiemens, with whom the discussion of ideas has always been constructive and helped me shape the experimental campaign and better understand the results of this work.

This work would not have been possible without the financial support of the Brazilian Government through a PhD. from the National Council for Scientific and Technological Development (CNPq). I sincerely hope that I can give back to the Brazilian people as much as possible of the knowledge I have obtained during my academic development. The German Academic Exchange Service (DAAD) is also thanked, especially in the person of Mr. Pedro Sousa, for the partnership in the Exchange program, which provided some support during my PhD. in Bonn and the German language courses.

Last but not least, I wish to mention special thanks to the following friends and colleagues, who provided me assistance in different ways: Guilherme Mallmann, Carlos A. Sommer, Rualdo Menegat, Francisco Garcia, Alex Heuser, Lina Michely, Karoline Brückel, Rommulo Conceição, Patricia Roeser, Markus Lagos, Chris Ballhaus, Ambre Luguet, Maria Kirchenbaur, Frank Tomaschek, Thorsten Geisler-Wierville, Thorsten Nagel, Christoph Lenting, Thomas Schulz, Georg Növer, Dieter Lülsdorf, Henrik Blanchard, Philipp Krämer, Alexandra Elbakyan, Alessandro Bragagni, Anastasia Dolgushina, Ashlea Wainwright, Sebastian Kommescher, Nils Jung, Daniela Bungartz, Renate Schumacher, Beate Spiering, David van Acken, Anne Zacke, Aurelia Zirner, Lisa Baldwin, Kerstin Stange, Dorothee Pahsmann, Dagmar Hambach, Lars Dohmen, Jörg Rothe, Jörg Göttlicher, Frank Wombacher, Davod Yosefnezhad, Ruth Keppler, Kathrin Fassmer, Irena Miladinova, Ralph Steininger.

Copyright Clearance

SPRINGER NATURE LICENSE
TERMS AND CONDITIONS

Mar 20, 2018

This Agreement between Mr. Felipe Leitzke ("You") and Springer Nature ("Springer Nature") consists of your license details and the terms and conditions provided by Springer Nature and Copyright Clearance Center.

License Number	4312981496743
License date	Mar 20, 2018
Licensed Content Publisher	Springer Nature
Licensed Content Publication	Contributions to Mineralogy and Petrology
Licensed Content Title	Competing effects of crystal chemistry and silicate melt composition on trace element behavior in magmatic systems: insights from crystal/silicate melt partitioning of the REE, HFSE, Sn, In, Ga, Ba, Pt and Rh
Licensed Content Author	L. T. Michely, F. P. Leitzke, I. M. Speelmanns et al
Licensed Content Date	Jan 1, 2017
Licensed Content Volume	172
Licensed Content Issue	6
Type of Use	Thesis/Dissertation
Requestor type	academic/university or research institute
Format	print and electronic
Portion	full article/chapter
Will you be translating?	no
Circulation/distribution	<501
Author of this Springer Nature content	yes
Title	Crystal chemistry, melt composition and redox controls on the behavior of trace elements during lunar magmatism
Instructor name	Raúl O.C. Fonseca
Institution name	University of Bonn
Expected presentation date	Aug 2018
Requestor Location	Mr. Felipe Leitzke Steinmann Institut Uni Bonn Poppelsdorfer Schloss Bonn, NRW 53115 Germany Attn: Mr. Felipe Leitzke
Billing Type	Invoice
Billing Address	Mr. Felipe Leitzke Steinmann Institut Uni Bonn Poppelsdorfer Schloss Bonn, Germany 53115 Attn: Mr. Felipe Leitzke
Total	0.00 USD
Terms and Conditions	

Springer Nature Terms and Conditions for RightsLink Permissions

Springer Customer Service Centre GmbH (the Licensor) hereby grants you a non-exclusive, world-wide licence to reproduce the material and for the purpose and requirements specified in the attached copy of your order form, and for no other use, subject to the conditions below:

1. The Licensor warrants that it has, to the best of its knowledge, the rights to license reuse of this material. However, you should ensure that the material you are requesting is original to the Licensor and does not carry the copyright of another entity (as credited in the published version).

   If the credit line on any part of the material you have requested indicates that it was reprinted or adapted with permission from another source, then you should also seek permission from that source to reuse the material.

2. Where **print only** permission has been granted for a fee, separate permission must be obtained for any additional electronic re-use.

3. Permission granted **free of charge** for material in print is also usually granted for any electronic version of that work, provided that the material is incidental to your work as a whole and that the electronic version is essentially equivalent to, or substitutes for, the print version.

4. A licence for 'post on a website' is valid for 12 months from the licence date. This licence does not cover use of full text articles on websites.

5. Where **'reuse in a dissertation/thesis'** has been selected the following terms apply: Print rights for up to 100 copies, electronic rights for use only on a personal website or institutional repository as defined by the Sherpa guideline (www.sherpa.ac.uk/romeo/).

6. Permission granted for books and journals is granted for the lifetime of the first edition and does not apply to second and subsequent editions (except where the first edition permission was granted free of charge or for signatories to the STM Permissions Guidelines http://www.stm-assoc.org/copyright-legal-affairs/permissions/permissions-guidelines/), and does not apply for editions in other languages unless additional translation rights have been granted separately in the licence.

7. Rights for additional components such as custom editions and derivatives require additional permission and may be subject to an additional fee. Please apply to Journalpermissions@springernature.com/bookpermissions@springernature.com for these rights.

8. The Licensor's permission must be acknowledged next to the licensed material in print. In electronic form, this acknowledgement must be visible at the same time as the figures/tables/illustrations or abstract, and must be hyperlinked to the journal/book's homepage. Our required acknowledgement format is in the Appendix below.

9. Use of the material for incidental promotional use, minor editing privileges (this does not include cropping, adapting, omitting material or any other changes that affect the meaning, intention or moral rights of the author) and copies for the disabled are permitted under this licence.

10. Minor adaptations of single figures (changes of format, colour and style) do not require the Licensor's approval. However, the adaptation should be credited as shown in Appendix below.

Appendix — Acknowledgements:

For Journal Content:
Reprinted by permission from [**the Licensor**]: [**Journal Publisher** (e.g. Nature/Springer/Palgrave)] [**JOURNAL NAME**] [**REFERENCE CITATION** (Article name, Author(s) Name), [**COPYRIGHT**] (year of publication)

For **Advance Online Publication papers:**
Reprinted by permission from [**the Licensor**]: [**Journal Publisher** (e.g. Nature/Springer/Palgrave)] [**JOURNAL NAME**] [**REFERENCE CITATION**

(Article name, Author(s) Name), [**COPYRIGHT**] (year of publication), advance online publication, day month year (doi: 10.1038/sj.[JOURNAL ACRONYM].)

For Adaptations/Translations:
Adapted/Translated by permission from [**the Licensor**]: [**Journal Publisher** (e.g. Nature/Springer/Palgrave)] [**JOURNAL NAME**] [**REFERENCE CITATION** (Article name, Author(s) Name), [**COPYRIGHT**] (year of publication)

Note: For any republication from the British Journal of Cancer, the following credit line style applies:

Reprinted/adapted/translated by permission from [**the Licensor**]: on behalf of Cancer Research UK: : [**Journal Publisher** (e.g. Nature/Springer/Palgrave)] [**JOURNAL NAME**] [**REFERENCE CITATION** (Article name, Author(s) Name), [**COPYRIGHT]** (year of publication)

For **Advance Online Publication** papers:
Reprinted by permission from The [**the Licensor**]: on behalf of Cancer Research UK: [**Journal Publisher** (e.g. Nature/Springer/Palgrave)] [**JOURNAL NAME**] [**REFERENCE CITATION** (Article name, Author(s) Name), [**COPYRIGHT**] (year of publication), advance online publication, day month year (doi: 10.1038/sj.[JOURNAL ACRONYM])

For Book content:
Reprinted/adapted by permission from [**the Licensor**]: [**Book Publisher** (e.g. Palgrave Macmillan, Springer etc) [**Book Title**] by [**Book author**(s)] [**COPYRIGHT**] (year of publication)

Other Conditions:

Version 1.0

Questions? customercare@copyright.com or +1-855-239-3415 (toll free in the US) or +1-978-646-2777.

Title: Redox dependent behaviour of molybdenum during magmatic processes in the terrestrial and lunar mantle: Implications for the Mo/W of the bulk silicate Moon

Author: F.P. Leitzke,R.O.C. Fonseca,P. Sprung,G. Mallmann,M. Lagos,L.T. Michely,C. Münker

Publication: Earth and Planetary Science Letters

Publisher: Elsevier

Date: 15 September 2017